

October 2013

Photothermal Deflection Spectroscopy of Amorphous, Nanostructured and Nanocomposite Thin Films

Muhammad Shafiq Ahmed
The University of Western Ontario

Supervisor
Dr. Giovanni Fanchini
The University of Western Ontario

Graduate Program in Physics

A thesis submitted in partial fulfillment of the requirements for the degree in Doctor of Philosophy

© Muhammad Shafiq Ahmed 2013

Follow this and additional works at: <https://ir.lib.uwo.ca/etd>

 Part of the [Condensed Matter Physics Commons](#)

Recommended Citation

Ahmed, Muhammad Shafiq, "Photothermal Deflection Spectroscopy of Amorphous, Nanostructured and Nanocomposite Thin Films" (2013). *Electronic Thesis and Dissertation Repository*. 1678.
<https://ir.lib.uwo.ca/etd/1678>

This Dissertation/Thesis is brought to you for free and open access by Scholarship@Western. It has been accepted for inclusion in Electronic Thesis and Dissertation Repository by an authorized administrator of Scholarship@Western. For more information, please contact tadam@uwo.ca, wlsadmin@uwo.ca.

PHOTOTHERMAL DEFLECTION SPECTROSCOPY OF AMORPHOUS,
NANOSTRUCTURED AND NANOCOMPOSITE THIN FILMS

(Thesis format: Integrated Article)

by

Muhammad Shafiq Ahmed

Graduate Program in Physics

A thesis submitted in partial fulfillment
of the requirements for the degree of
Doctor of Philosophy

The School of Graduate and Postdoctoral Studies
The University of Western Ontario
London, Ontario, Canada

© Muhammad Shafiq Ahmed 2013

Abstract

The energy needs of the modern world are growing day by day, while sources of non-renewable fossil fuels are limited, so there is a need to efficiently use the existing resources and explore renewable energy sources. In order to harvest, store and efficiently utilize renewable energy, we need to explore new materials and improve the performance of existing ones. Among others, hydrogenated amorphous silicon (a-Si:H) with high optical absorption in the visible range of electromagnetic spectrum, is a low cost material for solar cells. But the efficiency of such solar cells is comparatively low because of intrinsic defects associated with its material structure and its degradation under illumination. Also the optical transparency and electrical conductivity of the window electrode are important factors that affect solar cell performance. Transparent and conducting carbon-based films (TCCF) have great potential to be used as electrodes in optoelectronics due to their transparency and high electrical conductivity. TCCF are not yet as competitive with indium-tin oxide (ITO) as transparent electrical conductors. In order to improve the efficiency of such materials, one needs to understand and curtail the defects for better cell performance.

This study is an experimental investigation of the optical and thermal properties of solar-grade materials and nanocomposites using photothermal deflection spectroscopy (PDS). PDS is a non-contact experimental technique based on the mirage effect. An automated PDS setup was assembled that is capable of measuring weak optical absorptions and thermal properties of thin film samples. A complementary setup, the 3-omega method, for thermal conductivity measurement was also built and used to compare the results obtained by the two methods. However, our primary focus was on the PDS

setup as a non-contact, non-destructive and sensitive technique. Also the role of convection heat transfer in PDS in the presence of highly thermally conducting nanoparticles in photothermal fluid is investigated.

The defects formation in a-Si:H thin films under light soaking was investigated and a model is proposed for self-repair of defects in thin films. Also optical, electrical and thermal properties of a set of graphene/graphene-like platelet thin films were investigated. A relationship between the electrical and thermal conductivities of these samples was established that could be applied to a large class of graphene-based thin films. The trade-off between electrical and thermal properties, along with transparency, will help the design of applications where electrical conductance, thermal management and transparency are required.

Key words:

Photothermal deflection spectroscopy, atomic force microscopy, hydrogenated amorphous silicon, Staebler-Wronski effect, solar cells, graphene, nanocomposites, optical absorption, electrical and thermal conductivity.

Co-Authorship Statement

This thesis contains material from published and submitted papers. The list of co-authors includes Dr. Giovanni Fanchini, Dr. Franco Gaspari, Dr. Ranjith Divigalpitiya, Mr. Sabastine Ezugwu and Arash Akbari-Sharbat. Muhammad Shafiq Ahmed was supervised by Dr. Giovanni Fanchini during the course of this thesis work. Muhammad Shafiq Ahmed was the principal investigator and primary author and was responsible for the final revisions of the papers included in chapters 3 (unpublished), 4 (under revision), 5 (published in Carbon 2013) and 6 (unpublished). Scientific content and editing of all papers was provided by Dr. Giovanni Fanchini. Dr. Franco Gaspari from the University of Ontario Institute of Technology, Oshawa, provided hydrogenated amorphous silicon thin films samples and contributed to the editing of the corresponding paper included in chapter 4. Dr. Ranjith Divigalpitiya of 3M Canada Co. London, Ontario, provided carbon based transparent and conducting thin film samples that were used with another set of samples in chapter 5. The graphene-RNA nanomaterial thin films that form the subject of chapter 6 have been prepared by me by using the method originally developed by Ms. Faranak Sharifi in collaboration with others, including myself. Specifically, when developing such method, I was in charge of performing electrical conductivity measurement on the samples and gave advice on how to make them more electrically conducting. Mr. Sabastine Ezugwu helped in making aluminum contacts on hydrogenated thin film and graphene samples using a vacuum evaporation system, helped in the assembly of the 3-omega setup for the thermal conductivity measurement and mounting of the probe beam in the photothermal deflection spectroscopy setup. Arash Akbari-

Sharbaf recorded under my instructions the SEM image in Figure 6.2 as well as the corresponding energy-dispersive X-ray (EDX) spectrum.

Acknowledgments

I would like to sincerely thank and honour all those who directly or indirectly helped and supported me in the completion of this research work, especially:

My supervisor, Dr. Giovanni Fanchini for, giving me this opportunity to enrol at Western University for graduate study, his support, continuous guidance throughout this work and his help in building experimental setups;

My advisory committee members Prof. Mahi R. Singh and Prof. Martin Zinke-Allmang for their time, precious suggestions and guidance;

Prof. Franco Gaspari, Faculty of Science, University of Ontario Institute of Technology, Oshawa, ON for his support and for providing us with hydrogenated amorphous silicon thin film samples;

Dr. Ranjith Divigalpitiya of 3M Canada Co. London, ON for collaboration and providing carbon-based transparent and conducting thin film samples for study;

Dr. Kanthi Kaluarachchi, Shailesh Nene and Peter Frank for their support during teaching in first year labs and, for their words of encouragement;

Fellow graduate students: Sabastine C. Ezugwu, Arash Akbari Sharbaf, Faranak Sharifi and Reg Bauld for their company and support;

Office staff: Clara Buma, Jodi Guthrie, Jackie McLean, Lisa Tocker, Nelia Andrade-Lo Russo for their support and cooperation during the whole study period;

Phin Perquin and Henry Leparskas for their technical support in setting up labs and computers.

Doug Hie for building and fixing electronic equipment;

Brian Dalrymple and Frank Van Sas for training and helping me in using mechanical tools and making components for our experimental setups;

Many thanks to funding organizations like NSERC, OSAP and SGPS for their generous financial support during my stay at Western.

Finally, I would like to thank my family members to whom I owe more than thanks, for their support, patience and sacrifices during my study.

Table of Contents

Abstract	ii
Co-Authorship Statement.....	iv
Acknowledgments.....	vi
Table of Contents	viii
List of Tables	xiii
List of Figures	xiv
List of Appendices	xxiii
List of Symbols, Abbreviations and Nomenclature	xxiv
Chapter 1	1
1 Introduction to photothermal deflection spectroscopy.....	1
1.1 Introduction.....	1
1.2 Photothermal deflection spectroscopy (PDS) setup.....	6
1.2.1 Transverse PDS setup	7
1.2.2 Collinear PDS setup.....	7
1.3 Applications of PDS	17
1.3.1 Optical absorption.....	17
1.3.2 Sub-band gap optical absorption.....	18
1.3.3 Thermal properties	19
1.3.4 Depth profiling.....	23
1.3.5 Thermal imaging.....	25
1.3.6 Other applications	26
1.4 Summary and thesis outline	26
References.....	29

Chapter 2.....	33
2 Experimental Setup	33
2.1 Photothermal deflection spectroscopy (PDS) setup.....	33
2.1.1 Pump beam source	36
2.1.2 Optical chopper	39
2.1.3 Monochromator.....	40
2.1.4 Reference photodiode	41
2.1.5 Sample holder cell.....	43
2.1.6 Sample stage	44
2.1.7 Probe beam.....	44
2.1.8 Position detector.....	45
2.1.9 Lock-in amplifier	46
2.1.10 Optical table	46
2.1.11 Calibration of the PDS setup.....	47
2.2 3-Omega method for thermal conductivity measurement	47
2.3 Ultraviolet visible (UV-vis) spectrophotometer	51
2.4 Atomic force microscopy (AFM)	53
2.5 Summary.....	55
Reference	57
Chapter 3.....	58
3 Theory of photothermal deflection spectroscopy and the role of convection in photothermal fluids	58
3.1 Introduction.....	58
3.1.1 Conduction.....	59
3.1.2 Convection	60
3.1.3 Radiation.....	60

3.2	Theory of thermal conductivity in semiconductors	61
3.3	The heat conduction equation	67
3.4	Thermal waves in thermally ultra-thin films and their applications	72
3.4.1	One-dimensional heat conduction – Thin “pump beam”	72
3.4.2	One-dimensional heat conduction – Thick “pump beam”	75
3.5	PDS signal in thermally ultra-thin films	77
3.5.1	PDS signal with negligible convection in the photothermal fluid	78
3.5.2	PDS signal in the presence of convection in the photothermal fluid	81
3.6	Determination of the heat exchange coefficient of photothermal fluids with nanoparticles in suspension.....	84
3.7	Materials used for experimental validation.....	91
3.7.1	Photothermal nano-fluid used for experimental validation	91
3.7.2	Sample used for experimental validation.....	94
3.8	Results and Discussion	96
3.9	Conclusion	105
	References	107
	Chapter 4.....	109
4	Staebler-Wronski effect, thermal conductivity, and self-repair of hydrogenated amorphous silicon during light-induced degradation.....	109
4.1	Introduction.....	109
4.2	Electronic structure	111
4.3	Growth of hydrogenated amorphous silicon (a-Si:H) by saddle field glow discharge	114
4.4	Light induced degradation of a-Si:H.....	116
4.5	Characterization of a-Si:H thin films	119
4.6	Light-soaking experiments.....	120

4.7 Theory	122
4.7.1 Optical absorption	122
4.7.2 Tauc gap	123
4.7.3 Urbach energy	123
4.7.4 Excess absorption	124
4.7.5 Thermal conductivity	125
4.8 Results and discussion	126
4.9 Conclusion	134
References	135
Chapter 5	138
5 Relationship between electrical and thermal conductivity in graphene-based transparent and conducting thin films	138
5.1 Introduction	138
5.2 Vacuum filtration setup	140
5.3 Experimental	143
5.4 Results and discussion	149
5.5 Summary	156
References	157
Chapter 6	160
6 Thermophysical properties of thin film nanocomposites of ribonucleic acid and graphene nanoplatelets	160
6.1 Introduction	160
6.2 Experimental	163
6.2.1 Sample preparation	163
6.2.2 Thermal conductivity measurements	168
6.3 Results and discussion	170

6.4 Conclusion	183
References	185
Chapter 7	188
7 Conclusion and future work	188
7.1 Conclusion	188
7.2 Future work	191
Appendices	193
Curriculum Vitae	229

List of Tables

Table 1.1 Summary of PDS studies found in the literature.	9
Table 2.1 Thermophysical properties of some commonly used photothermal fluid.	43
Table 2.2 Optical and thermal properties of fluids used in this study	44
Table 3.1 Optical and thermal properties of fluids used in this study	87
Table 3.2 Dependency of dimensionless parameters, thickness of thermal boundary layer and heat exchange coefficient and heat exchange rate on fraction of nanoparticles.....	90
Table 3.3 Physical and fluid dynamic properties of CCl ₄ at room temperature [22,23]..	92
Table 3.4 Room temperature physical properties of carbon nanotubes used in this study [24,25].	92
Table 3.5 Physical properties of PEDOT:PSS sample used in this study[25-27].....	95
Table 4.1 Hydrogenated amorphous silicon (a-Si:H) samples parameters.	130

List of Figures

<p>Figure 1.1 Schematics of the excitation of a solid by light. The outcome may be 1) Radiative recombination with the re-emission of photon (luminescence) or 2) Non-radiative recombination with the capture of the photoexcited electron-hole pair by a defect or impurity state and the subsequent dissipation of energy as generation of heat and lattice vibrations. In solids, lattice vibrations can be of two forms: 2a) propagating lattice vibration, or acoustic phonons (which effect can be detected by photoacoustic spectroscopy) or 2b) non-radiative propagating lattice vibrations, or optical phonons (which effect can be detected by photothermal spectroscopy).</p>	3
<p>Figure 1.2 Schematic of transverse PDS setup where “pump beam” is perpendicular to the probe beam.</p>	8
<p>Figure 1.3 Schematic of collinear PDS setup where “pump beam” is oblique to the probe beam.</p>	8
<p>Figure 1.4 Schematic of thermal and optical thicknesses. (a) Thermally and optically thick sample whose thickness d is greater than both thermal diffusion length L_D and optical attenuation length l_α, (b) thermally thick and optically thin sample whose thickness d is greater than thermal diffusion length L_D but smaller than the optical attenuation length l_α, (c) thermally thin and optically thick sample whose thickness d is less than thermal diffusion length L_D and greater optical attenuation length l_α, and (d) thermally and optically thin sample whose thickness d is smaller than both thermal diffusion length L_D and optical attenuation length l_α of the sample.</p>	21
<p>Figure 1.5 Schematic illustration of thermal penetration depth. (a) Thermal diffusion length is shorter at higher modulation frequency of the “pump beam” than (b) the that at lower modulation frequency due to the fact that at lwer modulation</p>	

frequency more heat is deposited per cycle and thermal diffusion length increases.	24
Figure 2. 1 Schematic of transverse PDS setup, where ‘A’ is AM 1.5 light source for “pump beam”, ‘B’ is mechanical chopper, ‘C’ is movable monochromator, ‘D’ is reference photodiode, ‘E’ is sample in photothermal fluid cell, ‘F’ is probe laser beam, ‘G’ is position detector, ‘H’ is Lock-in mode data acquisition and ‘I’ is beam splitter.....	34
Figure 2.2 Pictures of different instruments used in the PDS setup.	35
Figure 2.3 Spectral response of (a) Xe lamp and (b) QTH lamp [3].	38
Figure 2.4 Thorlabs chopper wheels (a) for frequency range 1 Hz to 100 Hz and (b) for frequency range 20 Hz to 1 kHz) [4].....	40
Figure 2.5 Reference photodiode (PD)response at different pump beam powers. The output voltage of PD increases linearly with increasing “pump beam” power.	42
Figure 2.6 Schematic of 3-omega setup for thermal conductivity measurement. Sample is placed in a vacuum chamber to avoid the heat loss to surrounding.	49
Figure 2.7 Pictures of 3 ω Setup (a) Closed and (b) Open.	50
Figure 2.8 Schematic of a UV-vis spectrometer, where a rotating mirror directs the light beam to reference and sample alternatively.	52
Figure 2.9 Schematic of AFM. A probe reflecting from the back of the tip is detected by a quadrant detector magnifies the tip’s movement.	53
Figure 3.1 Schematic of phonon-phonon interaction (a) Normal three-phonon process and (b) Umklapp three-phonon process.	64
Figure 3.2 Summary of various phonon-scattering mechanisms affecting the lattice thermal conductivity in crystalline materials at different temperatures.	67

Figure 3.3 Volume element considered for heat balance equation.	68
Figure 3.4 The three different boundary conditions for the Fourier’s equation of heat (3.17): (a) Dirichlet, (b) Neumann and (c) Robin conditions.....	71
Figure 3.5 Thin film sample on a non-absorbing substrate, illuminated by a (a) thin pump beam in the y-direction, and very long and uniform in the z-direction, and (b) thick pump beam in the y-direction (length L_y) and very long in the z-direction. In both cases the probe beam is parallel to the y-axis.....	74
Figure 3.6 (a) UV-visible spectra of CCl_4 with different concentrations of CNTs and (b) transmittance of CNTs suspension versus CNTs concentration at 550 nm incident wavelength. It can be observed that the transmittance decreases with increasing CNTs concentration and drops to 65% for the undiluted CNTs suspension.	93
Figure 3.7 (a) Molecular structure of PEDOT:PSS [25] and (b) Image of typical PEDOT:PSS thin film.	95
Figure 3.8 Optical absorption coefficient of PEDOT:PSS thin film, dotted line is eye guide.	95
Figure 3.9 Measured (a) phase and (b) amplitudes of the PDS signal of our PEDOT:PSS thin film sample versus incident photon energy at different volume fractions of CNTs in carbon tetrachloride (CCl_4).....	96
Figure 3.10 (a) Phases, (b) normalized amplitudes and (c) heat exchange rates obtained using eq. (3.69) from the values of B_ϕ displayed in panel b. Data were recorded on the PEDOT:PSS film described in sec. 3.7.2 at different the volume fractions of CNTs dispersed in carbon tetrachloride (CCl_4). Data was measured at five different wavelengths of “pump beam” and used to get with error bars. It can be seen that the increase of H at increasing p is very slow with the exception of very low p. This was to be expected because the qualitative	

estimations that were summarized in Table 3.2 suggest that H increases a $p^{\zeta/6}$, in which $\zeta < 1$, according to relationship (3.57) or (3.58). 98

Figure 3.11 (a) Thermal conductivity, (b) density and (c) specific heat of CCl_4 :CNTs nanofluid with increasing volume fraction of CNTs. It can be seen that thermal conductivity increases significantly while density and specific heat remain almost unchanged at any fraction of CNTs. 100

Figure 3.12 (a) Effective thermal diffusivity and (b) effective kinematic viscosity of CCl_4 :CNTs suspension. It can be observed that at any fraction of CNTs increase in dynamic viscosity is relatively less significant but thermal diffusivity increases significantly with increasing fraction of CNTs. 101

Figure 3.13 Effect of increasing fraction of SWCNTs in the photothermal fluid on the dimensionless numbers used to characterize the fluid behaviour (a) Effective Rayleigh number, (b) Effective Prandtl number and (c) Effective Nusselt number, and (d) Effective thermal diffusion length. 102

Figure 3.14 (a) Convection heat exchange rate. (b) normalized amplitude of PDS signal in the presence of convection and (c) convection heat transfer coefficient as a function of CNTs fraction in the photothermal fluid. 104

Figure 4. 1 Schematic of RDF for c-Si and a-Si adopted from [5,6]. There are well defined peaks for c-Si but for a-Si first peak is clear , second is broadened and there is no peak after that showing that a-Si lacks long range order. 110

Figure 4. 2 A schematic representation of the electronic density of states (DOS) of a-Si:H. The dashed vertical lines show the mobility edges, which are defined as the energy level separating extended states from localized states. 112

Figure 4.3 Schematic of DC saddle-field deposition system. There are two cathodes symmetrically placed on both sides of central anode to increase the electrons collision path. 116

Figure 4.4 (a) Optical absorption coefficient for samples #1-3 as received, extracted from PDS data at low photon energy and spectroscopic ellipsometry data (Jobin-Yvon Uvisel ellipsometer coupled with Tauc-Lorenz model) at high photon energy - (b) Schematic density of states of the different regions of optoelectronic transitions in a-Si:H: i) Parabolic (Tauc-like) transitions ii) Urbach tails iii) Excess absorption related to dangling bonds. α_{exc} was determined by fitting this region using a Gaussian line..... 127

Figure 4.5 (a) Tauc band gap, E_g (b) Urbach energy, E_0 (c) defect density, N_d and (d) thermal conductivity (K_s) in samples #1-3 during light soaking experiments under the first AM 1.5 illumination cycle (solid dots) as a function of illumination time (t). In all of the panels, open dots refer to data recorded during a second light soaking cycle after annealing the samples at 200⁰C in Ar, which restored their properties. 128

Figure 4.6 (a) Thermal conductivity (K_s) as a function of defect density (N_d) for samples #1-3 at different stages of a Staebler-Wronski cycle. Samples #1 and #2 follow the same trend. The fact the trend of sample #1 is downshifted can be related to the higher porosity of this sample and lower sound velocity, (b) Temperature of the samples during AM 1.5 illumination (T_{ill}) determined using Fourier's equation of heat as a function of illumination time (t). In both panels, open dots refer to data recorded during a second light soaking cycle after annealing the samples at 200⁰C in Ar, which restored their properties. 131

Figure 4.7 Thermal conductivity of a-Si:H thin film as a function of light soaking time measured by PDS and 3-omega methods which is similar to the one measured by PDS. 133

Figure 5.1 Schematic of vacuum filtration setup used for the preparation of graphene and graphene-based nanocomposite thin films. The film shown in the picture is extremely thick and is only for visual demonstration. 142

Figure 5.2 (a) AFM image of the thinnest sample prepared using the vacuum-filtration method of Lotya *et al.* [11] (b) AFM image of the thickest sample prepared using the same method [11] (c) AFM image of a sample prepared by 3M Canada Co. f and N were determined for each one of our samples by processing and averaging ten AFM micrographs of this type. 145

Figure 5.3 (a) Transmittance of TCCF prepared using the method of Lotya *et al.* [11] and a proprietary method of 3M Canada. (b) Transmittance at 2.25 eV as a function of the thickness of graphitic platelets, and (c) Average number of graphene layers as a function of the fraction f of substrate area covered by the platelets. Dotted line represents the fit $N \approx A \cdot f$, with $A = 120$ 146

Figure 5.4 (a) Electrical conductivity (K_{el}) as function of the fraction f of surface area covered by graphene platelets and (b) as a function of number of layers. Solid lines represent simulation of experimental data according to eq. 5.2. (c) Thermal conductivity (K_s) determined by PDS as function of the fraction f of surface area covered by graphene platelets and (d) as a function of number of layers, N 149

Figure 5.5 (a) Schematic of the film model used to calculate the thermal conductivity as in eq. 5.8, with graphitic platelets of N layers and $2N$ -layer thick junctions between platelets. (b) Thermal conductivity vs. electrical conductivity. The dotted line is a simulation assuming the model given by eqs. 5.2 and 5.8 and leading to simplified eq. 5.9. 155

Figure 6.1 AFM phase and topography images of films made by (a) thinner graphene platelets of pre-treated n-G that is mostly free from RNA-VI and (b) thicker graphene platelets of mic-G which are mostly covered by RNA-IX that makes an insulating cover. 166

Figure 6.2 (a) SEM image and (b) EDX of a RNA/n-G nanocomposite thin film. Presence of Phosphorous in the EDX verifies the presence of RNA in the film and it is used to quantify the RNA content in the nanocomposite. 167

Figure 6.3 (a) AFM topography image of a thick film, (b) Optical image of very sparse film on silicon oxide coated silicon substrate, (c) thickness and (d) fraction of covered area of the films versus the filtration volume of the graphene suspension for sets of samples made from nG. (e) Thickness and (f) fraction of covered area of the films versus the filtration volume of the graphene suspension for the set of samples made from mic-G. It can be seen that films made from treated n-G are thinner than the ones made from untreated n-G while both sets of samples have same fraction of covered area of the substrate. 171

Figure 6.4 (a) Normalized amplitude of PDS signal versus modulation frequency measured at low modulation frequencies and (b) Fit of eq. (6.2) for different values of $L_y/2D_s$ that depend on thermal diffusivity. $D_s = 5 \cdot 10^{-5} \text{ m}^2 \cdot \text{s}^{-1}$ for our samples, it can be seen that at low frequencies PDS amplitude is inversely proportional to modulation frequency..... 174

Figure 6.5 (a) Normalized amplitude of PDS signal and (b) phase of PDS signal as function of square root of modulation frequency, for a typical sample. It can be seen that both $\ln(A_\phi \cdot \omega)$ and phase lag decrease linearly with square root of frequency..... 176

Figure 6.6 Effective thermal conductivity of thin film of RNA/n-G composite as function of RNA fraction in the nanocomposite. It can be seen that at a constant fraction of n-G the thermal conductivity of the nanocomposite decreases with increasing RNA content in the nanocomposite. The predictions of MEMT [23] are also shown. It can be seen that experimental data matches well with the prediction of MEMT including the effects of interface density..... 179

Figure 6.7 (a) Thermal conductivity and (b) Thermal diffusivity as a function of f for the sets of samples used in this study along with the data from Ref, 31. It can be seen that for any value of f , the thermal conductivity of RNA/graphene platelets thin films is less than the corresponding value for pure graphene samples..... 181

Figure 6.8 Thermal conductivity versus electrical conductivity of the samples used in the present study. Thermal conductivity decreases with increasing electrical conductivity due to increasing number of graphene layers.....	183
Figure A.1 Flow chart of data acquisition and automatic control of the PDS setup.....	193
Figure A.2 LabView front panel of data acquisition and automatic control of the PDS setup.	194
Figure A.3 LabView block diagram of data acquisition and automatic control of the PDS setup (The diagram is magnified and split into three parts - next 3 pages).	195
Figure A.3.1 (Left part) LabView block diagram of data acquisition and automatic control of the PDS setup.	196
Figure A.3.2 (Central part) LabView block diagram of data acquisition and automatic control of the PDS setup.	197
Figure A.3.3 (Right part) LabView block diagram of data acquisition and automatic control of the PDS setup.	198
Figure A.4 Flow chart of data acquisition and automatic control of the 3ω setup.	199
Figure A.5 LabView front panel of data acquisition and automatic control of the 3ω thermal conductivity measurement setup.....	200
Figure A.6.1 (First half) LabView block diagram of data acquisition and automatic control of the 3ω thermal conductivity measurement setup.	201
Figure A.6.2 (Second half) LabView block diagram of data acquisition and automatic control of the 3ω thermal conductivity measurement setup.	202
Figure B.1 Thin film sample on a non-absorbing substrate, illuminated by a (a) thin pump beam in the y-direction, and very long and uniform in the z-direction, and (b) thick pump beam in the y-direction (length L_y) and very long in the z-direction. In both cases the probe beam is parallel to the y-axis.	204

Figure B.2 Schematic of the temperature profile of photothermal fluid under illumination. 214

Figure B.3 Schematic of temperature profile of the fluid at the fluid-sample interface, used for the determination of amplitude and phase of angle of photothermal deflection signal. 215

List of Appendices

Appendix A: Computer control and data acquisition	193
Appendix B: Convection enhanced photothermal deflection spectroscopy	203
Appendix C: Matlab routine to simulate amplitude of PDS signal	218
Appendix D: Copyrights	223

List of Symbols, Abbreviations and Nomenclature

α	Optical absorption coefficient
β	Temperature coefficient of fluid
γ	Gruneisan parameter
$\delta, \varepsilon, \eta$ and ζ	Fitting parameters (used in fitting of effective thermal conductivity of nanofluid)
ρ	Mass density
σ_{SB}	Stephen Boltzmann constant
\mathcal{T}_{fp}	Nanofluid transmittance
ω	Modulation frequency
Λ	Phonon mean free path
Δ_{ϕ}	Phase of PDS signal
Φ	Interface density
a_R	Aspect ratio of CNT
A_{ϕ}	Amplitude of PDS signal
B_{ϕ}	Normalized amplitude of PDS signal
AFM	Atomic Force Microscopy
a-Si:H	Hydrogenated amorphous silicon
c	Specific heat
C_s	Thermal capacitance of sample
CNTs	Carbon nanotubes

DOS	Density of states
CVD	Chemical vapour deposition
D_i	Thermal diffusivity = s for sample, f for photothermal liquid and eff for effective value sample-fluid system
EDX	Energy dispersive X-ray spectroscopy
EQE	External quantum efficiency
f	Fraction of substrate area covered by the film
f_R	Fraction of RNA in RNA/graphene nanocomposite
GB	Grain boundary
h	Convection heat exchange coefficient
H	Heat transfer rate
IR	Infrared
ITO	Indium tin oxide
K_i	Thermal conductivity i = s for sample, i = f for photothermal liquid, i = G for graphene matrix and i = eff for effective value for mixture
L_x	Sample thickness
L_y	“Pump” beam width
L_z	“Pump” beam height
LabVIEW	Laboratory Virtual Instrument Engineering Workbench
micG	Microcrystalline graphite
MEMT	Modified effective medium theory
MFP	Mean free path

n	Refractive index
nG	Nanocrystalline graphite
N	Number of layer in graphene/graphitic flake
Nu	Nusselt number
NIR	Near-infrared
P ₀	“Pump” beam power
PCBM	Phenyl-C61-butyrac acid methyl ester
PDS	Photothermal deflection spectroscopy
PECVD	Plasma enhanced chemical vapour deposition
PEDOT:PSS	Poly (3,4-ethylenedioxythiophene):poly (styrene- sulfonate)
Pr	Prandtl number
PT	Photothermal
QTH	Quartz-tungsten-halogen
Ra	Rayleigh number
Re	Reynolds number
RNA	Ribonucleic acid
S ₀	Electrical conductivity at percolation threshold
SEM	Scanning electron microscope
STM	Scanning tunnelling microscope
SWE	Staebler-Wronski effect
TCCFs	Transparent carbon-based conducting films
TEM	Transmission electron microscopy
T _{ill}	Temperature under illumination

UV-vis

Ultraviolet-visible

XRD

X-Ray diffraction

Chapter 1

1 Introduction to photothermal deflection spectroscopy

Knowledge of the thermal and optical properties of materials can be achieved through systematic studies of light-matter interactions. Generation of heat in a solid as a consequence of the absorption of light and the subsequent transformation of photon energy into thermal energy produces the so called photothermal (PT) effect. Heat generated in this way induces a change in temperature, pressure, and refractive index of the background medium surrounding the solid, which can be measured by specific transducers. Photothermal deflection spectroscopy (PDS) is an experimental technique, which is able to measure the optical and thermal transport properties of solid by means of specific photo-induced relaxation (PIR) effects in these media. In this chapter an introduction to PDS, its brief history and some standard applications for material characterization are presented.¹

1.1 Introduction

Photothermal deflection spectroscopy (PDS) belongs to a class of high sensitivity spectroscopic techniques which are based on detecting the photo-induced (PI) effects of light [1-8] at the interface between a fluid for which the optical properties are known and a solid sample of unknown optical properties. Light may interact with solids in so many different ways. Light absorption, emission and inelastic scattering are a few different ways in which photons can interact with matter and result in an energy transfer to and

¹ Material presented in this chapter will be submitted as review paper.

from a solid sample [9,10]. Spectroscopy is the study of the interaction of electromagnetic radiation at specific wavelengths with matter. The nature of such interaction depends upon the properties of the sample. When a sample is irradiated with electromagnetic radiation, a part or whole of the incident light is absorbed by the material. Typically, visible and near infrared (NIR) radiation bring the electrons of the absorbing material to an excited state. In general, excited electronic state may relax either by radiative recombination including spontaneous and stimulated emission, or by non-radiative processes of photo-induced relaxation which mainly result in the generation of heat, sound or motion within a solid. A schematic of light–matter interaction is shown in Figure 1.1(a). In homogeneous solids, photo-excited electronic states mainly relax and de-excite via electron–phonon coupling with vibrations of the atoms forming the solid lattice [9].

Phonons are collective lattice vibrations of crystalline or partially ordered solids, which can be divided into three classes: acoustic phonons are propagating waves of lattice vibrations that involve the relative oscillatory motion between different unit cells of the solid lattice; optical phonons are quasi-stationary waves of lattice vibrations that involve the relative oscillatory motion of different atoms within individual cells of the solid lattice; and surface phonons are waves of lattice vibrations that are confined in the proximity of a solid surface. Photo-induced relaxation (PIR) effects involving electron coupling with acoustic phonons are called photoacoustic (PA) effects. PIR effects involving electron coupling with optical phonons are the most significant and are termed photothermal (PT) effects and will be subject of this study. PIR effects involving electron coupling with surface phonons in thin membrane are termed photothermal bending (PTB)

effects and involve the oscillation of the entire membrane in the surrounding background media.

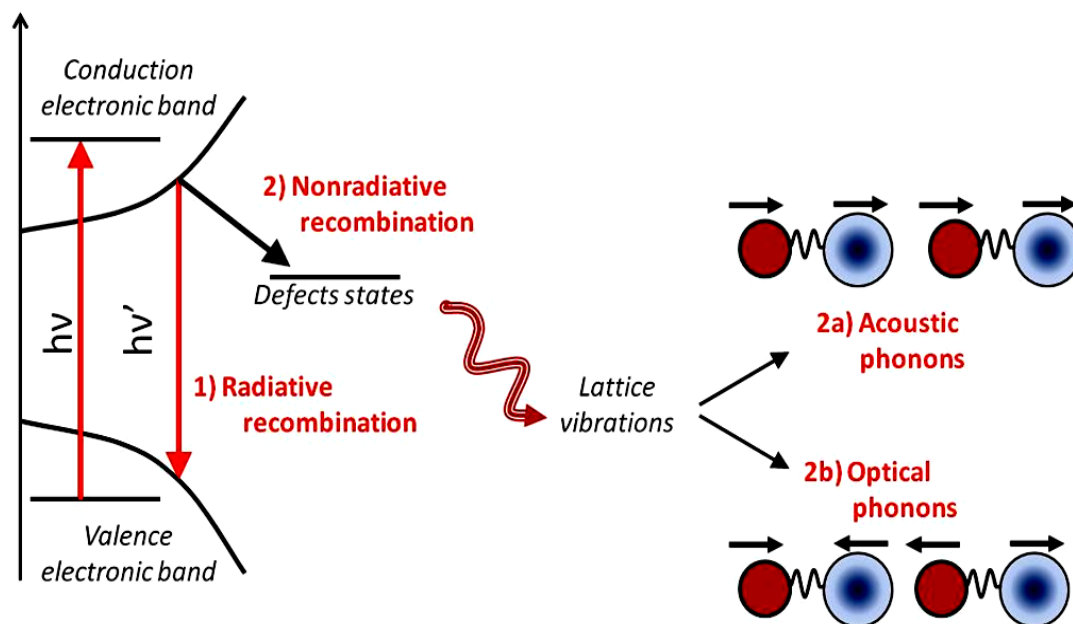


Figure 1.1 Schematics of the excitation of a solid by light. The outcome may be 1) Radiative recombination with the re-emission of photon (luminescence) or 2) Non-radiative recombination with the capture of the photoexcited electron-hole pair by a defect or impurity state and the subsequent dissipation of energy as generation of heat and lattice vibrations. In solids, lattice vibrations can be of two forms: 2a) propagating lattice vibration, or acoustic phonons (which effect can be detected by photoacoustic spectroscopy) or 2b) non-radiative propagating lattice vibrations, or optical phonons (which effect can be detected by photothermal spectroscopy).

The discovery of the PA effect dates back to 1880 when A.G. Bell patented the photophone. He noticed that an audible sound could be heard from a tube filled with selenium when the light shining the tube was modulated [9]. Periodic heat generated in the sample resulted in the excitation of periodic lattice oscillations of the sample which could be detected either by using a piezoelectric transducer directly in contact with the sample or detected by ear. An acoustic wave was generated in the adjoining medium when the sample was placed in a resonant cavity as the expansion of a material generates acoustic waves in the surrounding gas. A thin layer of gas adjacent to heated surface responds to periodic heat flow and acts as a piston to push the gas that produces acoustic signal [11]. After Bell's discovery, no or little advances in PIR technique had been reported for the following 100 years, until 1976. In that year, using a set of different samples that were placed in a more sophisticated photoacoustic cell equipped with an amplified microphone attached to it, Rosencwaig and Gersho [12] developed a more comprehensive theory of the photoacoustic effect in solids, which led to a rapid development of PA techniques in the 1980s and also generated a widespread interest in photothermal science due to relative similarity of the theoretical models underlying these two types of phenomenon.

The temperature rises as a result of heat generated in the sample and this can be directly measured with thermocouples and pyro-electric detectors [8], which can be subsequently used to determine the sample's optical and thermal properties using specific models based on the Fourier equation of heat. The rise in temperature can also be measured by using infrared (IR) detectors [13] since the thermal infrared emission is also related to the temperature of the sample, but maximizing the IR radiation reaching the

detector while keeping the incident radiation to a minimum is challenging [9]. Another problem in the measurement of emitted IR light consists of the low signal-to-noise ratio that results from the large background radiation relative to sample emission. M. Handke and N.J. Harrick [14] have used ellipsoidal mirrors to collect the emitted radiation over a very large solid angle and showed an improved signal-to-noise ratio, but practical measurements of the amplitude of the PT effect have been rarely demonstrated in this way. Fortunately, PT heating of an absorbing sample also results in strong thermal load in the adjoining background medium even though this is completely transparent. In specific fluids such thermal loads lead to even more important change in their refractive index. These fluids are called photothermal media. The change in refractive index of photothermal media can be probed by the deflection of a low intensity laser beam passing through the fluid region in which a gradient of refractive index is produced due to a temperature gradient. This detection technique forms the basis of Photothermal Deflection Spectroscopy and will be discussed in detail in section 1.2.

Photothermal heating of a sample can also result in a distortion of the sample surface due to localized thermal expansion and PTB effects [15-17]. Optical detection of the resulting surface displacement forms the basis of photothermal bending spectroscopy, which can be implemented by using a probe beam that is reflected from heated region and detected by an interferometer or position sensor. The sensitivity of photothermal displacement method is low and noise is high, however the advantage is that this method provides a detailed characterization of the surface optical properties of a solid sample and can be applied in vacuum without any need of a coupling medium.

The rise in temperature of a sample as a result of modulated heating causes a periodic change in the optical reflectivity of the sample. The subsequent change in the reflectance of the surface of the sample is proportional to the periodic increase in temperature [8]. This method, called thermorefectance, is well suited for the investigation of metallic thin films because of their high reflectivity in visible photon energy region. Ju and Goodson [18] have used thermorefectance for rapid thermal mapping of micro devices. Pulsed thermorefectance methods have been used to determine the thermal conductivity of metallized thin films on silicon dioxide [19], thin films of tetrahedral amorphous carbon [20] and aluminum oxide thin films. Wu et al. [21] used both photothermal reflectance and photothermal bending spectroscopy to measure the thermal conductivity of gold, SiO₂ and ZrO₂ films on different substrates.

1.2 Photothermal deflection spectroscopy (PDS) setup

PDS was first introduced by Boccara *et al.* [1] as a method to measure the optical absorption of a Nd₂(MoO₄)₃ crystal. It was subsequently utilized by Aamodt and Murphy [2, 3], and later by Jackson *et al.* [4]. PDS is based on the mirage effect [1-3,7,22]. Mirage effect is an optical phenomenon based on bending of light ray when it passes through a medium with varying refractive index. In a PDS spectrometer a sample is exposed to a periodically modulated light beam that is sometimes called “pump beam”. Periodic heat is produced in the sample as a result of the consequent absorption of light from the “pump beam”, which results in non-radiative de-excitation of electrons within the material. The heat generated in the sample diffuses into the adjoining background medium, that is generally chosen to be a transparent photothermal fluid, and the subsequent thermal load produces a periodic temperature gradient and refractive index

gradient in such medium. A low intensity laser beam that is sometimes called “probe beam” crosses the region of background medium in which a refractive index gradient is produced. The periodic deflection of the “probe beam” is detected by a position detector. The angle of deflection of the “probe beam” is proportional to the temperature [5]. The temperature variations resulting from optical absorption and energy thermalization within the sample can be related to the heat capacity and thermal conductivity of the sample via standard thermodynamic models based on the Fourier equation of heat. Depending upon the arrangement of the probe laser with respect to the “pump beam” and surface of the sample, a PDS setup can form either a transverse or a collinear configuration as will be discussed in the next two subsections.

1.2.1 Transverse PDS setup

In transverse PDS, a sample is illuminated with a modulated “pump” light beam that is perpendicular to the sample surface. A “probe” beam at lower intensity passes parallel to the sample surface as shown in Figure 1.2. Both opaque and transparent samples can be analyzed in transverse configuration. The photothermal deflection signal depends strongly on the distance between the “probe” beam and the sample surface [3]. With this configuration it is also possible to probe the temperature gradient within the solid if the sample is transparent. Spears et al. [23] used acrylic as a transparent substrate for investigating copper thin films.

1.2.2 Collinear PDS setup

In collinear PDS, the probe beam can be parallel or slightly oblique to the pump beam as shown in Figure 1.3. This configuration is only suitable for transparent samples because

the probe beam has to cross the solid sample [24,25]. A photothermal background medium is not necessarily required because the probe beam is deflected due to the change

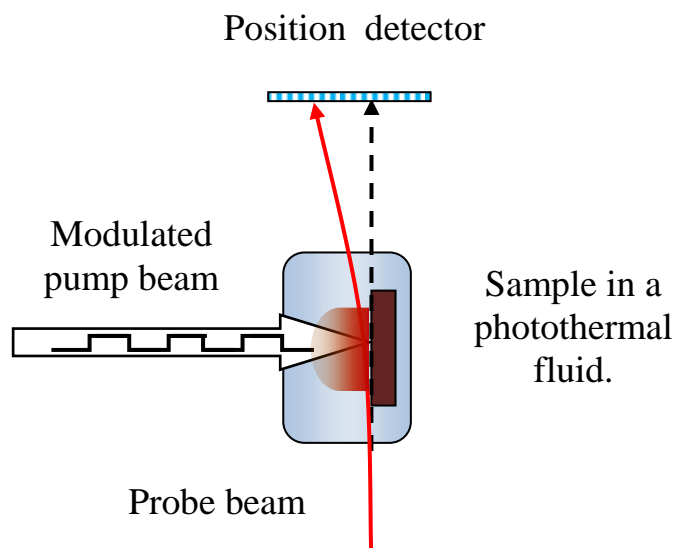


Figure 1.2 Schematic of transverse PDS setup where “pump beam” is perpendicular to the probe beam.

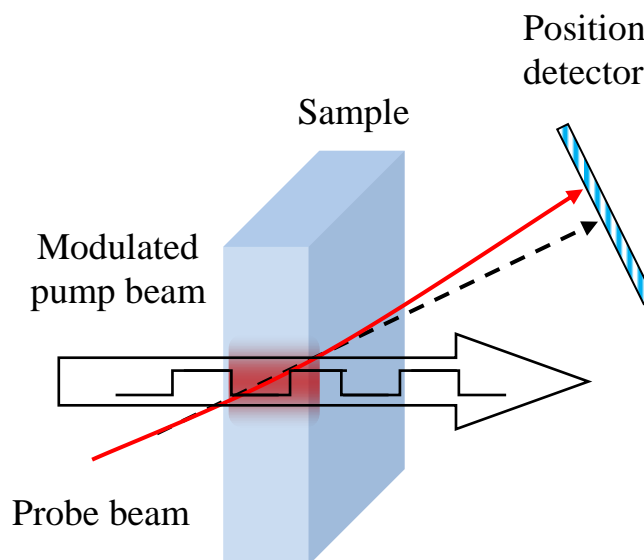


Figure 1.3 Schematic of collinear PDS setup where “pump beam” is oblique to the probe beam.

in refractive index of the sample itself. Another advantage of collinear PDS is that the pump beam and the probe beam overlap for a large region because they are almost parallel. In this way a large region with a refractive index gradient is produced, which yields to a stronger amplitude of the PDS signal.

The collinear configuration is more reliable for measurements in thick solid films because the probe beam, crossing the entire sample is affected by the absorption of light in the bulk of the sample [25]. Spears *et al.* [26] developed an analytical model to incorporate the effects of light scattering for collinear photothermal deflection spectroscopy and found that scattering effects could be minimized by focusing the excitation beam on the surface instead of in the middle of the sample. Subsequently they proposed that collinear PDS can be used to measure granular solid samples in which scattering of light is important provided that the diameter of the grains is small with respect to the wavelength of incident light.

A survey of the most relevant applications of PDS found in the literature is given in Table 1.1.

Table 1.1 Summary of PDS studies found in the literature.

Year	Author	Work title	Background medium	Ref
1980	A. C. Boccara <i>et al.</i>	Thermo-optical spectroscopy: Detection by the "mirage effect".	Air, liquid Helium	1
1980	J. C. Murphy and L. C. Aamodt	Photothermal spectroscopy using optical beam probing: Mirage effect	Air	2
1980	A. C. Boccara <i>et al.</i>	Sensitive photothermal deflection technique for measuring absorption in optically thin media.	Air	17

1981	W. B. Jackson <i>et al.</i>	Photothermal deflection spectroscopy and detection	Air	3
1981	L.C. Aamodt <i>et al.</i>	Photothermal measurements using a localized excitation source.	Unknown	4
1982	J. Opsal and A. Rosenweig	Thermal wave depth profiling: Theory	Unknown (theoretical work)	18
1982	W.B.Jackson and N.M Amer	Direct measurement of gap-state absorption in hydrogenated amorphous silicon by PDS.	Air	20
1983	A. Mandelis	Absolute optical absorption coefficient measurements using transverse PDS.	Unknown (theoretical work)	9
1983	M. A. Olmstead <i>et al.</i>	Photothermal Displacement Spectroscopy" An Optical Probe for Solids and Surfaces.	Air and Vacuum	55
1984	B. R. Weinberger and C. B. Roxlo	Optical Absorption in Polyacetylene: A direct measurement using PDS.	CCl ₄	89
1986	P. K. Kuo, <i>et al.</i>	Mirage-effect measurement of thermal diffusivity. Part I: experiment, Part 11: theory	Air	24 25
1986	D. Fournier <i>et al.</i>	Photothermal investigation of transport in semiconductors: Theory and experiment.	Air	40
1986	N. Yacoubi <i>et al.</i>	Determination of absorption coefficients and thermal conductivity of GaAlAs/GaAs	Cedar oil	44

		heterostructure using a photothermal method.		
1987	G. Suher <i>et al.</i>	Transverse PDS applied to thermal diffusivity measurements.	Air	43
1987	P.M. Patel <i>et al.</i>	Thermal-wave detection and characterization of sub-surface defects	Air	62
1989	A.Slazer <i>et al.</i>	Theory of thermal diffusivity by the "mirage" technique in solids	Unknown (theoretical work)	7
1991	J. D. Spear and R. E. Russo	Transverse Photothermal beam deflection within a solid	Acrylic	50
1991	Z.L.Wu <i>et al.</i>	Photothermal measurements of Optical coatings.	Air (Reflectance)	51
1991	A. Skumanich	Optical absorption spectra of C ₆₀ thin films from 0.4 to 6.2 eV	Unknown	82
1993	J. D. Spears <i>et al.</i>	Collinear Photothermal Deflection Spectroscopy of Liquid Samples at Varying Temperature	Water	19
1993	J. Ranalta <i>et al.</i>	Determination of thermal diffusivity of low-diffusivity materials using the mirage method with multi parameter fitting	CO ₂ at 2 atm. pressure	72
1994	O. W. Kading <i>et al.</i>	Thermal Conduction in metalized SiO ₂ on Si substrate.	Air (Reflectance)	14
1994	W. Hurler and M. Pietralla	Thermal characterization of bulk and thin film materials using the mirage-method	Air	31

1994	M. Bertolotti <i>et al.</i>	Measurements of thermal conductivity of diamond films by photothermal deflection technique	Air	34
1994	J. R. Barnes <i>et al.</i>	Photothermal spectroscopy with femtojoule sensitivity using micromechanical device	Air (Photobending)	90
1995	X. Quhlin <i>et al.</i>	Mirage effect: A theoretical and experimental study of anisotropic media in rear configuration	Air	57
1995	E. Welsch <i>et al.</i>	Photothermal measurements on optical thin films.	CCl ₄	61
1995	W. Hurler <i>et al.</i>	Determination of thermal properties of hydrogenated amorphous carbon films via mirage effect measurements.	Air	78
1996	M. Commandre and P. Roche	Characterization of optical coatings by photothermal deflection.	Air	68
1996	F. Hajiev <i>et al.</i>	Intra-cavity photothermal measurements of ultralow absorption.	Air	81
1997	M. Bertolotti <i>et al.</i>	New photothermal deflection method for thermal diffusivity measurement of semiconductor wafers.	Air	114
1999	G. Chen and P. Hui	Pulsed photothermal modeling of composite samples based on transmission-line theory of heat conduction.	Air (Reflectance)	46

2000	G.Chen <i>et al.</i>	Thermal conduction in metalized tetrahedral amorphous carbon (ta-C) films on silicon	Air (Reflectance)	79
2001	D. Chu <i>et al.</i>	Thermal conductivity measurements of thin-film resist.	Air (Reflectance)	32
2002	K. Chew <i>et al.</i>	Gap state distribution in amorphous hydrogenated silicon carbide films deduced from PDS.	CCl ₄	29
2002	E. Marin <i>et al.</i>	On the wave treatment of the conduction of heat in photothermal experiments with solids.	Unknown (theoretical work)	75
2004	E. D. Black <i>et al.</i>	Enhanced photothermal displacement spectroscopy for thin-film characterization using a Fabry-Perot resonator.	Unknown	54
2005	M. Paulraj <i>et al.</i>	Characterizations of undoped and Cu doped CdS thin films using photothermal and other techniques.	CCl ₄	47
2005	L. Goris <i>et al.</i>	Absorption phenomena in organic thin films for solar cell applications investigated by PDS.	CCl ₄ and Fluorinert®	67
2005	S. Aloulou <i>et al.</i>	Determination of absorption coefficients and thermal diffusivity of modulated doped GaAlAs/GaAs heterostructure by PDS.	CCl ₄	71
2005	M. Gunies <i>et al.</i>	Sub-band gap spectroscopy and minority carrier transport properties of hydrogenated microcrystalline silicon thin films.	Unknown	95

2007	T. Ghrib <i>et al.</i>	Simultaneous determination of thermal conductivity and diffusivity of solid samples using the “Mirage effect” method.	Air	23
2007	F. Saadallah <i>et al.</i>	Photothermal investigations of thermal and optical properties of liquids by mirage effect.	Paraffin oil and CCl ₄ .	58
2007	K. Lee <i>et al.</i>	Measurement of thermal conductivity for single- and bi-layer materials by using the photothermal deflection method.	Air	59
2007	K.J. Lee <i>et al.</i>	The measurements of thermal diffusivity dependent on temperature for pure metals by the new photothermal displacement configuration.	Air and N ₂	84
2007	J. Houel <i>et al.</i>	Ultra-weak absorption microscopy of a single semiconductor quantum dot in the mid IR range.	Unknown	96
2008	J. Bodzenta	Thermal wave methods in investigation of thermal properties of solids.	Air	39
2008	A. Dazzi <i>et al.</i>	Chemical mapping of the distribution of viruses into infected bacteria with a photothermal method.	Air	70
2008	I. Gaied <i>et al.</i>	Effect of beam sizes on the amplitude and phase of photothermal deflection signals for both uniform and nonuniform heating.	Paraffin oil	77

2008	P.S. Jeon <i>et al.</i>	Thermal conductivity measurement of anisotropic material deflection method using photothermal deflection method.	Air	83
2009	I. Gaied, <i>et al.</i>	Investigation of optical properties of SnSb_2S_4 and $\text{Sn}_2\text{Sb}_2\text{S}_5$ thin films by a non destructive technique based on photothermal deflection spectroscopy.	Paraffin oil	28
2009	A. Kazmierczak Bałata <i>et al.</i>	Determination of thermal conductivity of thin layers used as transparent contacts and antireflection coatings with a photothermal method.	Air	45
2009	E. Marín <i>et al.</i>	A simple approach to introduce photothermal techniques basic principles for thermal diffusivity measurement.	Air	48
2009	T. Gotoh	Photothermal technique using individual cantilevers for quality monitoring in thin film devices.	Air (Photobending)	93
2010	A R. Warriier <i>et al.</i>	Transverse photothermal beam deflection technique for determining the transport properties of semiconductor thin films.	CCl_4	41
2010	J. Bodzenta <i>et al.</i>	Photothermal methods for determination of thermal properties of bulk materials and thin films.	Transparent sample itself, Air	42

2010	J. Xia and A. Mandelis	Direct-search deep level photothermal spectroscopy: An enhanced reliability method for overlapped semiconductor defect state characterization.	Air	52
2010	A. Goren <i>et al.</i>	A systematic analysis of the influence of the surrounding media on the photothermal beam deflection signal.	Air, CCl ₄ , Water, Ethanol and Actone	60
2010	A. Gaiduk <i>et al.</i>	Room-Temperature Detection of a Single Molecule's Absorption by photothermal contrast.	Air	63
2010	I. Gaied <i>et al.</i>	Comparison between different photothermal deflection methods to determine thermal properties of bulk semiconductor samples.	CCl ₄	80
2011	F. Saadallah <i>et al.</i>	Optical and Thermal Properties of In ₂ S ₃ .	CCl ₄ or air	30
2012	P. G. Sionnest <i>et al.</i>	A mirage study of CdSe colloidal quantum dot films, Urbach tail, and surface states.	Hexane	38
2012	K. Hara and T. Takashi	Photothermal Signal and Surface Potential around Grain Boundaries in multicrystalline silicon solar Cells Investigated by Scanning Probe Microscopy.	Air	85

1.3 Applications of PDS

1.3.1 Optical absorption

PDS was introduced by Boccarda *et al.* [1] as a technique to measure small optical absorptions in solids. Subsequently a number of theoretical models and experimental setups have been developed to use PDS for the optical characterization of materials. Mandelis [5] had developed a one dimensional theoretical model to calculate the optical absorption coefficient of an opaque sample from the amplitude and phase of the angle of photothermal deflection of the probe light beam. Yacoubi *et al.* [27] and Aloulou *et al.* [28] measured the optical absorption coefficient and thermal conductivity of stacked heterostructures of GaAlAs/GaAs and found that their experimental results obtained by PDS agreed with the spectroscopic ellipsometry results obtained by the other authors. Gaid *et al.* [30] measured the optical absorption and the optical band gap energy of SnSb_2S_4 and $\text{Sn}_2\text{Sb}_2\text{S}_5$ thin films on glass substrates using transverse PDS. They were able to identify two different phases of $\text{Sn}_2\text{Sb}_2\text{S}_5$ and calculated the corresponding band gaps. Unlike in conventional optical transmission spectroscopy, PDS signal is based on periodic photo-induced changes in the thermal state of a sample due to the absorption of photons. Small effects of such optical absorptions, which are also periodic, can be selectively amplified by lock-in techniques that enhance electronic signals at a specific frequency over noise that is present at any frequency. Subsequently, photothermal spectroscopy is capable of measuring small optical absorptions more precisely as compared to conventional optical transmission spectroscopy [9].

1.3.2 Sub-band gap optical absorption

W. B. Jackson and N. M. Amer [31] have used PDS to measure the optical absorption coefficient of hydrogenated amorphous silicon (a-Si:H) down to 0.6 eV, well below the optical band gap of this material, and used it to calculate the density of optically active defects in these samples. A. Skumanich [32] has used PDS to measure the optical absorption of C₆₀ thin films down to 0.4 eV and was able to observe narrow vibronic peaks in the optical spectrum of his samples, which were extremely difficult to be observed with other techniques. B. R. Weinberger and C. B. Roxlo [33] measured the optical absorption of undoped and ammonia doped polyacetylene samples and used such measurements to study the sub-band gap nonmagnetic states that were compensated by ammonia. Hajiev *et al.* [34] have used an optical resonator to enhance the deflection of a PDS probe beam and used this scheme for the measurement of ultra low absorptions below the optical band gap of a-Si:H samples and showed a sensitivity improvement of four orders of magnitude for PDS using this method. Chew *et al.* [35] have studied the energy distribution of sub-band gap electron energy states in silicon rich hydrogenated amorphous silicon carbide ($a\text{-Si}_{1-x}\text{C}_x\text{:H}$, with $0 < x < 0.36$) by means of PDS measurements. They found that a wide range of defect states with broad energy distribution, were formed when carbon content increased, and attributed this phenomenon to dangling bond defects of carbon atoms. Guyot-Sionnest *et al.* [36] have used PDS to measure very small optical absorption tails well below the band gap photon energy of CdSe quantum dots and suggested that the broad energy distribution of electronic states in strongly interacting quantum dots may be due to coupling of these states with surface electronic states. Goris *et al.* [37] have used PDS to detect the small optical absorption spectra in pure and

blended organic thin films. They measured spectra of poly[2-methoxy-5-(3',7'-dimethyloctyloxy)-1,4-phenylenevinylene] (MDMO-PPV) thin films and interpreted their results in terms of defect induced absorption phenomena. They determined the spectral position of the observed transitions in [6,6]-phenyl-C₆₁-butyric acid methyl ester (PCBM). Their PDS study on thin films prepared from MDMO-PPV/PCBM blends demonstrated the interaction between the electron energy states of these two materials in the ground state when the two constituents were mixed at nanoscale. M. Gunes *et al.* [38] have used PDS to study sub-band gap absorption and minority carrier transport properties in hydrogenated microcrystalline silicon thin films.

1.3.3 Thermal properties

Saadallah *et al.* [29] have developed a model to find the expression for the photothermal deflection caused by a carbon black film for which the amount of generated heat was known from the knowledge of the optical absorption coefficient. In this way they could write the expression of photothermal deflection angle as a function of the thermal diffusivity of specific different liquids in which the carbon black reference sample was embedded. They applied this model to find the thermal diffusivity of paraffin oils. Salazar *et al.* [7] developed a complete theoretical model for interpreting the PDS data and extracting the thermal diffusivity of solids under specific conditions. They classified thin film materials as thermally thick and thermally thin depending upon the thermal and optical properties of the samples and their geometrical thickness. A thermally thick sample can be defined as a sample for which the thermal diffusion length L_D (related to thermal diffusivity) is much smaller than the geometrical thickness 'd' of the sample, like in Figures 1.4a and 4b. A thermally thick sample can be either optically thick (like in

Figure 1.4a) or optically thin (like in figure 1.4b) depending if the attenuation length of light (defined as the reciprocal of the optical absorption coefficient, $l_\alpha = 1/\alpha$) is much smaller than ($l_\alpha \ll d$) or comparable with ($l_\alpha \geq d$) the geometrical thickness of the sample. For optically thick, thermally thin samples the PDS signal is in phase with the pulses of the “pump” beam, the thermal properties cannot be measured and only surface optical properties can be measured. For optically thin and thermally thick samples heat is uniformly generated along the sample cross-section and slowly diffuses to the surface of the sample. In this case, the thermal wave has a phase difference with respect to the “pump” light pulse and allows the measurement of the thermal properties, provided the substrate is sufficiently thermally insulating. In all of the other situations, in which samples are thick or thin both thermally and optically, the PDS signal depends on both thermal and optical properties of the sample, so that knowledge on one type of properties is necessary for measuring the other type of properties. On the other hand, samples that are optically thin at specific wavelength of illumination (i.e. below the optical band gap) can be optically thick at other wavelengths (i.e. above the optical band gap). Instead, the thermal thickness of a sample depends not only on the thermal diffusivity but also on the modulation frequency of the “pump” light beam. This makes PDS a flexible technique for which the thermal and optical properties of solids can be very often simultaneously measured.

Fournier *et al.* [39] have developed a theoretical model to investigate optically thin and optically thick semiconductors and used it to measure the thermal diffusivity of silicon-based materials. Suher *et al.* [40] used transverse PDS to measure the thermal diffusivity of aluminum oxide and investigated the effect of porosity on the thermal

properties of this material. Kou *et al.* [41,42] have measured the thermal diffusivity of a number of pure materials, compounds and semiconductors, including silicon carbide, silicon nitride ceramics, and metal alloys. In these experiments, the samples surfaces

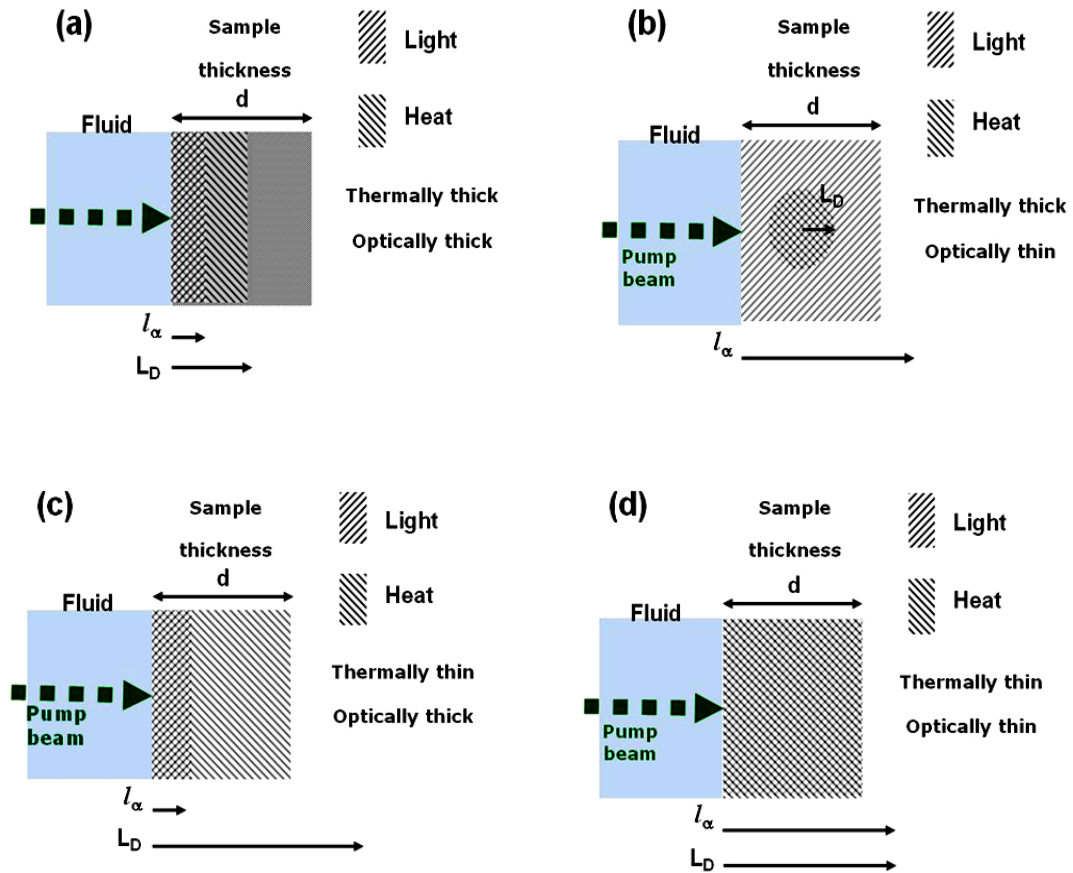


Figure 1.4 Schematic of thermal and optical thicknesses. (a) Thermally and optically thick sample whose thickness d is greater than both thermal diffusion length L_D and optical attenuation length l_α , (b) thermally thick and optically thin sample whose thickness d is greater than thermal diffusion length L_D but smaller than the optical attenuation length l_α , (c) thermally thin and optically thick sample whose thickness d is less than thermal diffusion length L_D and greater optical attenuation length l_α , and (d) thermally and optically thin sample whose thickness d is smaller than both thermal diffusion length L_D and optical attenuation length l_α of the sample.

were scanned by moving the probe beam away from the heating “pump” beam along the sample surface at a constant height from the sample surface. For a given modulation frequency, the scan effectively measured the thermal wave with the wavelength equal to the distance between the probe beam positions on the sample where the phase of PDS signals changes by 180° . By repeating the scan at different modulation frequencies, a number of wavelengths were measured. Thermal diffusivity was calculated from the slope of the plot of wavelength versus square root of frequency. Ranalta *et al.* [43] used the transverse PDS to measure the thermal diffusivity of soda lime glass and polypropylene. Bertolotti *et al.* [44] have measured the thermal conductivity of thin polycrystalline diamond films by PDS. Hurler *et al.* [45] used transverse PDS with a modulated light with line heating source instead of point source to determine the thermal properties of hydrogenated amorphous carbon thin films. The line source heating method was used to reduce the power density to which the sample was exposed, to avoid damage of the sample, and to obtain a good signal-to-noise ratio. Another advantage of the line source heating method is that it can average the response of small heterogeneities along the heating line. Chen *et al.* [20] used photothermal reflectance with a pulsed light beam to measure the thermal conductivity of tetrahedral amorphous carbon (ta-C) films coated with metal thin films.

Gharib *et al.* [46] have used transverse PDS to measure thermal diffusivity and thermal conductivity simultaneously by depositing a layer of graphite on top of the film samples so that the measured signal is sensitive to both thermal diffusivity and thermal conductivity and the quantity of heat deposited in graphite is known, since its optical and thermal properties are available in the literature. Bertolotti *et al.* [47] used PDS to

measure the thermal diffusivity of porous silicon thin films deposited on silicon wafer. Jeon *et al.* [48] measured by PDS and modeled the thermal conductivity of anisotropic materials and studied the effect on the PDS signal of the position of the probe beam with respect to the pump beam. They also studied the effect of the angle that was imposed between the probe beam and the crystallographic c-axis of Pyrolytic graphite and its effects on the measurement of the thermal conductivity along specific lattice directions in this thermally anisotropic solid. They found that their measured values agreed well with the theoretical prediction for isotropic iron and copper films but had significant deviations for pyrolytic graphite. N. A. George [49] used fibre optics to efficiently couple the PD signal to the position detector and determined the thermal diffusivity of indium phosphide wafers from the phase of the PDS signal. Saadallah *et al.* [50] used PDS to measure the thermal properties of thin layers of β -In₂S₃ grown on glass substrates by spray pyrolysis and investigated the effect of aluminum doping on the thermal properties of such films.

1.3.4 Depth profiling

PDS is based on thermal wave whose penetration depth is controlled by the modulation frequency of pump beam because the thermal diffusion length depends on the modulation frequency. The thermal diffusion length is the distance over which the amplitude of the thermal wave decays exponentially from its initial value to 1/e. Variation of thermal diffusion length with the modulation frequency of incident light beam is demonstrated Figure 1.5. For high modulation frequency of the excitation beam, the thermal diffusion length is smaller than the film thickness, the film is thermally thick and heat generation is localized in the proximity of the point at which light is absorbed as illustrated in Figure

1.5(a). Instead for low frequency modulation, the thermal diffusion length may become greater than the film thickness, the film is thermally thin as illustrated in Figure 1.5(b), care has to be exercised to avoid the contribution of the substrate in thermal measurements done by PDS and PDS cannot be used for depth profiling. Instead, by changing the frequency of modulation of excitation beam one can scan a thermally thin sample through its depth for measuring its thermal properties.

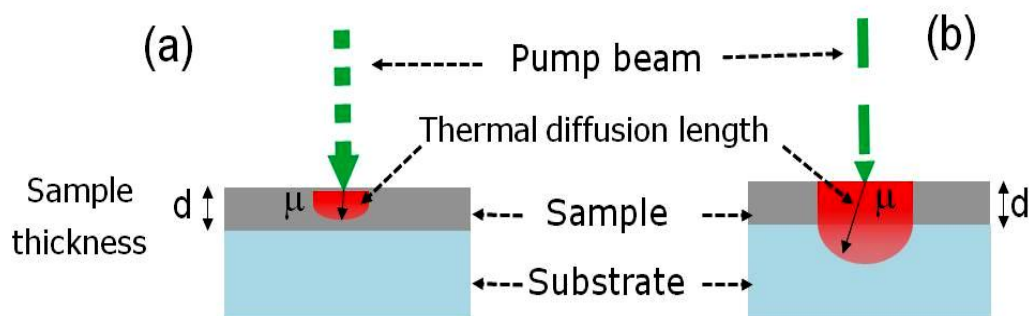


Figure 1.5 Schematic illustration of thermal penetration depth. (a) Thermal diffusion length is shorter at higher modulation frequency of the “pump beam” than (b) the that at lower modulation frequency due to the fact that at lwer modulation frequency more heat is deposited per cycle and thermal diffusion length increases.

Faubel *et al.* [51] developed and demonstrated a photothermal double beam laser scanning system that was used for scanning an artificial membrane. This system can be used for measuring thermal properties at the sample surface as well as measuring them in deeper layers of a sample without moving it, which can be used to monitor the drug delivery. Patel *et al.* [52] performed thermal depth profiles of specific samples by changing the modulation frequency of the incident “pump” beam and studied the defects in aluminum coated steel samples. They found that at low modulation frequencies, where the thermal diffusion length becomes comparable to the size of the defects, the one-

dimensional theory of heat conduction does not satisfactorily predict their experimental results and a three-dimensional thermal model is required to quantify these effects.

1.3.5 Thermal imaging

M. Commandre and P. Roche [25] have used photothermal deflection in three different configurations: skimming probe (transverse), transmission (collinear) and reflection. They calculated isotherms in the three media substrate, film and air, for a film on fused silica substrate. Isotherms were calculated at 50 Hz and 5000 Hz modulation frequencies. They mapped the absorption and scattering of BK7 bare substrates, which revealed the existence a nonuniform absorption localized at the surface of these samples. They also found that, in the transverse configuration, the photothermal deflection signal strongly depends on the distance between the probe-beam center and the sample surface. In the transmission and reflection configurations, the photothermal deflection signal increases greatly when the pump beam is tightly focused. The transmission configuration is more reliable for bulk absorption because the probe beam passed through the sample. Dazzi *et al.* [53] have used infrared spectromicroscopy method based on a photo-thermal effect to localize single viruses. An atomic force microscope coupled with a pulsed infrared laser was used to image a virus with lateral resolution of less than 50 nm. Gaiduk, *et al.* [54] have imaged single nonfluorescent azo-dye molecules in glycerol at room-temperature by the effect of heat released by the molecule upon intense illumination, on the refractive index of the embedding media. An average optical absorption cross section of 4 \AA^2 was estimated for a single chromophore.

1.3.6 Other applications

Fournier *et al.* [55] have used PDS for detection measurement of traces ethylene in other fluids down to 5 ppb and also demonstrated its use for *in situ* detection of trace of gases with very weak absorption. De Vries *et al.* [56] used PDS to detect the ammonia concentration in air. Opsal *et al.* [57] measured the thin-film thickness with laser beam deflection. J. A. Sell [58] determined the gas flow velocity by fitting the PDS data with known thermal conductivity. K. Hara and T. Takahashi [59] studied the nonradiative recombination of photo carriers around grain boundaries in multi-crystalline silicon solar cells via local measurements of the photothermal signal using an atomic force microscopy. They observed an enhancement of the photothermal signal around GBs, where a change in the surface potential was also observed by Kelvin probe force microscopy. They correlated such an enhancement in photothermal signal to impurities at grain boundary.

1.4 Summary and thesis outline

There are numerous theoretical models and experimental arrangement of PDS developed and used for non-destructive material characterization. However, careful alignment and calibration is necessary for accurate measurements. For optical characterization of samples, PDS technique has advantage over other optical techniques due to its sensitivity to measure sub-band gap absorption. PDS is non-destructive and contactless technique, and can be applied *in situ* for optical and thermal characterization of very thin samples and even for analysis of soft biological samples. Depending upon the nature of measurement and sample, a careful choice of working conditions is required. For instance, for optical absorption measurements, a range of incident photon energies is

required while for depth profiling a range of modulation frequencies of excitation beam is required, on which the data is to be recorded. Similarly thermal properties of the sample can be measured either from frequency scan or from special scan of probe beam with respect to position of excitation beam. Also one has to keep in mind the assumptions behind the model used for a particular measurement and that these assumption remain valid throughout the whole measurement cycle. For example, while changing modulation frequency of the excitation beam, a scan range is chosen such that it does not switch the thermal thickness limit (thin to thick or thick to thin) as compared to the sample thickness.

In order to have a flexible PDS setup that can adapt to the requirements of the measurement with little or no alteration, we have developed an automated PDS setup that is capable of collecting data at a range of incident photon energies, a range of modulation frequencies of excitation beam and a range of incident beam powers. Detail of experimental setup and its capabilities are discussed in Chapter 2. In Chapter 3, an introduction to the theory of PDS and role of convection in case of photothermal fluid containing nanoparticles is presented. In Chapter 4, photo induced degradation of hydrogenated amorphous (a-Si:H) thin films with a model on self repair of defects under intense illumination is presented. In Chapter 5, study of thermophysical properties of graphene thin films made by vacuum filtration method, is presented and a relationship between electrical and thermal conductivities of these films is derived. In chapter 6, thermophysical properties of RNA/graphene platelets nanocomposites are presented and effect of RNA content on the effective thermal properties of these composites is

investigated. Finally in chapter 7, a conclusion of present work is presented and future work directions are discussed.

References

- [1] A. C. Boccara, D. Fournier and J. Badoz, *Appl. Phys. Lett.*, **36** (1980) 130.
- [2] J. C. Murphy and L. C. Aamodt, *J. Appl. Phys.*, **51** (1980) 4580.
- [3] W. B. Jackson, N. M. Amer, A.C. Boccara, and D. Fournier, *Appl. Opt.*, **20** (1981) 1333.
- [4] L. C. Aamodt and J. C. Murphy, *J. Appl. Phys.*, **52** (1981) 4903.
- [5] A. Mandelis, *J. Appl. Phys.*, **54** (1983) 3404.
- [6] L. C. Aamodt and J. C. Murphy, *J. Appl. Phys.*, **58** (1983) 54.
- [7] A. Salazar, A. S. Lavega and J. Fernandez, *J. Appl. Phys.*, **65** (1989) 4150.
- [8] A. Mandelis, *Photoacoustic and Thermal Wave Phenomena in Semiconductors*, Elsevier Science Publishing Co., New York, 1987. P-102.
- [9] S. Bialkowski, *Photothermal Spectroscopy Methods for Chemical Analysis* John Wiley & Sons, New York, 1996.
- [10] M. Fox, *Optical Properties of Solids*, Oxford University Press, New York, 2001.
- [11] O. W. Kadling, H. Skuk and K. E. Goodson, *Appl. Phys. Lett.*, **65** (1994) 1629.
- [12] A. Rosenwaig and A. Gersho, *J. Appl. Phys.* **47**, (1976) 64.
- [13] S. O. Kanstad and P. E. Nordal, *Appl. Surf. Sci.*, **6** (1980) 372.
- [14] M. Handke and N. J. Harrick, *Appl. Spectroscopy*, **40** (1986) 401.
- [15] D. P. Almond and P. M. Patel, *Photothermal Science and Techniques*, Chapman & Hall, 1996.
- [16] M. A. Olmstead, N. M. Amer, and S. Kohn, *Appl. Phys. A*, **32** (1983) 141.
- [17] E. D. Black, Ivan S. Grudinin, Shanti R. Rao, and Kenneth G. Libbrecht, *J. of Appl. Phys.*, **95** (2004) 7655.

- [18] Y. S. Ju and K. E. Goodson, *Trans. of the ASME*, **120** (1998) 306.
- [19] O. W. Kading, H. Skurk and K.E. Goodson, *Appl. Phys. Lett.*, **65** (1994) 1629.
- [20] G. Chen, P. Hui and Shi Xu, *Thin Solid Films*, **366** (2000) 95.
- [21] Z. L. Wu, M. Reichling, H. Gronbeck, Z. X. Fan, D. Schaefer and E. Matthias, *SPIE: Laser Induced Damaeges in Optical Materials*, **1624** (1991) 331.
- [22] A. Salazar, A. Sanchez-Lavega, and J. Fernandez, *J. of Appl. Phys.*, **69** (1991) 1216.
- [23] J. D. Spears and R. E. Ruso *J. Appl. Phys.*, **70** (1991) 580.
- [24] A. C. Boccara, D. Fournier, W. B. Jackson and N. M. Amer, *Opt. Lett.*, **5** (1980) 377.
- [25] M. Commandre and P. Roche. *Appl. Optics*, **35** (1996) 5021.
- [26] J. D. Spears, R. E. Russo and R. J. Silva, *Appl. Optics*, **29** (1990) 4225.
- [27] N. Yacoubi, B. Girault, and J. Fesquet, *Appl. Optics*, **25** (1986) 4622.
- [28] S. Aloulou, M. Fathallah, M. Oueslati and A. Sfaxi, *American J. of Appl. Sciences*, **2** (2005) 1412
- [29] F. Saadallah, L. Attia, S. Abroug, N. Yacoubi, *Sensors and Actuators A*, **138** (2007) 335
- [30] I. Gaiied, A. Guassoumi, M. Kanzari and N. Yacoubi, *The 10th International Conference of the Slovenian Society for Non-Destructive Testing, September 1-3, 2009, Ljubljana, Slovenia*, 493.
- [31] W. B. Jackson and N. M. Amer, *Phys. Rev. B*, **25** (1982) 5559.
- [32] A. Skumanich *Chem. Phys. Lett.*, **182** (1991) 486.
- [33] B. R. Weinberger and C. B. Roxlo, *Phys. Rev. Lett*, **53** (1984) 86.

- [34] F. Hajiev, I. Malinovsky and H. Ugur, *Journal of Non-Crystalline Solids*, **198** (1996) 103.
- [35] K. Chew, Rusli, S. F. Yoon, J. Ahn, Q. Zhang, and V. Ligatchev, E. J. Teo, T. Osipowicz, and F. Watt, *J. Appl. Phys.*, **91** (2002) 4319.
- [36] P. Guyot-Sionnest, E. Lhuillier, and H. Liu, *J. Chem. Phys.*, **137** (2012) 154704.
- [37] L. Goris, K. Haenen, M. Nesl, A Dek, P. Wagner, D. Vanderzande, L. De Scheppe, J. D'Haen, L. Lutsen and J. V. Manca, *J. of Mat. Sci.*, **40** (2005) 1413.
- [38] M. Gunes, O. Goktas, S. Okur, N. Isik, R. Carius, J. Klomfass, F. Finger, *J. of Optoelect. and Adv. Mats.*, **7** (2005) 161.
- [39] D. Fournier, C. Boccara, A. Skumanich and N. M. Amer, *J. Appl. Phys.*, **59** (1986) 787.
- [40] G. Suher, M. Berlolotti, C. Sibia, A. Ferrari and F. G. Ricciardiello, *J. of Thermal Analysis*, **32** (1987) 1039.
- [41] P. K. Kuo, M. J. Lin, C. B. Reyes, L. D. Favro, R. L. Thomas, D. S. Kim, S. Y. Zhang, L. J. Inglehart, D. Fournier, A. C. Boccara, and N. Yacoubi, *Can. J. of Phys.*, **64** (1986) 1165.
- [42] P. K. Kuo, E. D. Sandler, L. D. Favro, and R. L. Thoma, *Can. J. of Phys.*, **64** (1986) 1165.
- [43] J. Rantala, L. Wei , P. K. Kuo, J. Jaarinen, M. Luukkala and R. L. Thomas, *J. Appl. Phys.*, **73** (1993) 2714.
- [44] M. Bertolotti, G. L. Liakhov, A. Ferrari, V. G. Ralchenko, A. A. Smolin, Elena Obraztsova, K. G. Korotoushenko, S. M. Pimenov and V. I. Konov, *J. Appl. Phys.*, **75** (1994) 7795.

- [45] W. Hurler, M. Pietralla and A. Hammerschmidt, *Diamond and Related Met.*, **4** (1995) 954.
- [46] T. Ghrib, N. Yacoubi and F. Saadallah, *Sensors & Actuators A: Physical.*, **135** (2007) 346.
- [47] M. Bertolotti, V. Dorogan, G. Liakhov, R. Li Voti, S. Paoloni, and C. Sibilìa, *Rev. Sci. Inst.*, **68** (1997) 1521.
- [48] P. S. Jeon, J. H. Kim, H. J. Kim, J. Yoo, *Thermochimica Acta* **477** (2008) 32.
- [49] N. A. George, *Appl. Phys. B.*, **77** (2003) 77.
- [50] F. Saadallah, N. Jebbari, N. Kammoun, and N. Yacoubi, *Int. J. Photoenergy Volume* 2011, Article ID 734574.
- [51] W. Faubel, B. Gotter, St. Heibler, M. Schlegel, R.H.H. Neubert, *J. of Physics: Conf. Series*, **214** (2010) 012062.
- [52] P. M. Patel, D. P. Almond and H. Reitte, *Appl. Phys. B*, **43** (1987) 9.
- [53] A. Dazzi, R. Prazeres, F. Glotin, J.M. Ortega, M. Al-Sawaftah and M. de Frutos, *Ultramicroscopy*, **108** (2008) 635.
- [54] A. Gaiduk, M. Yorulmaz, P. V. Ruijgrok and M. Orrit, *Science*, **330** (2010) 353.
- [55] D. Fournier, A. C. Boccara, N. M. Amer, and R. Gerlach, *Appl. Phys. Lett.*, **37** (1980) 519.
- [56] H. S. M. De Vries, F. J. M. Harren, G. P. Wyers, R. P. Otjes, J. Slanina and J. Reuss, *Atmosph. Envir.*, **29** (1995) 1069.
- [57] J. Opsal, A. Rosenowaig, and D. L. Willenborg, *Appl. Optics*, **22** (1983) 3169.
- [58] J. A. Sell, *Appl. Optics*, **24** (1985) 3725.
- [59] K. Hara and *Appl. Phys. Express*, **5** (2012) 022301.

Chapter 2

2 Experimental Setup

Developing experimental techniques for characterization represents a significant aspect of experimental research in materials science. As a part of this work, an automated photothermal deflection spectroscopy (PDS) and 3-omega setups for measuring the optical properties and thermal conductivity of materials were built. Instruments used in these setups were controlled by software programs that we developed using LabVIEW 8.6 to control a number of IEEE486 GPIB interfaces for real time data acquisition and analysis. Computer controlled instruments significantly decreased the amount of work that is necessary to perform the measurements and allowed us to collect the experimental data with greater accuracy and reliability. This chapter describes automated transverse PDS setup that was specifically developed and built for this thesis project. I shall also describe the 3-omega setup that I have assembled for validating the thermal conductivity measurements made by PDS as well as a number of additional pieces of equipment that were used for the characterization of the samples used for the present study, including the UV-visible spectrophotometer and the atomic force microscope.

2.1 Photothermal deflection spectroscopy (PDS) setup

A transverse photothermal deflection spectroscopy (PDS) setup for the investigation of optical and thermal properties of thin film samples was built and automated specifically for this thesis work. A schematic of this setup is shown in Figure 2.1. The essential components of a transverse PDS setup are pump beam source, probe beam, optical chopper, monochromator, reference signal photodiode (PD), sample cell, moveable stage to hold quartz cuvette that contains photothermal fluid and sample immersed in it,

position detector, lock-in amplifier, data acquisition and control system, and vibrations damping optical table. Some of these components are shown in Figure 2.1.

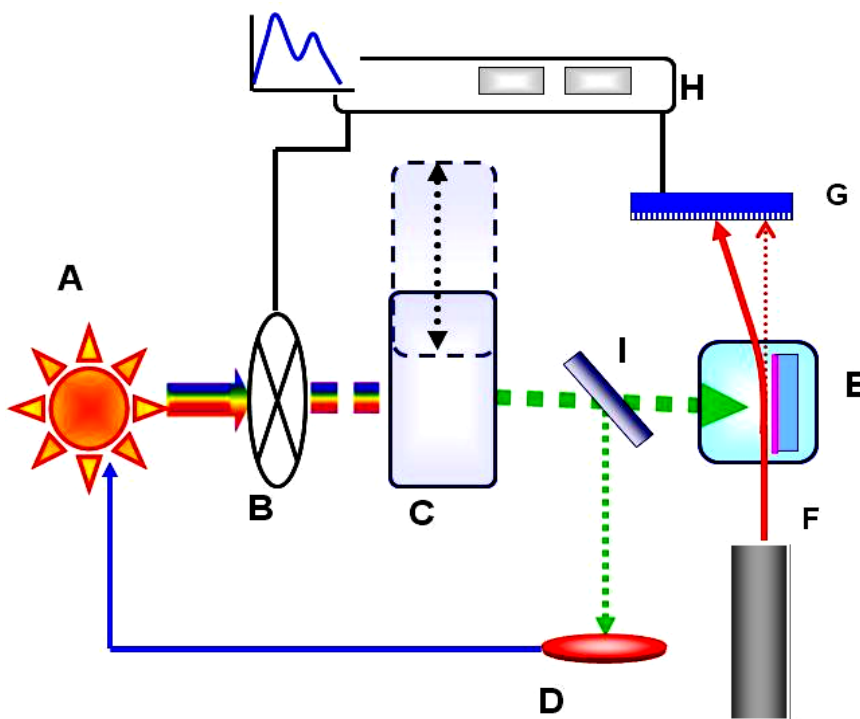


Figure 2. 1 Schematic of transverse PDS setup, where ‘A’ is AM 1.5 light source for “pump beam”, ‘B’ is mechanical chopper, ‘C’ is movable monochromator, ‘D’ is reference photodiode, ‘E’ is sample in photothermal fluid cell, ‘F’ is probe laser beam, ‘G’ is position detector, ‘H’ is Lock-in mode data acquisition and ‘I’ is beam splitter.

The PDS setup also has the capability to irradiate a sample with white light of AM 1.5 solar spectrum for *in situ* light soaking of the samples during the PDS experiments. Since PDS is often used to detect small absorption related to defects (as will be done by us in Chapter 4). The capability to irradiate the samples in-situ to form defects during the PDS measurements is of paramount importance in a PDS setup. Details of the individual components and their functions are discussed below.

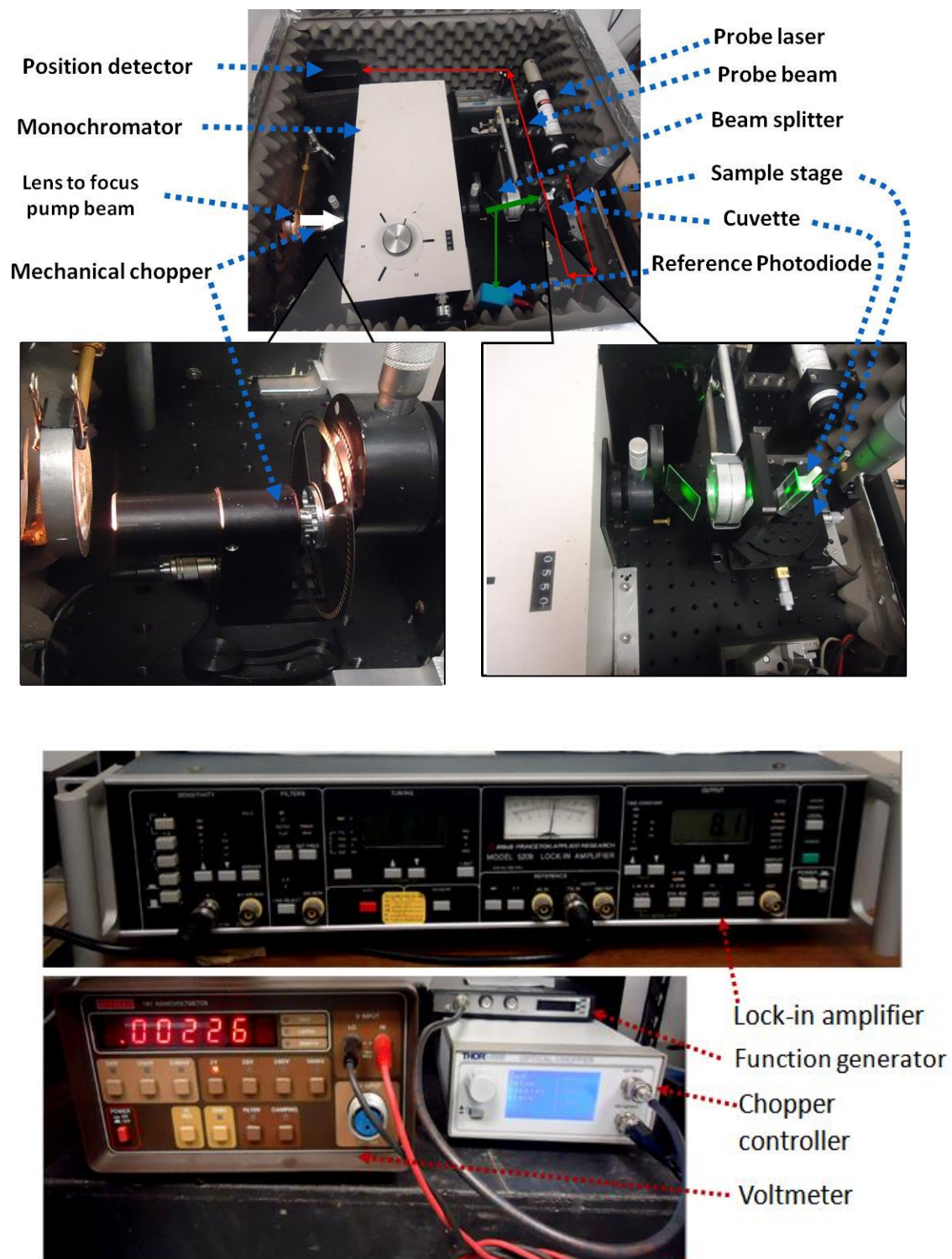


Figure 2.2 Pictures of different instruments used in the PDS setup.

2.1.1 Pump beam source

The optical pump beam is usually generated by high intensity light sources that, in specific PDS setups, have been implemented by laser or high power lamps with broad spectral range (infrared, visible or ultraviolet). Lasers provide highly focused light beams that can be used to generate thermal waves that are well localized at a specific point on the sample surface for high resolution thermal probing but tuneable lasers over wide ranges are necessary for PDS spectroscopic studies, so they are generally avoided. Super-quiet lamps based on high-stability arc discharges are a more common choice for PDS “pump” beams, but in this case a monochromator is required to select a particular wavelength from the spectrum of such lamps. Light sources with broad spectral range are good for spectroscopic studies because they have the advantage that a continuous spectrum of wavelengths can be generated from their output, but the intensity of monochromatic light beam emerging from the monochromator decreases significantly, which can be improved with the use of light sources with strong powers (1000W or more) and by using focusing optics to concentrate the beam on specific regions of the sample.

Among the high-stability high-power white light sources that can be used for PDS applications are: Xenon lamps, Globars, Nernst lamps and Quartz-Tungsten-Halogen (QTH) lamps. High pressure Xenon arc discharge lamps operate at pressure of 50 atm -70 atm and are efficient and stable sources of intense radiation in the visible near UV (200 nm – 700nm) photon energy range. Globars and Nernst lamps are infrared (IR) light sources with spectral range from 2 μ m to 30 μ m. Globar lamps consist of a silicon carbide rod that is electrically heated to emit IR radiations. Nernst glower lamps are made out of

mixtures of zirconia, yttria and thoria oxides and they operate at very high temperature (1700K). They are a source of intense IR radiation. Arc-discharge lamps use specific metallic electrodes or filaments that are placed inside a quartz enclosure that is filled with mixtures of inert and/or small amount of halogen gases. Current flowing through the filament heats to > 3000 K and it produced near infrared (NIR), visible (Vis) and some ultraviolet (UV) light. The spectral output is smooth and it approximately follows a black body radiation curve [1].

Our experimental setup uses a QTH lamp at 1 kW power, developed in London, Ontario by Sciencetech Inc. A 201-1K-QTH housing fitted with an air cooling fan and a 2" collimating glass lens houses the light source. This lamp is powered by a Sciencetech 500-1 kA adjustable AC power supply (label A in Figure 2.1) [2]. The output intensity can be controlled by adjusting the AC power supply, consisting of a variable transformer, depending upon the need of the experiment. The pump beam is modulated by an optical chopper and focused on the inlet slit of the monochromator. In the preliminary stages of our work a Newport (69907) super-quiet Xe lamp at 300 W power was also used. The halogen lamp was found to be more stable and has the advantage to be more powerful. The specific spectral output of our 201-1K-QTH lamp is reported in Figure 2.3 [2] where it is compared the corresponding output of the Newport (69907) Xe lamp [3] that was used in the preliminary stages of this study.

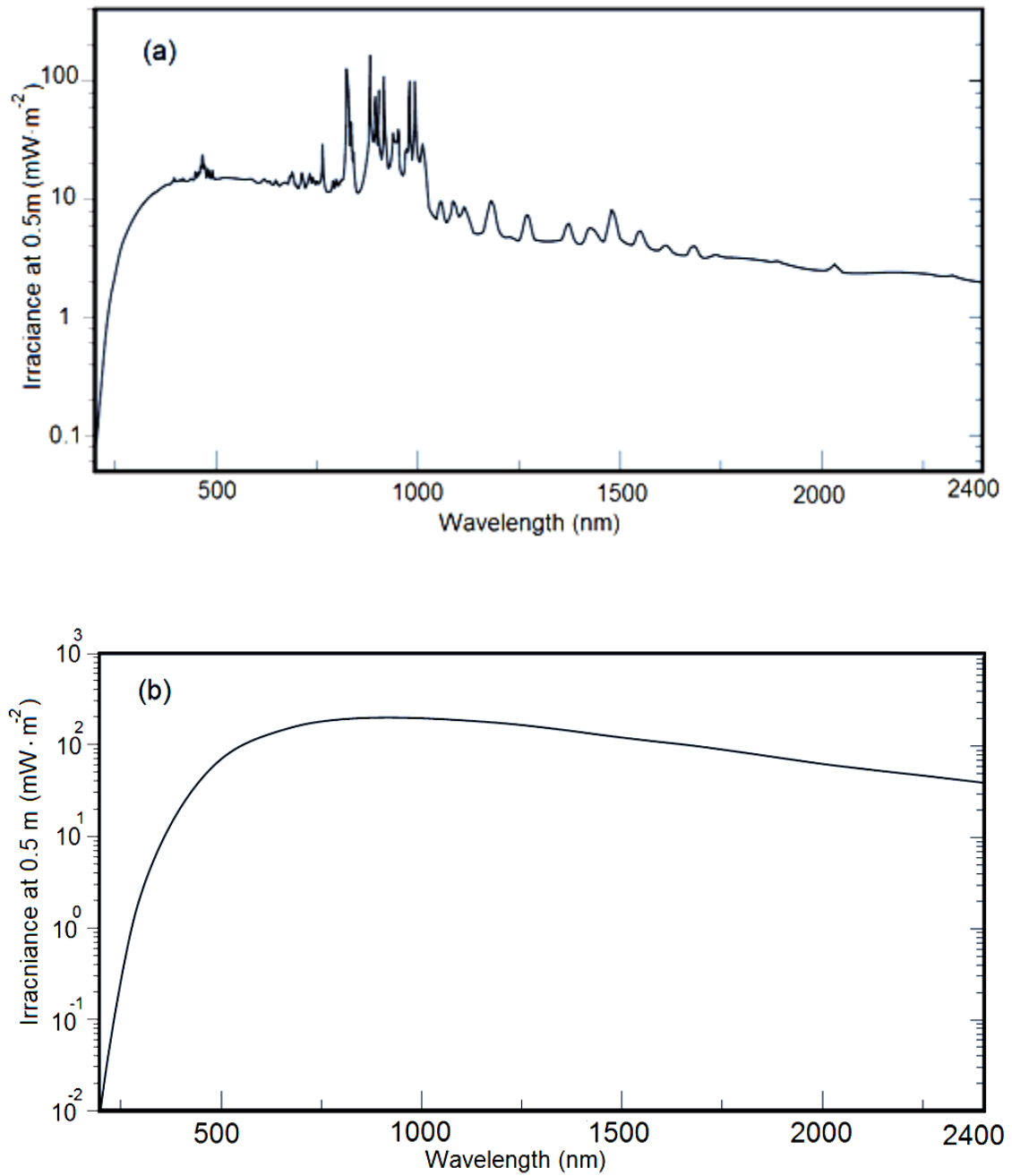


Figure 2.3 Spectral response of (a) Xe lamp and (b) QTH lamp [3].

2.1.2 Optical chopper

In PDS, the temperature change due to light absorption and subsequent thermalization may be quite small compared to the fluctuations of the ambient temperature in the laboratory. Typical temperature modulations in a good PDS system are ~ 0.1 °C to 10 °C. AC signal may be superimposed to a temperature drift background, and can be detected and measured with electronic instrumentation using lock-in amplifying techniques. In order to generate modulated temperature oscillations, pulsed heat generation and pulse illumination of the sample are required. Therefore, the “pump” beam needs to be modulated with a chopper. There are different types of choppers, including: mechanical, piezo-electrical, electro-optical and acousto-optical. Electro-optical and acousto-optical choppers are generally well suited for high-frequencies (~ 100 kHz or more) and piezo-electrical choppers are indicated for ultrahigh frequencies (i.e. > 10 MHz) but both systems can operate within a relatively limited range of frequencies. Instead, mechanical choppers can operate at frequencies that can be adjusted over several orders of magnitude (typically 1 Hz to 10 kHz), which makes them suitable for thermal conductivity PDS measurements, for which the thermal diffusion length in the sample needs to be adjusted and a frequency analysis of the PDS signal is required.

In our setup we have used mechanical chopper (ThorLabs MC2000) to modulate the pump beam at a chosen frequency. The mechanical chopper is placed before the monochromator (label B in Figure 2.1). A range of modulation frequencies from 1 Hz to 1 kHz can be chosen with this chopper. The whole frequency range operation required by PDS requires two different chopper wheels, one chopper wheel (ThorLabs MC1F2: a two slot wheel shown in Figure 2.4a [4]) for frequency from 1Hz to 99Hz and another

one (ThorLabs MC1F10: a 10-slot chopping wheel shown in Figure 2.4b) for frequencies from 20 Hz to 1 kHz. Any frequency step can be chosen using an automated controller [4]. A USB-controlled function generator (DDS-3X25 by Hantek) is used to trigger the chopper controller to the chosen frequency of modulation that, in turn, automatically controls the chopper wheel frequency via personal computer.

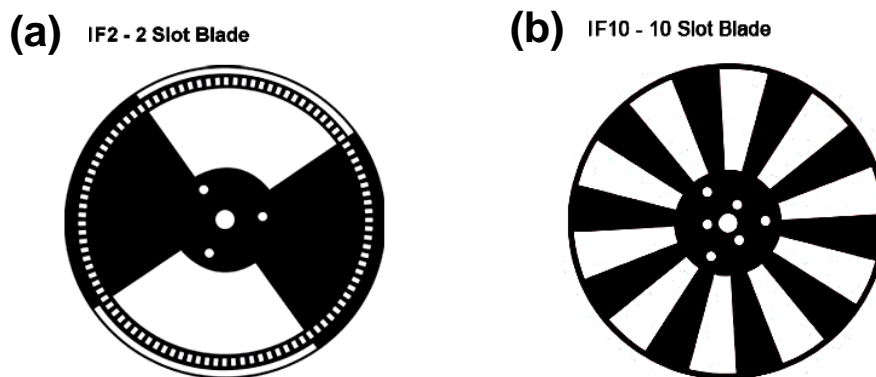


Figure 2.4 Thorlabs chopper wheels (a) for frequency range 1 Hz to 100 Hz and (b) for frequency range 20 Hz to 1 kHz) [4].

2.1.3 Monochromator

The modulated pump beam is focused on the inlet slit of a Jarrell-Ash 82-497 Czerny-Turner monochromator (label C in Figure 2.1) with 600 gr/mm. The widths of inlet and outlet slits are adjustable and are used to block the stray light and control the intensity of the output light from the monochromator. The monochromator is placed on a guiding track on an optical table that is decoupled from the table on which the lamp is placed. Guided tracks allow to retract the monochromator out of the path of the “pump” light beam and to reposition in the light path without affecting the alignment of the optical beam. Retracting the monochromator is necessary for PDS experiments requiring in-situ light soaking of a sample to white light. For acquiring the PDS spectra, the

monochromator is moved back into the path of pump beam after white light soaking, which makes it possible for sample to be illuminated by white light and re-measured multiple times. The monochromator used in the PDS setup we developed, comprises a turret that can accommodate three different sets of gratings that can be used to generate monochromatic light at different ranges of wavelengths. With the set of gratings that are currently installed, we can select wavelengths from 400 nm to 1200 nm with 0.4 nm resolution. An external stepper motor (Phidgets-1062-1 controlled using LabView 8.6) is used for orientating the controlling of the grating inside the monochromator and to determine the desired wavelength.

2.1.4 Reference photodiode

The actual power of the monochromatic pump beam to which the sample is exposed, depends on the electrical power supplied to the QTH lamp (which determines the spectral emissivity of the source via black-body temperature) and on the transmittance of the monochromator (that is also wavelength dependent). Therefore, the illumination power at the sample needs to be calculated by referencing the light beam in the proximity of the sample by means of a photodiode (Vishay PBW34, label D in Figure 2.1). A 10/90 beam splitter (label I in Figure 2.1) is inserted in the path of the optical beam emerging from the outlet slit of the monochromator to direct a part of the optical power to such photodiode. The transmitted 90% fraction of the incident beam, passing through the beam splitter is focused on the sample with a system of spherical and cylindrical lenses with nearly wavelength-independent transmittance. The 10% fraction of reflected beam redirected to the photodiode yields a signal that is proportional to the power of the incident monochromatic beam, which is used to calculate the power at the sample based

on the current output of the photodiode that operates in the wavelength range from 350 nm to 1200 nm, with excellent stability over time and temperature [5], and used to normalize the PDS signal. Since the amplitude of the PDS signal is proportional, at a constant absorbance of the sample, to the incident power, or at constant power to the absorbance of the sample, the normalized amplitude is compensated for the light intensity fluctuations and for the transfer function of the monochromator.

In order to produce reliable PDS measurements it is necessary to use the appropriate intensity of the reference beam that does not saturate the response of the reference photodiode. We have measured the response of the photodiode at different pump beam powers as shown in Figure 2.5, it can be observed that the diode current increases linearly with the increasing incident power and does not saturate.

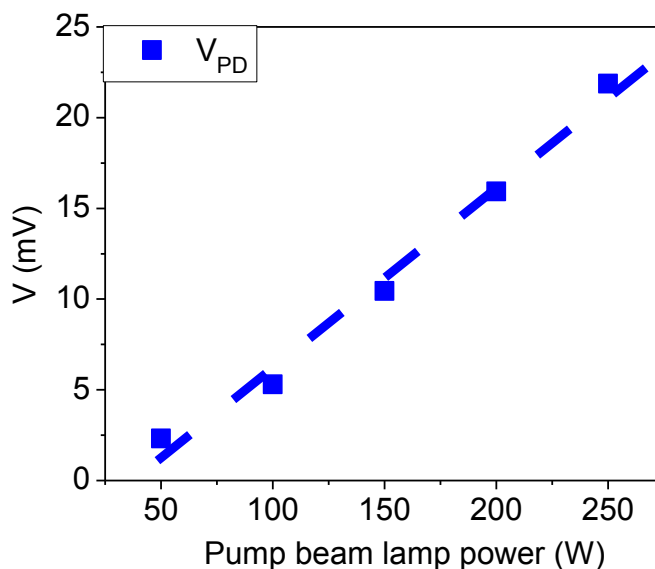


Figure 2.5 Reference photodiode (PD) response at different pump beam powers. The output voltage of PD increases linearly with increasing “pump beam” power.

2.1.5 Sample holder cell

A 10 mm x 20 mm x 50 mm quartz cuvette with Teflon lid (Label E in Figure 2.1) is used to hold the photothermal liquid and sample immersed in it. The lid of the cuvette is air tight and designed to hold the sample (up to 1mm thickness) vertically in front of the “pump” beam. The cuvette lid also has a small hole with an air tight stopper that is used to inject fluid into and withdraw out of the cuvette without disturbing the sample. This is necessary for irradiation and light-soaking experiments with white light at power levels that are significantly heating the sample, which would make the photothermal fluid to boil. Photothermal fluids with high temperature coefficient of the refractive index that are compatible with our cuvette including: air, methanol, ethanol, acetone, chloroform, Flouriner^(TM) and carbon tetrachloride are reported in table 2.1 [6,7]. Refractive index may change by: 1) changes in density and 2) change in susceptibility, with the 2nd effect generally dominating in solids.

Table 2.1 Thermophysical properties of some commonly used photothermal fluid.

Fluid	Refractive index n	Temperature coefficient of refractive index dn/dT (K⁻¹)
Air	1.0	- 9.8 x 10 ⁻⁷
Chloroform	1.444	- 6.0 x 10 ⁻⁴
Acetone	1.357	- 5.4 x 10 ⁻⁴
Methanol	1.326	- 3.9 x 10 ⁻⁴
Carbon tetrachloride	1.459	- 6.1 x 10 ⁻⁴
Flouriner ^(TM)	1.251	- 0.154 x10 ⁻⁴

For most of our experiments, we have used carbon tetrachloride (Aldrich Cat# 289116) because of its high value of temperature coefficient of refractive index compared to other fluids. However, CCl_4 is not environment friendly and is notorious ozone depleter, so its use and exposure must be kept to a minimum. As an alternative to CCl_4 we have also have used Flourinert^(TM) (3M Cat # 98-0211-0267-2), a synthetic photothermal fluid provided by 3M Canada Co. Another advantage of Flourinert^(TM) is that unlike CCl_4 , it is compatible with a number of organic thin films. Thermo optical properties of CCl_4 and Flourinert^(TM) are presented in Table 2.2.

Table 2.2 Optical and thermal properties of fluids used in this study

Fluid	$K_f (\text{W.m}^{-1}.\text{K}^{-1})$	$c (\text{J.kg}^{-1}.\text{K}^{-1})$	$D_f (\text{m}^2.\text{s}^{-1})$	T (%) at 550nm
CCl_4	0.099	850	7.3×10^{-8}	> 99%
Flourinert ^(TM)	0.057	1046	3.244×10^{-8}	> 99 %

2.1.6 Sample stage

Alignment of the sample and probe beam is crucial for getting a reliable PDS signal. In order to have a better control over alignment of the sample, vibrations must be kept to a minimum using an anti-vibration table. In our PDS setup the sample cell is placed on an adjustable stage that can move in all three X, Y and Z, directions in addition to rotation on XY plane. All three X, Y and Z movements of the stage are controlled with micrometers that allow a precise alignment and positioning of the sample.

2.1.7 Probe beam

Generally, a low power gas laser, or a semiconductor diode laser is used as a probe beam. A low power (< 5 mW) laser beam can be used as a probe to measure the temperature gradient as a result of heat generated in the sample. In our setup, a He-Ne laser (Melles

Griot, $\lambda = 650$ nm and Power < 5 mW, Label F in Figure 2.1) is used as a probe beam. Front-face reflecting mirrors mounted on moveable mounts are used to direct and align the probe laser.

In transverse PDS, probe beam passes through the photothermal fluid, skimming the sample surface at the interface between the fluid and the sample. Refractive index of the fluid adjacent to the sample surface changes periodically due to periodic heat generated in the sample and conducted to the fluid as a result of illumination by a modulated excitation beam. Probe beam passing through such a refractive index gradient, deflects periodically and directed to a position sensitive detector that is used to detect and such deflections by generating a voltage signal proportional to the change in position.

2.1.8 Position detector

The detection of probe beam deflection can be achieved by using various methods like, photo detector with split bi-cell or quadrant, lateral array of position sensors, a photo detector with knife edge or a photo detector with iris. The position of beam hitting the detector is detected with fractions of a micron by using such detectors. We have used a Silicon quadrant detector (Thorlabs PDP90S1, Label G in Figure 2.1) as a position detector for the probe beam deflection measurements. It has fast response time that is necessary for high speed operation and position resolutions [8]. Output of the position detector is a voltage signal normalized by finding the ratio of signals $(A-B)/(A+B+C+D)$ where A, B, C and D are voltage signal from four segments/quadrants of the quadrant detector. The normalized voltage signal is fed to a lock-in amplifier with built-in pre-amplifier that extracts the AC signal with frequency equal to the pump beam modulation frequency.

2.1.9 Lock-in amplifier

Lock-in amplifiers are used to detect and measure very small AC signals in the presence of large noise, using phase-sensitive detection technique. It is a powerful method for measuring a very small signal at a specific reference frequency and phase [9]. Output of an experiment is fed to the lock-in amplifier that filters the AC signal based on the reference frequency set by an internal or external reference. (Lock-in amplifiers can also generate their own internal reference signal). Generally, in an experiment either the output signal of a particular frequency is mixed with other signals or performed in such a way that the output signal is modulated at a fixed frequency (set by a function generator), and fed to the lock-in amplifier along with external or internal reference signal.

In our setup the normalized voltage output of position detector is connected to a Princeton Instruments 5209 lock-in amplifier (Label H in Figure 2.1) referenced at the chopper frequency. Lock-in is controlled by LabView driver using an IEEE486 interface. The LabView driver developed by “Ametek Signal Recovery” (free copy downloaded from National Instruments website) was used to control the lock-in amplifier. Flow chart explaining the control and data acquisition procedure is shown in (Appendix A) Figure A1 while view of front panel and the block diagrams of the controlling LabVIEW program are shown in Figure A2 and Figure A3 respectively.

2.1.10 Optical table

PDS is very sensitive to mechanical vibrations and stray light that can reach the position detector, so the setup needs to be placed on a vibration-damped stage and the position detector needs to be placed in a box that can block the entry of stray light. For this reason the pump beam source (whose fan and power supply are the main sources of vibrations)

is decoupled from rest of the setup by placing it on a separate table. Rest of the components like optical chopper, monochromator, sample holder (quartz cuvette and stage), probe beam and position detector are fixed on an optical bread-board and enclosed in a black wooden box, which is placed on an optical table (Newport) fitted with compressed air to dampen the mechanical vibrations. The inside of wooden box is fitted with noise damping foam, protects the detector from stray light and air movement around the cuvette, thus improving the signal to noise ratio. The position detector is placed in box with a very small opening that allows only the probe beam to enter and the stray light is blocked from reaching the detector.

2.1.11 Calibration of the PDS setup

Calibration is the process of comparison of measured values of a physical quantity with already known values. Thermal conductivity measurement data were calibrated using crystalline silicon sample. The process of calibration confirms that the apparatus can be used to determine thermal properties of other samples accurately. The calibrated setup was then used to measure the thermal properties of graphene thin films, samples provided by 3M Canada Co. and PEDOT coated TCFs [10,11].

2.2 3-Omega method for thermal conductivity measurement

The 3-omega (3ω) method for measurement of thermal conductivity was also built and used in this project. 3ω method is a more established method to measure the thermal conductivity of a solid, so it was used to double check our PDS measurements on specific samples. The advantage of PDS is that it is non-destructive and no-contact technique and therefore, more attractive. The 3ω method is based on the measurement of third-harmonic

component of voltage across a heater through which an alternating (AC) current with frequency ω is flowing. The existence of 3ω voltage signal was originally discovered by O.M. Corbino [12 and references mentioned in it]. Heat is produced when an alternating current at frequency ω flows through the metal line and creates an oscillating temperature gradient at 2ω . This in turn leads to changes in the electrical resistance of the heating metallic line at frequency 2ω resulting in a small AC voltage signal at 3ω superimposed on the applied AC voltage. Cahill and Pohl [13,14] developed the experimental technique based on the measurement of the AC voltage signal with frequency 3ω and used it to find the thermal conductivity of solid assuming that the metallic heating line is in perfect contact with the sample surface and the width of the heating line very small as compared to the diffusion length of the thermal wave generated by Joule heating. Schematic of our experimental setup is shown in Figure 2.6.

The 3ω method is based on the radial heat flows from a very thin but very long heating line deposited on a sample surface. The temperature difference at a distance r from heating line deposited on sample with thermal conductivity K_s , can be written as [15];

$$\Delta T(r) = (P/l \cdot \pi \cdot K_s) \cdot K_0(qr) \quad (2.1)$$

where

P/l is the power dissipated per unit length l , K_0 is the zero-th order modified Bessel Function and q is the wave vector of diffusive thermal wave, which depends upon the thermal diffusivity of the material and frequency ω of the thermal wave, and can be written as;

$$q = \left(\frac{D_s}{i \cdot 2 \cdot \omega} \right)^{-1/2} \quad (2.2)$$

It is assumed that heating line very thin as compared to the diffusion length of the thermal wave i.e. $1/q \gg$ thickness of heating line, and film surface very smooth and the heating line is in perfect contact with the sample surface.

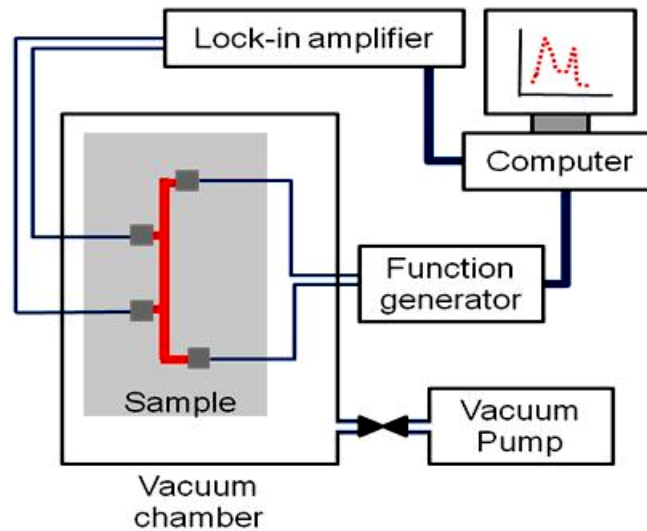


Figure 2.6 Schematic of 3-omega setup for thermal conductivity measurement.

Sample is placed in a vacuum chamber to avoid the heat loss to surrounding.

The temperature gradient can be expressed in terms of voltage drop $V_{3\omega}$ at frequency 3ω across the metallic heating line in terms of the temperature coefficient of resistance dR/dT , as [15];

$$\Delta T = 2 \cdot \frac{dT}{dR} \cdot \frac{R}{V} \cdot V_{3\omega} \quad (2.3)$$

where, R is the average resistance of the heating line and V is the voltage applied across the heating line. By measuring the $V_{3\omega}$ voltage at two different frequencies, the thermal conductivity of the sample can be calculated by using the following relation [15]:

$$K_s = \frac{V^3 \cdot \ln(\omega_2/\omega_1)}{4 \cdot \pi \cdot l \cdot R^2 \cdot (V_{1,3\omega} - V_{2,3\omega})} \cdot \frac{dR}{dT} \quad (2.4)$$

where $V_{1,3\omega}$ and $V_{2,3\omega}$ are the voltage drops across the metallic line at third harmonics of frequencies ω_1 and ω_2 respectively.

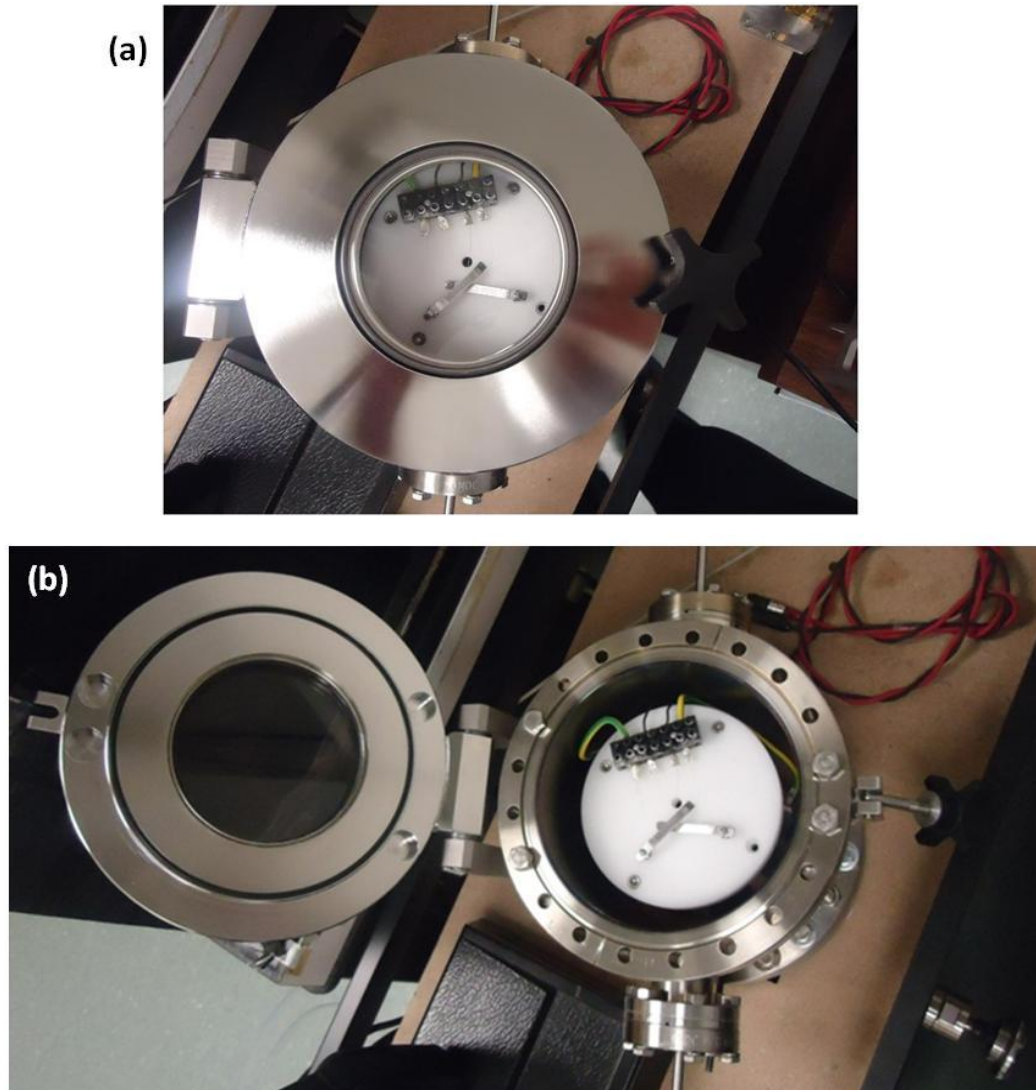


Figure 2.7 Pictures of 3ω Setup (a) Closed and (b) Open.

An aluminum heating line 1.2 cm long and 0.5 mm wide was deposited on the sample, by thermal evaporation in a high vacuum chamber. The samples were then loaded into the 3-omega sample chamber and the chamber was evacuated in order to prevent the heat loss to the surroundings. Pictures of sample chamber used in this study is shown in Figure 2.7 An AC current with frequency ω was applied across the aluminum strip and the AC voltage drop at 3ω across the two inner contacts was measured and recorded with a lock-in amplifier and subsequently used to calculate the thermal conductivity of the sample by using the equation (2.4).

2.3 Ultraviolet visible (UV-vis) spectrophotometer

A spectrophotometer used to measure optical transmittance [$\mathcal{T}(\lambda)$] for normal incidence consists of a light source, a monochromator or set of filters and a detector. A broadband light source is needed to cover the wide spectral range. Generally it is accomplished by using two lamps, one for UV and another visible light source. In the UV range, common sources are the Xenon (Xe) arc lamp and the deuterium (D_2) lamp. A Xe arc lamp has a continuous emission spectrum over a wide wavelength range of 200nm to 2000 nm. It covers both UV and visible spectral ranges. The D_2 lamp has short spectral range from 200 nm to 600 nm with very weak intensity above 400nm [12]. A schematic diagram showing the major optical components of a spectrometer is shown in Figure 2.8 where two different light source for UV and visible light are shown. A slit is use to control the intensity of the incident beam followed by a set of filters on a wheel that are used to select the required wavelength. Filter wheel can be replaced by a monochromator for better wavelength resolution, however light intensity is significantly reduced in this case. The incident light beam is alternatively directed on the sample and reference by a system

of rotating and fixed mirrors. Both reference and sample beams are detected by detectors. If I_0 is the intensity of reference light beam and I the intensity of the transmitted light through the sample, then the transmittance \mathcal{T} is given by the ratio of the two i.e. $\mathcal{T} = (I/I_0)$.

UV-vis transmittance of our samples was measured at normal incidence in a range of wavelengths range from 400 nm to 800 nm using a Varian DMS80 spectrophotometer, and data were collected by using an Emant300 USB data acquisition card controlled by a Matlab program.

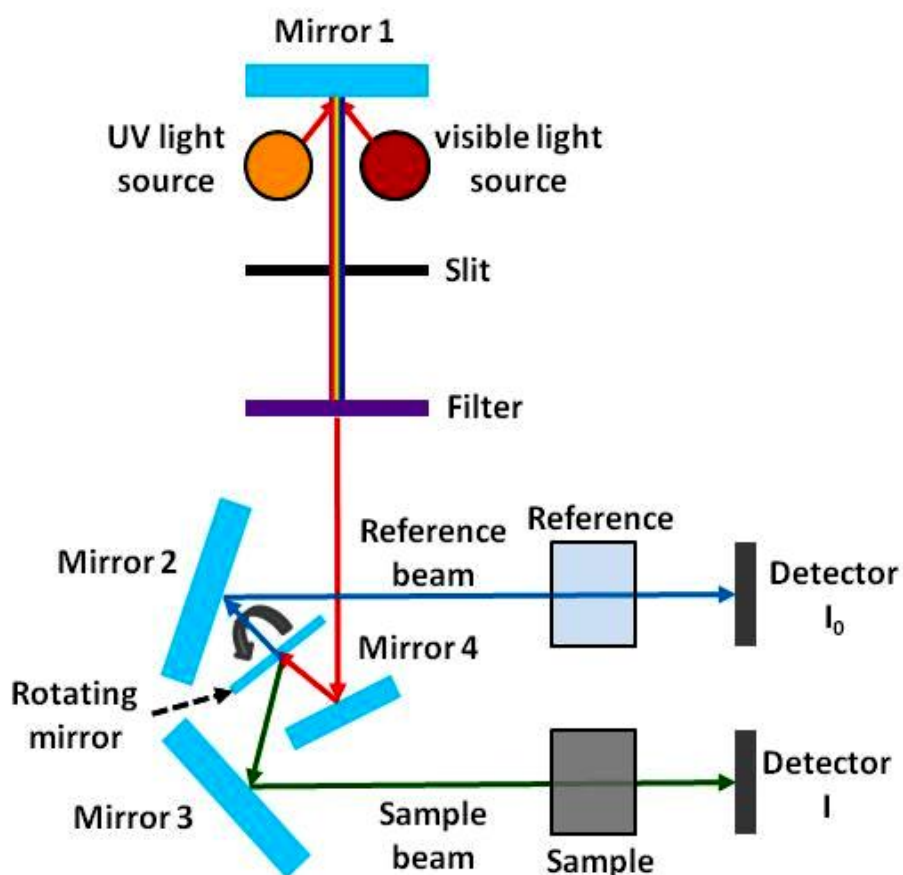


Figure 2.8 Schematic of a UV-vis spectrometer, where a rotating mirror directs the light beam to reference and sample alternatively.

2.4 Atomic force microscopy (AFM)

Atomic force microscopy (AFM) is a very sensitive technique that provides a three-dimensional (3D) profile of the surface of a sample on nanoscale, by making use of the force between a probe tip and the sample surface at very short distance. AFM can image surfaces in real space with resolution down to molecular level. AFM was invented by Binnig *et al.* [16] who, in 1986, demonstrated for the first time the idea of AFM, which used an ultra-small probe tip at the end of a cantilever. Atomic force microscopy (AFM) was developed as an extension of scanning tunnelling microscope (STM) technique to investigate the electrically non-conductive materials. The probe tip is attached to a flexible cantilever that acts as a spring. The amount of force between the probe and the sample depends on the spring constant and the distance between the probe and the sample surface. A schematic of probe beam deflection is shown in Figure 2.9. When the distance between the tip and the sample is too small (a fraction of a nano meter) then there is a strong repulsive force between the tip and the sample. The resolution of the scanned image depends upon the tip size (typically ~ 50 nm).

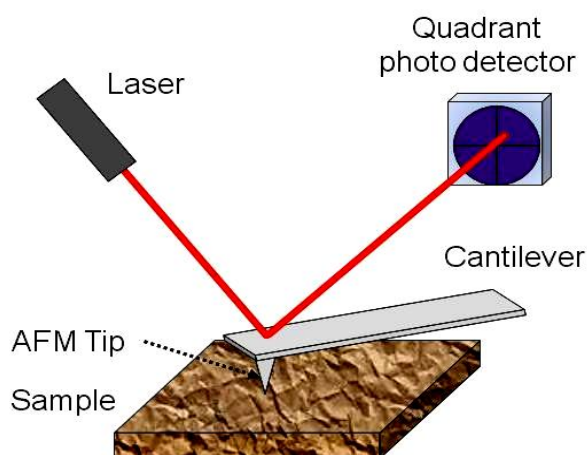


Figure 2.9 Schematic of AFM. A probe reflecting from the back of the tip is detected by a quadrant detector magnifies the tip's movement.

As the AFM tip moves on the surface of the sample (contact mode), the force between the sample and tip is measured and controlled by a feedback loop. When the force between the sample and tip is kept at a constant level with a feedback mechanism and the tip is moved across the sample surface then it produced the surface contours. Movement of the tip is amplified by a laser beam reflected from the back of the cantilever and detected by a quadrant position detector.

In 1987, Wickramasinghe *et al.* [17] developed an AFM setup with a vibrating tip technique (AC mode). The amplitude of vibration depends upon the tip-sample spacing which is used through a feedback loop (via piezoelectric transducer) to control the vertical movement of the tip to follow the profile of the surface [17]. The resonance frequency of the tip oscillating freely with amplitude A_0 , away from the sample surface is determined first and then tip is moved to the proximity of the sample surface where its oscillating amplitude decreases to A , as a result of interaction between the tip and sample surface while tip is still oscillating at its resonant frequency. The ratio of the two amplitudes A and A_0 is called damping. By keeping the damping of amplitude constant and scanning the sample, the surface topography can be imaged. Phase image of the surface can also be recorded simultaneously by using the phase difference between the phases of AC signal when the tip is freely oscillating and is in the vicinity of the sample surface. Phase shift depends upon the viscoelastic properties of the sample so phase image outlines the domains of varying material properties without describing the nature of the properties themselves. This AC mode AFM is particularly suitable for the samples that are soft or weakly bound to the substrate because it operates in the intermittent contact.

The surface analysis and morphological of our samples were studied using a Witec Alpha 300S atomic force microscope. The system can be used to perform a wide range of experiments such as Atomic Force Microscopy (AFM), Scanning Near Field Optical Microscopy (SNOM), confocal microscopy and Kelvin Probe Microscopy (KPM) [18]. An atomic force microscope is very sensitivity to mechanical vibrations and acoustic noise. For this reason, the AFM is placed in an anti-damping box with acoustic damping foam and the whole setup is place on an optical table with an air-pressured base to suppress the mechanical vibrations. Inside of walls of the box are covered with vibrations damping foam to suppress acoustic noise, and with aluminum foil to screen the electromagnetic noise. In the present study of graphene and graphene nanocomposites, the AFM was used to determine the surface topography of the films and thickness of thin films.

2.5 Summary

One of the major accomplishments of our thesis is the assembly and automation of PDS and 3-omega setups for measurement of thermal conductivity. Our PDS setup has flexibility to run measurements and collect the data with different pump beam powers and beam widths, automatic scan for user specified range of pump beam modulation frequencies, wavelength or combination of both with user chosen interval with specified steps and save data. The capability of the setup to repeatedly illuminate a sample with white light and then run spectroscopic measurements, has been successfully employed to investigate the Staebler-Wronski effect in hydrogenated amorphous silicon thin films (chapter 4), thermal conductivity measurements of graphene (chapter 5), RNA/graphene platelets nanocomposite thin films (chapters 6) and thermal conductivity measurement of

sample from 3M Canada Co. The setup is also in use by the members of our research group for the measurement of external quantum efficiency of organic solar cells.

The 3-omega method was built and used to double check the results of PDS measurements on specific samples. The advantage of PDS is that it is a non-destructive and contactless technique, so is more attractive than the 3-omega method in this respect.

Reference

- [1] D. P. Almond and P. M. Patel, *Photothermal Science and Techniques*, Chapman & Hall, 1996.
- [2] User manual of Sciencetech 201-1K-QTH lamp.
- [3] Newport, Product information sheet, courtesy of Newport Inc.
- [4] User manual of ThorLab MC2000 optical chopper.
- [5] Product specification note of photodiode Vishay PBW34.
- [6] S. Bialkowski, *Photothermal Spectroscopy Methods for Chemical Analysis* John Wiley & Sons, New York, 1996.
- [7] 3MTM FluorinertTM Liquids Properties, information sheet, courtesy of 3M.
- [8] Operational manual of Thorlabs PDP90S1 position detector.
- [9] Operational manual of lock-in amplifier model EG&G 5209.
- [10] M. S. Ahmed, S. Ezugwu, R. Divigalpitiya and G. Fanchini, *Carbon*, **61** (2013) 595.
- [11] S. Ezugwu, M. S. Ahmed, R. Bauld, R. Divigalpitiya, G. Fanchini, *Thin Solid Films*, **534** (2013) 520.
- [12] R. P. Prasankumar and A. J. Taylor *Optical Techniques for Solid-State Materials Characterization*, CRC Press Taylor & Francis Group, FL, 2012.
- [13] H. Wnag and M. Sen, *Int. J. Of Heat and Mass Trans.*, **52** (2009) 2102.
- [14] D. G. Cahill and R. O. Pohl *Phys. Rev. B.*, **35** (1987) 4067.
- [15] D. G. Cahill, *Rev. Sci. Inst.*, **61** (1990) 802.
- [16] G. Binnig, C. F. Quate and Ch. Gerber, *Phys. Rev. Letters*, **56** (1986) 930.
- [17] Y. Martin, C. C. Williams, and H. K. Wickramasinghe, *J. Appl. Phys.*, **61** (1987) 4723.
- [18] User manual of Witec Scanning Near-field Optical Microscope Alpha300S.

Chapter 3

3 Theory of photothermal deflection spectroscopy and the role of convection in photothermal fluids

An introduction to heat transfer is given in this chapter. In addition, the chapter presents a number of heat transfer models based on Fourier's equation of heat, which have been developed by us to describe pulsed heat dissipation from a thin film, deposited on an optically non-absorbing substrate, to an adjoining photothermal fluid. Specifically, one of such models will take into account for the first time the contribution of convective heat transfer from a sample to the fluid during photothermal deflection spectroscopy (PDS) measurements. In a specific version of our model, a photothermal fluid containing a small fraction of nanoparticles with high thermal conductivity is also considered. Finally, experiments validating this model (with single wall carbon nanotubes (CNTs) dispersed in carbon tetrachloride) have been performed by us and will be presented, which will allow us to quantitatively demonstrate the importance of heat convection in this specific system and to show its negligibility in other systems that are traditionally used to perform PDS experiments².

3.1 Introduction

Heat is a form of energy that transfers from one body to another, or within the same object, due to temperature gradients. Macroscopic heat transfer depends on the properties of solids and fluids at the atomistic level. Microscopic heat carriers include: phonons and

² Part of this chapter (Paragraphs 3.4-3.7) has been submitted as a research article to the Journal of Applied Physics (2013).

electrons, molecules of fluids, particles and nanoparticles diffusing in a fluid, and photons. Each one of these carriers contributes to the transfer of heat via one of three specific heat transfer mechanisms: conduction, convection and radiation.

3.1.1 Conduction

Conduction is the transfer of energy from a hot region of a material to a cold region as a result of drift of heat carriers, with negligible diffusion of atoms and molecules forming the substance. Conduction can take place both in solids and fluids. Although conduction is generally more relevant in solids and at fluid/solid interfaces, it also represents an important heat transfer mechanism in specific fluids such as helium and liquid metals [1]. In gases and liquids, conduction, if significant, may be due to the collision of molecules and/or suspended solid nanoparticles while, in solids, it is due to a combination of vibrations of atoms in crystalline or amorphous lattices and energy transport by diffusion of free electrons. In an isotropic and homogenous solid, the relationship between the heat flow and the temperature gradient is given by Fourier's law of diffusion of heat, which can be written as:

$$\dot{\mathbf{Q}}(\mathbf{r}, t) = -\mathbf{K} \cdot \nabla T(\mathbf{r}, t) \quad (3.1)$$

in which the temperature gradient $\nabla T(\mathbf{r}, t)$ is a vector normal to the isothermal surface.

The heat flux vector $\dot{\mathbf{Q}}(\mathbf{r}, t)$ represents the heat flow per unit time per unit area of the isothermal surface in the direction of decreasing temperature, which leads to the negative sign in eq.(3.1), and \mathbf{K} is the thermal conductivity, a positive scalar quantity that determines the ability of a material to efficiently transfer heat. The standard unit of thermal conductivity is $\text{W} \cdot \text{m}^{-1} \cdot \text{K}^{-1}$ [2-4].

3.1.2 Convection

Convection is the dominant mode of heat transfer within liquids or gases that are in macroscopic or microscopic motion. It involves the combined effects of heat conduction and motion of molecules and/or (nano)particles in the fluid. The rate of heat transfer by convection between the considered fluid and a rigid boundary is expressed by Newton's law of cooling:

$$\dot{Q}(\mathbf{r}, t) = -h \cdot (T_s - T_\infty) \quad (3.2)$$

where h , the heat exchange coefficient, depends on a number of variables including, but not limited to: geometry and roughness of the rigid boundary, nature of fluid motion, properties of the fluid and its bulk velocity. T_s is the temperature of the rigid boundary and T_∞ is the temperature of the fluid sufficiently far away from the surface. Both T_s and T_∞ may or may not explicitly depend on time. The standard unit of heat exchange coefficient is $\text{W} \cdot \text{m}^{-2} \cdot \text{K}^{-1}$.

3.1.3 Radiation

Radiation represents the energy emitted or absorbed by matter in the form of electromagnetic waves as a result of changes in the electronic configurations of atoms or molecules of a substance. Unlike conduction and convection, heat transfer by radiation does not require the presence of an intervening medium and can also occur in vacuum. It is the fastest energy transfer mechanism, since heat carriers, photons, propagate at the speed of light. All solids, liquids and gases emit, absorb or transmit radiation to varying degrees. The maximum rate of radiation that can be emitted from a surface is given by Stefan-Boltzmann (SB) law:

$$\dot{Q}(\mathbf{r}, t) = -\sigma_{\text{SB}} \cdot T_s^4 \quad (3.3)$$

where $\sigma_{\text{SB}} = 5.67 \times 10^{-8} \text{ W} \cdot \text{m}^{-2} \cdot \text{K}^{-4}$, is the SB constant. The relatively low value of the SB constant suggests that heat transfer by radiation is negligible over conduction and/or convection at low or moderate temperatures, while it may become very significant at high T_s due to the strong power law in eq. (3.3). Heat transfer by radiation will be generally neglected in our work since our measurements have been carried out at room temperature.

3.2 Theory of thermal conductivity in semiconductors

In solids, heat is transported by diffusion of both electrons and lattice waves. Quanta of lattice vibrations are called phonons. Although the contribution of electrons is overwhelming in metals, phonon thermal conductivity becomes important in semiconductors and semimetals, for which the concentration of free electrons is relatively low. In crystalline carbon-based materials, including graphite, diamond and carbon nanotubes, heat transport is dominated by phonons [2,5]. In graphitic amorphous carbons, in which a significant concentration of free electrons exists, but disorder prevents the formation of propagating lattice waves and coherent phonon modes, the electronic contribution to the thermal conductivity dominates [6]. In crystalline insulators heat is transmitted entirely by phonons, since there are no free electrons in these substances. In general, the total thermal conductivity of a solid is the parallel of the lattice (K_p) and electronic (K_e) contributions:

$$K = K_e + K_p \quad (3.4)$$

The magnitude of both K_p and K_e is limited by scattering of heat carriers. For a free electron gas, electron scattering mainly occurs via electron-phonon interaction and the

electron-phonon relaxation time controls both the electrical and thermal conductivities [6]. For a gas of phonons, no limitations in thermal conductivity might be observed if phonons did not scatter with each other or with specific impurities in the lattice. Limitations of lattice thermal conductivity by scattering of phonons with impurities (including defects, contaminations, lattice distortions and grain boundaries) are critical in microcrystalline or low-purity crystals of semiconductors and electrical insulators. Phonon-phonon scattering limits the lattice thermal conductivity of sufficiently pure crystals of intrinsic semiconductors and insulators. Since the population of phonons increases with temperature, phonon-phonon scattering becomes more important at high temperatures, even in relatively impure solids. Below, we will describe the theory of lattice thermal conductivity that has been developed in multiple stages between 1930 and 1950 [6].

Specifically, P. Debye assumed that waves of lattice vibrations propagate through an elastic continuum. Applying the kinetic theory of gases to phonon gases in solids, he wrote the lattice thermal conductivity as [5]:

$$K_p = \frac{1}{3} c \cdot v \cdot \Lambda \quad (3.5)$$

where c is the specific heat, v is the velocity of acoustic phonons and sound in that solid and Λ is phonon mean free path between randomized collisions of phonons.

Scattering of phonons by other phonons is the result of anharmonic interactions between oscillating atoms in the solid lattice. If forces between atoms were purely harmonic, there would be no collisions between phonons [6]. At higher temperatures, the phonon mean free path is inversely proportional to the lattice temperature, because the higher the temperature, the higher population of phonons that are excited and such

population is proportional to T . In a periodic lattice, if two phonons with wave vectors \mathbf{k}_1 and \mathbf{k}_2 collide, they produce an outgoing phonon and, according to the conservation of momentum

$$\mathbf{k}_1 + \mathbf{k}_2 = \mathbf{k}_3 \quad (3.6)$$

Although both \mathbf{k}_1 and \mathbf{k}_2 lie inside the first Brillouin zone, the outgoing phonon possesses a wave vector \mathbf{k}_3 that may or may not lie in such zone. In the first case, crystal momentum is conserved before and after the phonon collision, entropy is not generated in the phonon gas, the process has no effect in limiting the propagation of phonons and the thermal conductivity associated to these crystal modes is infinite. Phonon collision processes in which crystal momentum is conserved are called normal processes or “N-processes”. On the other hand, if the outgoing phonon possesses a wave vector that lies outside the first Brillouin zone, then its total momentum can always be written as:

$$\mathbf{k}'_3 = \mathbf{k}_3 + \mathbf{G} \quad (3.7)$$

which represents the sum of a reciprocal vector \mathbf{G} and a crystal wave vector \mathbf{k}'_3 . In this second case, collision between two phonons is described by:

$$\mathbf{k}_1 + \mathbf{k}_2 = \mathbf{k}_3 + \mathbf{G} \quad (3.8)$$

The difference between three-phonon process for which \mathbf{k}_3 lies inside and outside the first Brillouin zone is illustrated in Figure 3.1. Collisions in which $\mathbf{G} \neq \mathbf{0}$ are called Umklapp processes (after the German word for “flipping over”) or “U-processes” and do not conserve the crystal momentum, although the total momentum and energy are always conserved for both N- and U-processes. Umklapp processes introduce at each point \mathbf{r} of the real lattice a phase lag $\mathbf{G} \cdot \mathbf{r}$ between the incoming lattice waves with modulations $\exp[i(\mathbf{k}_1 \cdot \mathbf{r} - \Omega(\mathbf{k}_1) \cdot t)]$ and $\exp[i(\mathbf{k}_2 \cdot \mathbf{r} - \Omega(\mathbf{k}_2) \cdot t)]$, and the outgoing lattice wave, with

modulation $\exp[i(\mathbf{k}_3 \cdot \mathbf{r} - \Omega(\mathbf{k}_3) \cdot t + \mathbf{G} \cdot \mathbf{r})]$. Such a phase lag is responsible for the delay in transferring a signal via lattice waves in a crystal and, therefore, it is responsible for the finite thermal conductivity in infinite and perfect crystals, as well as other phenomena including, but not limited to, the generation of entropy and the attenuation of sound in solids.

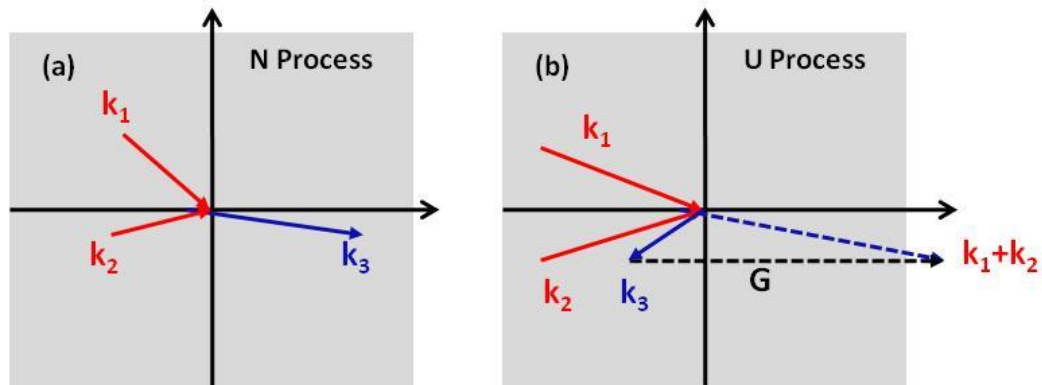


Figure 3.1 Schematic of phonon-phonon interaction (a) Normal three-phonon process and (b) Umklapp three-phonon process.

The Debye temperature

$$\Theta_D = \frac{2\hbar \cdot \Omega_D}{k_B} \quad (3.9)$$

represents the Brillouin zone-boundary frequency Ω_D of the phonon modes of a specific solid expressed in Kelvin. Subsequently, at temperatures $T > \Theta_D$ all of the zone-boundary phonon modes of the solid are excited. Due to the proximity of their momenta to the boundary of first Brillouin zone, most of such phonon modes give rise to U-processes when they collide, by transferring the excitation to another Brillouin zone and introducing a phase-lag in the propagation of heat via lattice waves. Therefore, Θ_D expresses a cut-off temperature between a low temperature behavior of the thermal

conductivity, in which it is controlled by the probability of an Umklapp process to occur, and a high-temperature behavior, in which the fraction of Umklapp processes over the total number of phonon-phonon scattering processes tends to 100%. In this second regime, the thermal conductivity is controlled by the length of the mean free path of phonons between two consecutive collisions, both of them giving rise to U-processes.

Since the mean free path of a given phonon mode is inversely proportional to the density of all of the other phonons with which it interacts and the total phonon population is proportional to the lattice temperature, then we have:

$$\Lambda \propto T^{-1} \quad (3.10)$$

and, at sufficiently high temperatures, it is expected that the lattice thermal conductivity decreases as T^{-1} as can be shown by replacing eq.(3.10) into eq.(3.5).

The energy of phonons suitable for an U-process to happen is of the order of $\frac{1}{2} \cdot k_B \cdot \Theta_D$. Therefore, two phonons with energy that is significant lower than such threshold cannot give rise to Umklapp scattering. At low enough temperatures, $T \ll \Theta_D$ and the number of phonons with energy of the order of $\frac{1}{2} \cdot k_B \cdot \Theta_D$ is expected to vary exponentially as $\exp(-\Theta_D/2T)$, according to Boltzmann's law. Thus U-processes lead the thermal conductivity to decrease exponentially with T in the low temperature regime and as T^{-1} in the high temperature regime [2,5] in which $T \gg \Theta_D$.

At even lower temperatures, there are only a few available phonon modes, so phonon-phonon collisions become ineffective, the wavelength of such phonons is very long and phonons are not effectively scattered by impurities, which are much smaller in size than a phonon wavelength. In these cases, scattering from crystal grain boundaries becomes the primary mechanism leading to finite phonon mean free path, which also

leads the thermal conductivity to depend on the size of the crystal. Therefore, $\Lambda \approx d$, where d represents the thickness (in the case of a thin film crystal) or the diameter of the grains (in the case of a microcrystalline specimen) and the mean free path becomes independent of temperature. However, specific heat is another factor affecting the thermal conductivity in addition to mean free path. At low enough temperatures, the specific heat varies as $c \propto T^3$ [6] so the d -dependent thermal conductivity will also vary with the very same temperature trend of specific heat.

Crystal imperfections including impurities and defects also scatter phonons because they destroy the perfect coherence of lattice waves. For instance, a guest atom different from the host atoms in the crystalline lattice is a source of two-phonon scattering processes of lattice waves that introduces an uncertainty in crystal momentum proportional to the mass difference between the two atoms. The greater the density of impurities, the larger the amount of scattering processes and the shorter the phonon mean free path. The variation of lattice thermal conductivity with temperature from a range of different scattering mechanisms are summarized in Figure 3.2.

In this thesis, we are mostly interested in the variations of thermal conductivity of specific semiconductors at room temperature, at which the phonon mean free path, thermal capacity, phonon population, specimen size and defects may all play a role in determining such quantity. Therefore accurate experiments and phenomenological models specific to the semiconductor under investigation are both of paramount importance. Specific phenomenological models will be described in Chapters 4-6. In the next section of this chapter we will describe the macroscopic models that will allow us to

measure the thermal conductivity of semiconductors from photothermal deflection experiments.

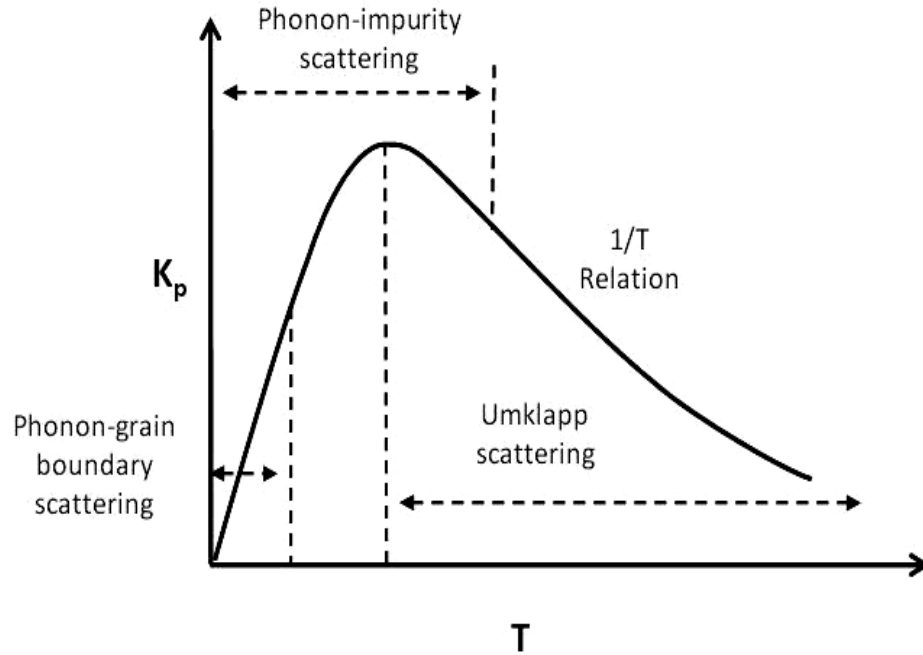


Figure 3.2 Summary of various phonon-scattering mechanisms affecting the lattice thermal conductivity in crystalline materials at different temperatures.

3.3 The heat conduction equation

Fourier's equation of heat for a stationary, homogenous and isotropic medium can be derived by considering the energy balance for a control region of volume V of such medium, which can be written in the form:

$$\left\{ \begin{array}{l} \text{Rate of Heat entering through} \\ \text{the boundary of volume } V \end{array} \right\} + \left\{ \begin{array}{l} \text{Rate of heat generation} \\ \text{in the volume } V \end{array} \right\} = \left\{ \begin{array}{l} \text{Rate of heat storage} \\ \text{in the volume } V \end{array} \right\} \quad (3.11)$$

in which

$$\left\{ \begin{array}{l} \text{Rate of heat entering through} \\ \text{the boundary of volume } V \end{array} \right\} = -\oint_A \dot{\mathbf{Q}} \cdot \hat{\mathbf{n}} \cdot dA = -\int_V \nabla \cdot \dot{\mathbf{Q}} \cdot dV. \quad (3.12)$$

where \dot{Q} is the heat flux exiting a portion dA of the closed surface with area A surrounding the control region as shown in Figure 3.3 and \hat{n} is unit vector normal to the area element dA (with conventionally positive sign for outward heat flux) and divergence theorem was used to transform the surface integral into a volume integral in the equation above. Let $g(\mathbf{r},t)$ indicate the amount of thermal power that is internally generated at point \mathbf{r} of the control region at the time t . For the second term in eq. (3.11) we then write

$$\left\{ \begin{array}{l} \text{Rate of heat generation} \\ \text{in the volume } V \end{array} \right\} = \int_V g(\mathbf{r},t) \cdot dV . \quad (3.13)$$

The third term in eq. (3.11) can be written as

$$\left\{ \begin{array}{l} \text{Rate of heat storage} \\ \text{in the volume } V \end{array} \right\} = \int_V \rho \cdot c \cdot \frac{\partial T(\mathbf{r},t)}{\partial t} \cdot dV \quad (3.14)$$

where $T(\mathbf{r},t)$ is the temperature at each point and time, and ρ and c are the mass density and the specific heat of the considered medium, respectively. The third term in eq. (3.11) is a dynamic term that is non-zero only in the case of transitory thermal phenomena dictated by time-dependent heat generation $g(\mathbf{r},t)$ or by specific initial conditions.

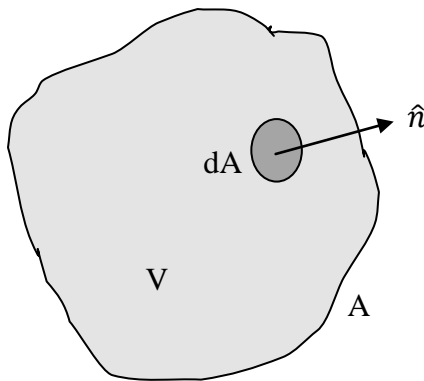


Figure 3.3 Volume element considered for heat balance equation.

By substituting eqs. (3.12) – (3.14) into eq. (3.11), we obtain the following balance equation for each macroscopic volume V :

$$\int_V \left(-\nabla \cdot \dot{\mathbf{Q}} + \mathbf{g}(\mathbf{r}, t) - \rho \cdot \mathbf{c} \cdot \frac{\partial T(\mathbf{r}, t)}{\partial t} \right) \cdot dV = 0 \quad (3.15)$$

Such equation represents the sum of multiple energy balances, each one computed on a microscopic volume element dV for which identity (3.15) must hold. We therefore obtain a differential form that is equivalent to the integral form eq. (3.15):

$$-\nabla \cdot \dot{\mathbf{Q}} + \mathbf{g}(\mathbf{r}, t) = \rho \cdot \mathbf{c} \cdot \frac{\partial T(\mathbf{r}, t)}{\partial t} \quad (3.16)$$

If we assume that the control region is entirely occupied by a homogeneous and isotropic solid of thermal conductivity K , for which thermal power $\dot{\mathbf{Q}}$ propagates according to eq. (3.1), we then obtain by substitution:

$$\nabla^2 T(\mathbf{r}, t) + \frac{1}{K} \cdot \mathbf{g}(\mathbf{r}, t) = \frac{1}{D} \cdot \frac{\partial T(\mathbf{r}, t)}{\partial t} \quad (3.17)$$

Eq. (3.17), originally derived by Fourier in 1801 represents the differential form of the equation of heat, and is a second order partial differential equation that can be solved by separation of variables. In such equation, we have defined the quantity

$$D = \frac{K}{\rho \cdot \mathbf{c}} = \frac{K}{C} \quad (3.18)$$

as the thermal diffusivity of the solid, which indicates how fast heat flux propagates through a material. $C = \rho c$ represents the thermal capacitance of the material. D depends on both the transport properties of the material (via K) and the quasi-static thermodynamic properties (via C).

The differential equation of heat has an infinite set of solutions unless specific boundary and initial conditions are imposed. Boundary conditions may specify either the temperature or the heat flow on the contour of the control region. Initial conditions specify the temperature at the beginning of the process, which is generally set to start at $t = 0$. The boundary conditions can be derived by writing an energy balance equation. There are a number of different types of boundary conditions that may be used to describe the temperature, the heat flux transferred by conduction or the heat exchanged by convection from the control region to another medium. In general, for a continuous temperature profile at a rigid interface between two media, 1 and 2, it must always be $T_1(\mathbf{r} = \mathbf{r}_0, t) = T_2(\mathbf{r} = \mathbf{r}_0, t)$ and the temperature must be a continuous function. More specifically, there may be three different types of boundary conditions that can be imposed to the equation of heat at the interfaces, as shown in Figure 3.4.

In boundary conditions of the first type also known as Dirichlet conditions, the temperature at the interface remains constant over time:

$$T_i(\mathbf{r} = \mathbf{r}_0, t) = T_0(\mathbf{r}_0) = \text{const}, \quad \text{for } i = 1, 2 \quad (3.19)$$

where $\{\mathbf{r}_0\}$ represents the collection of points of space that form the interface.

In boundary conditions of second type also known as Neumann conditions, the heat flux transferred by conduction normally to the interface is conserved and for a perfect thermal contact between two media with thermal conductivities K_1 and K_2 , and temperatures T_1 and T_2 . Therefore, we have:

$$K_1 \cdot \nabla T_1(\mathbf{r} = \mathbf{r}_0, t) \cdot \hat{\mathbf{n}} = K_2 \cdot \nabla T_2(\mathbf{r} = \mathbf{r}_0, t) \cdot \hat{\mathbf{n}} \quad (3.20)$$

where the indices 1 and 2, in eq. (3.20) indicate that the two gradients have to be calculated in two different media.

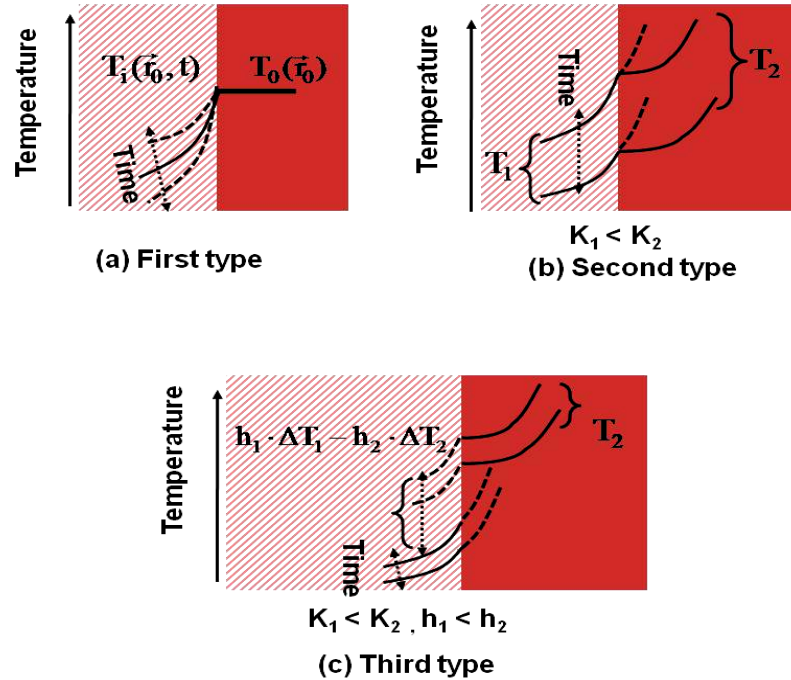


Figure 3.4 The three different boundary conditions for the Fourier's equation of heat (3.17): (a) Dirichlet, (b) Neumann and (c) Robin conditions.

In boundary conditions of third type also known as Robin conditions, the total heat flux transferred by conduction and convection at the interface between two media with thermal heat exchange coefficients h_1 and h_2 is conserved. Therefore, we have:

$$h_1 \cdot \Delta T_1 + K_1 \cdot \nabla T_1(\mathbf{r} = \mathbf{r}_0, t) \cdot \hat{n} = h_2 \cdot \Delta T_2 + K_2 \cdot \nabla T_2(\mathbf{r} = \mathbf{r}_0, t) \cdot \hat{n} \quad (3.21)$$

where $\Delta T_1 = T(\mathbf{r} = \mathbf{r}_0, t) - T_{\infty 1}$ and $\Delta T_2 = T(\mathbf{r} = \mathbf{r}_0, t) - T_{\infty 2}$ are the differences of fluid temperatures between the interfaces $T_i(\mathbf{r} = \mathbf{r}_0, t)$ and far away from the interfaces ($T_{\infty 1}$ and $T_{\infty 2}$) for media 1 and 2, respectively. Depending upon the specific nature of the problem, the most appropriate type of boundary conditions can be chosen and they will determine the specific nature of thermal wave that will form within the control region.

3.4 Thermal waves in thermally ultra-thin films and their applications

Thermal waves are generated in a system when part of it is exposed to periodic internal heating at a specific frequency ω , which results in subsequent periodic variations of temperature. Such temperature variations depend on the boundary conditions, on the amount of heat generated in the control region and on the thermal properties of the medium, and can be used to determine such properties. Ångström used the temperature-wave method to determine the thermal conductivity of a solid rod [7]. The theoretical models that are most commonly used for studying thermal waves in order to understand PDS experiments are based on the theory of photoacoustic effect that was originally developed by Rosencwaig and Gersho [8]. These authors applied acoustic waves for the characterization of materials by photoacoustic spectroscopy. Boccara *et al.* [9] demonstrated the formal analogy between acoustic waves in photoacoustic spectroscopy and thermal waves in PDS and exploited such analogy to study the temperature gradients in the proximity of the surface of a solid sample. In next two sections we will develop a model that will allow us to calculate the temperature profile and the expressions of the amplitude and phase of the PDS signal by solving the equation of heat (3.17) in one dimension under the assumption that samples are thermally ultra-thin and are deposited on thermally insulating and optically transparent substrates, irrespectively of the optical thickness of such films.

3.4.1 One-dimensional heat conduction – Thin “pump beam”

Consider a thin film deposited on an optically transparent and thermally non-conducting substrate which is immersed in a photothermal fluid and is exposed to a “pump” beam

that is very long in vertical direction and is modulated at a pulse frequency ω . Assume that all of the light that is absorbed in the thin film is converted into heat and that the film is much thinner than the diffusion length [$l_D = (D_s/2\omega)^{1/2}$] of the thermal wave, while the width of the sample is much bigger than l_D : this assumption is valid for most solar-grade semiconductors irrespectively of their optical absorption coefficient.

Let us also initially assume that the illuminating beam is a thin line source with negligible thickness in the y -direction in which it can be represented by a delta-shaped function, $g(y,t) = P_0 \cdot \delta(y - y_0 = 0) \cdot \exp(j\omega t)$, while it is very long and uniform in the z -direction, as schematically shown in Figure 3.5(a). In these conditions, the one-dimensional Fourier equation for in-plane diffusion of heat along the y -direction of the film can be used. In such a configuration, equation (3.17) can be written as:

$$\frac{\partial^2 T_s(y,t)}{\partial y^2} = \frac{1}{D_s} \cdot \frac{\partial T_s(y,t)}{\partial t} \quad (3.22)$$

where $T_s(y,t)$ and D_s indicate the temperature and thermal diffusion coefficient of the film, respectively. Far away from the point of illumination, which is set at $y = 0$ as in Figure 3.5(a), the sample is at ambient temperature. An inspection of eq. (3.22) suggests that, if $T_s'(y,t)$ is a solution for such equation, also $T_s(y,t) = T_s'(y,t) + \text{constant}$, will satisfy it. Therefore, we will set the ambient temperature as the “zero-temperature” and T_s will represent temperature in excess to the ambient level. Under this assumption, First type boundary conditions for eq.(3.22) can be written at $y = \pm \infty$:

$$T_s(y = \pm \infty, t) = 0 \quad (3.23)$$

At the point of illumination, $y = 0$, the amount of heat generated from the absorption of light must equal to the flux of heat that diffuses away from such point, both to the left (y

> 0) and to the right ($y < 0$) of it. Symmetry considerations suggest that the heat flux diffusing in each of the two directions is the same and is proportional to the thermal conductivity (K_s) of the thin film sample. Subsequently, boundary conditions of the

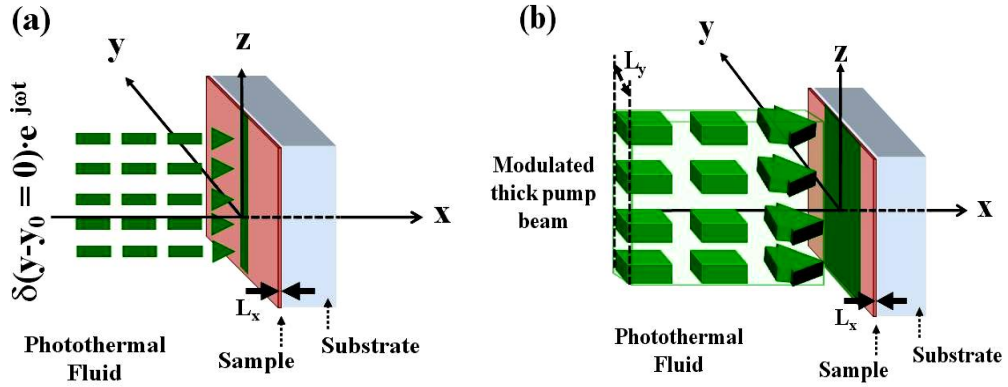


Figure 3.5 Thin film sample on a non-absorbing substrate, illuminated by a (a) thin pump beam in the y -direction, and very long and uniform in the z -direction, and (b) thick pump beam in the y -direction (length L_y) and very long in the z -direction. In both cases the probe beam is parallel to the y -axis.

second type can be written at $y = 0$:

$$\frac{Q_0}{2} \cdot e^{j\omega \cdot t} = -K_s \frac{\partial T_s(y=0, t)}{\partial y}, \quad (3.24)$$

where Q_0 is the maximum illumination power per unit area of the thin film that is deposited at each pulse of light from pump beam. Q_0 depends on the power P_0 carried at each pulse by the “pump” beam as well as on the optical absorption coefficient (α_s) of the thin film sample. Specifically, given an incident modulated pump beam of power density (P_0), the illumination power that is deposited within the thin film is given by

$$Q_0 = \frac{P_0}{L_y \cdot L_z} \cdot \int_0^{L_x} e^{-\alpha_s \cdot x} \cdot dx = \frac{P_0}{L_y \cdot L_z} \cdot \left(\frac{1 - e^{-\alpha_s \cdot L_x}}{\alpha_s \cdot L_x} \right) \quad (3.25)$$

where the x-axis is oriented as in Figure 3.5 and L_x is the film thickness. It is worth noting that, for optically ultra-thin films, $1 - \exp(-\alpha_s \cdot L_x) \approx \alpha_s \cdot L_x$ so that T_s , as well as the PDS signal, is independent of α_s and no optical properties of the film can be measured by PDS, as predicted in Chapter 2. By replacing eq. (3.25) into eq. (3.24), and by considering that $K_s = C_s \cdot D_s$ as for eq.(3.17), we obtain that

$$\frac{P_0}{L_y \cdot L_z} \cdot \left(\frac{1 - e^{-\alpha_s \cdot L_x}}{\alpha_s \cdot L_x} \right) \cdot e^{-j\omega t} = -C_s \cdot D_s \cdot \frac{\partial T_s(y=0, t)}{\partial t} \quad (3.26)$$

The solution of eq. (3.22) with boundary conditions (3.23) and (3.26) leads to the following temperature profile at the sample surface as discussed in detail in Appendix B.

$$T_s(y, t) = \frac{P_0}{2 \cdot L_y \cdot L_z \cdot C_s \cdot \sqrt{D_s \cdot \omega}} \cdot \left(\frac{1 - e^{-\alpha_s \cdot L_x}}{\alpha_s \cdot L_x} \right) \cdot e^{-\sqrt{\frac{\omega}{2 \cdot D_s}} \cdot |y|} \cdot e^{j(\omega \cdot t - \sqrt{\frac{\omega}{2 \cdot D_s}} \cdot |y| - \pi/4)} \quad (3.27)$$

Although the most general solution of eq. (3.22) is a linear superposition of thermal waves (3.27), each one with its own oscillation frequency, only the particular wave solution with the same pulse frequency of the illuminating “pump” light beam will be excited in the stationary regime. From eq. (3.27) it can be observed that such thermal wave propagates transversally to the “pump” beam and along the thin film surface.

3.4.2 One-dimensional heat conduction – Thick “pump beam”

Recall that in our specific PDS setup, described in Chapter 2, the beam is relatively uniform and is approximately long $L_z = 20$ mm in z-direction, while it is significantly less wide in y-direction, approximately $L_y = 5$ mm or less, depending on the chosen aperture of the monochromator slits. These construction dimensions justify the use of a simple one-dimensional heat conduction models to analyze our experiments, with remarkable simplifications in terms of data interpretation. On the other hand, in

several practical cases, in which $L_y \ll (2D_s/\omega)^{1/2}$, a too thin beam may detrimentally effect the magnitude of T_s given by eq.(3.27) proportional to the “pump” beam power and decreases exponentially with y , resulting in a low signal to noise ratio. Consequently, the development of a thick beam heat conduction model is essential for the scopes of our work.

We can determine the temperature profile at the sample surface upon illumination with a thick beam as shown in Figure 3.5(b) by superimposing a set of solutions for thin beams using the Green’s function method [10]. A uniform thick beam of width L_y can be considered as a linear combination of an infinite number of thin beams. Each one of such thin beams has an intensity $dP_0 = (P_0/L_y) \cdot dy_0$ and is located at $y = y_0$ (where $-L_y/2 < y_0 < +L_y/2$). As detailed in Appendix B, the resulting temperature profile within the sample in the case of thick beam can be written as:

$$T_s^I(y,t) = \frac{P_0}{2 \cdot L_y^2 \cdot L_z \cdot C_s \cdot \omega} \cdot \left(\frac{1 - e^{-\alpha_s \cdot L_x}}{\alpha_s \cdot L_x} \right) \cdot \left[e^{-\frac{(1+j)\sqrt{\frac{\omega}{2 \cdot D_s}} \cdot (y - L_y/2)}{}} \right] \cdot e^{j(\omega \cdot t - \pi/2)} \quad \text{for } y \geq 0 \quad (3.28a)$$

and

$$T_s^{II}(y,t) = \frac{P_0}{2 \cdot L_y^2 \cdot L_z \cdot C_s \cdot \omega} \cdot \left(\frac{1 - e^{-\alpha_s \cdot L_x}}{\alpha_s \cdot L_x} \right) \cdot \left[e^{\frac{(1+j)\sqrt{\frac{\omega}{2 \cdot D_s}} \cdot (y + L_y/2)}{}} \right] \cdot e^{j(\omega \cdot t - \pi/2)} \quad \text{for } y \leq 0 \quad (3.28b)$$

For optically thin films for which the condition $\alpha_s \cdot L_x \ll 1$ holds, eqs. (3.28) can be simplified to

$$T_s^I(y,t) = \frac{P_0}{2 \cdot L_y^2 \cdot L_z \cdot C_s \cdot \omega} \cdot \left[e^{-\frac{(1+j)\sqrt{\frac{\omega}{2 \cdot D_s}} \cdot (y - L_y/2)}{}} \right] \cdot e^{j(\omega \cdot t - \pi/2)} \quad \text{for } y \geq 0 \quad (3.29a)$$

and

$$T_s^{\text{II}}(y,t) = \frac{P_0}{2 \cdot L_y^2 \cdot L_z \cdot C_s \cdot \omega} \cdot \left[e^{(1+j) \sqrt{\frac{\omega}{2 \cdot D_s}} \cdot (y+L_y/2)} \right] \cdot e^{j(\omega \cdot t - \pi/2)} \quad \text{for } y \leq 0 \quad (3.29b)$$

This means that the temperature difference between the sample and the fluid, on average during a heating cycle, is

$$\langle T_s \rangle = \frac{P_0}{\sqrt{2} \cdot L_y^2 \cdot L_z \cdot C_s \cdot \omega} \cdot \sinh \left(\sqrt{\frac{\omega}{2 \cdot D_s}} \cdot \frac{L_y}{2} \right) \quad (3.30)$$

Therefore, for an optically thin sample with thermal diffusivity $D_s \sim 10^{-6} \text{ m}^2 \cdot \text{s}^{-1}$ and $C_s \sim 10^{-4} \text{ J} \cdot \text{m}^{-3} \cdot \text{K}^{-1}$, a “pump” light intensity $P_0 \sim 10 \text{ mW}$ gives $\langle T_s \rangle = 3.5 \text{ K}$ at $\omega = 20 \text{ Hz}$. This is a quite significant temperature gradient that is able to produce a significant and detectable deflection angle of the “probe” beam, as will be discussed in the next section.

3.5 PDS signal in thermally ultra-thin films

The angle of deflection for a transversal probe beam that is directed in y-direction, parallel to the surface of a sample immersed in a photothermal liquid, is given by [11]

$$\Phi(t) = \frac{1}{n_f} \cdot \frac{dn_f}{dT_f} \int_{-\infty}^{+\infty} \frac{\partial T_f(x=0, y, t)}{\partial x} \cdot dy \quad (3.31)$$

where n_f is the refractive index of the photothermal fluid, dn_f/dT_f is the temperature coefficient of the index of refraction and $T_f(x=0, y, t)$ is the temperature of the fluid close to the sample surface.

In eq. (3.31), the specific form of $T_f(x, y, t)$ that needs to be used depends on the specific properties of the fluid. It may be reasonable to assume that, in the first few molecular layers of a liquid, the molecules are strongly adhering to the adjoining surface of a solid sample. In such case, they will have a limited mobility and convective heat transfer may be negligible. This is the assumption that has been made by all of the

literature on PDS that was accessible to us (see e.g. refs.) [11-15]. In section 3.5.1, we also will exploit such an assumption in order to determine the phase and amplitude of the PDS signal in our specific experimental setup. The assumption of purely conductive dissipation of heat will be released by us in section 3.5.2, in which convection in the fluid will be considered, and we will obtain a more general expression for the phase and amplitude of the PDS signal that will also depend on the heat exchange coefficient at the fluid/sample interface.

3.5.1 PDS signal with negligible convection in the photothermal fluid

If convection in the photothermal fluid can be ignored, then the Fourier's equation of heat in such liquid can be written as:

$$D_f \cdot \left[\frac{\partial^2 T_f(x, y, t)}{\partial x^2} + \frac{\partial^2 T_f(x, y, t)}{\partial y^2} \right] = \frac{\partial T_f(x, y, t)}{\partial t} \quad (3.32)$$

where D_f is the thermal diffusion coefficient of the fluid that is modelled as semi-infinite convective medium with much larger thermal capacitance than the sample, for which eq. (3.32) can be solved by imposing the Dirichlet conditions (3.19) at the fluid/solid interface, from which we must have

$$T_f(x=0, y, t) = T_s(y, t), \quad (3.33)$$

where the right hand side of the eq. (3.33) is given by eq. (3.27) or eq.(3.28) for thin or thick film, respectively. The solution of eq. (3.32) by using boundary condition (3.33) is given in Appendix B. Basically, this can be done by separating the variables as $T_f(x, y, t) = \chi_f(x) \cdot \psi_f(y) \cdot \exp(j\omega t)$. The attenuation of the temperature in the fluid at a distance x from the sample provides an expression for $\chi_f(x)$, that is exponentially decaying with x . The temperature profile longitudinally to the sample surface is given by $\psi_f(y)$ that has the

same dependence of y as that of sample temperature, which is given by $T_s(y,t)$ [eq. (3.28)]. Overall, the temperature in the fluid in the absence of convection is given by eq. (B23). By differentiating this expression over x and replacing it into eq. (3.31) we obtain:

$$\Phi(t) = \frac{1}{n_f} \left| \frac{dn_f}{dT} \right| \cdot \frac{P_0}{C_s \cdot L_y^2 \cdot L_z \cdot \omega} \cdot \left[\frac{1 - \exp(-\alpha_s \cdot L_x)}{\alpha_s \cdot L_x} \right] \cdot \sqrt{\frac{D_s}{D_{\text{eff}}}} \cdot \exp\left(\sqrt{\frac{\omega}{2 \cdot D_s}} \cdot L_y\right) \cdot \exp\left[j \cdot \left(\omega \cdot t - \frac{\pi}{2} + \sqrt{\frac{\omega}{2 \cdot D_s}} \cdot L_y\right)\right] \quad (3.34)$$

where

$$A_{\phi}^{(K)} = \frac{1}{n_f} \left| \frac{dn_f}{dT} \right| \cdot \frac{P_0}{C_s \cdot L_y^2 \cdot L_z \cdot \omega} \cdot \left[\frac{1 - \exp(-\alpha_s \cdot L_x)}{\alpha_s \cdot L_x} \right] \cdot \sqrt{\frac{D_s}{D_{\text{eff}}}} \cdot \exp\left(\sqrt{\frac{\omega}{2 \cdot D_s}} \cdot L_y\right) \quad (3.35)$$

and

$$\Delta_{\phi}^{(K)} = \sqrt{\frac{\omega}{2 \cdot D_s}} \cdot L_y - \frac{\pi}{2} \quad (3.36)$$

are the amplitude and phase of the angle of photothermal deflection, respectively. D_{eff} is the effective thermal diffusivity of the fluid-sample system that can be defined as the series of the diffusivities of the two media:

$$D_{\text{eff}}^{-1} = D_s^{-1} + D_f^{-1} \quad (3.37)$$

Eqs. (3.35) and (3.36) are critical for our work since they will allow us to analyze our PDS experiments that produce the amplitude and phase of deflection angle at the specific wavelength and chopping frequency of the pulsed “pump” light beam.

Eq. (3.36) demonstrates that under assumptions for which this expression is calculated, it is always possible to extract the thermal diffusivity of a thin film from the phase of the PDS signal. The phase must be independent of the use wavelength of the “pump” beam. From eq. (3.35), we can observe that there are two unknown properties of the sample that determine the amplitude of the PDS signal if the thermal diffusivities of

the fluid and the sample are known: the thermal capacitance and the optical absorption coefficient of thin film. If the film is optically thin and $1 - \exp(-\alpha_s L_x) \approx \alpha_s L_x$, then dependency of $A_\phi^{(K)}$ on α_s is negligible and $A_\phi^{(K)}$ is also independent of the used wavelength of the “pump” beam, so this hypothesis can be easily verified. In such case knowledge of $A_\phi^{(K)}$ immediately offers the possibility to determine the thermal capacitance of the film and, subsequently, the thermal conductivity via eq. (3.17).

If the film is optically thick, the dependency of $A_\phi^{(K)}$ on the wavelength of the “pump” beam offers an avenue for determining both $\alpha_s(\lambda)$ and C_s , if $\alpha_s(\lambda)$ is known at a specific wavelength λ_0 from an independent measurement – typically from a transmittance measurement performed with a UV-visible spectrophotometer at a λ_0 shorter than the optical band gap of the material. This measurement allows the “calibration” of the PDS spectrum and the extraction of C_s at that wavelength by replacing the known value of $\alpha_s(\lambda_0)$ in eq. (3.35) and by expliciting it as a function of the thermal capacitance. Subsequently, by expliciting eq. (3.35) as a function of $\alpha_s(\lambda)$ at wavelength at which α_s is unknown, it is also possible to estimate the optical absorption spectrum of the thin film. This option is particularly valuable for spectral regions of λ in which $\alpha_s(\lambda)$ is very low (down to $0.1 - 10 \text{ cm}^{-1}$ in $0.1 - 1 \text{ }\mu\text{m}$ thick samples) because available UV-visible spectrophotometric techniques (as described in Chapter 2, section 2.3) are unsuitable at those poor levels of optical absorption. Therefore, simultaneous determination of small values of $\alpha_s(\lambda)$, as well as C_s , D_s and K_s , is possible by PDS (as will be exploited by us in Chapter 4) and the underlying hypothesis can be rigorously tested.

3.5.2 PDS signal in the presence of convection in the photothermal fluid

In the presence of convective heat transfer, the heat diffusion equation for the fluid can be written as

$$D_f \cdot \frac{\partial^2 T_f(x, y, t)}{\partial x^2} = \frac{\partial T_f(x, y, t)}{\partial t} - H \cdot T_s(y, t), \quad (3.38)$$

where H is the heat transfer rate at the fluid/sample interface which is defined as:

$$H = \frac{h_f}{\rho_f \cdot c_f \cdot L_f} \quad (3.39)$$

where h_f is the heat transfer coefficient, ρ_f is density of the fluid, L_f is the thickness of thermal boundary layer and c_f is heat capacity of the fluid. It is worth noting that H is measured in Hz. Boundary conditions for eq. (3.38) are given by eq. (3.33) so that

$$T_f(x = -\infty, y = \pm\infty, t) = 0 \quad (3.40a)$$

and

$$T_f(x = 0, y, t) = T_s(y, t) \quad (3.40b)$$

These boundary conditions mean that the temperature of the fluid far away from the sample is the same as the ambient temperature [eq. (3.40a)]. Conversely, at the interface between the fluid and sample the fluid temperature must be same as the sample temperature [eq. (3.40b)]. By solving eq. (3.38) with such boundary conditions, the temperature profile of the fluid is obtained:

$$T_f^I(x, y, t) = \frac{P_0}{2 \cdot L_y^2 \cdot L_z \cdot C_s \cdot \omega} \cdot \left(\frac{1 - e^{-\alpha_s \cdot L_x}}{\alpha_s \cdot L_x} \right) \cdot \left[e^{-\frac{(1+j)\sqrt{\frac{\omega}{2 \cdot D_s}} \cdot (y - L_y/2)}{\dots}} \right] \cdot \left[e^{\frac{(1+j)\sqrt{\frac{\omega}{2 \cdot D_{eff}}} \cdot x}{\dots}} + e^{j \sqrt{\frac{H}{D_{eff}}} \cdot x} \right] \cdot e^{j(\omega \cdot t - \pi/2)} \quad \text{for } y \geq 0 \quad (3.41a)$$

and

$$T_f^{\text{II}}(x, y, t) = \frac{P_0}{2 \cdot L_y^2 \cdot L_z \cdot C_s \cdot \omega} \cdot \left(\frac{1 - e^{-\alpha_s \cdot L_x}}{\alpha_s \cdot L_x} \right) \cdot \left[e^{(1+j) \sqrt{\frac{\omega}{2 \cdot D_s}} \cdot (y + L_y/2)} \right] \cdot \left[e^{(1+j) \sqrt{\frac{\omega}{2 \cdot D_{\text{eff}}}} \cdot x} + e^{j \sqrt{\frac{H}{D_{\text{eff}}}} \cdot x} \right] \cdot e^{j(\omega \cdot t - \pi/2)} \quad \text{for } y \leq 0 \quad (3.41b)$$

In the presence of convection, the expression for photothermal deflection angle is obtained from eq. (3.31) by substituting into it the expression of T_f obtained from eq. (3.41), as given below:

$$\Phi(t) = \frac{1}{n_f} \left| \frac{dn_f}{dT_f} \right| \cdot \frac{P_0}{C_s \cdot L_y^2 \cdot L_z} \cdot \frac{1}{\omega} \cdot \left(\frac{1 - e^{-\alpha_s \cdot L_x}}{\alpha_s \cdot L_x} \right) \cdot \sqrt{\frac{D_s}{D_{\text{eff}}}} \cdot \exp\left(\sqrt{\frac{\omega}{2 \cdot D_s}} \cdot L_y\right) \cdot \exp\left[j \cdot \left(\omega \cdot t - \frac{\pi}{2} + \sqrt{\frac{\omega}{2 \cdot D_s}} \cdot L_y \right)\right] \cdot (M + j \cdot N) \quad (3.42)$$

where

$$M = 1 + \sqrt{\frac{H}{2\omega}} \quad (3.43)$$

and

$$N = \sqrt{\frac{H}{2\omega}} \quad (3.44)$$

With these substitutions the amplitude of the PDS signal can be written as:

$$A_{\phi}^{(h)} = \frac{1}{n_f} \left| \frac{dn_f}{dT_f} \right| \cdot \frac{P_0}{C_s \cdot L_y^2 \cdot L_z} \cdot \frac{1}{\omega} \cdot \left(\frac{1 - e^{-\alpha_s \cdot L_x}}{\alpha_s \cdot L_x} \right) \cdot \sqrt{\frac{D_s}{D_{\text{eff}}}} \cdot e^{\sqrt{\frac{\omega}{2 \cdot D_s}} \cdot L_y} \cdot \sqrt{M^2 + N^2} \quad (3.45)$$

The phase of the PDS signal

$$\Delta_{\phi}^{(h)} = \sqrt{\frac{\omega}{2 \cdot D_s}} \cdot L_y - \frac{\pi}{2} + \text{atan}\left(\frac{N}{M}\right) \quad (3.46)$$

It is interesting to note that in the case of negligible convection i.e. $h_f = 0$, the expressions for the phase and amplitude of the photothermal deflection signal can be reconciled to eqs. (3.35) and (3.36) that were obtained under the assumptions that heat transfers only by conduction.

Conversely, in the case of very high convection, for which

$$\sqrt{\frac{H}{2\omega}} \gg 1 \quad (3.47)$$

and the convection heat transfer rate is higher than the “pump” pulse frequency, the amount of heat that is transferred to the fluid by convection at any single pulse saturates. Therefore, eq. (3.43) can be approximated for practical circumstances, so that also equations (3.45) and (3.46) simplify into the following expressions:

$$A_{\phi}^{(h)} \approx \frac{1}{n_f} \left| \frac{dn_f}{dT_f} \right| \cdot \frac{P_0}{C_s \cdot L_y^2 \cdot L_z} \cdot \frac{1}{\omega^{3/2}} \cdot \left(\frac{1 - e^{-\alpha_s \cdot L_x}}{\alpha_s \cdot L_x} \right) \cdot \sqrt{\frac{D_s}{D_{\text{eff}}}} \cdot e^{\sqrt{\frac{\omega}{2 \cdot D_s}} \cdot L_y} \cdot H^{1/2} \quad (3.48)$$

and

$$\Delta_{\phi}^{(h)} \approx \sqrt{\frac{\omega}{2 \cdot D_s}} \cdot L_y - \frac{\pi}{2} \quad (3.49)$$

It is worth noting that eq. (3.49) is identical to eq. (3.36). Therefore the phase of the thermal wave is unchanged in the absence and in the presence of convection, which also means that the thermal diffusivity given by eq. (3.49) is the same that is calculated without convection [eq. (3.35)]. This is indeed the expected result, because the phase of the PDS signal is known to only depend on the thermal properties of the sample and is nearly independent of the photothermal fluid in which the sample is immersed [15]. Instead, a relevant difference between conduction-driven and convection-driven PDS is in the dependency of the amplitude on the pulse frequency of the “pump” beam. As can

be observed from eq. (3.48), if convection is dominant and the thermal diffusion length along the sample is small compared to the “pump” beam width, we will have

$$A_{\varphi}^{(h)} \propto \omega^{-3/2}. \quad (3.50)$$

Instead, from eq. (3.35), we obtained that

$$A_{\varphi}^{(K)} \propto \omega^{-1} \quad (3.51)$$

if conduction is dominant.

Such a difference can be used to discriminate the two regimes of dissipation of heat towards the fluid: convection and conduction. We found that in all of the practical cases of interest for our project, which will be discussed in Chapters 4-6, the frequency dependence of the “pump” beam was in good agreement with eq. (3.51) and, consequently, the effects of convection can be neglected. This can be ascribed to the fact that the thermal conductivities of both the sample and the photothermal fluid are relatively high. On the other hand, we also searched for specific samples and systems obeying eq. (3.50), for which convection dominates over conduction, in order to validate the theoretical considerations. One of such systems will be presented in the next section.

3.6 Determination of the heat exchange coefficient of photothermal fluids with nanoparticles in suspension

A system in which a small fraction of highly thermally conducting nanoparticles is suspended at different concentrations in a photothermal fluid represents an ideal playground to test our model of convection-based PDS. It will allow us to tune the thermal conductivity of the liquid system relative to the heat exchange coefficient at the liquid-solid interface. This happens because the ratio between h_f and K_f , related to the Nusselt number (Nu_f) of the system [16,17]

$$\text{Nu}_f = \frac{h_f}{K_f} \cdot L_c, \quad (3.52)$$

may be strongly affected by the presence of the nanoparticles. In eq. (3.52), L_c is the radius of the circular pipe in which the fluid is confined or, for micrometer vessel the area/ perimeter ratio for the section of the vessel can be used. As we will show below, Nu_f will strongly decrease at increasing volume fraction p of nanoparticles that are dispersed in the fluid, provided that such nanoparticles are sufficiently thermally conducting and the laminar regime of fluid motion is maintained.

In our experimental setup, there is no forced convection because the vessel in which the nanofluid is confined is a cuvette of rectangular cross-section, in which there can be only natural convection, or buoyancy, due to the vertical and horizontal gradients in the density of the liquid adjacent to the heated sample surface. Horizontal density gradients are due to the fact that the fluid experiences different temperatures in the bulk, in which $T = T_\infty$ and at the interface with the heated solid thin film, in which $T = T_\infty + T_s$. Vertical density gradients occur due to gravity effects that lead to pressure gradients within a non-compressible fluid. When the two effects are considered, the Nusselt number can be expressed in terms of the Rayleigh number (Ra_f), and the Prandtl number (Pr_f), according to the following empirical relationship proposed by Churchill and Chu [18,19]:

$$\text{Nu}_f^{1/2} = 0.825 \cdot \frac{0.387 \cdot \text{Ra}_f^{1/6}}{\left[1 + \left(\frac{0.492}{\text{Pr}_f} \right)^{9/16} \right]^{8/27}} \quad (3.53)$$

where:

$$\text{Ra}_f = \frac{g \cdot \beta_f \cdot \langle T_s \rangle \cdot L_z^3}{\mu_f \cdot D_f} \quad (3.54)$$

and

$$\text{Pr}_f = \frac{\mu_f}{D_f} \cdot \quad (3.55)$$

In eqs. (3.54)-(3.55), g is the acceleration of gravity, ρ_f is the fluid density, β_f is thermal expansion coefficient of the fluid, $\langle T_s \rangle$ [given by eq.(3.30)] is the temperature difference between the solid surface and the bulk of the fluid, ρ_f is the density of the fluid and μ_f is the kinematic viscosity of the fluid.

The Rayleigh number is a dimensionless quantity representing the ratio between the buoyancy forces, determining natural convection in the liquid, and the resisting effects of thermal diffusion and viscous dissipation opposing natural convection. Consequently, Ra_f is also related to the transition threshold between laminar motion and turbulence in a fluid. Typically, for $\text{Ra}_f > 10^9$, buoyancy is strong enough that the fluid flow is turbulent [16]. We do not expect that our experiments are in this regime, however. Indeed, as we will verify in section 3.6, $\text{Ra}_f < 10^5$ in our case. The Prandtl number, also appearing in eq. (3.53), is used as a measure of the momentum diffusivity (which is proportional to its kinematic viscosity, μ_f/ρ_f) relative to the thermal diffusivity of the fluid. Typical values of Pr_f are $\sim 10^{-3} - 10^5$ [19]. A low Prandtl number means that heat diffuses quickly in the medium, like in liquid metals at high temperatures.

Considering fluid systems comprising small fractions of nanoparticles suspended in a photothermal liquid, we expect that the particles have a very limited effect on the viscosity, while they may have more significant effects on the thermal properties of the

system. Consequently, we also expect that Pr_f may dramatically decrease at increasing fractions of dispersed nanoparticles. If the system is considered as a single phase solution rather than a solid-liquid mixture, the effective thermal conductivity (K_{fp}) of the suspension is often expressed in terms of the thermal conductivity of the pure fluid and the volume fraction (p) of nanoparticles, by relationships of the form:

$$K_{fp} = K_f \cdot [1 + \mathbf{a} \cdot p^\zeta] \quad (3.56)$$

where \mathbf{a} is a factor that depends on the thermophysical properties of the specific type of particles being used and on the characteristics of the interfacial layer between the fluid and the particles. For instance, Corcione [20] proposed a relationship of the type of eq. (3.56) for spherical nanoparticles in which $\zeta = 2/3$ and

$$\mathbf{a} = 4.4 \cdot Re_f^{2/5} \cdot Pr_f^{2/3} \cdot \left(\frac{\langle T_s \rangle}{T_{FR}} \right)^{10} \quad (3.57)$$

where T_{FR} is the freezing temperature of the fluid. Henneke and coworkers [21] proposed a similar relationship that is specific for carbon nanotubes in which $\zeta = 3/4$ and

$$\mathbf{a} = \eta \cdot \left(\frac{1}{d} \right)^\delta \cdot a_R^\varepsilon \quad (3.58)$$

In eq. (3.58), η is a factor that depends on type of CNTs and fluid being used, d is diameter of the CNTs, a_R is their aspect ratio, and δ and ε are exponents determined from the experiments [20]. Values of η , δ and ε taken from Ref. [21] are reported in Table 3.1. Other relationships of the type of eq. (3.56) are available in the literature [21].

Table 3.1 Optical and thermal properties of fluids used in this study

δ	ε	η ($W \cdot m^{-1} \cdot K^{-1}$)
0.441	0.14	51.84

In the presence of small fractions of CNTs dispersed in a fluid, not only the thermal conductivity, but a number of other physical properties of the nanofluid may be affected, at least in principle. Such properties include: dynamic viscosity, specific heat, mass density and coefficient of thermal expansion. All of these property variations may lead to strong changes in the Nusselt number and the heat transfer coefficient. In the case of a nanofluid, the effective mass density (ρ_{fp}), the effective coefficient of thermal expansion (β_{fp}), the effective specific heat capacity (c_{fp}) and the effective viscosity (μ_{fp}) can be defined as the weighted average of the corresponding physical properties of the pure fluid and those of the solid nanoparticles. Specifically, the effective medium theory indicates that [16,17]

$$\rho_{fp} = (1-p) \cdot \rho_f + p \cdot \rho_p \approx \rho_f , \quad (3.59)$$

$$\mu_{fp} = \frac{\mu_f}{1 - 34.87(d_p/d_f)^{-0.3} \cdot p^{1.03}} \approx \mu_f , \quad (3.60)$$

$$\beta_{fp} = \frac{(1-p) \cdot \rho_f \cdot \beta_f + p \cdot \rho_p \cdot \beta_p}{(1-p) \cdot \rho_f + p \cdot \rho_p} \approx \beta_f \quad (3.61)$$

and

$$c_{fp} = \frac{(1-p) \cdot \rho_f \cdot c_f + p \cdot \rho_p \cdot c_p}{(1-p) \cdot \rho_f + p \cdot \rho_p} \approx c_f , \quad (3.62)$$

where ρ_p , β_p and c_p are the density, thermal expansion coefficient and specific heat of the nanoparticles respectively, and d_p is the nanoparticle diameter. d_f , the hydrodynamic diameter of a molecule in the fluid, is given by [16]:

$$d_f = 0.1 \cdot \left(\frac{6M}{N_A \cdot \pi \cdot \rho_f} \right), \quad (3.63)$$

in which M is the molecular mass, N_A is the Avogadro's number and ρ_f is the density of the pure fluid at the relevant temperature. We do not expect that eqs. (3.59) to (3.62) lead to significant changes of these properties for small volume fraction of p .

Using equation (3.56), the effective thermal conductivity of the nanofluid can be determined from the physical properties of the pure photothermal fluid as a function of the nanoparticle concentration. K_{fp} calculated in this way can be combined it with all of the effects presented in eqs. (3.59) to (3.63) to determine the dimensionless parameters Pr_{fp} [eq. (3.55)] and Ra_{fp} [eq. (3.54)]. From these parameters Nu_{fp} can be estimated via the empirical Churchill-Chu relationship (3.53). Also the thickness of the thermal boundary layer (L_{fp}) will be affected by the introduction of nanoparticles. In the laminar flow regime, for which buoyancy is equilibrated by friction, L_{fp} can be estimated to be inversely proportional to the Rayleigh number that expresses the balance between such two phenomena:

$$L_{fp} \sim Ra_{fp}^{-1/4}, \quad (3.64)$$

where the index “fp” indicates that these quantities refer to the fluid containing a volume fraction p of nanoparticles. Therefore, L_{fp} can be written as a function of the corresponding quantity in the pure photothermal fluid as:

$$L_{fp} = L_f \cdot \left(\frac{Ra_f}{Ra_{fp}} \right)^{1/4} \quad (3.65)$$

By combining the above mentioned effects, we can determine the effective heat transfer coefficient from eqs. (3.53) and (3.56) as

$$h_{fp} = \frac{Nu_{fp} \cdot K_{fp}}{L_c} \quad (3.66)$$

and the heat exchange rate controlling the amplitude of the PDS signal in eq. (3.48) can be determined via eqs. (3.39), (3.65) and (3.66) as

$$H = \frac{h_{fp}}{C_f \cdot L_{fp}} \approx \frac{Nu_{fp} \cdot Ra_{fp}^{1/4} \cdot K_{fp}}{C_f \cdot L_c \cdot L_c \cdot Ra_f^{1/4}} \quad (3.67)$$

The approximations leading to the second equality in eq. (3.67) where we have assumed that the density and specific heat of the nanofluid do not significantly change with the introduction of small fraction of CNTs, as will be demonstrated later on, and the same approximation can be used to calculate the Pr_{fp} and Ra_{fp} . By considering a dependence $K_{fp} \sim p^\zeta$ of the thermal conductivity of the nanofluid as in eq. (3.56), and, subsequently, a similar dependence for the $D_{fp} \sim p^\zeta$, the dependencies on p of the dimensionless parameters determining the heat exchange processes between our photothermal nanofluid and a thin solid film in the presence of convection can be summarized as in Table 3.2. Since, both h_{fp} and H can be tuned by changing the concentration of the nanoparticles, we

Table 3.2 Dependency of dimensionless parameters, thickness of thermal boundary layer and heat exchange coefficient and heat exchange rate on fraction of nanoparticles.

Parameter	eq.	Trend
K_{fp}, D_{fp}	(3.56)	p^ζ
Ra_{fp}	(3.54)	$p^{-\zeta}$
Pr_{fp}	(3.55)	$p^{-\zeta}$
L_{fp}	(3.65)	$p^{\zeta/4}$
Nu_{fp}	(3.53)	$p^{-\zeta/3}$
h_{fp}	(3.66)	$P^{5\zeta/12}$
H_{fp}	(3.67)	$P^{\zeta/6}$

can confirm that a photothermal nanofluid offers an ideal system for PDS experiments aimed at quantifying heat exchange by convection, which will be discussed in the next section. Specifically by changing p in our nanofluid we will be able to quantify for the first time h_{fp} and, subsequently, H and, therefore, the parameters controlling the thermal exchange between a fluid and a solid sample using PDS.

3.7 Materials used for experimental validation

3.7.1 Photothermal nano-fluid used for experimental validation

For the validation of our convection-based PDS model, we used carbon tetrachloride (CCl_4) as a photothermal fluid, because of its high value of temperature coefficient of the refractive index, and single wall carbon nanotubes as thermally conducting nanoparticles to be dissolved in such fluid, because they are widely available and can be easily dispersed in a number of organic solvents. Thermophysical properties of CCl_4 (Aldrich Cat. No. 289116) and CNTs (From Carbolex Inc., Aldrich CAS 308068-56-6) that were used in this study are given in table 3.3 and 3.4 respectively.

A suspension of CNTs was prepared by adding them at 0.1 mg/mL to CCl_4 and by sonicating the system for two hours in a beaker using a bath sonicator (Branson DHA 1000). For a number of PDS measurements with different nanofluids, the concentration of CNTs was varied by adding 0.1 mL of 0.1 mg/mL suspension, after removing from the cuvette a corresponding amount of nanofluid used in the previous measurement, without moving the sample, in a way that the alignment of the sample in the PDS apparatus also remained unchanged. A syringe with its needle passing through the Teflon lid of the cuvette was used for this operation.

Table 3.3 Physical and fluid dynamic properties of CCl₄ at room temperature [22,23].

Refractive index n	Temperature coefficient of refractive index dn/dT (K ⁻¹)	Density ρ_f (kg.m ⁻³)	Thermal expansion coefficient β (K ⁻¹)	Specific heat c_f (J.kg ⁻¹ .K ⁻¹)
1.5	6.1 X10 ⁻⁴	1.6 X10 ³	1.2 X10 ⁻⁴	850
Thermal diffusivity D_f (m ² .s ⁻¹)	Thermal conductivity K_f (W.m ⁻¹ .K ⁻¹)	Kinematic Viscosity μ_f (m ² .s ⁻¹)	Molecular mass M	Hydro-dynamic diameter d_f (nm)
7.31X10 ⁻⁸	0.106	5.63 X10 ⁻⁷	154	0.686
Rayleigh number Ra_f	L_f (μ m)	Prandtl Number Pr_f	Nusselt number Nu_f	Freezing Temperature T_{FR} (K)
4.14X10 ⁵	300	7.7	15.8	250

Table 3.4 Room temperature physical properties of carbon nanotubes used in this study [24,25].

Physical Property	Value
Type	Single wall
Diameter (nm)*	0.7 – 1.3
Aspect ratio	200
Density (kg.m ⁻³)	1.34X10 ³
Purity**	> 75 %
Thermal conductivity (W.m ⁻¹ .K ⁻¹)	2000
Specific heat (J.kg ⁻¹ .K ⁻¹)	600
Thermal expansion coefficient (K ⁻¹)	<<10 ⁻⁴ (assumed)

* These nanotubes are known to form bundles ~ 20nm in size in organic fluid.

** Most impurities are known to be amorphous carbons that are insoluble in CCl₄ and have been removed by sedimentation prior to PDS measurements

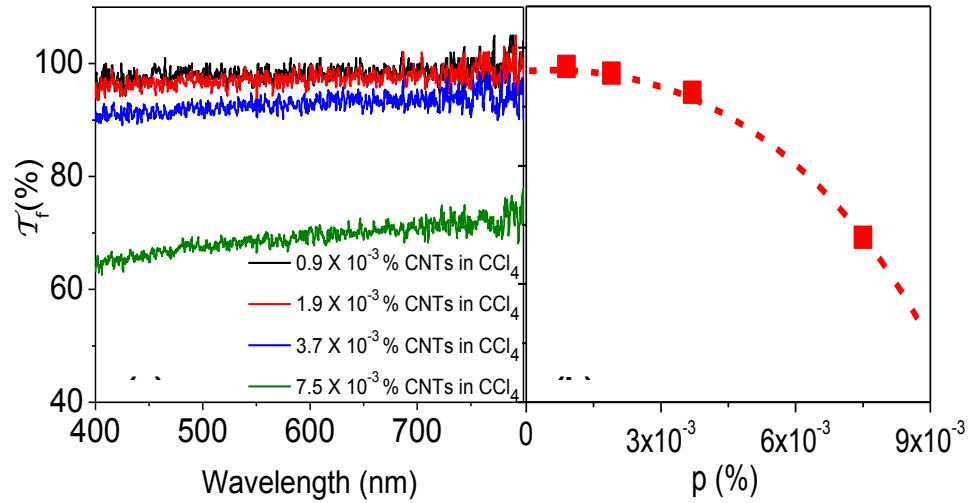


Figure 3.6 (a) UV-visible spectra of CCl₄ with different concentrations of CNTs and (b) transmittance of CNTs suspension versus CNTs concentration at 550 nm incident wavelength. It can be observed that the transmittance decreases with increasing CNTs concentration and drops to 65% for the undiluted CNTs suspension.

UV-visible transmission spectra of suspensions with varying concentrations of CNTs were recorded by us and are shown in Figure 3.6. It can be observed that the transmission coefficient decreases with increasing CNT fraction. For $p \leq 3 \times 10^{-3}$ % in volume, suspensions have transmittances > 90 % in the entire visible photon energy range and, therefore, can be considered to be reasonably non-absorbing, with a negligible amount of heat generated directly inside the fluid. In any case, the actual amount of radiation power reaching the sample has been normalized with the transmittance \mathcal{T}_{fp} of the nanofluid by UV-visible spectrophotometry in order to take into account the decreasing transparency.

3.7.2 Sample used for experimental validation

To validate our convection-based PDS model, we measured a Poly(3,4-ethylenedioxythiophene)-poly-(styrene-sulfonate) (PEDOT:PSS) thin film with the above mentioned set of nanofluids. The chemical structure of PEDOT:PSS is presented in Figure 3.7(a). We have chosen PEDOT:PSS because it is well known for its relatively low thermal conductivity. The substrate was a plastic sheet from cross-linked polyurethane resin ($K < 0.01$ W/m/K). We expect the fact that the thermal conductivity of the film-substrate system on the whole is so low, may promote convective heat transfer to the fluid, because eq. (3.50) could be observed when varying the measurement frequency. The data more specifically discussed below were measured at $\omega = 20$ Hz.

The PEDOT:PSS thin film was prepared by spin coating an aqueous commercial suspension (Sigma Aldrich, batch # 483095) of a blend of these two polymers. The role of transparent and insulating PSS in such blend is to act as a surfactant to suspend transparent and conducting PEDOT in water [24]. A WS-400 spin coater (Laurell Technologies Co.) operating at 100 rpm has been used to deposit the film. We have chosen a very low spin speed because PEDOT:PSS remains optically thin also at relatively large thicknesses. Furthermore, although the thermal conductivity of this polymer blend is poor, its thermal diffusivity is relatively large, which ensures that even a micrometric film is still thermally thin. The physical properties of PEDOT are given in Table 3.4. A picture of our sample is shown in Figure 3.7(b). A optical absorption coefficient of PEDOT:PSS in the entire visible photon energy range is well known from the literature [25-27], and is reported in Figure 3.8. The thickness of our film has been measured using a Dektak³ Profilometer at the Western Nanofabrication Facility and is also reported in Table 3.5.

Table 3.5 Physical properties of PEDOT:PSS sample used in this study[25-27].

Physical Property	Value
Thermal conductivity ($\text{W.m}^{-1}.\text{K}^{-1}$)	0.17
Density (kg.m^{-3})	1.5×10^3
Specific heat ($\text{J.kg}^{-1}.\text{K}^{-1}$)	17.87
Film thickness (m)	1.94×10^{-6}
pH	Acidic

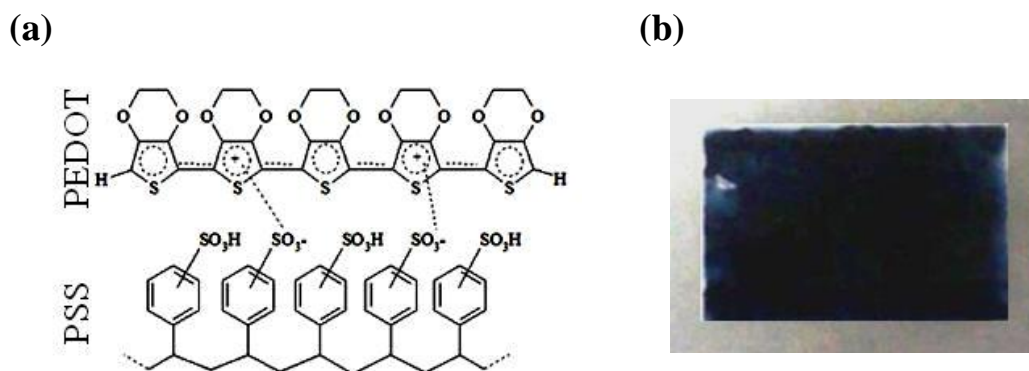


Figure 3.7 (a) Molecular structure of PEDOT:PSS [25] and (b) Image of typical PEDOT:PSS thin film.

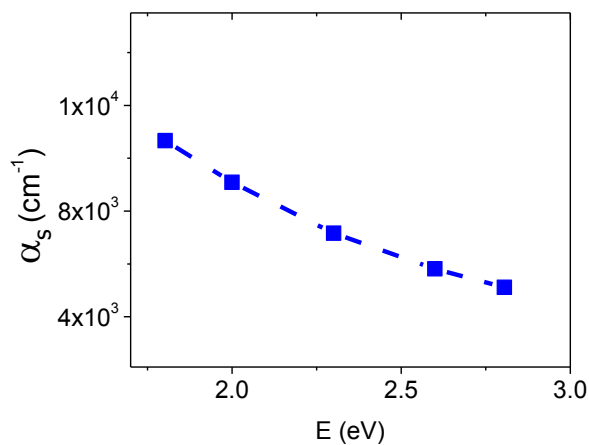


Figure 3.8 Optical absorption coefficient of PEDOT:PSS thin film, dotted line is eye guide.

3.8 Results and Discussion

A set of PDS data were recorded, with pristine CCl_4 and with increasing concentrations of CNTs in CCl_4 as the photothermal fluid, using the PDS setup shown in Figure 2.2 and the materials described in section 3.7. The measured amplitude and phase of the PDS signal measured as a function of photon energy of the “pump” beam are shown in Figure 3.9 for a set of measurements recorded with nanofluids at different concentrations of CNTs. A convenient way to present the measured amplitude is to

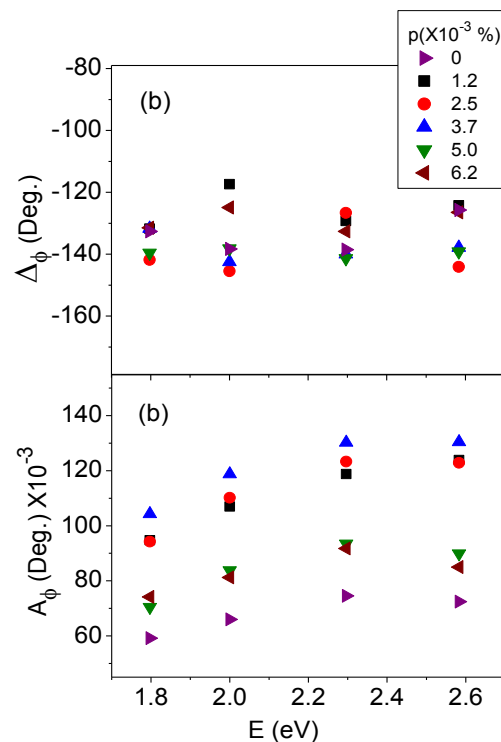


Figure 1.6 Figure 3.9 Measured (a) phase and (b) amplitudes of the PDS signal of our PEDOT:PSS thin film sample versus incident photon energy at different volume fractions of CNTs in carbon tetrachloride (CCl_4).

normalize it with the “pump” beam power P_0 , the optical absorption coefficient of the thin film and the transmittance \mathcal{T}_{fp} of the fluid at the specific photon energies used for the

measurement. In this way, the normalized amplitude (B_ϕ) should be independent of the intensity and wavelength of the “pump” beam:

$$B_\phi = A_\phi \cdot \frac{\alpha_s \cdot L_x}{1 - \exp(\alpha_s \cdot L_x)} \cdot \frac{1}{P_0 \cdot \mathcal{T}_{fp}}. \quad (3.68)$$

B_ϕ , averaged over the various photon energies that have been used for the measurements, is plotted in Figure 3.10(a) as function of p and will be used to experimentally determine the thermal exchange rate from the amplitude of the photothermal deflection angle by inverting eq. (3.48) under the assumption $D_{\text{eff}} \approx D_s$:

$$H = \frac{n_f^2 \cdot C_s^2 \cdot L_y^4 \cdot L_z^2 \cdot \omega^3}{|dn_f / dT_f|^2} \cdot e^{-2 \left(\sqrt{\frac{\omega}{2 \cdot D_s}} \right) \cdot L_y} \cdot B_\phi^2 \quad (3.69)$$

Figure 10(a) reports the mean values and standard deviation for the phase Δ_ϕ of the PDS measurements, which is independent of p as can be expected from the fact that no parameter involved in eq. (3.49) depends upon the properties of the nanofluid. The values of H resulting from the values of B_ϕ displayed in Figure 3.10(b) are plotted in Figure 10(c). The error bars have been obtained [like the corresponding error bars in Figure 10(b)] by averaging the PDS measurements obtained at different wavelengths and by calculating the standard deviation between such measurements. Figure (3.13c) demonstrates that the increase of the amplitude of the PDS signal is due to the increased heat transfer rate from the sample to the liquid in the presence of increasing amounts of CNTs in the photothermal fluid, which strongly changes the thermophysical properties of the fluid while negligibly affecting its kinematic viscosity, and other physical properties, as predicted in sec. 3.6.

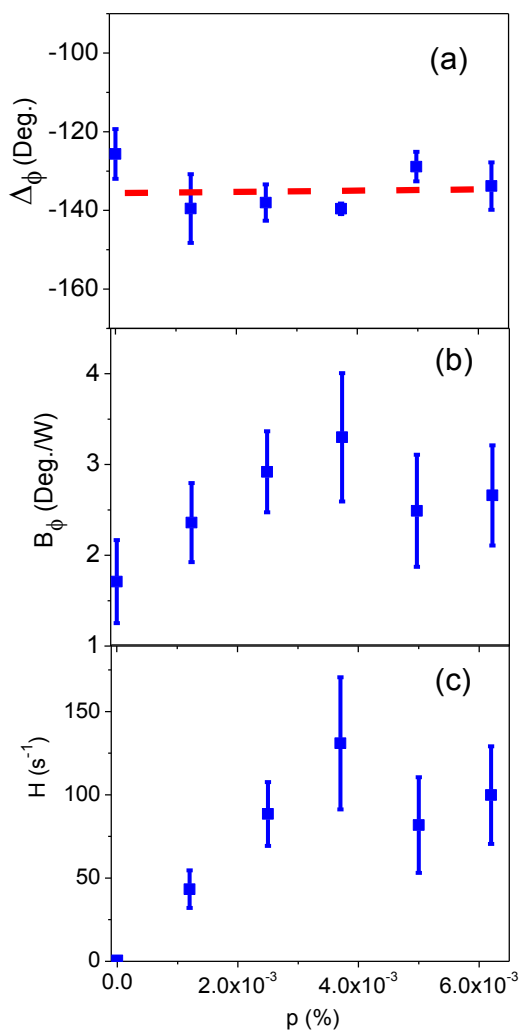


Figure 3.10 (a) Phases, (b) normalized amplitudes and (c) heat exchange rates obtained using eq. (3.69) from the values of B_ϕ displayed in panel b. Data were recorded on the PEDOT:PSS film described in sec. 3.7.2 at different the volume fractions of CNTs dispersed in carbon tetrachloride (CCl_4). Data was measured at five different wavelengths of “pump beam” and used to get with error bars. It can be seen that the increase of H at increasing p is very slow with the exception of very low p . This was to be expected because the qualitative estimations that were summarized in Table 3.2 suggest that H increases a $p^{\zeta/6}$, in which $\zeta < 1$, according to relationship (3.57) or (3.58).

In order to gain deeper insight on the factors controlling H in our system and use them to determine the heat transfer coefficient, we performed a numerical simulation of the various parameters that are involved in the process. First of all, the quantities determining the thermal diffusivity of the nanofluid have been determined as a function of the concentration of CNTs, as shown in Figure 3.11. Specifically, since Henneke's relationship (3.56) - (3.58) was particularly designed for CNTs, we used it to determine K_{fp} without any adjustment parameters, by utilizing the values of δ , ε and η reported in Table 3.1 by this author. The experimental parameters for our CNTs are those reported by us in Table 3.4. The thermal conductivity of the CNT- CCl_4 effective medium increases significantly with p as shown in Figure 3.11(a) because CNTs have very high thermal conductivity and relatively high aspect ratio, which helps them in efficiently spreading the heat to the fluid. Conversely, the density and specific heat of the CNT- CCl_4 effective medium remain almost unchanged as shown in Figures 3.11(b) and 3.11(c) because the quantity of CNTs that were dispersed was extremely small and their density is comparable to CCl_4 . Therefore, the approximation $\rho_{fp} \approx \rho_f$ and $c_{fp} \approx c_f$ used in eq. ((3.59), (3.62), (3.66) and for calculating Pr_{fp} , Re_{fp} and L_{fp} in Table 3.2 is reliable. The effect of these factors in the variations of the effective thermal diffusivity of the nanofluid with increasing p is shown Figure 3.12(a). As expected, thermal diffusivity and thermal conductivity exhibit the very same trend, as can be seen by comparing Figure 3.12(a) with Figure 3.11(a).

While the effective kinematic viscosity of the nanofluid also increases with increasing p as predicted by eq. (3.60) and shown in Figure 3.12(b). CNTs may agglomerate and turn into aggregates that increase friction within the fluid. However, the

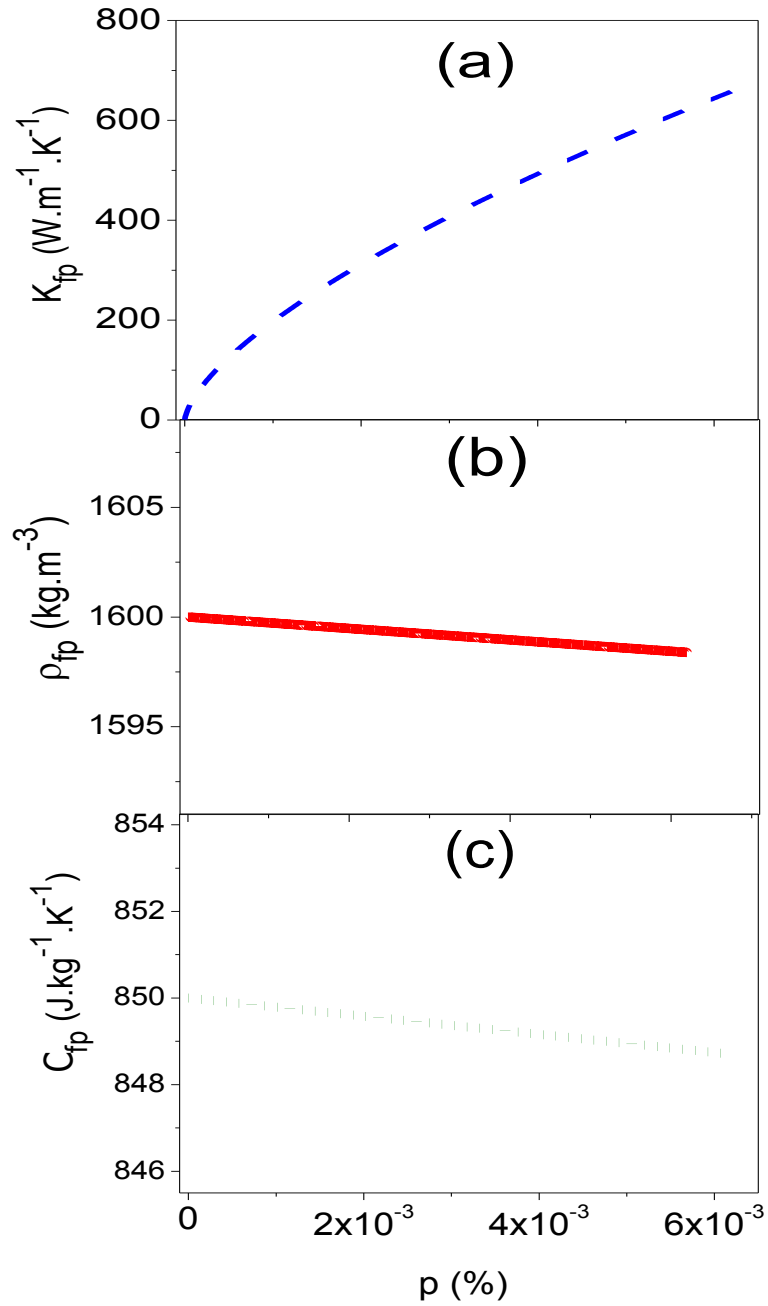


Figure 3.11 (a) Thermal conductivity, (b) density and (c) specific heat of CCl_4 :CNTs nanofluid with increasing volume fraction of CNTs. It can be seen that thermal conductivity increases significantly while density and specific heat remain almost unchanged at any fraction of CNTs.

effects of CNTs on viscosity are not as significant as the variations of the thermophysical properties. In the range of p considered in our system, the kinematic viscosity increases less than 10 % while K_{fp} and D_{fp} increase by a factor $\sim 10^3$. Subsequently, the variations in thermal diffusivity dominate over the corresponding changes in viscosity in determining the consequent changes in the values of the dimensionless numbers Ra_{fp} , and Pr_{fp} that are shown in Figures 3.13(a), and 3.13(b), respectively. Both parameters, calculated exactly from eqs. (3.54) and (3.55), drop quickly with increasing p and the log-log plots shown in Figure 3.13 demonstrate that their decrease closely follow a $p^{-\zeta}$ law, as

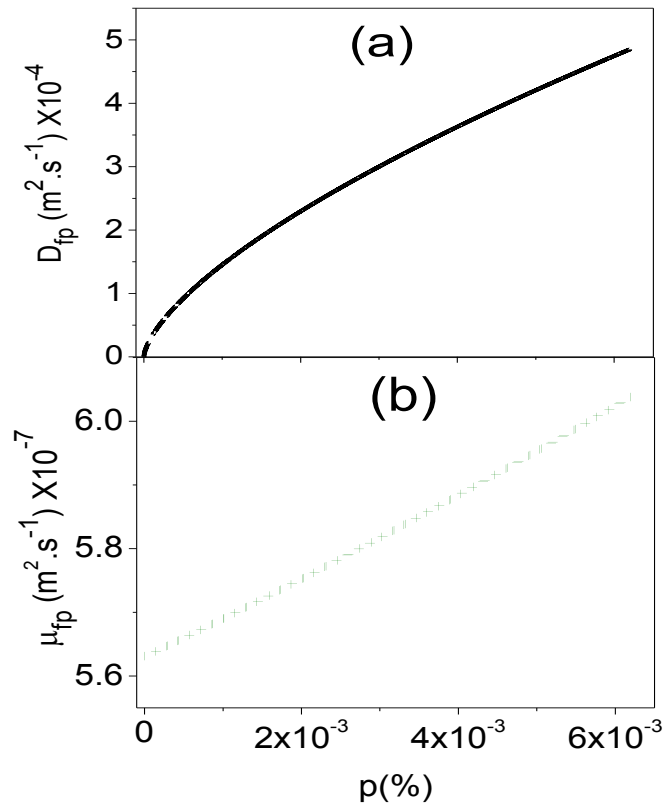


Figure 3.12 (a) Effective thermal diffusivity and (b) effective kinematic viscosity of CCl_4 :CNTs suspension. It can be observed that at any fraction of CNTs increase in dynamic viscosity is relatively less significant but thermal diffusivity increases significantly with increasing fraction of CNTs.

predicted in Section 3.6. Consequently, the Nusselt number also decreases with increasing p . However, its dependency on p is more complicated than Ra_{fp} and Pr_{fp} because of the more complicated structure of the Churchill-Chu relationship (3.53). For

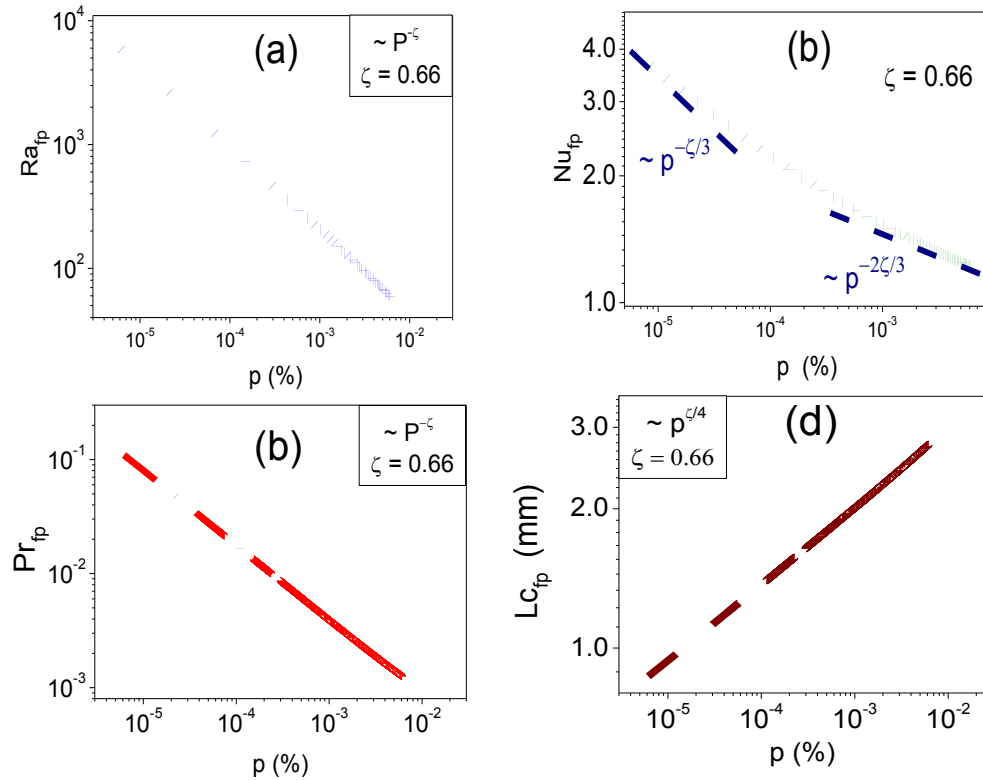


Figure 3.13 Effect of increasing fraction of SWCNTs in the photothermal fluid on the dimensionless numbers used to characterize the fluid behaviour (a) Effective Rayleigh number, (b) Effective Prandtl number and (c) Effective Nusselt number, and (d) Effective thermal diffusion length.

high enough Pr_{fp} the denominator of eq. (3.53) tends to one, so a $Nu_{fp} \sim Ra_{fp}^{1/3} \sim p^{-\zeta/3}$ can be expected as predicted in Table 3.2. $Pr_f \sim 7$ in pure CCl_4 is high enough to ensure such a trend. On the other hand, Pr_{fp} significantly decreases with p and, for low enough values of Pr_{fp} , buoyancy in the nanofluid is balanced by inertia, and not by viscosity [15]. Therefore, a significant vertical gradient in density in the nanofluid can be expected and Churchill-Chu relationship (3.53) predicts that $Nu_{fp} \sim (Ra_{fp} \cdot Pr_{fp})^{1/3} \sim p^{-2\zeta/3}$. This twofold

dependency of Nu_{fp} on p (as $p^{-\zeta/3}$ at low p and as $p^{-2\zeta/3}$ at high p) is shown in Figure 3.13(c). We can expect that, according to eqs. (3.68) and (6.69), a similar dependency also reflects on the thermal exchange rate, H , and on the thermal exchange coefficient h_{fp} . Specifically, the values of the thermal boundary layer predicted from eq. (3.65) by assuming $\zeta = 0.66$ and an initial boundary layer $L_f = 300 \mu\text{m}$ for the pure fluid have been calculated by us and are plotted in Figure 3.13(d). When these values are replaced in eq. (3.67), they are found to perfectly fit the measured values of H as shown in Figure 3.14(a) and, consequently, they can also be used to calculate the amplitude of the angle of photothermal deflection during PDS measurements, as shown in Figure 3.14(b). Therefore, we can conclude that, when PDS experiments are dominated by convective heat transfer, they are in good agreement with the most conventional models for heat convection at a fluid-solid interface.

Specifically, convection-driven PDS can be used to simultaneously measure H (directly) and the heat exchange coefficient h_{fp} can be measured as shown in Figure 3.14(c), it can be observed that it increases with increasing fraction of CNTs. The increase is stronger at lower values of p , for which, indeed, our qualitative model developed in Section 3.6 predicts that $h_{fp} \sim p^{-5\zeta/12}$. However, at higher concentrations of CNTs, the effect is not as strong as at low concentrations because Pr_{fp} is significantly lower than one, so it also significantly affects both the Nusselt number [via eq. (3.53)] and the thickness of the thermal boundary layer [15]. This explains the plateau in the values of h_{fp} that can be noticed in Figure 3.14(c).

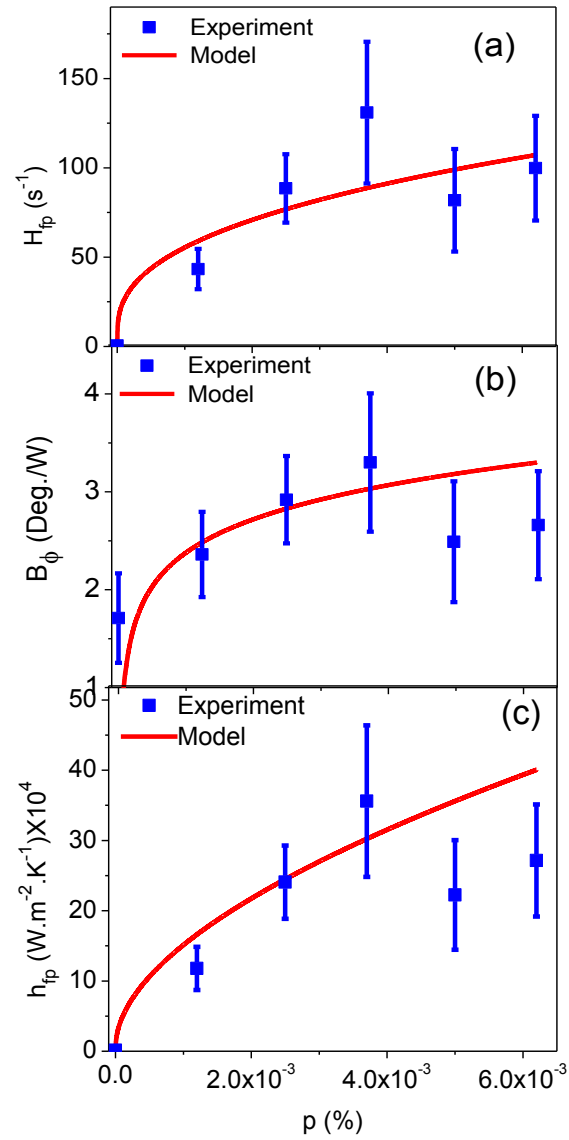


Figure 3.14 (a) Convection heat exchange rate. (b) normalized amplitude of PDS signal in the presence of convection and (c) convection heat transfer coefficient as a function of CNTs fraction in the photothermal fluid.

3.9 Conclusion

We identified for the first time a specific case in which convection of heat is critical in the accurate modeling of PDS experiments. Specifically, when a sample-substrate system has very low thermal conductivity and a photothermal fluid contains a small fraction of highly thermally conducting nanoparticles, convection becomes important to analyze PDS data. We developed two different models for conduction-driven and convection-driven PDS experiments and we experimentally quantified the contribution of convective heat transfer in the case of a photothermal fluid in which highly thermally conducting nanoparticles are dispersed. For our quantitative measurements, we used carbon tetrachloride (CCl_4) with varying fractions of CNTs dispersed in it as the photothermal fluid and the effect of such dispersion on the amplitude and phase of PDS signal during the spectroscopic PDS measurements of a PEDOT:PSS thin film on a thermally insulating substrate. We find that the amplitude of angle of deflection increases with increasing concentrations of CNTs in CCl_4 provided that the suspension retains a sufficiently high transparency and the change in the fluid viscosity is minimal. Our results support the experimental evidence reported in the literature [28] about the heat transfer processes between a nanofluid and a solid surface in the case of natural convection. When nanoparticles concentration is above a certain value, the Prandtl number of nanofluid becomes significantly low ($\sim 10^{-3}$) and buoyancy equilibration by inertia determines the heat transfer coefficient that only increases very slowly with the CNTs concentration. When heat transfer in PDS is driven by convection, the amplitude of the PDS signal decreases as $\omega^{-3/2}$ (where ω is the pulse frequency of “pump” beam) while the amplitude decreases as ω^{-1} when heat transfer to the fluid mainly occurs by

conduction. In this second case, the amplitude of the PDS signal immediately provides the thermal capacity of the sample while, in both conduction-driven and convection-driven PDS the phase of the PDS signal provides the thermal diffusivity. We can therefore conclude that, where as PDS is not convection-driven, it is a very useful technique for simultaneously measuring the thermal capacity and thermal diffusivity and, subsequently, the thermal conductivity of ultr-thin films, as will be widely explored in the next chapters of our work.

References

- [1] T. E. Faber, *Introduction to the Theory of Liquid Metals*, Cambridge University Press, 1972.
- [2] C. Kittel, *Introduction to Solid State Physics*, 7th Ed. John Wiley and Sons, Inc., 1996.
- [3] M. N. Ozisik, *Heat Conduction*, John Wiley and Sons, Inc., 1980.
- [4] H. S. Carslaw and J. C. Jaeger *Conduction of Heat in Solids* 2nd Ed. Oxford University Press, 1959.
- [5] M. Kaviany, *Heat Transfer Physics*, Cambridge University Press, 2008.
- [6] N. W. Ashcroft and N. D. Mermin, *Solid State Physics*, Holt, Rinehart and Winston, 1976
- [7] D. P. Almond and P. M. Patel, *Photothermal Science and Techniques*, Chapman & Hall, 1996.
- [8] A. Rosencwaig and A. Gersho, *J. Appl. Phys.*, **47** (1976) 64.
- [9] A. C. Boccara, D. Fournier, W. B. Jackson and N. M. Amer, *Optics Lett.*, **5** (1980) 377.
- [10] K. D. Cole, A. H. Sheikh, J. V. Beck and B. Litkouhi, *Heat Conduction Using Greens's Function*, Taylor and Francis, CRC press, 2011.
- [11] A. Salazar, A. Sanchez-Lavega and J. Fernandez, *J. Appl. Phys.*, **65** (1989) 4150.
- [12] J. C. Murphy and L. C. Aamodt, *J. Appl. Phys.*, **51** (9) (1980) 4580.
- [13] W. B. Jackson, N. M. Amer, A. C. Boccara and D. Fournier, *Appl. Opt.*, **20** (1981) 1333.
- [14] A. Mandelis, *J. Appl. Phys.*, **54** (6) (1983) 3404

- [15] A. Mandelis, *Photoacoustic and Thermal Wave Phenomena in Semiconductors*, Elsevier Science Publishing Co., New York, 1987.
- [16] S. M. Ghiaasiaan, *Convective Heat and Mass Transfer*, Cambridge University Press, New York, 10013-2473, USA, 2011.
- [17] M. Corcione, *J. Heat Trans.*, **134** (2012) 042501.
- [18] M. Corcione, *Energy Conversion and Management*, **52** (2011) 789.
- [19] L. M. Jiji, *Heat Convection*, 2006, Springer-Verlag Berlin Heidelberg, 2006.
- [20] M. Corcione, *Energy Conversion and Management*, **52** (2011) 789.
- [21] S. M. Hosseini, A. Moghadassi and D. Henneke, *Canadian J. of Chem. Engn.*, **89** (2011) 183.
- [22] S. Bialkowski, *Photothermal Spectroscopy Methods for Chemical Analysis* John Wiley & Sons, New York, 1996.
- [23] A. Salloum and Y. Atassi, *Thermochimica Acta*, **409** (2004) 87.
- [24] H. E. Patel, K. B. Anoop, T. Sundararajan and S. Das, *Bull. Mat. Sci.*, **31** (2008) 387.
- [25] Product information from Sigma Aldrich.
- [26] F. X. Jiang, J. K. Xu, B. Y. Lu, Y. Xie, R. J. Huang, and L. F. Li, *Chin. Phys. Lett.*, **25** (2008) 2002.
- [27] S. Ezugwu, M. S. Ahmed, R. Bauld, R. Divigalpitiya, G. Fanchini, *Thin Solid Films*, **534** (2013) 520.
- [28] S. U. S. Choi, Z. G. Zhang, W. Yu, F. E. Lockwood, and E. A. Grulke, *Appl. Phys. Lett.*, **79** (2001) 2252.

Chapter 4

4 Staebler-Wronski effect, thermal conductivity, and self-repair of hydrogenated amorphous silicon during light-induced degradation

An introduction to amorphous silicon (a-Si), hydrogenated amorphous silicon (a-Si:H) and experimental methods to grow a-Si:H thin films are presented. The main focus is on the investigation of the effect of light soaking on the optical and thermal properties of a set of a-Si:H thin films. Experimental results reveal that defects that are formed under illumination deteriorate the thermal conductivity of the thin films samples, which in turn leads to a rise in temperature of the samples resulting in self-repair of the defects. A model is proposed to explain the self repair of the defects created in a-Si:H thin films under illumination.

4.1 Introduction

Silicon is the element of choice in electronic and optoelectronics, and more than 90 % of solar cells on the market are based on this element [1]. Therefore, a good test for our photothermal deflection spectroscopy (PDS) apparatus consists in demonstrating its ability to understand the interplay between the optical and thermal properties in solar-grade, silicon-based, thin films. While crystalline silicon is extremely popular as photovoltaic material, amorphous silicon solar cells also have excellent market share due to their cost efficiencies [1,2]. PDS has been extensively utilized to study small optical absorptions in hydrogenated amorphous silicon (a-Si:H) and, historically important processes in understanding the relationship between topological disorder and optical

properties in this material have been achieved by PDS [3,4]. Conversely, investigations of thermal properties of a-Si:H by PDS have been very limited, so far, due to the fact that most PDS apparatuses are designed for and dedicated to studying the optical properties.

In the case of crystalline silicon (c-Si), atoms are arranged in long-range ordered tetrahedral lattice, with four nearest neighbours each. Conversely, in amorphous silicon (a-Si), there is structural disorder due to fluctuations in bond lengths and bond angles. Since deviations of Si-Si bond lengths and bond angles from their values in a perfect tetrahedron are very small, short-range order still exist in a-Si. The covalent bonds between the silicon atoms in a-Si are same as in c-Si. The disorder is represented by the radial distribution function (RDF) which is the probability of finding an atom at a distance r from another atom. Schematic RDF for c-Si and a-Si are shown in Figure 4.1. [5,6]. D. E. Polk [7] showed that the radial distribution function (RDF) in a-Si obtained from electron

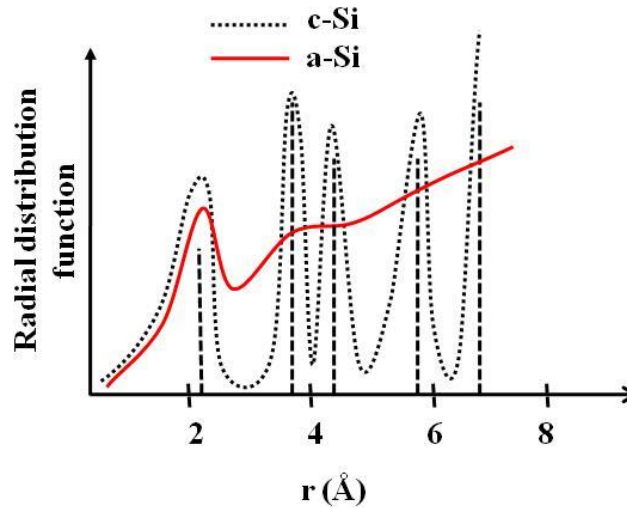


Figure 4. 1 Schematic of RDF for c-Si and a-Si adopted from [5,6]. There are well defined peaks for c-Si but for a-Si first peak is clear , second is broadened and there is no peak after that showing that a-Si lacks long range order.

diffraction experiments show that the first peak matches with that of c-Si but second peak is broadened as compared to c-Si and third peak disappears. Typically, deviations in bond angle and bond length in amorphous silicon are $\sim 5\%$ and $\sim 1\%$ respectively [2,6].

This fact implies that chemical bonding and coordination number are the same in crystalline Si and in the corresponding amorphous materials. On the other hand, the lack of long-range order has strong implications on the optical and thermal properties of amorphous silicon, which are profoundly different from those of its crystalline counterpart.

4.2 Electronic structure

In an amorphous semiconductor, the effects of structural disorder on their electronic properties have been studied by Mott and Davis [8,9]. They concluded that the electronic properties of materials are not only determined by the long range order, but are also determined by atomic and short range properties in which the average mean free path of an electron is of the order of inter-atomic spacing. When the interaction between an electron and the ions core becomes so strong that electron cannot go any further than the atom to which it is tied, the wavefunction decays exponentially with respect to distance 'r' i.e. $\exp(-\alpha \cdot r)$ where α is decay constant on which the wavefunction of single potential well falls off with distance. The electronic wave function in such case becomes localized in small region in space resulting in very low electron mobility, and limited transport properties.

Presence of short range order gives rise to similar overall band structure for amorphous materials as compared to its crystalline counterpart but with extended tails into the gap which arise from the variations in the bond length and bond angle due to

long range disorder, and electronic states deep within the band gap which arise from the coordination defects [5]. The electronic density of states (DOS) of a-Si:H is illustrated in Figure 4.2.

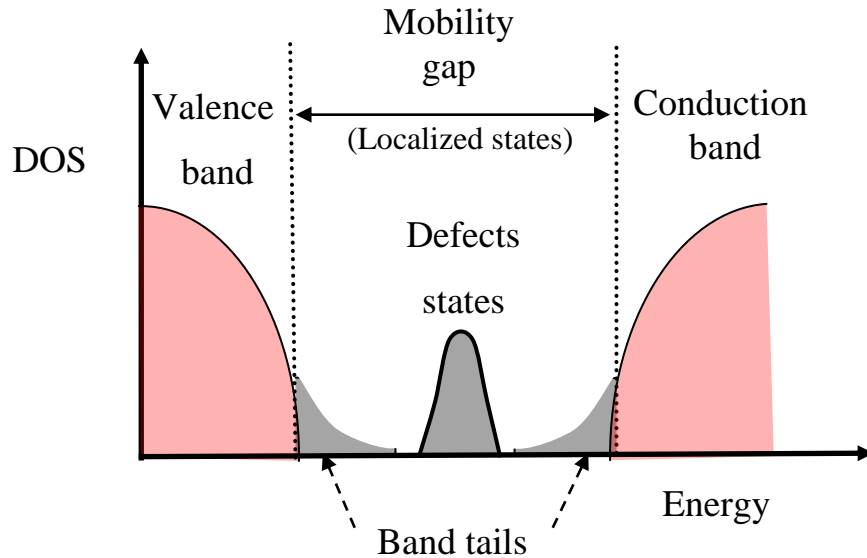


Figure 4. 2 A schematic representation of the electronic density of states (DOS) of a-Si:H. The dashed vertical lines show the mobility edges, which are defined as the energy level separating extended states from localized states.

The main implications of the lack of long-range order are:

- i. No reciprocal lattice can be defined in amorphous materials, because in a significant portion of the Brillouin zone, it would be that $\Delta\mathbf{k} \sim \mathbf{k}$ of corresponding crystalline material. However, the optical properties of an amorphous material can still be understood from the density of states, which can be defined also in the absence of long-range order.
- ii. Since \mathbf{k} is not a good quantum number in amorphous materials, selection rules are released. There is no formal distinction between direct and indirect optical transitions

in amorphous solids. This concept is critical for silicon, because the optical band-gap of c-Si is indirect, $E_g^{(i)} = 1.1$ eV. The zone boundary direct band-gap of c-Si is significantly higher, $E_g^{(d)} = 3.2$ eV [10]. The band gap of amorphous silicon depends on the fabrication properties of this material (and specifically on the mass density) but generally takes values from $E_g = 1.6$ eV to 1.7 eV. However a significant amount of electronic transitions also occur at photon energies $E < E_g$.

- iii. The localized states in the band tails become delocalized at a critical boundary called the mobility edge. A mobility gap (like in crystals) is defined as the energy separation between the two mobility edges of the conduction and valence bands.
- iv. Shape of DOS of a-Si is different from that of DOS for c-Si because the bonding disorder of the amorphous structure results in localized tail states that decay exponentially in to the mobility gap and the width of tail states is associated with a “degree” of disorder. The exponential tail value below the mobility gap is called Urbach energy and gives the measure of the width of the tail states [11]. The optoelectronic properties of a-Si:H depend on width of the tail states.
- v. Unlike localized states related to impurities in crystals, there is a possibility of localized states in amorphous materials, for which electronic wave functions overlap.
- vi. The density of coordination defects (also known as DBs) is higher than the point-defect density in the corresponding crystalline materials because amorphous materials are out of thermodynamic equilibrium.

Due to the lack of periodicity in amorphous structure, the bonding arrangement within a particular volume of the material represents one of many alternative configurations. These materials are in thermodynamically non-equilibrium state and can

take different macroscopic states depending upon the growth conditions. The structure of the grown materials and its physical properties are strongly influenced by the growth conditions and methods. Samples used in the present study were grown by Saddle-Field glow discharge technique that is discussed in the next section.

4.3 Growth of hydrogenated amorphous silicon (a-Si:H) by saddle field glow discharge

Amorphous solids can be prepared by non-equilibrium process like: rapid quenching of liquid, or by condensation of gas at a solid surface or a physical or chemical process at the gas – solid interface, or by modification of a solid using ion implantation [9]. Since the crystalline form is the preferred arrangement of matter under thermodynamic equilibrium, out-of-equilibrium growth processes are generally used to form amorphous materials. In the case of amorphous silicon, many of these out-of-equilibrium processes produce materials of poor quality, which are not suitable for electronic or solar applications, because the dangling bond (DB) defect density is too high. DB defects produce states at mid gap that act as traps for charge carriers and in solar cells, they favour the non-radiative recombination of photo-generated carriers, which limit the efficiency of these devices. Typically a-Si prepared by thermal evaporation or fast cooling of liquid silicon have dangling bond densities $\sim 10^{19} - 10^{20} \text{ cm}^{-3}$. To reduce the DB's densities, defects can be passivated by incorporating hydrogen in the material. In this way it is possible to obtain solar-grade a-Si:H ($N_d < 10^{17} \text{ cm}^{-3}$) or electronic grade a-Si:H ($N_d < 10^{15} \text{ cm}^{-3}$) [5]. However, in order to incorporate significant amount of hydrogen in a-Si:H, in a way to passivate most of the defects (H \sim 10%- 15%), growth methods operating strongly out-of-equilibrium are required.

These methods are generally based on plasmas. Plasmas are partially ionized gases far from thermodynamic equilibrium. The role of the plasma is to provide a source of energy to decompose silane gas. This is done by collisions of the electrons with the gas molecules which build up their energy by acceleration in an electric field [9,11]. The kinetic energy of electrons is responsible for the decomposition of gas molecules. Some of the energy transferred to the gas molecules is radiated as visible light, for this reason the deposition method is also referred to as glow discharge. Our a-Si:H thin film samples were prepared by Saddle field glow discharge technique that is discussed below.

The saddle-field glow discharge technique is based on the idea of oscillation of an electron gas in a symmetric DC electric field [12] in order to form plasma. The deposition chamber is fitted with three mesh electrodes. The DC electric field is created in a volume between a central anode, which is semi-permeable wire grid, and two cathodes both of which are parallel to the anode and are symmetrically positioned on both sides of the anode as illustrated in Figure 4.3. An electrically isolated substrate holder is fitted with a heater to control the substrate temperature. The substrate holder can be electrically biased. A substrate is loaded into the sample holder inside a stainless steel chamber. The chamber is evacuated to high vacuum ($\sim 10^{-5}$ Torr) and the silane gas is diluted with argon and hydrogen, and fed into the reaction chamber in a controlled way using a gas flow meter.

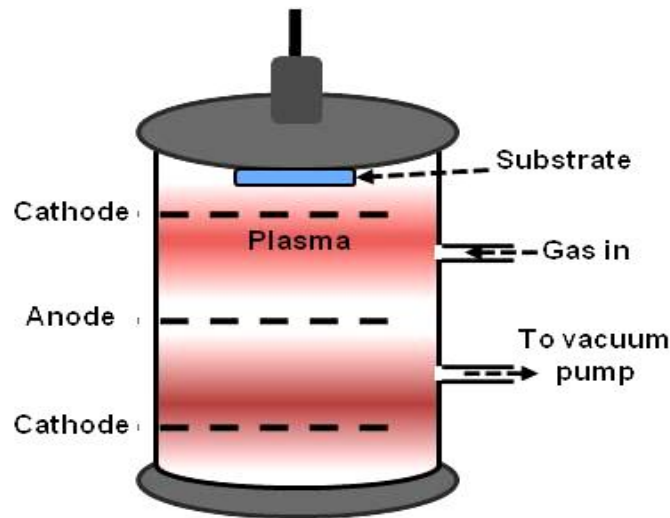


Figure 4.3 Schematic of DC saddle-field deposition system. There are two cathodes symmetrically placed on both sides of central anode to increase the electrons collision path.

The density of high energy electrons between the two cathodes is increased many folds over a conventional DC discharge and the probability of impact ionization of gas phase species is greatly increased. The cathodes are also made semi-permeable so that the gas species may pass through the cathodes towards substrate positioned outside of the plasma region. Silicon obtained from the decomposition of silane condenses on the substrate for form a-Si film. Substrate temperature can be controlled by the heater attached to the substrate holder, which in turn controls the hydrogen content of the film. With this method uniform a-Si:H films with controlled amount of hydrogen can be grown.

4.4 Light induced degradation of a-Si:H

Light-induced phenomena in amorphous semiconductors were first observed for chalcogenide glasses as photo-darkening, photoluminescence (PL) fatigue and photo structural changes associated with illumination whose energy equals to or exceeds the

energy band-gap of these materials [6]. Photostructural changes are observed as changes in volume of the sample during illumination. As an amorphous solid is a non-equilibrium substance, it takes different macroscopic states depending upon the preparative process. Any external disturbance, either thermal or optical, will induce structural changes. In case of a-Si:H based solar cells, the degradation caused by long-time intense illumination is an obstacle in their application. Staebler and Wronski [13] found that both photoconductivity and dark conductivity of a-Si:H films decrease significantly when these films were exposed to intense illumination for several hours. Degradation can be reversed by thermal annealing of a-Si:H at temperatures that are comparable to the films growth temperatures. Stutzmann, Jackson and Tsai (SJT) [14] have done a detailed study of light-induced defect creation in undoped hydrogenated amorphous silicon, using electron-spin-resonance and photoconductivity measurements. The model proposed by them is based on the assumption that non-radiative direct recombination of electron-hole pairs provides the energy for the defect formation and the metastable changes are caused by recombination-induced breaking of weak Si-Si bonds, rather than by trapping of excess carriers in already existing defects.

They have used electron-spin resonance (ESR) and photoconductivity experiments to systematically study the microscopic and macroscopic changes in a-Si:H under different internal and external parameters. Internal parameters like sample thickness and impurity concentration, and external parameter like different illumination intensities, illumination times, photon energy and annealing temperatures were investigated. In terms of sample thickness they found that for sample thickness less than 1 micrometer the defects density increases with increasing sample thickness while thicker

sample is less susceptible to the metastable changes. They attributed such thickness dependence of defects density to bond-bending at surface and sample/substrate interface. The effect of presence of nitrogen and oxygen as impurities in a-Si:H sample was also investigated and it was found that the ESR signal was independent of concentration of such impurities and thus they concluded that the SWE is intrinsic to a-Si:H, and not related to defect states created by incorporation of oxygen or nitrogen. They also studied the kinetics of defect formation in a-Si:H i.e. the dependence of the number of metastable defects on the external parameters like illumination time and intensity and found that the number of defects is proportional to $t_{\text{ill}}^{1/3} \cdot I^{2/3}$, where t_{ill} is illumination time and I is the illumination intensity at 1.9 eV photon energy. They also found that under illumination when $T_{\text{ill}} > 90^\circ\text{C}$ the ESR signal saturate indicating a balance between light induced defects creation and simultaneous annealing.

H. M. Branz [15] proposed a model of light-induced metastability (SWE) in hydrogenated amorphous silicon known as hydrogen collision model. According to this model, when a mobile hydrogen atoms generated by photo-induced carriers forms a metastable and immobile complex containing two Si-H bonds, leaving behind a defect (DB) on the site from which the hydrogen atom was excited. The mobile hydrogen atom can also be trapped by another DB.

While knowledge on the mechanisms at the atomistic level which lead to Staebler-Wronski effect (SWE) has greatly improved during the last few years [15-18], the process that limits the formation of defects, preventing a-Si:H to completely remove hydrogen from Si-H bonds upon prolonged light-soaking, is still controversial [18]. Understanding

of such process is vital to develop a-Si:H solar cells that self-repair during prolonged exposure to sunlight.

4.5 Characterization of a-Si:H thin films

Structural information of a-Si:H can be obtained from X-ray, electron and neutron diffraction, scanning electron microscopy (SEM), transmission electron microscopy (TEM), infrared (IR) spectrum analysis, Raman spectroscopy and nuclear magnetic resonance (NMR) [2,6]. A number of techniques have been developed for optical and thermal characterization of a-Si:H thin films. For the measurement of thermal conductivity of thin films the most common techniques are the 3-omega (3ω) method [19], the flash technique [20] and photothermal deflection spectroscopy (PDS) [21-23]. PDS is the technique of choice for determining the optical absorption related to defects states in the sub-band gap region where the light absorption is small or the incident light energy is smaller than the band gap. PDS is based on the heat generated in the sample due to non-radiative recombination of light induced carriers resulting from the absorption of light. Subsequently, heat diffuses towards the transparent photothermal fluid that undergoes strong changes in refractivity. Such changes are monitored by a “probe” laser beam at wavelength different from the heating light beam. The probe beam deflects away from the sample surface as a consequence of thermal lensing effects in the fluid and such deflection is detected by a position sensor. The amplitude of the angle of deflection in the fluid depends on the amount of the light absorbed in the solid at the specific wavelength of the “pump” beam and the thermal capacitance of the sample, while the phase of the photothermal signal depends on the localization of the absorption and the diffusivity of heat along the sample surface.

In the present work we have performed Staebler-Wronski cycles of illumination and annealing on a set of solar-grade a-Si:H thin films, using PDS. Our PDS setup shown in Figure 2.2 enables the measurement of thermal conductivity in addition to the determination of the optical absorption of a-Si:H. The sub-band gap absorption was then used to calculate the excess absorption and density of defects [3].

4.6 Light-soaking experiments

Experiments were carried out on three high quality, solar grade a-Si:H (with defect density less than 10^{18} cm^{-3}) thin films that were grown by the saddle-field glow discharge technique [12]. The growth conditions and relevant characteristics of our a-Si:H thin film samples are summarized in Table 4.1. Samples were deposited on highly thermally insulating and optically transparent glass substrates, in order to limit the impact of the substrate on the model used to determine the thermal and optical properties of our films by PDS.

Our dedicated PDS setup for the measurement of thermal conductivity and optical absorption properties of a-Si:H is shown in Figure 2.2. Our setup allows us to change the chopper frequency, ω , as well as the width of the pump light pulses from the aperture of the slits at the monochromator. Three different beam widths ($B = 1 \text{ mm}$, 3 mm and 6 mm) have been used to double-check our measurements, although the largest possible beam size provided the most accurate results. A range of different chopping frequencies ($\omega = 20\text{-}700 \text{ Hz}$) has also been used for our measurements. Data discussed below were determined at $\omega = 20 \text{ Hz}$, which provided the highest signal and signal-to-noise ratio, while measurements at lower values of B and higher frequencies were used to estimate the uncertainties in the measured quantities. Monochromator was used to select the

incident photon energies from $E = 1.0$ eV to 2.2 eV to perform scan for each spectrum.

The amplitude (A_φ) and phase (Δ_φ) of the deflection angle of the probe laser beam, $\varphi(t) = A_\varphi \cdot \exp[j \cdot (\omega \cdot t + \Delta_\varphi)]$, can be expressed as [23]:

$$A_\varphi = \frac{1}{n_f} \left| \frac{dn_{fl}}{dT} \right| \cdot \frac{P_0}{\omega \cdot C_s \cdot L_y^2 \cdot L_z} \cdot \left[\frac{1 - e^{-\alpha_s(\lambda) \cdot L_x}}{\alpha_s(\lambda) \cdot L_x} \right] \cdot \sqrt{\frac{D_s}{D_{eff}}} \cdot \exp\left(\sqrt{\frac{\omega}{2D_s}} \cdot L_y\right) \quad (4.1)$$

$$\Delta_\varphi = \frac{\pi}{2} + \sqrt{\frac{\omega}{2 \cdot D_s}} \cdot L_y \quad (4.2)$$

where P_0 is the specific power deposited per unit area of the sample by the pump beam at the photon energy E . $\alpha_s(\lambda)$ is the optical absorption coefficient of the film, L_x is the film thickness, L_z is the height of the excitation light beam (that, in our setup, is known to be rectangular, with $L_z \gg L_y$), and D_{eff} is the effective diffusivity of the film-photothermal fluid system, which can be defined as a “parallel” between the thermal diffusivities of the film (D_s) and CCl_4 (D_f): $D_{eff}^{-1} = D_s^{-1} + D_f^{-1}$. Thus, our data allow determining D_s from the phase of the PDS signal (eq. 4.2). Since $\alpha(\lambda)$ is known above the optical band gap, where it is known to experience negligible changes upon light soaking (in our case, from ellipsometry measurements at $E > 2$ eV), D_s can be replaced into eq. 4.1 that can be inverted to extract the thermal conductivity of the films. Finally, after K_s is calculated, PDS measurements at $E \leq 2$ eV, eq.4.1 can be explicitated in terms of $\alpha(\lambda)$ that can be determined in the proximity and below the optical band gap of a-Si:H. In such spectral region, films are weakly absorbing and PDS is known to be more accurate than conventional UV-Vis spectrophotometry and ellipsometry [3].

Thermal conductivity was also measured by 3ω method by applying an AC voltage across a metallic strip deposited on the sample that serves as a heater as well as a thermocouple. The experimental setup is shown in Figure 2.7. An aluminum heating line

1.2 cm long, 0.5 mm wide and 100 nm thick was deposited on the sample, by thermal evaporation of aluminum in high vacuum chamber. Sample with aluminum strip, was then loaded into the 3-omega vacuum chamber and the chamber was evacuated in order to prevent the heat loss to the surroundings. AC current with frequency ω was applied across the aluminum strip and the AC voltage drop at 3ω across the two inner contacts was measured and recorded with a lock-in amplifier, and subsequently used to calculate the thermal conductivity K_s of the sample by using equation (2.4).

4.7 Theory

4.7.1 Optical absorption

In a-Si, the structural disorder is due to angle and distance bond fluctuations and to the coordination defects arising from dangling bonds. The inherent disorder of the amorphous structure and the presence of dangling bonds lead to broadening of the electronic density of states (DOS) of amorphous silicon near the valence and conduction band edges, and to the appearance of localized states in the gap [9] as shown in Figure 4.4b. The localized tail states are a consequence of the disorder inherent to the amorphous structure while the localized defect states in the middle of the gap are associated with the formation of DBs.

Optical absorption occurs by transition of electrons between electronic states such as valence band, tail states and gap states. The absorption of photons which results in inter band transition in crystalline semiconductors, is also observed in amorphous semiconductors like a-Si:H but the absorption edge is not so sharp as that for crystalline semiconductors [6,9]. For a-Si:H optical absorption coefficient increases from 10 cm^{-1} to

10^4 cm^{-1} over 0.5 eV. Such an absorption edge for amorphous semiconductors is called non-direct absorption edge and the corresponding energy gap is called non-direct gap. Incident photons may excite electrons from extended states in valence band into localized and extended states in the conduction band or from localized states in the valence band into extended states in the conduction band.

4.7.2 Tauc gap

The absence of long range order in amorphous semiconductors eliminates the first principles calculations of the band gap [11], so to explain the experimental results physical models were proposed. The physical model that is used to explain the experimental optical data involving transition of electrons from occupied valence band to unoccupied conduction band was presented by Tauc and the relationship between the photon energy $h\nu$, optical gap (also known as Tauc gap) E_g and optical absorption coefficient α is given by [11],

$$(\alpha \cdot h\nu)^{1/2} \propto (h\nu - E_g) \quad (4.3)$$

The characteristic value for the Tauc gap of a-Si:H ranges from 1.7 eV to 1.9 eV. Tauc gap of a-Si:H thin film samples depends upon the growth conditions like substrate temperature, hydrogen content and the density of the thin film.

4.7.3 Urbach energy

Urbach [24] first identified exponential (not Gaussian) tails at the edges of optical inter band transitions in nanocrystalline materials. The states which extend from the edge of the gap into the "forbidden region" is referred to as band-tail. The density of states typically decreases exponentially into the gap for several orders of magnitude. The slope

of this decay is thus called the Urbach energy, and is closely related to the amount of disorder in the material [16,17]. The relationship between absorption coefficient α and the photon energy ($h\nu$) for a-Si:H is expressed as:

$$\alpha = \alpha_0 \cdot \exp(h\nu/E_u) \quad (4.4)$$

where E_u is “Urbach energy” which is the broadening of the absorption edge due to disorder and related to the transitions from the extended valance band tail states to localized states at the conduction band tail. When an a-Si:H film is illuminated, an increase in E_u with increasing illumination time occurs due to increase in the density of defects. Upon annealing at 200°C in an inert atmosphere defects can be recovered which means that hydrogen that remains trapped within the sample, fills the dangling bonds and decreases the defect density.

4.7.4 Excess absorption

Amorphous semiconductors have defects states in the mobility gap. At low energies (<1.5eV) the absorption takes place at the defect states and it is proportional to the density of defect states. Transition from and into the localized defect states in the mobility gap result in the excess absorption. Upon illumination, structural defects are created due to breaking of weak bonds and the density of defect states increases leading to more sub-band gap absorption. The excess absorption $\alpha_{exc}(E)$ is related to the defect density N_d (in cm^{-3}) by the relationship [3]:

$$N_d = 7.9 \cdot 10^{15} \cdot \int \alpha_{exc}(E) \cdot dE \quad (4.5)$$

Using the area under the optical absorption curve below the optical gap, the defect density can be calculated.

4.7.5 Thermal conductivity

Physical properties of amorphous materials are quite different from their crystalline counterparts because of lack of long range order in amorphous structure. In the case of the crystalline dielectric materials where heat is carried by quantized lattice vibrations - phonons, by applying the kinetic theory of gases to phonon gas, the thermal conductivity K_s of the material can be expressed as [19,25]:

$$K_s = \frac{1}{3} \cdot C \cdot v \cdot \Lambda \quad (4.6)$$

where C is specific heat, v is velocity of phonon and Λ is phonon mean free path.

In the case of amorphous solid there is no long range order and concept of phonon (lattice wave) is less applicable [26]. Vibration of atoms in amorphous materials is localized so they should be considered as damped localized oscillators instead of phonons. Einstein developed a theory for such solids by considering atoms as harmonic oscillators with same frequency of oscillation, to explain the specific heat of such solids. Cahill and Pohl [27] modified Einstein theory by considering larger oscillating entities than single atom [eq. (3.9) Chapter 3] and found better agreement with experimental data above 50K. However, this expression has been found to be applicable only for relatively defect-free amorphous materials [19]. In defective amorphous materials, the mean free path for coherent lattice vibrations (Λ) will also depend on scattering from defects if the average distance between defects (Λ_d) becomes comparable to Λ_E . This concept can be quantified by expressing Λ using the Matthiessen's rule:

$$\frac{1}{\Lambda} = \frac{1}{\Lambda_E} + \frac{1}{\Lambda_d} \quad (4.7)$$

When defects are formed in a-Si:H under light soaking, the distance between defects decreases accordingly.

4.8 Results and discussion

The effect of illumination on the optical and thermal properties of a-Si:H thin films was investigated. The optical properties of our a-Si:H thin films, determined by combining spectroscopic ellipsometry in the fundamental absorption region and PDS at $E \leq 2$ eV are shown in Figure 4.4a. For all of such films, three distinct spectral regions, dominated by different types of opto-electronic processes, are observed as in Figure 4.4b: i) parabolic optical transitions at photon energies higher than the optical band gap, E_g ii) sub-gap exponential Urbach tails from optical transitions involving localized band edges, and iii) sub-gap absorption in excess to the Urbach tails, related to transitions involving dangling bond defects.

We have monitored E_g (Tauc gap), the Urbach energy (E_0), and N_d from the optical absorption spectra that were recorded during 3-hr AM 1.5 light-soaking cycles of our a-Si:H samples (Figure 4.5a-c). A PDS scan was taken every 15 min. The defect density N_d (in cm^{-3}) was calculated from excess absorption $\alpha_{exc}(E)$ using relation (4.5). Sample #1 has the highest defect density, which can be attributed to large quantities of unbound hydrogen in this sample and lower passivation of dangling bonds [17,28]. For all our three samples, we found that E_0 and N_d , increased with increasing light soaking time, while E_g slightly decreased. These results are consistent with the literature that shows the formation of defects and an increase of disorder during light soaking [29]. The excess absorption and dangling bond density increase during light-soaking for all the samples as in Figure 4.5c. Open dots in Figure 4.5 also show that, after annealing at 200°C , the optical properties, including the excess absorption, revert back to their original values, which indicates that the defects formed during light soaking were repaired, as

expected for Staebler-Wronski effect. In the annealing process, the hydrogen atoms revert back to form Si:H bonds and decrease the defect states.

The determination of thermal conductivity of a-Si:H is important to understand the heat propagation, temperature control and growth conditions to make thin films for specific use. Despite the intensive characterization efforts, thermal conductivity of aSi:H have been reported to have values varying over a wide range (0.01 W/m.K to 6 W/m.K) and depend upon the method of sample preparation [33-35]. We have also measured the thermal conductivity of a-Si:H films by PDS and studied the effect of defects density under illumination.

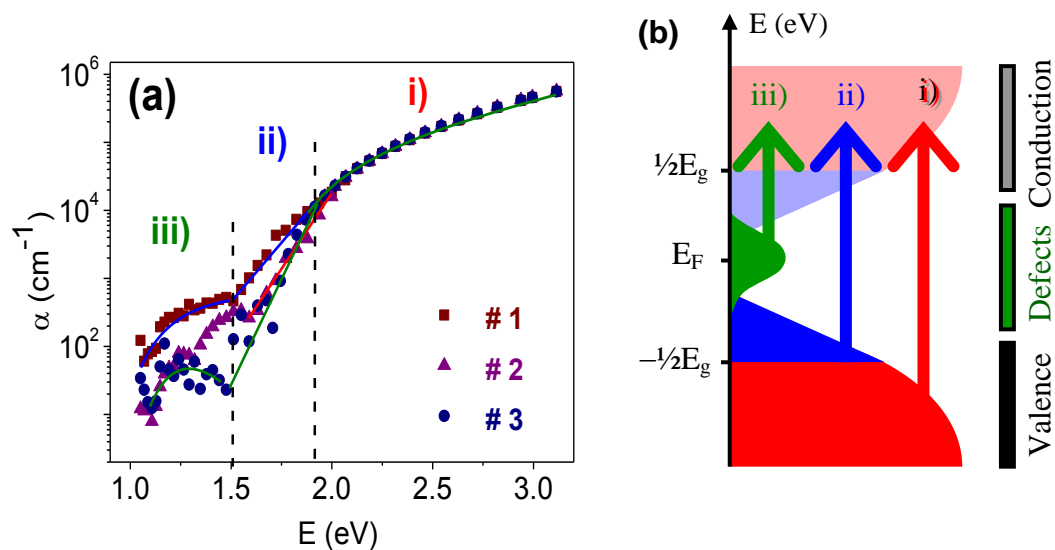


Figure 4.4 (a) Optical absorption coefficient for samples #1-3 as received, extracted from PDS data at low photon energy and spectroscopic ellipsometry data (Jobin-Yvon Uvisel ellipsometer coupled with Tauc-Lorenz model) at high photon energy - (b) Schematic density of states of the different regions of optoelectronic transitions in a-Si:H: i) Parabolic (Tauc-like) transitions ii) Urbach tails iii) Excess absorption related to dangling bonds. α_{exc} was determined by fitting this region using a Gaussian line.

From the amplitude of the PDS signal, the thermal conductivity was calculated using eq.(4.1) as shown in Figure 4.5(d). From Table 4.1, it can be seen that sample #2 has a higher thermal conductivity as compared to the other two samples, while sample #1 has the lowest conductivity, corresponding to the highest defects density among the three samples.

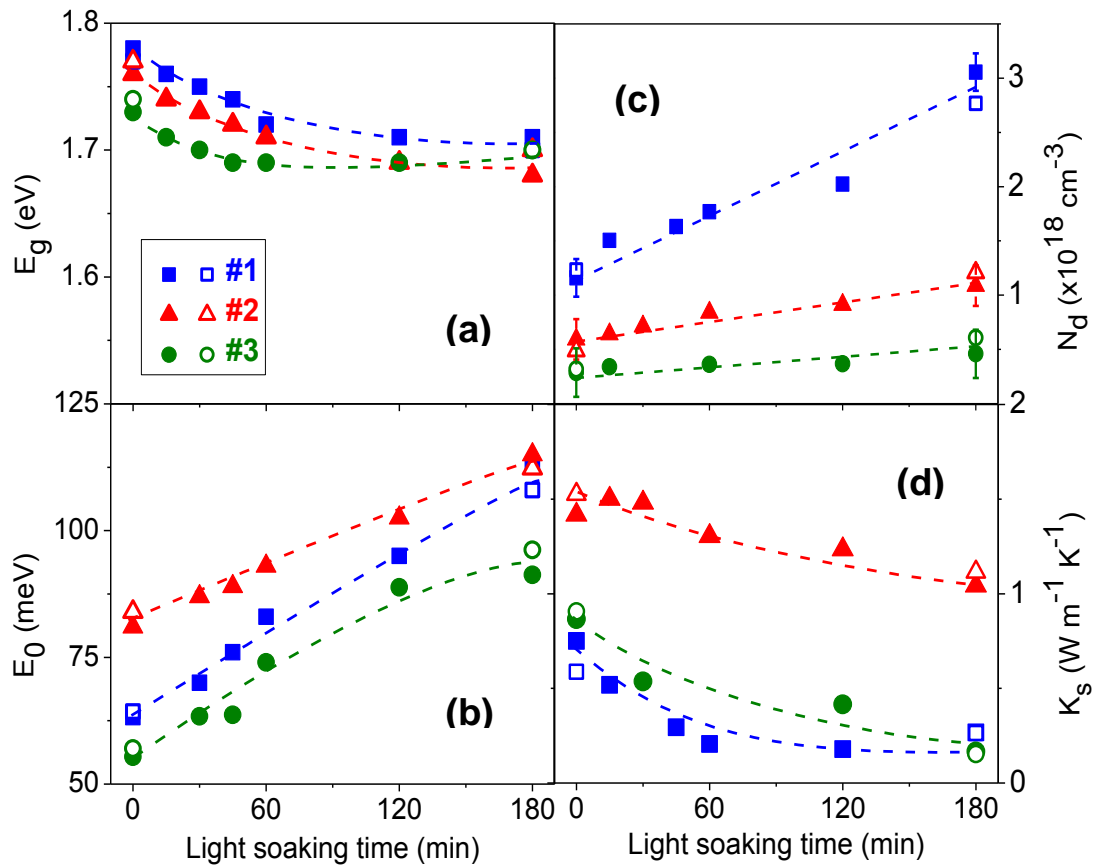


Figure 4.5 (a) Tauc band gap, E_g (b) Urbach energy, E_0 (c) defect density, N_d and (d) thermal conductivity (K_s) in samples #1-3 during light soaking experiments under the first AM 1.5 illumination cycle (solid dots) as a function of illumination time (t). In all of the panels, open dots refer to data recorded during a second light soaking cycle after annealing the samples at 200°C in Ar, which restored their properties.

If we assume that defects are point-like dangling bonds uniformly distributed in the film, we can infer that their distance is [8]:

$$\Lambda_d \approx [3/(4\pi)]^{-1/3} \cdot N_d^{-1/3} \quad (4.8)$$

From eq. 4.6, Λ and K_s are consequently expected to decrease as $N_d^{-1/3}$ when $\Lambda_d \ll \Lambda_E$.

Although a more detailed model is necessary for a quantitative agreement, Figure 4.6a shows that K_s decreases with N_d for all of our samples, which indicates that these considerations are sufficient to capture at least the basic physics of degradation and recovery of thermal conductivity during Staebler-Wronski cycles. Figure 4.6a also shows that, in sample #2, K_s starts to decrease at N_d as low as $6 \cdot 10^{17} \text{ cm}^{-3}$, which corresponds to $\Lambda_E \approx \Lambda_d \approx 25 \text{ nm}$ and is consistent with data available in the literature [33].

The fact that, in Figure 4.6a, the decrease of K_s in sample #3 occurs at lower defect density than in samples #1 and #2 can be explained by a lower thermal capacity or lower sound velocity in this sample, which is consistent with the different physical properties, as reported in Table 4.1.

On the other hand, increasing the defect concentration (and, therefore, decreasing the thermal conductivity) also increases the maximum temperature that can be reached in our a-Si:H thin films during light soaking because of the increased difficulty of the films to evacuate heat. We calculated the temperatures (T_{ill}) reached in the samples at different times of light-soaking using Fourier's equation in 2-D [34] as shown in Figure 4.6b. The thermal power released in the films was estimated from the integrated optical absorption coefficients. After 3-hr light-soaking and intense formation of defects, maximum temperatures $T_{ill} \approx 100^\circ\text{C}$ are reached for samples #1 and #2, which are particularly high and consistent with rapid self annealing of defects in these samples. Conversely, in the

case of sample #3 (with relatively high K_s as a consequence of a lower N_d) T_{ill} has not yet reached, at the end of light soaking process, a value sufficient to repair the defects, so the defect density continues to increase, with decreasing thermal conductivity, even after 3 hrs of illumination.

Table 4.1 Hydrogenated amorphous silicon (a-Si:H) samples parameters.

#	D (nm)	Hydrogen bonding type	Initial			Final		
			N_d $\times 10^{18}$ (cm^{-3})	K_s ($\text{W}\cdot\text{m}^{-1}\cdot\text{K}^{-1}$)	T_{ill} ($^{\circ}\text{C}$)	N_d $\times 10^{18}$ (cm^{-3})	K_s ($\text{W}\cdot\text{m}^{-1}\cdot\text{K}^{-1}$)	T_{ill} ($^{\circ}\text{C}$)
1	400	Mono hydride	1.146	0.750	27	3.017	0.267	94
2	900	Poly hydride	0.585	1.417	25	1.074	1.042	40
3	800	Mono hydride with lower bonded H content	0.283	0.866	27	0.363	0.166	101

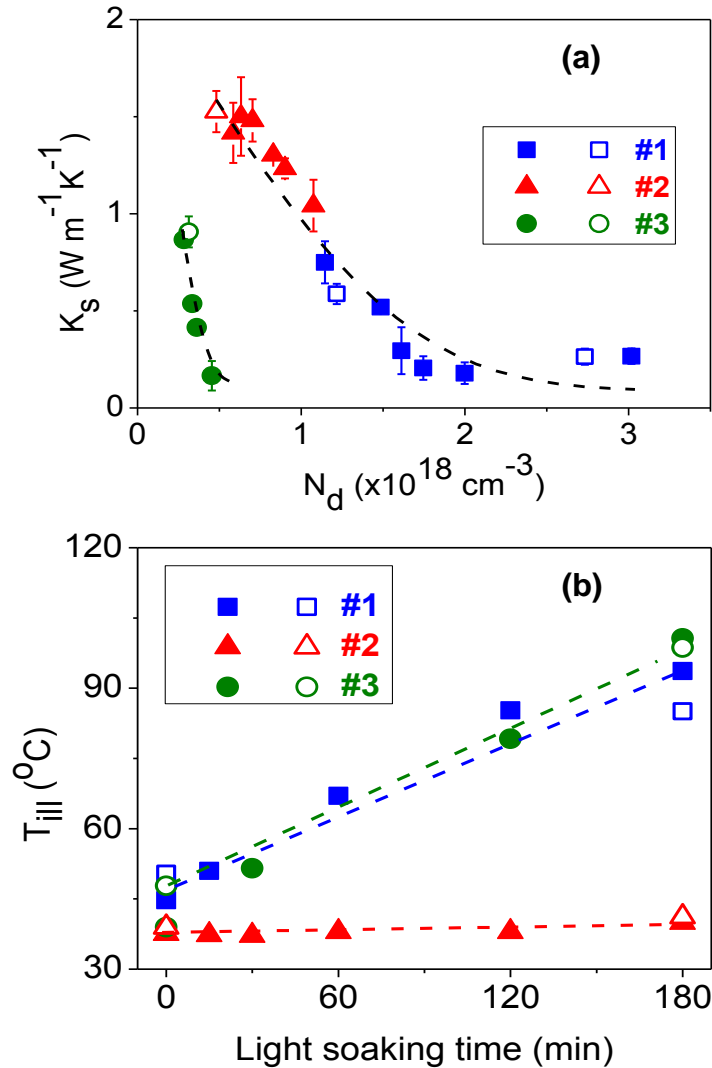


Figure 4.6 (a) Thermal conductivity (K_s) as a function of defect density (N_d) for samples #1-3 at different stages of a Staebler-Wronski cycle. Samples #1 and #2 follow the same trend. The fact the trend of sample #1 is downshifted can be related to the higher porosity of this sample and lower sound velocity, (b) Temperature of the samples during AM 1.5 illumination (T_{ill}) determined using Fourier's equation of heat as a function of illumination time (t). In both panels, open dots refer to data recorded during a second light soaking cycle after annealing the samples at 200°C in Ar, which restored their properties.

Thermal conductivity was also measured by 3ω method and the thermal conductivity value of as grown sample was found to be $(0.73 \pm 0.03) \text{ W}\cdot\text{m}^{-1}\cdot\text{K}^{-1}$ while the one found by PDS was $(0.75 \pm 0.11) \text{ W}\cdot\text{m}^{-1}\cdot\text{K}^{-1}$. The effect of light soaking on thermal conductivity of the sample # 1 was also investigated using 3ω method. Sample was illuminated with white light for different time intervals from 15 minutes to 180 minutes and after each interval of illumination thermal conductivity was measured. It was observed that thermal conductivity decreased with increasing illumination time and then started to recover after one hour of illumination. The results are shown in Figure 4.7 along with the results of photothermal deflection spectroscopy (PDS). However the effect of light illumination on thermal conductivity is not as severe as it was in case of illumination in PDS experiments and also the recovery of thermal conductivity was also observed after one hour of illumination.

The difference in two experimental configurations, (PDS and 3ω) for the study of thermal conductivity, was the presence of metallic strip on the surface of the sample and shadow of the metallic line may have prevented that region of the sample from degrading. The recovery of thermal properties after one hour of illumination could be due to the intense illumination that resulted in annealing of the sample. It is possible because in the case of 3ω setup, sample is in vacuum ($\sim 10^{-2}$ Torr) while in PDS sample was in air at ambient pressure. Other factors could be different sample to source distance and possibly different focusing, although every effort was made to keep the conditions similar to PDS setup. However, both methods yielded the qualitatively matching thermal conductivity trends, which confirmed that there exists some mechanism for the self repair of defects.

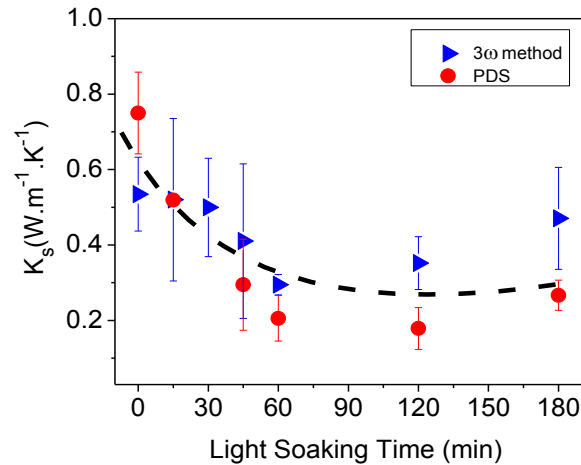


Figure 4.7 Thermal conductivity of a-Si:H thin film as a function of light soaking time measured by PDS and 3-omega methods which is similar to the one measured by PDS.

While our experiments are specifically aimed at demonstrating the factors limiting the Staebler-Wronski effect under AM1.5 light-soaking and sunlight illumination, they also shed light on other forms of reversible degradation of a-Si:H. Previous work by one of us [35] examined tritiated amorphous silicon (a-Si:H:T) and showed similar self-limiting phenomena in the reversible formation of defects. Although the formation of defects in this case was due to β -decay of Si-bonded tritium into helium and the subsequent formation of Si- dangling bonds in the absence of illumination, an important consequence of β -decay is the formation of a gas of hot carriers [35]. White et al [36] showed that the lattice temperature can strongly increase due to hot carriers shedding their energy via lattice modes. A similar (or higher) increase in lattice temperatures is not unreasonable for hot carriers induced in a-Si:H:T by β -decay. Temperatures for slow self-annealing as low as 50⁰C have been reported [37], which are consistent with the temperatures reached in a-Si:H during light soaking and in a-Si:H:T as a consequence of intense β -decay, upon defect-induced degradation of thermal conductivity.

4.9 Conclusion

We have measured the optical and thermal properties of a set of a-Si:H samples during repeated cycles of degradation under light soaking from AM 1.5 illumination and recovery via thermal annealing. We found that, during light-soaking, the thermal conductivity of the samples decreased at increasing density of dangling bond defects. At the lowest values of thermal conductivity, films soaked by AM1.5 light at 1 Sun reach internal temperatures $T_{\text{ill}} > 100^{\circ}\text{C}$, which are comparable to the annealing temperatures that can be used to recover low defect densities in a-Si:H. As the annealing at 200°C for 30 minutes in Argon is shown to completely restore the original defect density and thermal conductivity of a-Si:H, this allows us to establish a general correlation between these two quantities.

Our experiments lead us to conclude that while the thermal properties of a-Si:H are controlled by defects, the Staebler-Wronski effect and the formation of defects under light soaking are promoted, controlled and limited via thermal conductivity. We have demonstrated for the first time that when sufficiently high defect densities allow for low enough values of thermal conductivity in a-Si:H thin films, the degradation of defects (from light soaking [13,17,18] or tritium decay [35]) comes to an end because moderate heating allows for temperatures consistent with self-annealing of the defects. Previously hypothesized complicated mechanisms of self-repair at the atomistic level [18] can be reconsidered. Engineered a-Si:H thin films with low thermal conductivity will be vital for developing a-Si:H devices free from Staebler-Wronski effect.

References

- [1] A. Goetzberger and C. Hebling, *Solar Energy Materials and Solar Cells*, **62** (2000) 1.
- [2] J. D. Joannopolous and G.D.Lukovsky (Eds.), *The Physics of Hydrogenated Amorphous Silicon*, vol **55**, Springer Verlag, Heidelberg Germany, 1984.
- [3] W. B. Jackson and N. M. Amer, *Phys. Rev. B*, **25** (1982) 5559.
- [4] G. D. Cody, T. Tiedje, B. Abeles, B. Brooks and Y. Goldstein. *Phys. Rev. Lett.*, **47** (1981) 1480.
- [5] R. A. Street, *Hydrogenated Amorphous Silicon*, Cambridge University Press, Cambridge, Great Britain, 1991.
- [6] *Handbook of Electronic and Photonic materials*, S. Kasap and P. Kapper, Springer New York, 2006.
- [7] D. E. Polk, *J. of Non-Crystalline Solids*, **5** (1971) 365.
- [8] Mott and Davis, *Electronic Processes in Non-crystalline Materials*, Clarendon Press, Oxford, 1979.
- [9] K. Tanaka. E. Maruyama, T. Shimada and H. Okmoto, *Amorphous Silicon*, John Wiley & Sons Inc. Chichester, England, Great Britain, 1999.
- [10] C. Kittel, *Introduction to Solid State Physics*, 7th Ed. John Wiley and Sons, Inc., 1996.
- [11] F. Demichelis (Ed.), *Physics and Applications of Amorphous Semiconductors*, World Scientific Publishing Co. Ltd. 1990, P-28.
- [12] F. Gaspari, S. O'Leary, S. Zukotynski, and J. Perz, *J. non-Cryst.Sol.*, **155** (1993) 149.
- [13] D. L. Staebler and C. R. Wronski, *Appl. Phys. Lett.*, **31** (1977) 292.

- [14] M. Stutzmann, W. B. Jackson, and C. C. Tsai *Phys. Rev. B*, **32**, 23 (1985).
- [15] H. M. Branz, *Solid State Comm.*, **105** (1998) 387.
- [16] F. Gaspari, I. M. Kupchak, A. I. Shkrebtii and J. M. Perz, *Phys. Rev. B*, **79** (2009) 224203.
- [17] H. M. Branz, *Phys. Rev. B*, **59** (1999) 5498.
- [18] K. Morigaki, *Phys. Status Solidi A*, **206** (2009) 868.
- [19] D. G. Cahill *Rev. Sci. Instrumentation*, **61** (1990) 802.
- [20] W. J. Parker et al. *J. Appl. Phys.*, **32** (1961) 1679.
- [21] W. B. Jackson, N.M.AmerA.C.Boccara and D. Fournier, *Appl. Optics*, **20** (1981) 1333.
- [22] A. C. Boccara, D. Fournier, W. Jackson and N. M. Amer, *Opt. Lett.*, **5** (1980) 377.
- [23] S. Ezugwu, M.S. Ahmed, R. Bauld, R. Divigalpitiya, G. Fanchini, *Thin Solid Films*, **534** (2013) 520.
- [24] F. Urbach, *Phys. Rev.*, **92** (1953) 1324.
- [25] J. Bodzenta *Chaos, Solutions & Fractals*, **10** (1998) 2087.
- [26] Y. He, D. Donadio and G. Galli, *Appl. Phys. Lett.*, **98** (2011) 14401.
- [27] D. G. Cahill and R. O. Pohl, *Solid State Comm.*, **70** (1989) 927.
- [28] G. Lucovsky, R.J. Nemanich and J.C. Knights, *Phys. Rev. B*, **19** (1979) 2064.
- [29] C. Longeaud, D. Roy, Z. Teukam Hangouan, *App. Phys. Lett.*, **77** (2000) 3604.
- [30] N. Attaf, M.S. Aida and L. Hadjeris, *Solid State Comm.*, **120** (2001) 525.
- [31] Xiao Liu J. L. Feldman, D. G. Cahill, R. S. Crandall, N. Bernstein, D. M. Photiadis, M. J. Mehl, and D. A. Papaconstantopoulos, *Phys. Rev. Lett.*, **102** (2009) 035901.

- [32] H. Yang, David G. Cahill, X. Liu, J. L. Feldman and R. S. Crandall, Phys. Rev., B **81** (2010) 104203.
- [33] B. L. Zink, R. Pietri and F. Hellman, Phys. Rev. Lett., **96** (2006) 055902.
- [34] H. S Carslaw and J.C. Jaeger, *Conduction of Heat in Solids*, Clarendon Press, Oxford, 1959.
- [35] F. Gaspari et al. Phil. Mag. B, **80** (2000) 561.
- [36] J. O. White et al., J. Appl. Phys., **84** (1998) 4984.
- [37] O. Astakhov et al., J. Non-Cryst. Solids, **352** (2006) 1020.

Chapter 5

5 Relationship between electrical and thermal conductivity in graphene-based transparent and conducting thin films

An introduction to graphene, methods to make graphene films, experimental results of measurements of electrical, optical and thermal properties of transparent and conducting thin films based on graphene and graphene-based platelets, are presented. A model to explain the relationship between the thermal and electrical conductivity in our samples, which is general enough to be applied to a large class of graphene-based thin films, is presented.³

5.1 Introduction

Graphene, an individual layer of carbon atoms, is shown to possess exceptional thermal conductivity, up to $5,000 \text{ W m}^{-1} \text{ K}^{-1}$ [1] in addition to superior electronic [2], optical [3] and mechanical [4] properties. Single- and few-layer graphene can be fabricated in number of ways. In 2004, Novoselov *et al.* [5] first reported graphene sheets prepared by mechanical exfoliation of highly oriented pyrolytic graphite (HOPG). This method yields small sized samples useful for proof of concept experiments. Other methods include epitaxial growth of graphene on ruthenium [6], chemical vapor deposition (CVD) on metal substrates [7,8], substrate free graphene sheets by plasma enhanced chemical vapor deposition (PECVD) [9], Langmuir–Blodgett [10] and solution processing of exfoliated graphite with surfactants [11], Recently, ribonucleic acid (RNA) has been shown as an

³ This chapter is reproduced with permission from Ref. [32].

efficient non-ionic surfactant to exfoliate and stabilize the exfoliated graphene and few layer graphene flakes [12].

Graphene has great potential to be used in optoelectronics and electronics, due to its high charge mobility, optical transparency, mechanical strength and flexibility, and thermal conductivity [1-4], as a transparent and flexible electrode that was electrically and thermally conducting. The exceptional thermal properties of graphene-based nanomaterials make them commercially viable for thermal management [13,14]. Incorporation of small quantities of graphitic nanoplatelets and graphene flakes into epoxy resins significantly improve the thermal conductivity of these materials [15-17]. While transparent and conducting carbon-based films (TCCF) prepared from graphene platelets are not as of yet competitive with indium-tin oxide (ITO) as transparent electrical conductors, they are superior to ITO for thermal management applications, since the thermal conductivity of ITO was quite low ($5.9 \text{ W m}^{-1} \text{ K}^{-1}$) [18]. Interestingly, the thermal properties of single-layer graphene are also retained, to a large extent, in thin graphite multilayer [14], TCCF and insulating nanocomposites including small amounts of graphene [15] and are preserved even when few-layer graphene and thin graphite are placed on a substrate [19]. However, a physical model describing the thermal properties in TCCF and related composite materials was still missing.

While the thermal properties of ITO at room temperature are determined by the electronic band structure (and, therefore, related to the electrical conductivity via the Wiedemann-Franz law) the thermal properties of graphene-based materials are dominated by lattice vibrations [13,20], which makes the relationship between the thermal and electrical conductivity more complicated to be determined. Limited information exists in

the existing literature to determine such relationship as a function of the average number of layers and the fraction of voids in TCCF prepared from graphene-based platelets. We investigated the optical, electrical and thermal properties of TCCF and derived a correlation between the thermal and electrical conductivity of these thin films, based on the observation that both of these properties were strongly dependent on the average number of graphene layers forming the platelets, and on their lateral size. Special attention will also be paid to the role of voids and edges in determining the thermal properties of our samples.

5.2 Vacuum filtration setup

Filtration is a technique used to isolate solid contents of a solution on a filter membrane. There are two types of commonly used filtration techniques; gravity filtration and suction/vacuum filtration. Vacuum filtration was introduced by J. R. Brown [21] as a faster filtration technique. It is generally preferred for the filtration of thick/dense suspensions but it is also well suited for the filtration of suspension containing small particle e.g. nanoparticles because gravity filtration is not so effective due to very light weight of nanoparticles and also because nanoparticles tend to agglomerate as filtration time is prolonged which is undesired. Wu *et al.* [22] used vacuum filtration to filter carbon nanotubes suspension to make transparent and electrically conducting uniform and ultrathin films consisting of networks of carbon nanotubes. Eda *et al.* [23] adopted this method to make graphene films by filtering graphene suspensions through nitrocellulose filter membranes and transferring the films onto glass substrates. A schematic of the vacuum filtration setup used to prepare graphene and graphene nanocomposites thin films is shown in Figure 5.1. In this method, first graphene

suspension was prepared by exfoliating graphite in water by sonication and stabilized with the use of a surfactant. Suspension was then left overnight so that heavier particles sediment and then top 60-70% solution was decanted and centrifuged at a few thousand rotations per minutes (rpm). Supernatant was then used to make graphene films using the vacuum filtration setup as explained below.

A nitrocellulose filter with few nanometre pore size was placed on smooth top surface of a sponge-like frosted glass between the funnel and a spouted flask that is connected to vacuum system. Specific amount of graphene suspension was poured into the funnel and vacuum is turned on to suck the suspension through the filter. Solvent flowed through the filter as a result of suction and the solute formed a uniform layer on top of the filter membrane. When a graphene flake deposits on a part of the filter, it prevents suction from that part while suction continues from the uncovered part of the filter. This prevents the deposition of multiple flakes until whole surface of the filter is covered by single layer of graphene flakes. This way the thickness of the deposited film can be controlled by the amount and concentration of the suspension being filtered. The filter membrane with film was then transferred to any desired substrate by placing the filter with film side down on the substrate and then dried under load in an oven. After the samples were dried, the filter membrane was etched with sequential baths of acetone and methanol leaving behind the graphene film on the substrate. The advantage of this method is that the size of funnel and filter membrane are scalable from a fraction of an inch up to several inches in diameter and samples with different sizes can be prepared.

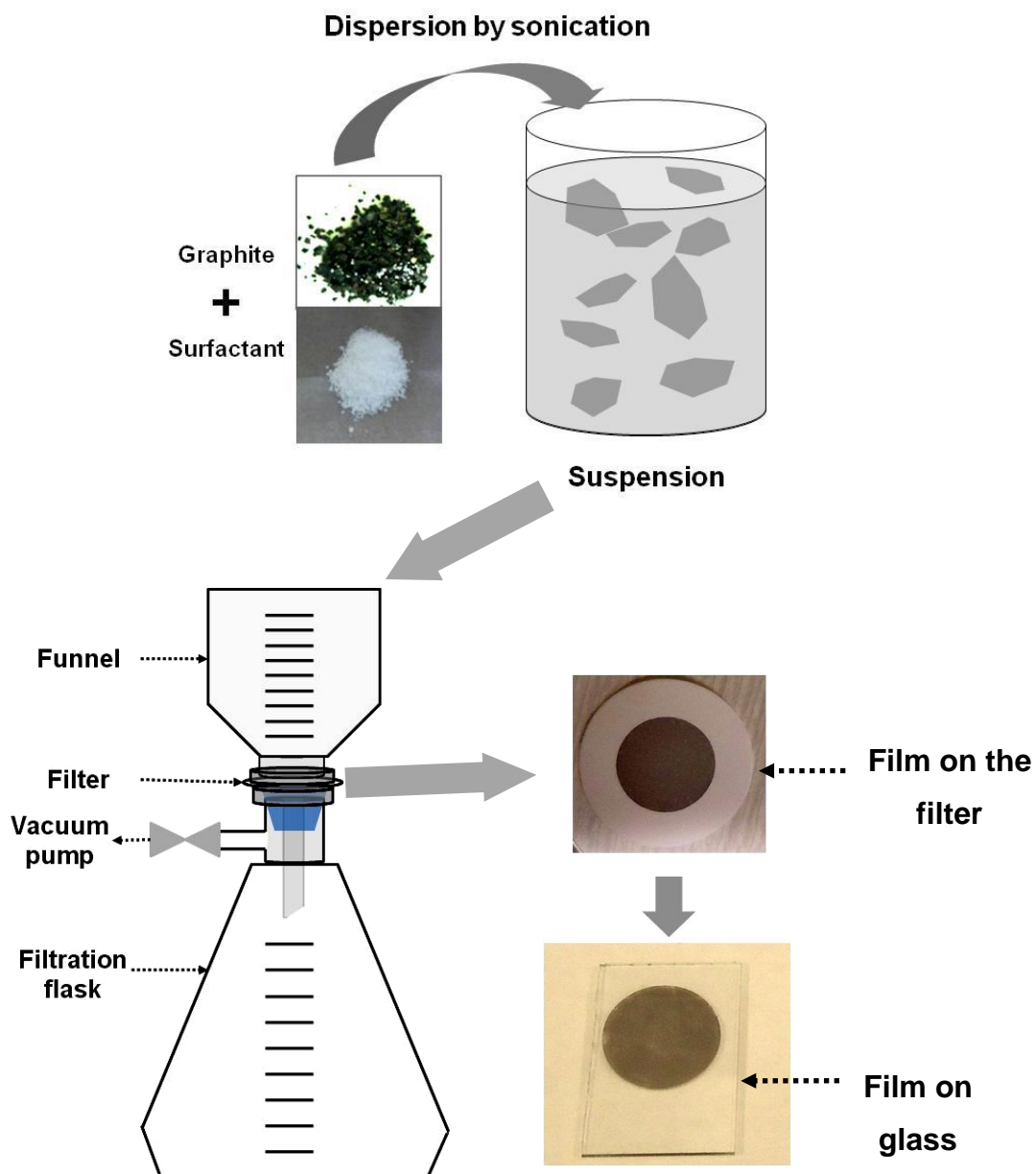


Figure 5.1 Schematic of vacuum filtration setup used for the preparation of graphene and graphene-based nanocomposite thin films. The film shown in the picture is extremely thick and is only for visual demonstration.

5.3 Experimental

Two different sets of graphene-based thin films, both deposited on glass substrates, have been investigated in our study: a set of films prepared by the vacuum filtration method described by Lotya *et al.* [11] and commercial-grade prototypes of TCCF developed by 3M Canada Co. For the first set of samples, the suspensions for vacuum filtration were obtained from turbostratic graphite flakes (Aldrich cat. no. 332641) which were sieved and dispersed in a 5 g/L aqueous suspensions of Sodium Dodecylbenzene Sulfonate (SDBS) by the aid of a bath sonicator for 3 hrs using the procedure described in ref. [11]. The resulting suspension of graphite and graphene-based flakes was left to sediment and then centrifuged at 6,000 rpm for 90 min. prior to vacuum filtration. A relevant advantage of this method is that SDBS can be completely removed from the samples by repeatedly washing them in water, which also does not remain trapped in the films because graphene is hydrophobic. For the second set of samples, smaller graphite flakes, with diameter of less than 0.5 μm , were utilized. Comparison of the two sets will allow us to demonstrate the effects on the thermal conductivity of “large” and “small” flakes with respect to the phonon mean free path.

We studied the morphology of our films by using tapping-mode atomic force microscopy (AFM). AFM data were recorded on a Witec Alpha300S microscope, as demonstrated in Figure 5.2. A number of AFM images on different regions of each sample were used to extract the fraction (f) of substrate area covered by graphene platelets and the average thickness of the films. The average number (N) of graphene layers per platelet could be determined from the thickness by assuming an interlayer spacing of 0.35 nm in graphite [2]. UV-Visible transmittance (T) data were recorded on a

Varian DMS 80 spectrophotometer. For all of our samples, T is nearly independent on the wavelength, as shown in Figure 5.3a. Figure 5.3b shows that, within our set of samples, T experiences an exponential decay with increasing N :

$$T = 100 \cdot \exp(-N/M) \quad (5.1)$$

This behavior can be easily understood if we assume that M layers of graphene are necessary to attenuate a light beam by a factor $1/e$. By fitting the data in Figure 5.3(b) using eq. 5.1, it can be found that $M = 50$. Nair *et al.* [3] showed that an individual layer of graphene has a transmittance $T = \exp(-1/M) \approx 98\%$ which also implies $M \approx 50$. Thus, the values of N we directly measured by AFM as in Figure 5.2 are consistent with our optical data and in agreement with the literature [3].

The electrical properties of our films were measured at room temperature using a Keithley 2400 source meter attached to a four-point probe station. Room-temperature sheet conductivity as a function of surface area covered by graphene platelets is shown in Figure 5.4a. Voids are expected to play an important role in limiting the electrical conductivity in TCCF: according to percolation theory [24], no percolating pathway can be drawn through the platelets below a critical threshold of covered area (f_0) of the substrate. Therefore, films at $f < f_0$ are highly insulating. For $f > f_0$ and neglecting the contribution of the contact resistance between platelets, the electrical conductivity is given by the following relationship [24]:

$$K_{el} = S_0 \cdot (f - f_0)^x = S_0' \cdot (N - N_0)^x \quad (5.2)$$

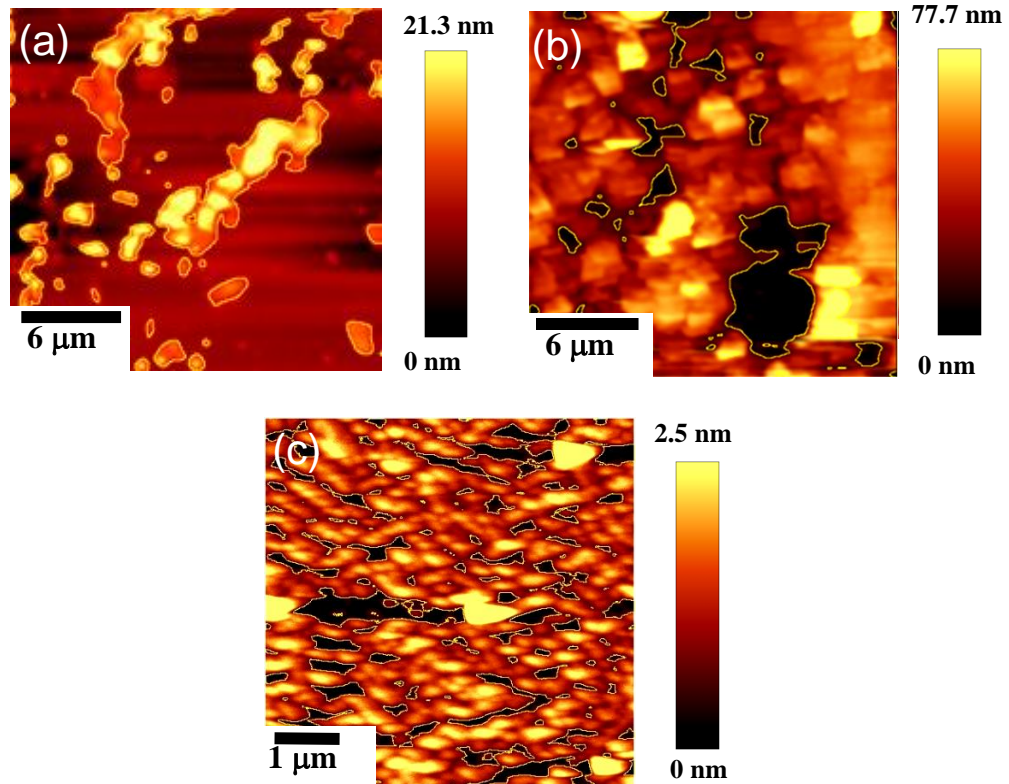


Figure 5.2 (a) AFM image of the thinnest sample prepared using the vacuum-filtration method of Lotya *et al.* [11] (b) AFM image of the thickest sample prepared using the same method [11] (c) AFM image of a sample prepared by 3M Canada Co. f and N were determined for each one of our samples by processing and averaging ten AFM micrographs of this type.

As shown by our AFM data, summarized in Figure 5.3c, a linear trend, $N \approx A \cdot f$, exists for all of the samples prepared by the method of Lotya *et al.* [11]. Therefore, for these samples, eq. 5.2 can be written both in terms of $(f - f_0)^x$ and $(N - N_0)^x$ (with $N/N_0 = f/f_0$ and $S_0' = S_0/A^x$). As shown in Figures 5.4a-b, eq. 5.2 is best fitted with $x = 2.25$, $S_0 = 400 \text{ S m}^{-1}$ and $f_0 = 0.25$ (or $S_0' = 8.4 \cdot 10^{-2} \text{ S m}^{-1}$ and $N_0 = 30$). Such trend is consistent with modeling these films as having a fraction of the total surface occupied by conducting platelets and a complementary fraction $(1-f)$ occupied by voids.

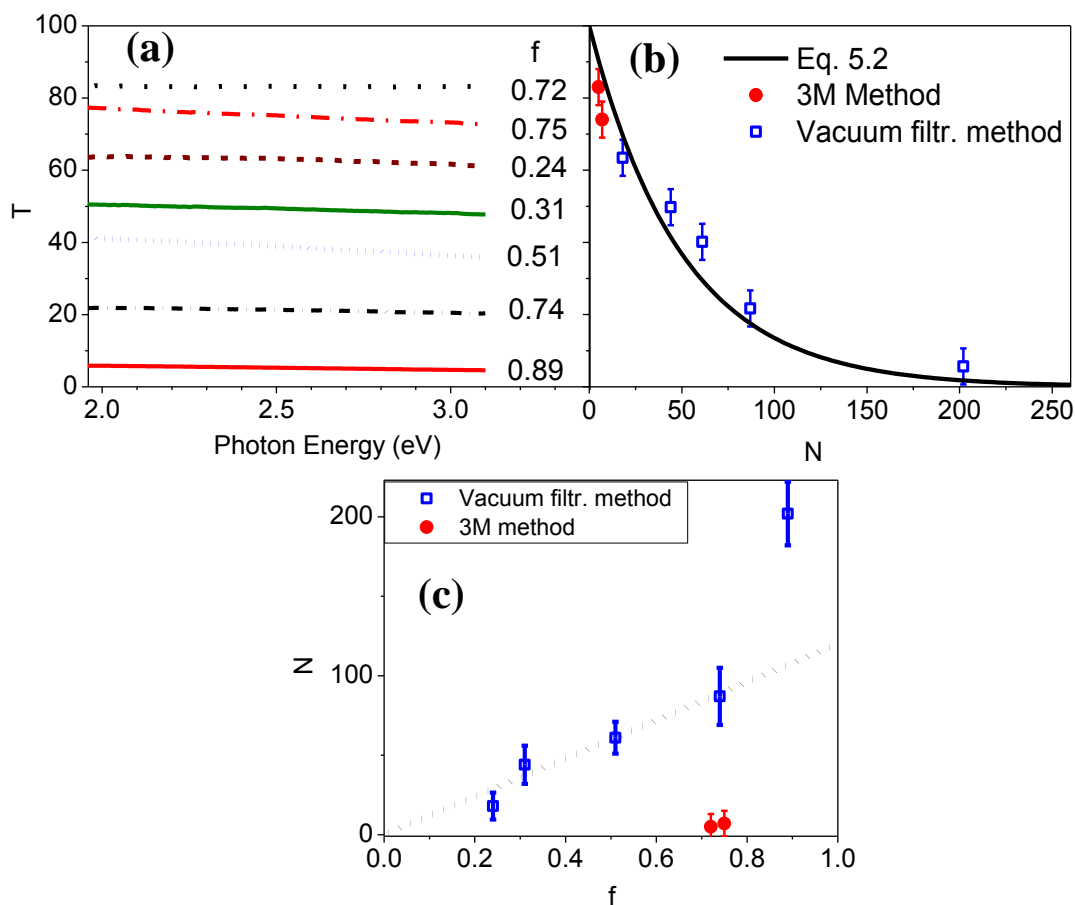


Figure 5.3 (a) Transmittance of TCCF prepared using the method of Lotya *et al.* [11] and a proprietary method of 3M Canada. (b) Transmittance at 2.25 eV as a function of the thickness of graphitic platelets, and (c) Average number of graphene layers as a function of the fraction f of substrate area covered by the platelets. Dotted line represents the fit $N \approx A \cdot f$, with $A = 120$.

Thermal properties of our films were measured by photothermal deflection spectroscopy (PDS) [25]. In PDS, the heat generated in a weakly optically absorbing thin film by a chopper-modulated light beam diffuses through a transparent photothermal liquid in which the film is embedded [25]. The thermal gradient experienced by the liquid in the proximity of the film can be probed by a laser beam grazing the film surface and

periodically deflected away from the surface by thermal lensing effects. The phase (Δ_{PDS}) and amplitude (A_{PDS}) of the photothermal deflection angle Φ were measured by using a position detector (Thorlabs PDQ8051) attached to a lock-in amplifier (Princeton Instruments 5209). Carbon tetrachloride (CCl_4) was used as a photothermal liquid and the pulsed light beam was obtained from a 1-kW Xe lamp (Sciencetech Inc.) coupled with a mechanical chopper operated at $\omega = 20$ Hz and a Jarrell-Ash 82-497 monochromator. A second photothermal fluid with substantially different thermal properties (FluorinertTM, 3M Canada Co.,) has been used to confirm our thermal measurements with uncertainties within $\pm 5\%$. Five excitation wavelengths from 400 nm to 700 nm were used to check the validity of our PDS measurements. Solving the Fourier equation of heat [25], the independent measurement of Δ_{PDS} and A_{PDS} allowed us to determine the thermal capacitance (C_s) and the thermal diffusivity (D_s) of our thin films by inverting the following expressions:

$$\Delta_{\phi} = \frac{\pi}{2} + \sqrt{\frac{\omega}{2D_s}} \cdot L_y \quad (5.3a)$$

$$A_{\phi} = \frac{1}{n_f} \left| \frac{dn_f}{dT} \right| \cdot \frac{P_0}{\omega \cdot C_s \cdot L_y^2 \cdot L_z} \cdot \sqrt{\frac{D_s}{D_{\text{eff}}}} \cdot e^{\sqrt{\frac{\omega}{2D_s}} L_y} \quad (5.3b)$$

where

$|dn_f/dT|/n_f$ is the temperature coefficient of the refractive index of the photothermal liquid with the units K^{-1} ($4.2 \cdot 10^{-4} \text{ K}^{-1}$ for CCl_4 and $8.7 \cdot 10^{-3} \text{ K}^{-1}$ for FluorinertTM), $D_{\text{eff}}^{-1} = D_s^{-1} + D_f^{-1}$ is the effective diffusivity of the system, which can be defined as the parallel of the thermal diffusivities of the film (D_s) and the photothermal liquid (D_f). Diffusivity has units $\text{m}^2 \cdot \text{s}^{-1}$. P_0 is the power in Watts, of the pulsed light beam reaching the sample, C_s is

the thermal capacitance of the film measured in $\text{J} \cdot \text{m}^{-3} \cdot \text{K}^{-1}$ and L_y and L_z are the width and height of such beam in the directions parallel and perpendicular to the probe laser, respectively with units m.

Once D_s [$\text{m}^2 \cdot \text{s}^{-1}$] and C_s [$\text{J} \cdot \text{m}^{-3} \cdot \text{K}^{-1}$] are calculated by inverting eq. 5.3, the thermal conductivity can be immediately determined as $K_s = C_s \cdot D_s$ [$\text{W} \cdot \text{m}^{-1} \cdot \text{K}^{-1}$]. Our measurements indicate that, in the specific case of our TCCF, D_s is much larger than both D_f and the thermal diffusivity of the substrate. Therefore, heat is expected to mainly propagate along the liquid/TCCF interface in our system and, in our configuration, PDS mainly measures the ordinary component of the thermal conductivity, along the surface of the films. This is an important point since thermal conductivity of graphene is highly anisotropic, with an extraordinary component orthogonal to the surface which is generally lower than the ordinary components [13]. The boundary thermal resistance between the TCCF and the glass substrate is also expected to be large in our case, since the large mismatch in phonon density of states between graphene [26] and glass [27] has to be considered. This is an additional indication that the values of K_s measured in our study mostly refer to in-plane heat conduction parallel to the platelet surface. Figure 5.4c and d show that K_s decreases with increasing f and N for the set of samples considered in this study.

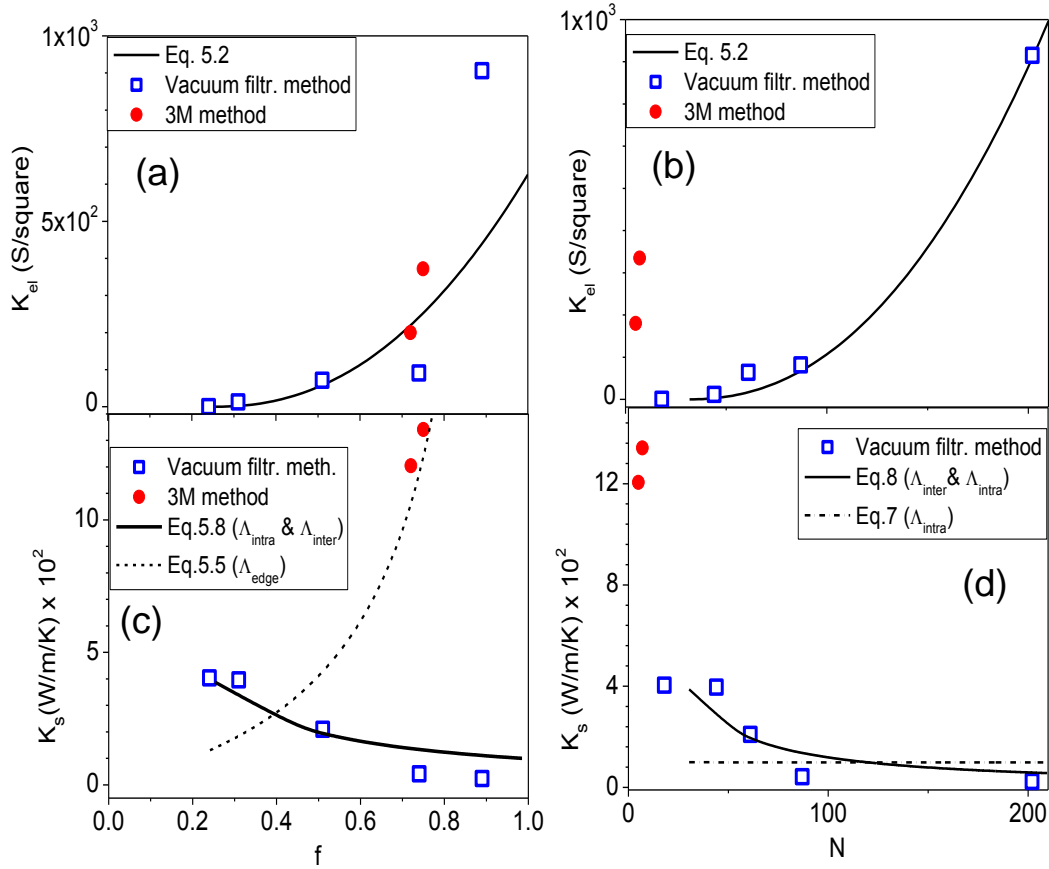


Figure 5.4 (a) Electrical conductivity (K_{el}) as function of the fraction f of surface area covered by graphene platelets and (b) as a function of number of layers. Solid lines represent simulation of experimental data according to eq. 5.2. (c) Thermal conductivity (K_s) determined by PDS as function of the fraction f of surface area covered by graphene platelets and (d) as a function of number of layers, N .

5.4 Results and discussion

Several physical phenomena may affect the thermal conductivity in graphene-based thin films, including: i) phonon scattering due to overlap of multiple graphene layers ii) phonon scattering within an individual graphene layer, and iii) phonon scattering due to the presence of edge and voids. These effects can be superimposed according to the Matthiassen's rule,

$$\frac{1}{\Lambda} = \frac{1}{\Lambda_{\text{intra}}} + \frac{1}{\Lambda_{\text{inter}}} + \frac{1}{\Lambda_{\text{edge}}} \quad (5.4)$$

where Λ is the effective mean free path (MFP), Λ_{edge} is the phonon MFP due to scattering processes from platelet edges and voids, Λ_{intra} is the MFP due to phonon-phonon scattering within an individual graphene layer, and Λ_{inter} is the MFP due to out-of-plane phonon-phonon scattering between overlapped graphene platelets or stacked graphene layers. Expectably, the role of Λ_{intra} in eq. 5.4, is negligible in our films, because the measured thermal conductivity is much lower than in individual platelets of graphene or thin graphite [25,32].

Scattering of phonons from the edges of the platelets affects the thermal conductivity of TCCF only if Λ_{edge} is smaller than the shortest of Λ_{intra} and Λ_{inter} . Using simple geometrical arguments [28], it can be shown that $\Lambda_{\text{edge}} = d_0 / [4 \cdot (1-f)]$, where $d_0 = d(f_0)$ is the typical size of a void at the percolation threshold, which is independent of f and is only determined by the spatial scale of the system and, therefore, by the typical lateral size of the platelets. If the thermal conductivity were limited by the edges of the platelets, we would then have $\Lambda \approx \Lambda_{\text{edge}}$ and

$$K_s = \frac{1}{2} \cdot c \cdot v \cdot \Lambda \approx c \cdot v \cdot d_0 \cdot f / [8 \cdot (1-f)], \quad (5.5)$$

where $v = 1.86 \cdot 10^4$ m/s [20] is the in-plane velocity of sound in graphite. Eq. 5.5 is represented by the dotted line in Figure 5.4c and is able to reproduce our experimental data for the samples prepared by 3M Canada Co., but not for the vacuum-filtrated films prepared using the method of Lotya *et al.* [11]. Specifically, eq. 5.5 predicts that K_s increases with increasing f and this is the opposite of what we experimentally observe in such films. This observation suggests that platelet edges play a negligible role in

controlling the thermal conductivity in vacuum-filtrated samples [11], which is also consistent with platelet diameters of a few μm in these films, a length consistent with our AFM images in Figures 5.2a-b and, expectably, larger than Λ_{intra} . Ghosh *et al.* [14] determined $\Lambda_{\text{intra}} = 775 \text{ nm}$ in relatively ideal graphene flakes, so it should be even lower in our non-ideal platelets. Conversely, the contribution of platelet edges to the thermal conductivity can be expected to be important in the samples prepared by 3M Canada Co. because they have smaller platelets and smaller sizes of voids, as indicated by the AFM image in Figure 5.2c.

The decrease in thermal conductivity observed in the vacuum filtrated samples prepared by the method of Lotya *et al.* [11], can be modeled assuming that the actual phonon MFP in such films is controlled by a combination of inter-platelet and intra-platelet processes, consistently with the Klemens model [20] for the thermal conductivity of N-layer graphene. In this model, the thermal conductivity is limited by out-of-plane vibrational modes coupling neighboring graphene planes, and can be expressed by the following relationship:

$$K_{s,N} = B \cdot \ln[\omega_D/\omega_c(N)] \quad (5.6)$$

where $B = \rho \cdot v_f^4 / (\gamma^2 \cdot \omega_D \cdot T) \approx 780 \text{ W m}^{-1} \text{ K}^{-1}$ [20] is a constant determined by the lattice temperature ($T = 300 \text{ K}$), the density of graphite ($\rho = 2.25 \text{ g cm}^{-3}$), the Debye frequency ($\omega_D = 2.88 \cdot 10^{13} \text{ Hz}$) and the Gruneisen parameter ($\gamma = 2$).

In eq. 5.6, $\omega_c(N)$ represents the cutoff frequency at which the phonon spectrum changes from two-dimensional to three-dimensional and Umklapp processes from inter-layer phonons start to affect the lattice thermal conductivity [20]. At decreasing number of stacked layers, softer inter-layer phonon modes are available, which give rise to a

lower cutoff frequency. For ideal platelets, $\omega_C(N \rightarrow \infty) = 2.51 \cdot 10^{13}$ Hz in bulk graphite and considerably decreases at decreasing number of layers, which explains the subsequent increase of K_s at decreasing N from graphite to bilayer graphene [20]. While we assume this model to still remain qualitatively valid in our samples, we expect that the values of $\omega_C(N)$ must be higher (or even much higher) in our case, because stacking in vacuum-filtrated thin films mainly occur as a consequence of re-layering of few-layer graphene platelets during the filtration process [23]. This leads to a substantial amount of stacking imperfections that may significantly increase the onset frequency for out-of-plane Umklapp phonon scattering processes.

In order to predict how the thermal properties of our films depend on N , we adopted a model that was recently introduced by Tan *et al.* [29] for describing how the frequencies of out-of-plane, inter-layer phonon modes of N -layer graphene decrease at decreasing number of layers. Accordingly to this model, by assuming that a graphitic stack is formed by N layers connected by a series of springs, the cutoff frequency for the out-of-plane phonon modes increases from $\omega_2 = \omega_C(N=2)$ to $\omega_C(N \rightarrow \infty)$ following the relationship $\omega_C(N) = \omega_2 \cdot [1 + \cos(\pi/N)]^{1/2}$ [27]. By replacing this expression into eq. 5.6, we obtain

$$K_{s,N} = B \cdot \ln \frac{\omega_D}{\omega_2 \cdot \sqrt{1 + \cos(\pi/N)}} \quad (5.7)$$

where $K_{s,N}$ in eq. 5.7 expresses the thermal conductivity of a sufficiently large graphitic platelet formed by N layers of graphene. While this expression may be suitable to describe the thermal properties of a relatively uniform film with N graphene sheets, it does not account for the fact that our films are highly non uniform in thickness, since

they are formed by a large number of partially overlapped platelets. Subsequently, eq. 5.7 is found to not satisfactorily fit our experimental data, as shown in Figure 5.4d.

We expect that junctions between platelets are critical in determining the thermal properties of our vacuum filtrated films since, according to eq. 5.7, the bottleneck for thermal conductivity rests in the regions where platelets overlap and form a stack of $2N$ graphene layers at their junctions. Junctions possess a lower thermal conductivity than individual platelets, since eq. 5.7 indicates that $K_{s,2N} < K_{s,N}$. Consequently, a model suitable of describing the thermal properties of our vacuum-filtrated TCCF must include: i) a fraction f_0 of surface area of the substrate occupied by individual platelets, ii) an additional fraction of surface where platelets overlap, for a total thickness of $2N$ layers ($f-f_0$), and iii) a complementary fraction of voids ($1-f$). Under these assumptions, highlighted in Figure 5.5a, the effective thermal resistivity of our film is the series of the resistivity from areas where platelets do and do not overlap: $1/K_{s,eff} = (f-f_0)/K_{s,2N} + f_0/K_{s,N}$. In the case of vacuum-filtrated films, where $N \approx A \cdot f$, we obtain:

$$\frac{1}{K_{s,eff}} = \frac{N/A - f_0}{K_{s,2N}} + \frac{f_0}{K_{s,N}} = \frac{1}{B} \cdot \left(\frac{N/A - f_0}{\ln(\omega_D/\omega_2) - 1/2 \cdot \ln[1 + \cos(\pi/2N)]} + \frac{f_0}{\ln(\omega_D/\omega_2) - 1/2 \cdot \ln[1 + \cos(\pi/N)]} \right) \quad (5.8)$$

where the second equality in eq. 5.8 is obtained by substituting eq. 5.7 in the first equality. As shown in Figures 5.4c and 5.4d, eq. 5.8 reproduces well the trend of the thermal conductivity in films with “large” N -layer graphene platelets as a function of N , with only one adjustable parameter, the cutoff frequency for out-of-plane modes in bilayer graphene, which is set as $\omega_2 = 1.8 \cdot 10^{13}$ Hz.

As highlighted by Nika *et al.* [31], it is important to remind that $\omega_C(N)$ and, consequently, ω_2 have nothing to do with the low-bound frequency for an infinite single-

layer graphene sheet, which is higher and it is generally made to coincide with the out-of-plane optical phonon branch in graphene ($\omega_B = 2.88 \cdot 10^{12}$ Hz). ω_B is expected to significantly increase for decreasing lateral size d_0 of the graphene platelets, as $\omega_B = [(m \cdot v_f \omega_D) / (4\pi \cdot \gamma^2 \cdot k_B T \cdot d_0)]^{1/2}$, where m is the carbon ion mass. However, for values of $d_0 \approx 5\text{-}10 \mu\text{m}$ which are observed by AFM in the films grown with the method of Lotya *et al.* [11], ω_B is still at least one order of magnitude lower than ω_2 . This clearly indicates that the thermal conductivity of these films is limited by the presence of N-layer graphene platelets and their junctions, not by domains of single-layer graphene with finite size.

Recent investigations have also led to suggest that the Gruneisen parameter ($\gamma = 2$) originally proposed by Klemens for graphite [20] may be overestimated in few-layer graphene and thin multilayer graphite and that lower values (down to $\gamma = 1.8$ for the longitudinal branch and $\gamma = 0.75$ for the transversal branch) are more likely [30]. A smaller value of γ , which leads to a change of the value of B in eq. 5.8, can be adjusted in our model by using a different value of ω_2 , up to 50% smaller. Therefore, while our model is not able to offer a conclusive determination of the Gruneisen, it is flexible enough to accommodate some variations of such parameter. Specifically, eq. 5.8 is well suited for describing the thermal conductivity behavior of non-uniform TCCF films with thick junctions between partially overlapped platelets formed by N-layer graphene. This equation predicts a decrease of the thermal conductivity with increasing N that is much stronger than in eq. 5.7 and is in good agreement with the experiment.

By eliminating N from eqs 5.2 and 5.8, a relationship between the electrical and thermal conductivity in our films can be established, as shown in Figure 5.5b. The quality of the obtained best fits is remarkably good considering that only one free parameter, ω_2 ,

is involved. An analytical relationship correlating $K_{s,eff}$ and K_{el} can also be established from equations 5.8 and 5.2, by developing the last term of eq. 5.8 in Taylor series:

$$\frac{1}{K_{s,eff}} \approx \frac{\ln(\omega_2/\omega_D)}{B} \left[\left(\frac{K_{el}}{S_0} \right)^{1/x} + f_0 \right] \quad (5.9)$$

Eq. 5.9 demonstrates that, at the opposite of what is happening in electron-dominated thermal conductors such as ITO, the thermal conductivity of our vacuum-filtrated TCCF decreases with increasing electrical conductivity. This behavior is extremely peculiar for transparent and conducting thin films and may have relevant applications in thermoelectric devices.

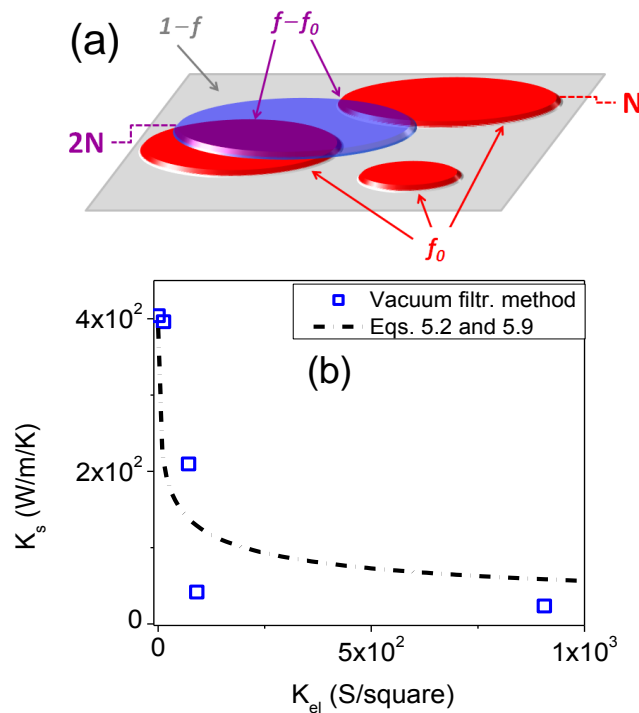


Figure 5.5 (a) Schematic of the film model used to calculate the thermal conductivity as in eq. 5.8, with graphitic platelets of N layers and $2N$ -layer thick junctions between platelets. (b) Thermal conductivity vs. electrical conductivity. The dotted line is a simulation assuming the model given by eqs. 5.2 and 5.8 and leading to simplified eq. 5.9.

5.5 Summary

We measured the optical, electrical and thermal properties of two different sets of TCCF. For vacuum-filtrated TCCF [11], our results showed an increase in electrical conductivity and a decrease in optical transmittance and thermal conductivity with increasing film thickness. We have established a relationship between the electrical and thermal conductivity of vacuum-filtrated TCCF, which is suitable to be extended to a large class of graphene-based thin films. Our model suggests that, for sufficiently “large” graphene platelets, the most important role in determining the thermal conductivity of TCCF is played by the number of overlapped graphene layers at the junctions between neighboring platelets. In its simplest form, our model is not suited for graphene-based thin films in which platelets are “small” with respect to the phonon MFP, because it is based on the assumption that the thermal properties are determined by phonon scattering at the overlap between neighboring platelets (i.e. it assumes $\Lambda \approx \Lambda_{\text{intra}}$ in eq. 5.4). However, we have also extended the model to “small” platelets by including the effects of platelet edges, as seen in Figure 5.4c, showing that the thermal conductivity of the films supplied by 3M Canada Co. can be described by assuming $\Lambda \approx \Lambda_{\text{edge}}$ as in eq. 5.5. Our models can be used for the optimization of the tradeoff between electrical, optical and thermal properties of TCCF and are critical to design graphene-based thin films for specific applications in which electrical conductivity, optical transparency and ability to evacuate heat are simultaneously required.

References

- [1] A. A. Balandin, S. Ghosh, W. Bao, I. Calizo, D. Teweldebrhan, F. Miao and C. N. Lau, *Nano Lett.*, **8** (2008) 902.
- [2] A. K. Geim and K.S.Novoselov, *Nat. Materials*, **6** (2007) 183.
- [3] R. R. Nair, P. Blake, A. N. Grigorenko, K. S. Novoselov, T. J. Booth, T. Stauber, N. M. R. Peres and A. K. Geim, *Science*, **320** (2008) 1308.
- [4] C. Lee, X. Wei, J. W. Kysar and J. Hone, *Science*, **321** (2008) 385.
- [5] K. S. Novoselov, A. K. Geim, S. V. Morozov, D. Jiang, Y. Zhang, S. V. Dubonos, I. V. Grigorieva, A. A. Firsov, *Science*, **306** (2004) 666.
- [6] P. W. Sutter, J. Flege and E.A. Sutter, *Nat. Materials*, **7** (2008) 406.
- [7] A. Reina, X. Jia, J. Ho, D. Nezich, H. Son, V. Bulovic, M. S. Dresselhaus and J. Kong, *Nano Lett.*, **9** (2009) 30.
- [8] X. Li, Y. Zhu, W. Cai, M. Borysiak, B. Han, D. Chen, R. D. Piner, L. Colombo and R. S. Ruoff, *Nano Lett.*, **9** (2009) 4359.
- [9] A. Dato, V. Radmilovic, Z. Lee, J. Phillips and M. Frenklach, *Nano Lett.*, **8** (2008) 2012.
- [10] X. Li, G. Zhang, X. Bai, X. Sun, X. Wang, E. Wang and H. Dai, *Nat. Nanotechnology*, **3** (2008) 538.
- [11] M. Lotya, Y. Hernandez, P. J. King, R. J. Smith, V. Nicolosi, L.S. Karlsson, F. M. Blighe, S. De, Z. Wang, I. T. McGovern, G.S. Duesberg and J.N. Coleman: *J. Am. Chem. Soc.*, **131** (2009) 3611.
- [12] F. Sharifi, R. Bauld, M.S. Ahmed and G. Fanchini, *Small*, **8** (2012) 699.
- [13] A. A. Balandin, *Nat. Materials*, **10** (2011) 569.

- [14] S. Ghosh, W. Bao, D. L. Nika, S. Subrina, E. P. Pokatilov, C. N. Lau and A. A. Balandin *Nat. Materials*, **9** (2010) 555.
- [15] A. Yu, P. Ramesh, M.E. Itkis, E. Bekyarova and R. C. Haddon, *J. Phys. Chem. C*, **111** (2007) 7565.
- [16] K. M. F. Shahil, A. A. Balandin, *Nano Letters*, **12** (2012) 861.
- [17] K. M. F. Shahil, A. A. Balandin, *Solid State Comm.*, **152** (2012) 1331.
- [18] D. S. Ginley and J. D. Perkins, *Handbook of Transparent Conductors*. New York-Heidelberg: Springer; 2010, p-110.
- [19] Z. Yan, G. Liu, J. M. Khan, A. A. Balandin, *Nat. Comm.*, **3** (2012) 827.
- [20] P. G. Klemens, *Int. Journal of Thermophysics*, **22** (2001) 265.
- [21] J. R. Brown. *J. Chem. Educ.* **34** (1957) 165.
- [22] Z. Wu, Z. Chen, X. Du, J. M. Logan, J. Sippe;, M. Nikolou, K, Kamaras, J. R. Reynolds, D. B. Tanner, A. F. Hebard and A. G. Rinzler, **305** (2004) 1273.
- [23] G. Eda, G. Fanchini and M. Chhowalla, *Nat. Nanotechnology*, **3** (2008) 270.
- [24] L. Hu, D. S. Hecht, and G. Gruner, *Nano Letters*, **4** (2004) 2513.
- [25] S. Ezugwu, M. S. Ahmed, R. Bauld, R. Divigalpitiya, G. Fanchini, *Thin Solid Films*, **534** (2013) 520.
- [26] J. C. Charlier, P. C. Eklund, J. Zhu, A. C. Ferrari, *Topics in Applied Physics Series*, **111** (2008) 673.
- [27] R. Shuker and R. W. Gammon, *Phys. Rev. Lett.*, **25** (1970) 222.
- [28] A. Minnich and G. Chen, *Appl. Phys. Lett.*, **91** (2007) 073105.

- [29] P. H. Tan, W. P. Han, W. J. Zhao, Z. H. Wu, K. Chang, H. Wang, Y. F. Wang, N. Bonini, N. Marzari, G. Savini, A. Lombardo, and A.C. Ferrari, *Nat. Materials*, **11** (2012) 294.
- [30] D. L. Nika, S. Ghosh, E. P. Pokaitilov, A. A. Balandin, *Appl. Phys. Lett.*, **94** (2009) 203103.
- [31] D. L. Nika, E. P. Pokaitilov, A. A. Balandin, *Phys. Status Solidi B*, **248** (2011) 2609.
- [32] M. S. Ahmed, S. Ezugwu, R. Divigalpitiya, G. Fanchini, *Carbon*, **61** (2013) 595.

Chapter 6

6 Thermophysical properties of thin film nanocomposites of ribonucleic acid and graphene nanoplatelets

Photothermal deflection spectroscopy (PDS) is introduced as a novel technique for measuring the thermophysical properties of transparent and conducting thin films made by few-layer and multi-layer graphene-like platelets. PDS is utilized for the investigation of thin film composites of ribonucleic acid (RNA) and graphene-based materials in which highly electrically insulating (RNA) and highly electrically conducting (graphene-like) regions are mixed at the nanoscale. Effect of RNA on the thermal conductivity of thin films of RNA and graphene-like platelets nanocomposites is investigated.

6.1 Introduction

The peculiar properties of graphene can be utilized by incorporating small quantities of graphene in other materials because thermophysical properties of single-layer graphene are retained, to a large extent, in thin multilayer graphite-like materials [1]. Graphene-based composites that are obtained by mixing small quantities of graphene into other materials have also shown improvement in their respective properties. Graphene-based nanocomposites are attractive because of their nanostructure and extraordinary properties [2,3], and have great potential as new energy materials to be used in Lithium ion batteries, in supercapacitors, and transparent and conducting electrodes in solar cells [4]. Electrical conductivity [5], mechanical strength [6,7] and thermal stability [8] of graphene-filled polymers have shown a significant enhancement. Graphene-based nanocomposites do not required precise control of size and position of graphene in the

composite instead a homogeneous distribution of relatively similar flakes is required. Incorporation of small quantities of graphite-like or graphene-like nanoplatelets into non-thermally conducting resins significantly improves the thermal conductivity of these composites [9-12]. Thermal conductivity in graphite and graphene-based samples has been measured by Raman optothermal [13,14] and electrical methods [15,16]. In electrical methods in which heat is supplied via electrical current, for instance the 3ω method [16], a strip of metal is deposited on the sample which serves as a heater as well as a thermistor. However, the usefulness of these techniques is debatable in inhomogeneous thin films in which highly electrically conducting and highly electrically insulating regions are mixed, because electrical-based techniques may overestimate the contribution to the thermal conductivity from the electrically conducting portions of the sample.

Biological applications are an area in which graphene-based nanocomposites have the potential to play a critical role due to the excellent biocompatibility of graphitic and graphene-based materials [17]. A host of devices have been proposed, including biosensors [9] and scaffolds for bone tissue growth [18]. Specifically, our group has devised a method to prepare thin films based on few layer graphene and Ribonucleic Acid (RNA) suitable for biological applications [17]. Thermal properties are extremely important for these films in light of such applications, but have not been studied so far. For instance, the distribution of heat is critical for incubating living cells and for the electrical performance of biosensors. In general, the thermal properties of graphene and graphite-based nanocomposites designed for biological applications have received little attention to date because of the above mentioned difficulties in accurately measuring the

thermal conductivity of these normally inhomogeneous thin film materials.

Photothermal deflection spectroscopy (PDS) [19] is introduced as a suitable technique for measuring the thermophysical properties of nanostructured thin films made by few-layer graphene and Ribonucleic acid (RNA). PDS is a thermo-optical technique that can be used to investigate a number of properties of thin solid films by embedding the sample into a photothermal fluid, which can be defined as a fluid that possess a strong temperature coefficient of the refractive index. PDS is based on the mirage effect, for which a “probe” light beam, traveling through a transparent photothermal fluid, is deflected by thermal lensing effects at the interface between the fluid and the surface of the measured sample, as a consequence of sample heating due to light absorption from a modulated “pump” light beam and the subsequent heat transfer to the non absorbing fluid. PDS does not require any electrical heating of the sample. It is a contactless technique that is well suited to non-destructively characterize thin films on which the deposition of contacts may prevent the final use.

We demonstrate that PDS measurements compare reasonably well with the 3ω method in relatively homogeneous samples, in which 3ω is expected to offer relatively accurate estimates of the thermal conductivity. We show that, at any specific proportion of RNA and graphene platelets, a correlation exists between the thermal properties of the films and the fraction of substrate area that is coated by the platelets. We explain this correlation in the framework of a theoretical model, for which the thermal properties of the graphene platelets are described by a modified version of the Klemens model [20] for few-layer graphene using model for interlayer phonon model of Tan *et al.* [21] and the RNA phase is considered as an electrically and thermally insulating impurity that reduces

the effective thermal conductivity of the nanocomposite in the films. The decrease of thermal conductivity with increasing RNA content in the films is consistent with the predictions of the modified effective medium approximation [22,23] for RNA as an inclusion in the matrix of graphene platelets.

6.2 Experimental

6.2.1 Sample preparation

Transparent and conducting graphene-RNA nanocomposite thin films have been prepared using a solution based method that was originally developed by our group [17]. Specifically, it was shown [17] that two different types of RNA extracted from *torula utilis* are able to exfoliate graphite in water and produce suspensions of few-layer graphene flakes: type VI RNA (Cat. no. 109K1389, Aldrich Inc.) tends to form aggregates and is suitable for the exfoliation of nano-crystalline graphite (n-G, Cat. no. MKBD6452, Aldrich Inc.), while monodispersed type IX RNA (Cat. no. 129K1222, Aldrich Inc.) is suitable for the dispersion of graphene flakes obtained from microcrystalline graphite (mic-G Cat. no. MKBB1222, Aldrich Inc.). In ref. 17 we also discuss that n-G is not compatible with type IX RNA and mic-G cannot be exfoliated by type VI RNA.

For the present study, three different suspensions of graphene-based material in aqueous solutions of RNA were prepared. We prepared a first suspension by dispersing n-G without any preliminary treatment in an aqueous solution at 0.6 mg/mL of type VI RNA. To prepare the second suspension, n-G was pre-treated in an acid mixture ($\text{H}_2\text{SO}_4:\text{HNO}_3 = 3:1$) which was followed by a second treatment in Piranha solution [24]; the as treated graphite flakes were subsequently recovered on 400-nm pore size filter

membranes, washed with deionized water, and re-dispersed in an aqueous solution of 0.6 mg/mL type VI RNA. A third suspension was prepared by dispersing, mic-G (without any preliminary treatment) in an aqueous solution of 0.6 mg/mL type IX RNA. In all three suspensions the ratio of RNA and graphitic material was kept constant at 10:1. The suspensions were sonicated for 4 hrs in an ice bath, left to sediment overnight at 2°C in a beaker and were subsequently centrifuged at 6000 rpm for 1 hr.

Using the supernatant from the centrifugation process, a set of transparent and conducting thin films formed by RNA and graphene platelets was prepared from each of the three suspensions by means of the vacuum-filtration technique originally developed by Wu *et al.* [25] for carbon nanotubes networks and subsequently adapted by Eda *et al.* [26] for graphene-based thin films. With this technique, variable amounts of suspensions of graphene platelets and RNA were filtered through 0.5-inch diameter nitrocellulose filter membranes (MCE, Millipore). From each suspension, we prepared a set of five thin films on their membranes by varying the filtration volume from 5 mL to 25 mL for n-G suspensions in type VI RNA and from 30 mL to 70 mL for mic-G suspensions in type IX RNA. The filter membranes loaded with the RNA and graphene platelets thin films were subsequently transferred onto optical-grade glass substrates and dried under load. Consecutive acetone and methanol baths were used to etch the membranes leaving behind RNA/graphene thin film nanocomposites on their substrates.

We have previously shown [17] that graphene surfaces in n-G/RNA-VI nanocomposites are relatively free from RNA which tends to segregate and adhere to graphitic flakes only in the correspondence of specific, presumably defective regions, as shown in Figure 6.1a. Conversely, nanocomposites from type IX RNA and mic-G are

formed by graphene flakes that are completely enveloped in RNA, as demonstrated in Figure 6.1b. Instead, the differences between films of the same set, but prepared at a different filtration volume are in the amount of suspension filtered, which leads to different film thicknesses and to different fractions of substrate area which are covered by RNA and graphene platelets.

The thicknesses of our films and the fraction of substrate area covered by RNA and graphene platelets were calculated from a large number of 50 μm X 50 μm atomic force microscopy (AFM) micrographs of the films. AFM images were recorded using a Witec Alpha 300S microscope operating in tapping-mode. To measure the thickness, sections of the films in the proximity of a tranche were measured by AFM. The fraction f of substrate area covered by graphene platelets was automatically calculated from the AFM images, using ImageJ [27] an image processing software that determines the contours of the outstanding features in the AFM topography at a user selected z -axis level. For our calculations of f , the z -axis level was adjusted at half of the maximum thickness recorded in the AFM image.

Energy dispersive X-ray (EDX) spectroscopy was used to analyze the chemical composition of our thin films. A Zeiss 1540 XB scanning electron microscope (SEM) fitted with X-ray detector for elemental analysis (Oxford Instruments) was used to investigate our films on Si substrates. RNA fibers are formed by nucleotides: Uracil (U), Guanine (G), Adenine (A) and Cytosine (C) [28]. Each nucleotide of RNA contains a phosphate (HPO_4^-) group. RNA contains $9 \pm 1\%$ Wt of phosphorous [29] so the amount of RNA in the film was quantified from the phosphorous content found in the samples by

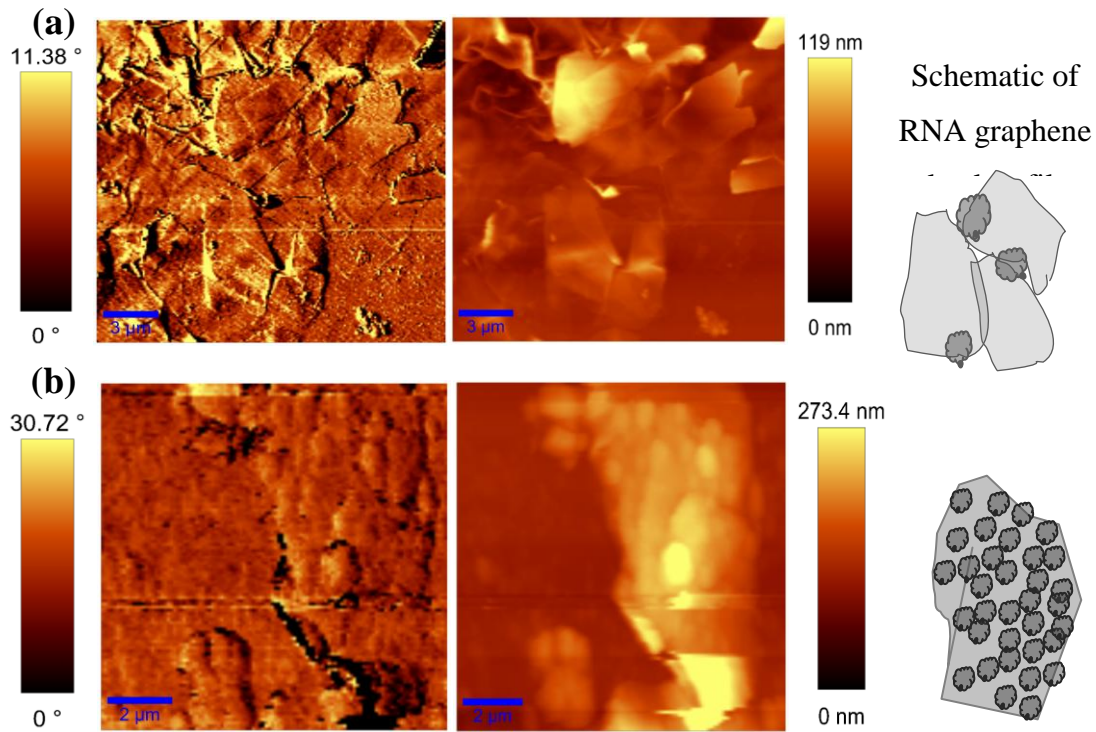


Figure 6.1 AFM phase and topography images of films made by (a) thinner graphene platelets of pre-treated n-G that is mostly free from RNA-VI and (b) thicker graphene platelets of mic-G which are mostly covered by RNA-IX that makes an insulating cover.

EDX. An SEM image and EDX spectrum of thin film of RNA/graphene platelets nanocomposite are shown in Figures 6.2(a) and 6.2(b) respectively. RNA content was estimated using the phosphorous content in the EDX spectrum and assuming that its sole source is RNA content in the sample. In EDX spectrum, carbon content of the sample includes carbon from both graphene and RNA. Based on the chemical composition, the contribution of carbon from RNA is found to be 0.52% wt, out of the total carbon content of 67.37% wt. RNA content was estimated from the phosphorous content in the EDX spectrum using the relation,

$$\text{RNA} = \left[\frac{P_{\text{EDX}} \cdot (100 / P_{\text{RNA}})}{C_{\text{EDX}} - (2.17 \cdot P_{\text{EDX}})} \right] \text{ wt\%} \quad (6.1)$$

where P_{EDX} is weight percent of phosphorous (assuming that its sole source is RNA content in the sample) and C_{EDX} is weight percent of carbon, measured by EDX, and P_{RNA} is phosphorous content in RNA provided by supplier[29]. Due to the nature of the vacuum filtration process all of the samples made from the same suspension are expected to possess the same RNA to graphene ratio.

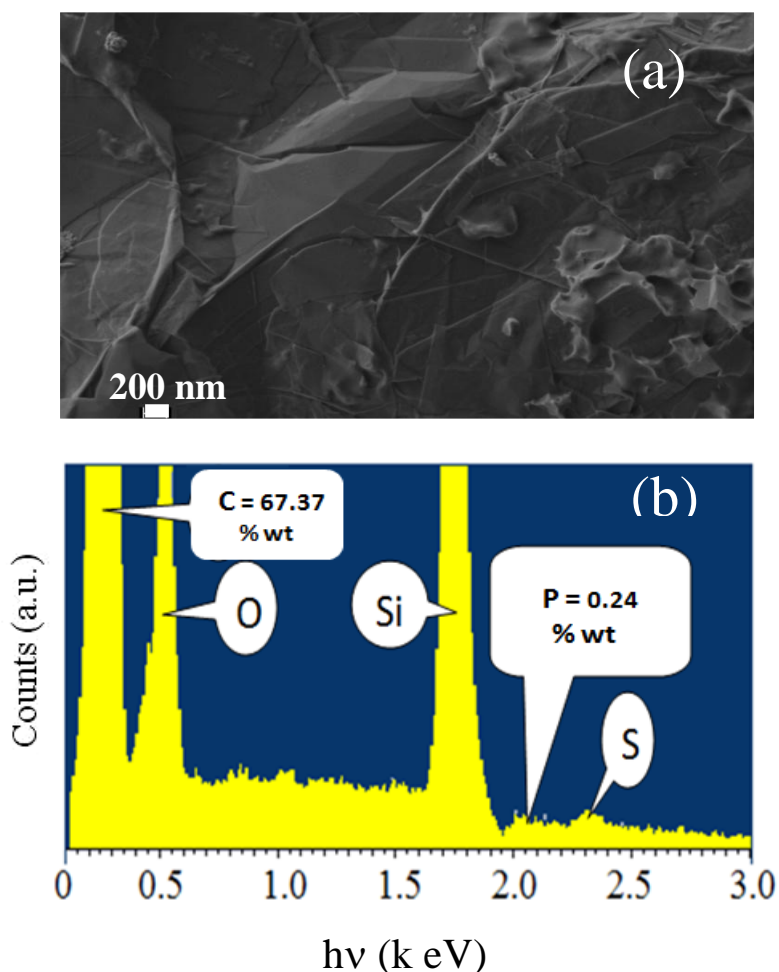


Figure 6.2 (a) SEM image and (b) EDX of a RNA/n-G nanocomposite thin film. Presence of Phosphorous in the EDX verifies the presence of RNA in the film and it is used to quantify the RNA content in the nanocomposite.

For the study of effect of RNA content on the thermal conductivity of RNA/graphene platelets thin film, we measured the thermal conductivity of the sample with different RNA fractions at a constant graphene platelets fraction. RNA content was increased by drop casting RNA suspension on a film with moderate fraction of substrate area coverage. PDS data were collected after each drop and thermal conductivity was calculated. Measurements with increasing RNA content were continued until the thermal conductivity value reached a plateau with minimum value of thermal conductivity ($\sim 20 \text{ W.m}^{-1}.\text{K}^{-1}$) of RNA/graphene platelets nanocomposite.

6.2.2 Thermal conductivity measurements

PDS setup used to measure the thermal conductivity is illustrated in Figure 2.2a (Chapter 2). The sample was placed in a photothermal fluid (CCl_4) in a quartz cuvette and illuminated by a modulated light “pump” beam. Heat generated in the sample as result of light absorption and subsequent thermalization, flow from the sample to the adjoining photothermal fluid resulting in a local change in refractive index of the fluid. Another low intensity laser “probe” beam passing through the fluid’s refractive index gradient and skimming the sample surface is used to measure the photothermal signal by recording the probe beam deflection with a position detector. Because of the modulated changes in the refractive index and consequently modulated deflection of “probe” beam, the voltage signal of position detector - the photothermal deflection signal has amplitude and phase. The amplitude of photothermal signal depends on the quantity of heat emanating from the illuminated sample. Amount of the heat generated in the sample depends upon amount of light absorbed irrespective of the position of absorption (on surface or within the volume of the sample) and the energy of the incident photon. While the phase of the photothermal

signal, depends upon the localization of the absorption and that how quickly heat spreads in the material. The phase of the photothermal signal depends on the diffusion length of the wave which in turn depends upon the diffusivity of the material and modulation frequency of the pump beam. We have used pump beam with three different wavelengths from 500 nm to 700 nm with a step of 100 nm and modulation frequencies from 5 Hz to 50 Hz with a step of 1 Hz, and measured the amplitude and phase of the PDS signals.

A one dimensional heat conduction model [30,31] was used to find in-plan thermal conductivity of the films, assuming that films are optically and thermally thin. The amplitude and phase of the PDS signal are given by:

$$A_{\varphi} = \frac{1}{n_f} \left| \frac{dn_f}{dT} \right| \cdot \frac{P_0}{\omega \cdot C_s \cdot L_y^2 \cdot L_z} \left(\frac{1 - e^{-\alpha_s \cdot L_x}}{\alpha_s \cdot L_x} \right) \cdot \sqrt{\frac{D_s}{D_{\text{eff}}}} \cdot e^{\sqrt{\frac{\omega}{2D_s}} \cdot L_y} \quad (6.2)$$

$$\Delta_{\varphi} = \sqrt{\frac{\omega}{2 \cdot D_s}} \cdot L_y - \frac{\pi}{2} \quad (6.3)$$

where $|dn_f/dT|/n_f$ is the temperature coefficient of the refractive index for the photothermal liquid (i.e. $4.2 \cdot 10^{-4} \text{ K}^{-1}$ for CCl_4 [32]), $D_{\text{eff}}^{-1} = D_s^{-1} + D_f^{-1}$ is the effective diffusivity of the film-substrate system, which can be defined as a parallel between the thermal diffusivities of the liquid ($D_f = 7.0 \cdot 10^{-8} \text{ m}^2 \cdot \text{s}^{-1}$ for CCl_4 [32]) and the film. In eq. 6.2, C_s , D_s , α_s and L_x indicate the thermal capacitance, thermal diffusivity, optical absorption coefficient and thickness of the film, respectively, while ω and P_0 are the frequency of modulation and the power of the pump beam incident to the sample. In eq. 6.2, the pump beam is assumed to be homogeneous and rectangular and L_y and L_z are the width and height of the beam in the direction parallel and perpendicular to the probe laser, respectively.

Thermal conductivity was also measured by 3ω method [16]. In this method, a metallic line is used both as a heater to heat the sample and as a thermometer to detect the measure the temperature change, as illustrated in Figure 2.9 (Chapter 2). An AC current flowing through the metallic line, at frequency ω , produces heat as a result of Joule heating. The periodic change in temperature of the metallic strip results in a corresponding change in the resistance of the metal line that is determined from the AC voltage drop across the line at 3ω . In order to make the metallic heating line, a 1.2 cm long and 0.5 mm wide aluminum strip was deposited on the sample, by thermal evaporation of aluminum in high vacuum chamber. Sample with aluminum strip, was then loaded into the 3-omega vacuum chamber and the chamber was evacuated in order to prevent the heat loss to the surroundings. AC current with frequency ω was applied across the aluminum strip and the AC voltage drop at 3ω across the two inner contacts was measured and recorded with a lock-in amplifier and subsequently used to calculate the thermal conductivity of the sample by using eq. (2.4).

6.3 Results and discussion

A typical AFM image of a nanocomposite thin film of RNA and graphene platelets is shown in Figure 6.3(a), where platelets covering a large area fraction of the substrate can be observed. An optical image of a very sparse film on a 300 nm SiO_2 coated Silicon substrate is shown in Figure 6.3(b), where few-layer graphene platelets can be noticed. For each set of films, the average thickness and the fraction f of the substrate area coated by the graphene platelets increases with the increasing amount of the suspension filtered, as shown in Figure 6.3(c-f). This is a general characteristic of vacuum filtered graphene thin films because one entire first layer of flakes needs to be formed on the vacuum

filtration membrane before additional flakes deposit on the top of it [25].

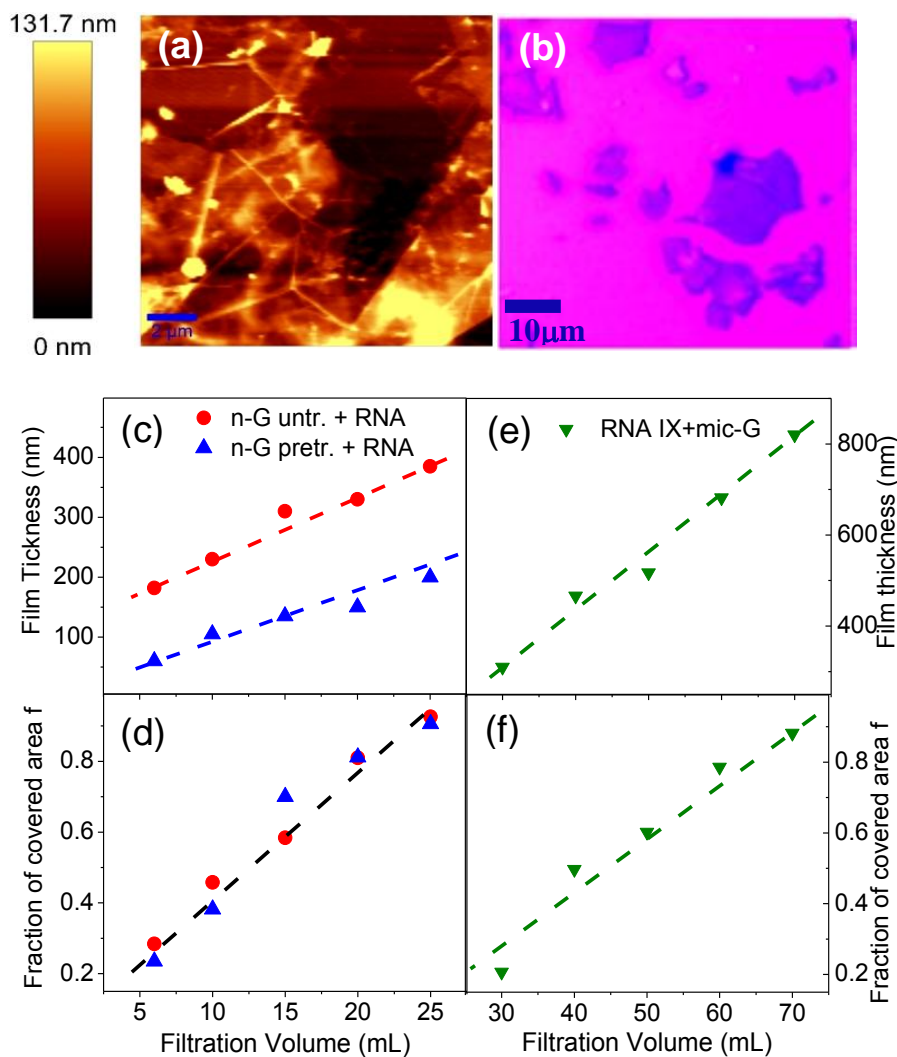


Figure 6.3 (a) AFM topography image of a thick film, (b) Optical image of very sparse film on silicon oxide coated silicon substrate, (c) thickness and (d) fraction of covered area of the films versus the filtration volume of the graphene suspension for sets of samples made from nG. (e) Thickness and (f) fraction of covered area of the films versus the filtration volume of the graphene suspension for the set of samples made from mic-G. It can be seen that films made from treated n-G are thinner than the ones made from untreated n-G while both sets of samples have same fraction of covered area of the substrate.

By comparing the thickness versus filtration volume for different sets of samples in Figures 6.3(c) we notice that films from untreated n-G are, at a constant filtration volume, thicker than the films made from treated n-G. The average number of layers N , determined as a ratio between the film thickness and the thickness of a single layer of graphene, is proportional to f and the proportionality constant $A = N/f$ is an indicator of the quality of the dispersion [31]. For instance, we see that $A = 510$ for the films made from n-G pre-treated with an acid mixture when a better dispersion could be obtained, while it is higher for the set of films from untreated n-G ($A = 892$) and mic-G ($A = 2148$). Therefore, we conclude that the acid treatment of graphite prior to dispersion in an aqueous solution of RNA helped to exfoliate the starting material into thinner flakes of few layer graphene, which is consistent with similar results available in the literature [12,17]. Conversely, at a constant volume of graphene suspension filtered, f is nearly the same for both pre-treated and untreated n-G as shown in Figure 6.3(d). Therefore, mild pre-treatment of n-G represents a useful tool in order to explore the effects of changes of f on thermal conductivity at a constant thickness.

Figure 6.4a shows the amplitude of photothermal deflection for a typical RNA-graphene thin film as a function of the “pump” beam modulation frequency, which is proportional to the quantity of heat generated in the sample and, subsequently, via eq. (6.2), on the total amount of light absorbed through the sample cross section. The amplitude of the PDS signal is expected to indirectly depend on the wavelength of the “pump” light beam via the absorption coefficient of the thin film. From the illuminated region of film, heat diffuses along the sample surface and to the adjoining photothermal fluid and the higher the thermal conductivity the larger the diffusion of heat along the

surface of the sample. Heat is subsequently transferred from the solid surface to the adjoining fluid, which indicates that the amplitude of the photothermal signal, at a constant absorption coefficient of the film, is inversely proportional to the thermal capacitance, as predicted by eq. (6.2). In addition, the shorter the pulses of the “pump” beam, the smaller the quantity of heat that can be stored within the thin film. Therefore, the amplitude of the PDS signal depends on the chopper modulation frequency, as $\omega^{-1} \cdot \exp[(\omega/2D_s)^{1/2} \cdot L_y]$, as predicted by eq.(6.2). In the low frequency regime that is of interest for us, $A \propto \omega^{-1}$. This dependence is fitted in Figure 6.4(a) for a specific sample and the corresponding theoretical behaviour according to eq. (6.2) is shown in Figure 6.4(b) for different values of $L_y/(2D_s)^{1/2}$.

The phase lag of the photothermal signal depends on the thermal diffusivity of the sample, as well as the width of the illuminating “pump” beam, as predicted by eq. (6.3). Depending upon the thermal diffusivity of the material, a thermal wave generated at the sample surface as a consequence of the illumination by a modulated “pump” beam, propagates to the photothermal fluid with a specific time delay. As demonstrated in Figure 6.5(b), if the phase of the PDS signal is plotted as a function of the square root of the modulation frequency, the thermal diffusivity of the sample can be determined from the slope of the resulting linear plot.

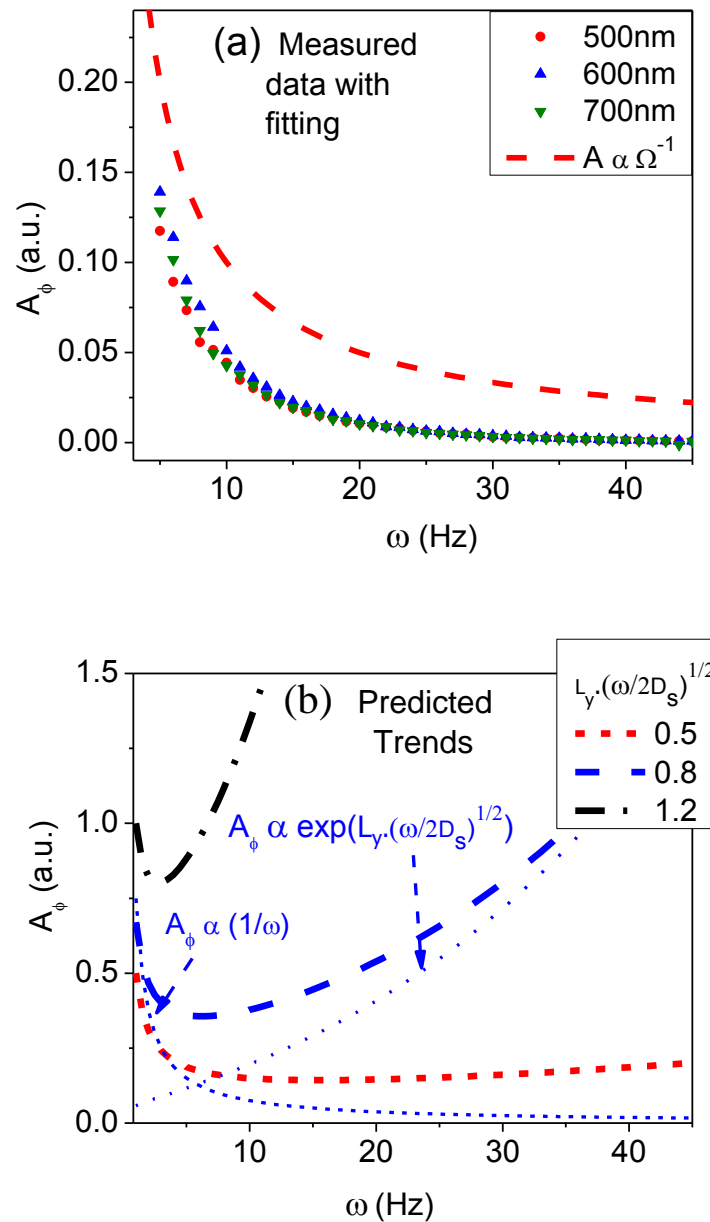


Figure 6.4 (a) Normalized amplitude of PDS signal versus modulation frequency measured at low modulation frequencies and (b) Fit of eq. (6.2) for different values of $L_y/\sqrt{2D_s}$ that depend on thermal diffusivity. $D_s = 5 \cdot 10^{-5} \text{ m}^2 \cdot \text{s}^{-1}$ for our samples, it can be seen that at low frequencies PDS amplitude is inversely proportional to modulation frequency.

Figure 6.6(a) shows the measured thermal conductivity of the three sets of RNA/graphene platelets nanocomposite samples discussed in this paper, and compares them with the pure graphene thin film from ref. 31. It can be seen that at a constant fraction of the substrate area covered by platelets, the thermal conductivity of RNA/graphene platelets nanocomposite is lower than the thermal conductivity of the pure graphene films from Ref. 31 even though the thermal conductivity of our films is still superior to those of many biocompatible coatings. The thermal conductivity decreases with increasing RNA content in the sample; therefore, RNA is assumed to be responsible for this phenomenon. RNA tends to coat the surface and the edges of graphene platelets, as can be seen in our AFM images in Figures 6.1(a) and 6.1(b). Therefore, we assign the decreased thermal conductivity in the presence of RNA to the increased contact thermal resistance between the nearest neighboring graphene-like platelets when they are covered by RNA. This assignment is also corroborated by the observation that the effect of RNA in decreasing the thermal conductivity is more drastic in the films prepared by mic-G, in which our AFM analysis (and Ref. 17) demonstrates that RNA entirely coats the surface of the graphene platelets and, therefore, completely prevents the neighboring graphene platelets from making thermal contact.

We have previously demonstrated [31] that in graphene thin films not containing RNA or other impurities, the thermal conductivity can be limited by the contact resistance at the junctions between two N-layer graphene platelets that behave like a stack of 2N graphene layers and can be written as:

$$\frac{1}{K_{th,eff}} = \frac{f-f_0}{K_{th,2N}} + \frac{f_0}{K_{th,N}} = \frac{1}{B} \cdot \left(\frac{f-f_0}{\ln(\omega_D/\omega_2)^{-1/2} \cdot \ln[1 + \cos(\pi/(2A \cdot f))]} + \frac{f_0}{\ln(\omega_D/\omega_2)^{-1/2} \cdot \ln[1 + \cos(\pi/(A \cdot f))]} \right) \quad (6.4)$$

where $B = \rho \cdot v_f^4 / (\gamma^2 \cdot \omega_D \cdot T) \approx 780 \text{ W m}^{-1} \text{ K}^{-1}$ is a constant determined by the lattice

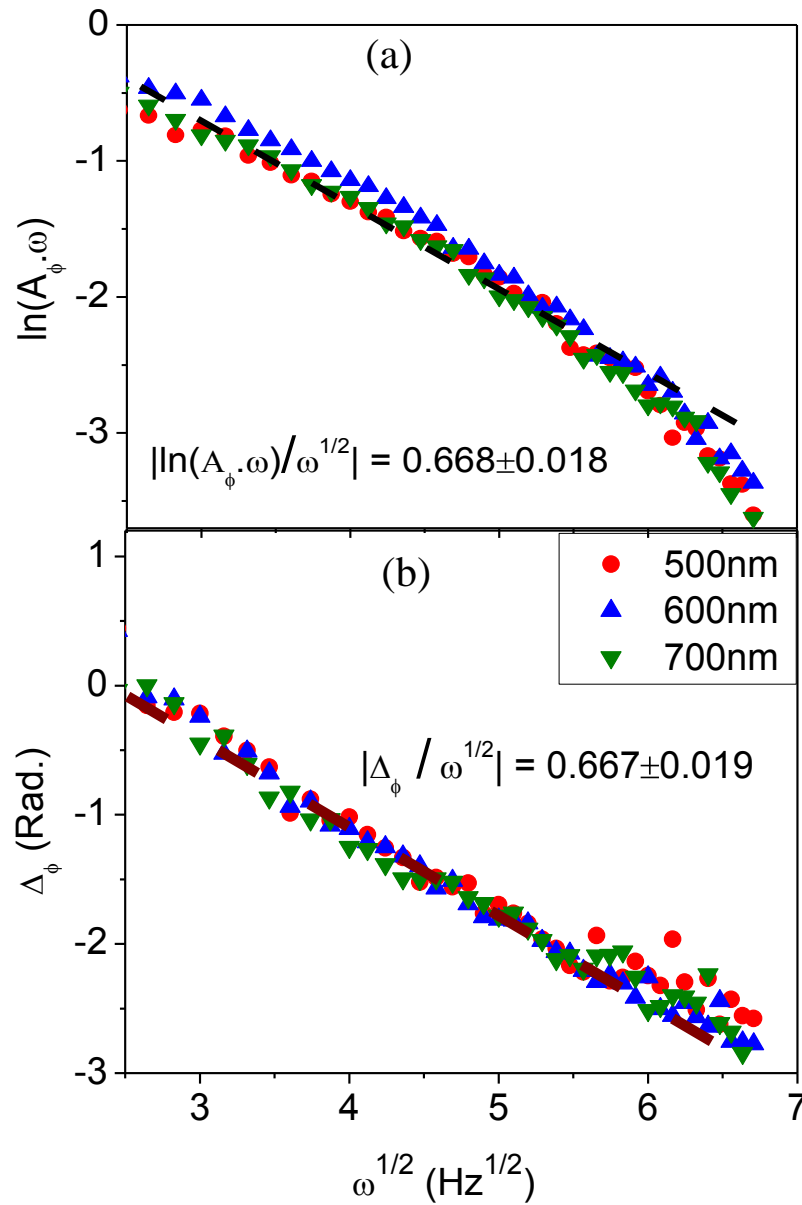


Figure 6.5 (a) Normalized amplitude of PDS signal and (b) phase of PDS signal as function of square root of modulation frequency, for a typical sample. It can be seen that both $\ln(A_\phi \cdot \omega)$ and phase lag decrease linearly with square root of frequency.

temperature T , the density of graphite $\rho = 2.25 \text{ g}\cdot\text{cm}^{-3}$, sound velocity $v_f = 18.6 \text{ km s}^{-1}$ and the Gruneisen parameter $\gamma = 2$ [20]. The Debye frequency $\omega_D = 2.88 \cdot 10^{14} \text{ Hz}$ and $\omega_c(N)$ is the cut-off frequency for the out-of-plane phonon modes that depends on the number of layers in the graphitic material.

However, the presence of RNA in the films affects the thermal conductivity in two ways: (i) by increasing the thermal contact resistance between the nearest neighboring graphene-like platelets of the RNA-graphene nanocomposite, which, we assume, is the dominant factor at low RNA content and (ii) by making thermally insulating aggregates (analogous to voids) in the matrix of the graphene. To investigate the effect of varying fractions of RNA on the thermal properties of our films, a set of thermal conductivity data for constant content of n-G and an increasing amount of RNA is shown in Figure 6.6, and it can also be seen that the thermal conductivity decreases significantly from 4% to 30%wt RNA content but becomes nearly constant at higher RNA contents. It can be noticed that RNA content above 40%wt in the nanocomposite significantly deteriorate the thermophysical properties. Interestingly, the critical concentration of RNA for which the thermal conductivity of graphene is significantly degraded is close to the percolation threshold for spherical RNA aggregates. If the fraction of RNA in the nanocomposite is larger than such a threshold, the thermophysical properties of the nanocomposite are not controlled anymore by the graphene phase, but by RNA, which is poorly thermally conducting.

In the composite of RNA/graphene platelets, when treating RNA as defects in a matrix of graphene platelets, the overall thermal conductivity of the film can be estimated using the modified effective medium theory (MEMT) [23]. The thermal conductivity of

RNA is negligible as compared to the thermal conductivity of graphene, which leads to the simplification of MEMT (eq.10 of Ref. 23) and the effective thermal conductivity of graphene platelets matrix with the fraction of RNA f_R , is,

$$K_{\text{eff}} = K_{\text{GR}} \cdot \left[\frac{1 - f_R}{1 + 0.5 \cdot f_R} \right] \quad (6.5)$$

where K_{GR} is the thermal conductivity of the graphene matrix including the effect of the interfaces between the graphene platelets and the spherical aggregates of RNA with diameter d , which is given by,

$$K_{\text{GR}} = K_G \cdot \left[\frac{1}{1 + 0.25 \cdot \Phi \cdot \Lambda} \right] \quad (6.6)$$

where Λ is the phonon mean free path in the defect free graphene, K_G is the thermal conductivity of starting the graphitic material and Φ is the interface density of the RNA aggregate with diameter d , given as [23];

$$\Phi = \frac{6f_R}{d} \quad (6.7)$$

Substituting eqs. (6.6) and (6.7) in eq. (6.5), we get,

$$K_{\text{eff}} = K_G \cdot \left[\frac{1}{1 + 1.5 \cdot (f_R / d) \cdot \Lambda} \right] \cdot \left[\frac{1 - f_R}{1 + 0.5 \cdot f_R} \right] \quad (6.8)$$

Predictions of MEMT given by eqs. (6.5) and (6.8) with and without the effect of interface density, respectively, are shown in Figure 6.6. It can be seen that experimental data matched well with the effective thermal conductivity including the effect of interfaces with an average defect diameter of 100 nm and phonon mean free path = 750 nm. The strong decrease in thermal conductivity with increasing fraction of RNA is thus attributed to the thermal contact resistance between the graphene platelets due to the

presence of highly insulating RNA aggregates that tend to attach to the edges of the graphene platelets. The thickness of thin films of RNA-graphene nanocomposites is nearly ten times higher than the graphene films made from a similar volume of RNA free suspensions [31], which is another indication of the presence of RNA in the form of aggregates.

Using the procedure detailed in section 6.2, an RNA content of 4.6 wt% was estimated in our samples prepared from water suspensions with RNA to graphite ratio of 10:1. The amount of RNA that is present in the solid films is significantly lower than in the starting suspensions because most of the RNA sediments with the heavier graphitic flakes and some drains out with water during the filtration process. Nevertheless, it is apparent that even small amounts of RNA in the films are sufficient to deteriorate to a

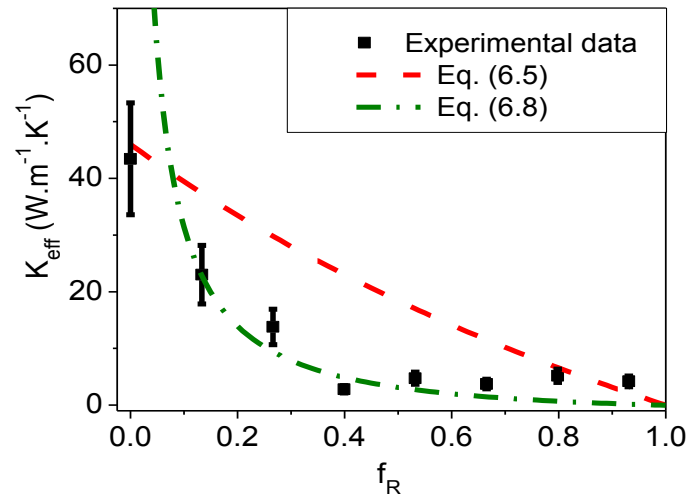


Figure 6.6 Effective thermal conductivity of thin film of RNA/n-G composite as function of RNA fraction in the nanocomposite. It can be seen that at a constant fraction of n-G the thermal conductivity of the nanocomposite decreases with increasing RNA content in the nanocomposite. The predictions of MEMT [23] are also shown. It can be seen that experimental data matches well with the prediction of MEMT including the effects of interface density.

certain extent, and their thermal properties as shown in Figure 6.7(a). Although, on the other hand, presence of RNA in the graphene matrix has the advantage of making graphene nanoplatelets hydrophilic, which is highly desired for their use in biological applications.

Figure 6.7(b) shows the thermal diffusivity (D_s) of the same samples shown in Figure 6.7(a). It can be noticed that D_s varies less than the thermal conductivity within a particular set of samples, but it is strongly enhanced in the set of samples in which graphene-like platelets obtained from n-G were pre-treated in $H_2SO_4:HNO_3$ and Piranha solution ($H_2SO_4:H_2O_2$). Such pre-treatment yields thinner graphene platelets at a constant fraction of the substrate area covered by platelets and this may offer an explanation of the improved thermal diffusivity of this set of films. Thinner graphene platelets are less affected by phonon-phonon scattering processes, which lead to better thermal conductivity leading, in turn to the better thermal properties of the entire nanocomposite.

Carbon allotropes may exhibit an extremely wide range of values of thermal conductivity, from the lowest values in amorphous carbons to the highest values in graphene [33]. These differences arise from the different structural properties of the samples, crystalline or amorphous, and the type of bonding between the carbon atoms. In graphene, heat is mostly conducted by phonons and intrinsically limited by phonon-phonon interaction [34]. Several physical phenomena may affect the thermal conductivity in composite graphene-based thin films. The thermal conductivity of graphitic materials diminishes because of the small size of crystalline domains, impurities within the individual crystallites and the van-der Waals interactions between the neighboring layers [35].

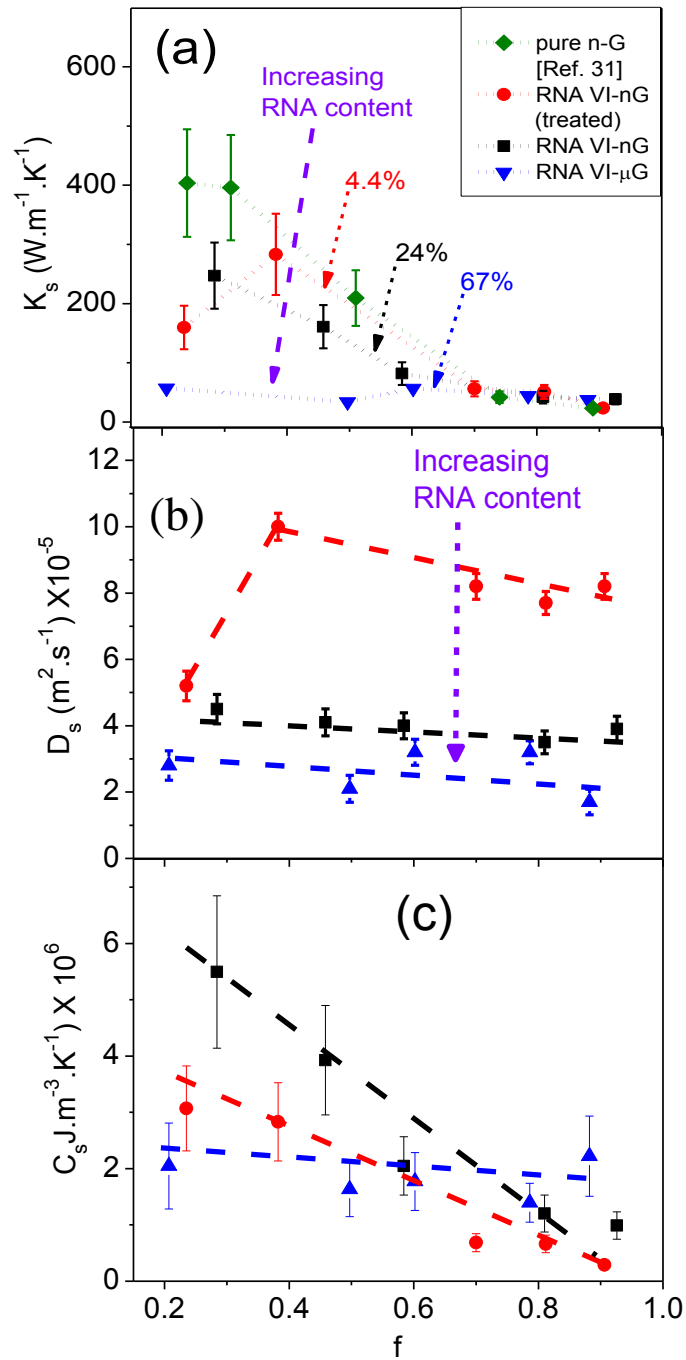


Figure 6.7 (a) Thermal conductivity and (b) Thermal diffusivity as a function of f for the sets of samples used in this study along with the data from Ref, 31. It can be seen that for any value of f , the thermal conductivity of RNA/graphene platelets thin films is less than the corresponding value for pure graphene samples.

The thermal conductivity of RNA/graphene platelets thin films was also measured with the 3ω method. For a typical sample, the measured value of the thermal conductivity is $(47 \pm 6) \text{ W}\cdot\text{m}^{-1}\cdot\text{K}^{-1}$, which is slightly lower (nearly 2%) than the one obtained from the PDS measurement (i.e. $49 \pm 11 \text{ W}\cdot\text{m}^{-1}\cdot\text{K}^{-1}$) but lies within the experimental uncertainty. In the case of inhomogeneous but electrically conducting samples, the electrical method may overestimate the thermal conductivity where contributions from insulating constituents may be ignored due to the bridging of the conducting network. By comparison PDS is free from such complications because it uses an optical probe beam to measure indirectly the temperature rise. In carbon-based materials, heat is mostly carried by phonon so the interface between electrically conducting graphene platelets has very little or no electrical resistance but they offer thermal resistance by scattering the phonons and dramatically decreasing the thermal conductivity.

The relationship between the thermal and electrical conductivities of our samples is shown in Figure 6.8. It can be seen that the thermal conductivity drops sharply with increasing electrical conductivity, which is the consequence of increased film thickness with increasing overlaps and interfaces with an increasing fraction of the substrate area covered by RNA-graphene platelets nanocomposite thin films. Thermal conductivity decreases with increasing film thickness due to increased phonon scattering at the interfaces. Electrical based methods that rely on measurement of change in electrical resistance (that decreases with increasing film thickness), can overestimate the thermal conductivity of thicker and inhomogeneous samples because of low electrical resistance, while PDS relies on the measurement of a temperature gradient that is a direct consequence of heat produced and spread in the sample. So, PDS is a more reliable

technique to measure the thermophysical properties of such composites. Another advantage of PDS is that it is a contactless technique and does not require sample preparation, while in the 3ω method contact deposition on the sample is required, which may affect the intended use of the sample.

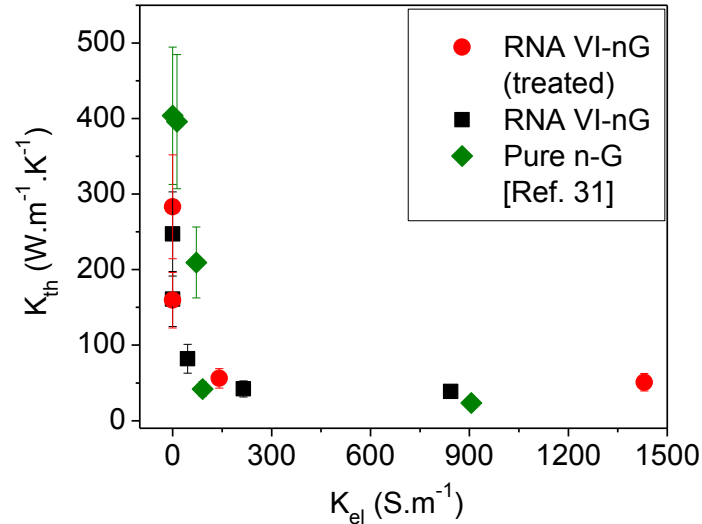


Figure 6.8 Thermal conductivity versus electrical conductivity of the samples used in the present study. Thermal conductivity decreases with increasing electrical conductivity due to increasing number of graphene layers.

6.4 Conclusion

It was demonstrated that PDS is a suitable technique for measuring the thermophysical properties of transparent and conducting thin films of RNA-graphene platelets nanocomposite as it is a contactless and non-destructive technique. Electrical based methods that rely on measurement of change in electrical resistance can overestimate the thermal conductivity of thicker and inhomogeneous samples because of low electrical resistance, while PDS relies on the measurement of a temperature gradient that is a direct consequence of heat produced and spread in the sample. So, we believe that PDS is a

more reliable technique to measure the thermophysical properties of such composites.

We show that the thermal conductivity of our nanocomposites is controlled by the thermal insulation properties of RNA, and, as the concentration of RNA increases, the thermal conductivity is significantly degraded. RNA tends to form aggregates with the increasing fraction of RNA in the films and acts as voids in the matrix of the graphene and decreases the effective thermal conductivity of the nanocomposite because of the increasing interface density. The thermal contact resistance between the graphene platelets is also due to the presence of highly insulating RNA aggregates that tend to attach to the edges of the graphene platelets. When RNA makes a continuous envelope around the graphene platelets, the thermal conductivity of the nanocomposite degrades significantly, while thin films in which a fraction of the platelet surface is free from RNA still retain the excellent thermal transport properties of graphene in a significant proportion. However, the presence of RNA in the nanocomposite has the advantage that it makes the nanocomposite hydrophilic, which makes them an attractive choice for applications where hydrophilicity is required, especially in biological applications.

References

- [1] S. Ghosh, W. Bao, D. L. Nika, S. Subrina, E. P. Pokatilov, C. N. Lau and A. A. Balandin, *Nat. Materials*, **9** (2010) 555.
- [2] Y. Sun, Qiong Wu and Gaoquan Shi, *Energy Environ. Sci.*, **4** (2011) 1113.
- [3] H. Chang and H. Wu, *Adv. Funct. Materials*, Featured Article, 1, 2012.
- [4] Y. Shao, J. Wang, H. Wu, J. Liu, I. A. Aksay and Y. Lin, *Electroanalysis* **22** (2010) 1027.
- [5] H. B. Zhang, W. G. Zheng, Q. Yan, Y. Yang, J. W. Wang, Z. H. Lu, G. Y. Ji and Z. Z. Yu, *Polymer*, **51** (2010) 1191.
- [6] D. Y. Cai, K. Yusoh and M. Song, *Nanotechnology*, **20** (2009) 085712.
- [7] C. Hu, X. Wang, L. Yang, and Y. Wu, *J. of Solid State Chem.*, **182** (2009) 2486.
- [8] T. Ramanathan, A. A. Abdala, S. Stankovich, D. A. Dikin, M. Herrera-Alonso, R. D. Piner, D. H. Adamson, H. C. Schniepp, X. Chen, R. S. Ruoff, S. T. Nguyen, I. A. Aksay, R. K. Prud'homme and L. C. Brinson, *Nat. Nanotechnology*, **3** (2008) 327.
- [9] K.M.F. Shahil and A. A. Balandin, *Nano Lett.*, **12** (2012) 861.
- [10] K. Chu, C. Jia and W. Li, *Appl. Phys. Lett.*, **101** (2012) 121916.
- [11] A. Yu, P. Ramesh, M.E. Itkis, E. Bekyarova and R. C. Haddon, *J. Phys. Chem. C*, **111** (2007) 7565.
- [12] X. Huang, X. Qi, F. Boey and H. Zhang, *Chem. Soc. Rev.*, **41** (2012) 666.
- [13] A. A. Balandin, S. Ghosh, W. Bao, I. Calizo, D. Teweldebrhan, F. Miao and C. N. Lau, *Nano Lett.*, **8** (2008) 902.
- [14] W. Cai, A. L. Moore, Y. Zhu, X. Li, S. Chen, Li Shi and R. S. Ruoff, *Nano Lett.*, **10** (2010) 1645.

- [15] J. H. Seol, I. Jo, A. L. Moore, L. Lindsay, Z. H. Aitken, M. T. Pettes, X. Li, Z. Yao, R. Huang, D. Broido, N. Mingo, Rodney S. Ruoff and Li Shi, *Science*, **328** (2010) 213.
- [16] D. G. Cahill, *Review of Scientific Instruments*, **61** (1990) 802.
- [17] F. Sharifi, R. Bauld, M. S. Ahmed and G. Fanchini, *Small*, **8** (2012) 699.
- [18] H. N. Lim, N.M. Huang, S.S. Lim, I. Harrison and C. H. Chia, *Int. J. of Nanomedicine*, **6** (2011) 1817.
- [19] W. B. Jackson, N. M. Amer, A. C. Boccara, and D. Fournier, *Appl. Optics*, **20** (1981) 1333.
- [20] P. G. Klemens, *Int. Journal of Thermophysics*, **22** (2001) 265.
- [21] P. H. Tan, W. P. Han, W. J. Zhao, Z. H. Wu, K. Chang, H. Wang, Y. F. Wang, N. Bonini, N. Marzari, G. Savini, A. Lombardo, and A.C. Ferrari, *Nat. Materials*, **11** (2012) 294.
- [22] F. Hao, D. Fang and Z Xu, *Appl. Phys. Lett.*, **99** (2011) 041901.
- [23] A. Minnich and G. Chen, *Appl. Phys. Lett.*, **91** (2007) 073105.
- [24] J. Liu, A. G. Rinzler, H. Dai, J. H. Hafner, R. K. Bradley, P. J. Boul, A. Lu, T. Iverson, K. Shelimov, C.B. Huffman, F. Rodriguez-Macais, Y. S. Shon, T. R. Lee, D. T. Colbert, R. E. Smalley, *Science*, **280** (1998) 1253.
- [25] Z. Wu, Z. Chen, X. Du, J. M. Logan, J. Sippel, M. Nikolou, K. Kamaras, J. R. Reynolds, D. B. Tanner, A. F. Hebard, A. G. Rinzler, *Science*, **305** (2004) 1273.
- [26] G. Eda, G. Fanchini, and M. Chhowalla, *Nat. Nanotechnology*, **3** (2008) 270.
- [27] ImageJ is a public domain Java image processing program by NIS Image, (<http://rsb.info.nih.gov/nih-image/>).

- [28] S. Clancy, Chemical structure of RNA. Nat. Education, **1** (2008) 1.
- [29] Sigma Aldrich, Technical Specifications of RNA VI.
- [30] M. N. Ozisik, *Heat Conduction* 2nd Ed., Wiley, New York, 1993.
- [31] M. S. Ahmed, S. Ezugwu, R. Divigalpitiya and G. Fanchini, Carbon, **61** (2013)595.
- [32] S. Bialkowski, *Photothermal Spectroscopy Methods for Chemical Analysis*, John Wiley & Sons, New York, 1996.
- [33] A. A. Balandin, Nat. Materials, **10** (2011) 569.
- [34] D. L. Nika, E. P. Pokatilov, A. S. Askerov and A. A. Balandin, Phys. Rev. B, **79** (2009) 155413.
- [35] D. L. Nika, E. P. Pokatilov and A. A. Balandin, Physics Status Solidi **B**, (2011) 1.

Chapter 7

7 Conclusion and future work

7.1 Conclusion

Photothermal deflection spectroscopy (PDS) is a material characterization technique that is based on Mirage-effect. In PDS, a sample is placed in a photothermal fluid that has a high temperature coefficient of refractive index. Heat generated in the sample upon illumination is transferred to the adjoining photothermal fluid causing a change in its refractive index that is detected by the deflection of a probe laser beam passing through it. PDS is a non-destructive and contactless technique that can be applied *in situ* for optical and thermal characterization of the material samples. For optical characterization of samples, the PDS technique has advantages over other optical techniques due to its sensitivity. This technique can be used on very thin samples and even for analysis of soft biological samples due to its non-destructive nature. In the present work, an automated PDS setup is built that is capable of collecting data at a range of incident photon energies (from 1.1 eV to 3.2 eV), a range of modulation frequencies (from 2Hz to 1 kHz) of excitation beam and a range of incident beam powers as described in Chapter 2.

In most of the theoretical models developed to explain the probe beam deflection, the heat transfer from sample to adjoining photothermal fluid is assumed to be purely conductive and contributions of convective and radiative heat transfer are ignored, which is valid for the photothermal fluids with low thermal conductivity and small temperature rise on the sample surface. In the case of photothermal fluid with highly thermally conducting nanoparticles dispersed in it and having its heat exchange coefficient enhanced, the contribution of convective heat transfer cannot be ignored. We have

investigated such effects with a photothermal fluid in which carbon nanotubes (CNTs) were dispersed. We found that the amplitude of angle of deflection increased with increasing volume fraction of CNTs and nearly doubled for volume fraction $f_{\text{opt}} = 3.7 \cdot 10^{-3} \%$. The increase in PDS signal is due to enhanced heat exchange coefficient of the photothermal fluid in the presence of CNTs. We have developed and used a one dimensional heat conduction model including the effect of convective heat transfer from the sample to the photothermal fluid and have shown that convective heat transfer cannot be ignored in the presence of CNTs in the photothermal fluid. So with the use of nanofluid as a deflection medium, an enhancement in the amplitude of angle of deflection, and thus the sensitivity of the PDS technique, has been achieved that will result in its use in characterizing the materials with low defects and weak optical absorption. However, one has to be careful about the possible effect of nanoparticles on the sample that may contaminate or influence the sample properties.

The PDS setup was used to study the Staebler-Wronski effect and the formation of defects in a set of a-Si:H thin films samples under light soaking. The optical and thermal properties of these samples during repeated light soaking from AM1.5 illumination were measured. It was found that, during light-soaking, the thermal conductivity of the samples decreased with increasing density of dangling bond defects. At the lowest values of thermal conductivity, films soaked by AM1.5 light at 1 Sun reach internal temperatures $T_{\text{ill}} > 100^{\circ}\text{C}$, which are comparable to the annealing temperatures that can be used to recover low defect densities in a-Si:H. Engineered a-Si:H thin films with low thermal conductivity can be designed for developing a-Si:H devices free from Staebler-Wronski effect.

The PDS setup was also used to study the thermophysical properties of graphene-based thin films. Two different sets of transparent carbon-based conducting films (TCCFs), both deposited on glass substrates: a set of films prepared by the vacuum filtration method described in Chapter 2 and another commercial-grade prototype of TCCF developed by 3M Canada Co., have been investigated. The results showed an increase in electrical conductivity, and a decrease in optical transmittance and thermal conductivity with increasing film thickness. A relationship between the electrical and thermal conductivity of vacuum-filtrated TCCFs was established, which is suitable to be extended to a large class of graphene-based thin films. The model suggests that, for sufficiently “large” graphene platelets, the most important role in determining the thermal conductivity of TCCF is played by the number of overlapped graphene layers and the junctions between neighbouring platelets. Our models can be used for the optimization of the trade-off between electrical, optical and thermal properties of TCCF and are critical to design graphene-based thin films for specific applications in which electrical conductivity, optical transparency and ability to evacuate heat are simultaneously required.

Finally, the thermophysical properties of RNA/graphene platelet nanocomposites were investigated and the effect of RNA content on the effective thermal properties of these composite films was investigated. It was found that the thermal conductivity of these nanocomposites is controlled by the thermal insulation properties of RNA, as the concentration of RNA increased the thermal conductivity was significantly degraded because of the thermal insulating properties of RNA and increasing interface density. When RNA makes a continuous envelope around the graphene platelets, the thermal

conductivity of the nanocomposite degrades significantly, while thin films in which a fraction of the platelet surface is free from RNA still retain the excellent thermal transport properties of graphene in a significant proportion. However, the presence of RNA in the nanocomposite has the advantage that it makes the nanocomposite hydrophilic, which makes them an attractive choice for applications where hydrophilicity is required especially in biological applications.

7.2 Future work

A PDS mapping of surface of a solar cell and thin films of its constituent materials will help us understand optical absorption and the thermal properties of solar cells and possible ways to improve their performance. This mapping can be achieved with a little modification of the present PDS setup by using stepper motors to control the sample stage movement in the directions parallel and transversal to the probe beam.

We identified that when heat transfer in PDS is driven by convection, the amplitude of the PDS signal decreases as $\omega^{-3/2}$ (where ω is the pulse frequency of “pump” beam) while the amplitude decreases as ω^{-1} when heat transfer to the fluid mainly occurs by conduction, a parametric study of convection driven PDS can be done by using different types of nanoparticles, different types of photothermal fluid, different types of samples and in different modulation frequency ranges. An enhancement in the PDS signal was obtained with the use of carbon nanotubes in photothermal fluid but was not used to analyze any sample. One can make use of enhancement in the PDS signal to analyze samples to see if it really helps in the resolution of the PDS mapping, but one has to be careful about possible interaction/contaminations of the sample with the nanotubes.

Interfacing the existing PDS setup with a Witec alpha 300S near field scanning optical microscope (NSOM) in our laboratory is another opportunity to have a high resolution PDS mapping of nanomaterials and nanocomposites.

Appendices

Appendix A: Computer control and data acquisition

A1. PDS Setup - computer controlled data acquisition.

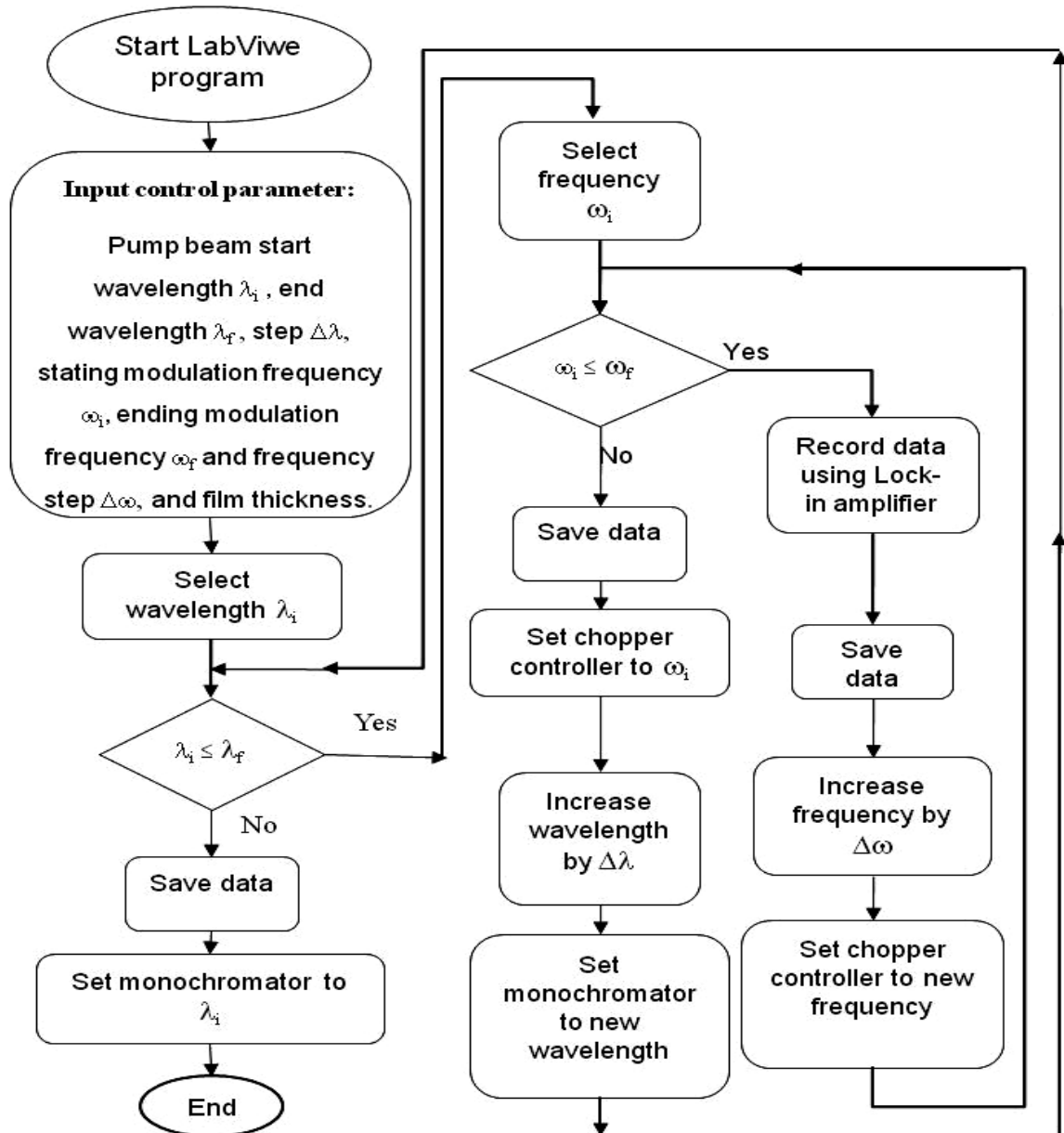


Figure A.1 Flow chart of data acquisition and automatic control of the PDS setup.

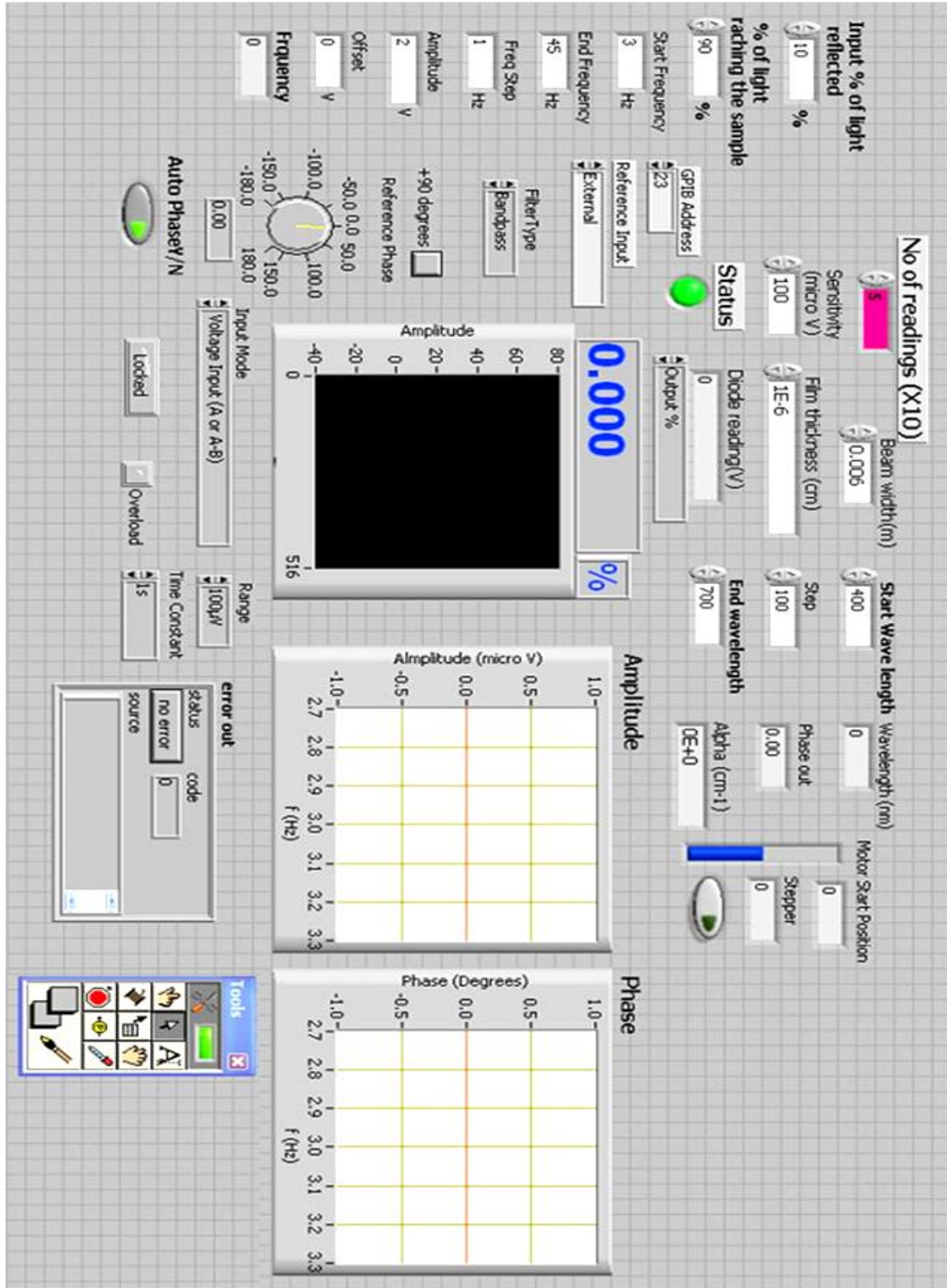


Figure A.2 LabView front panel of data acquisition and automatic control of the PDS setup.

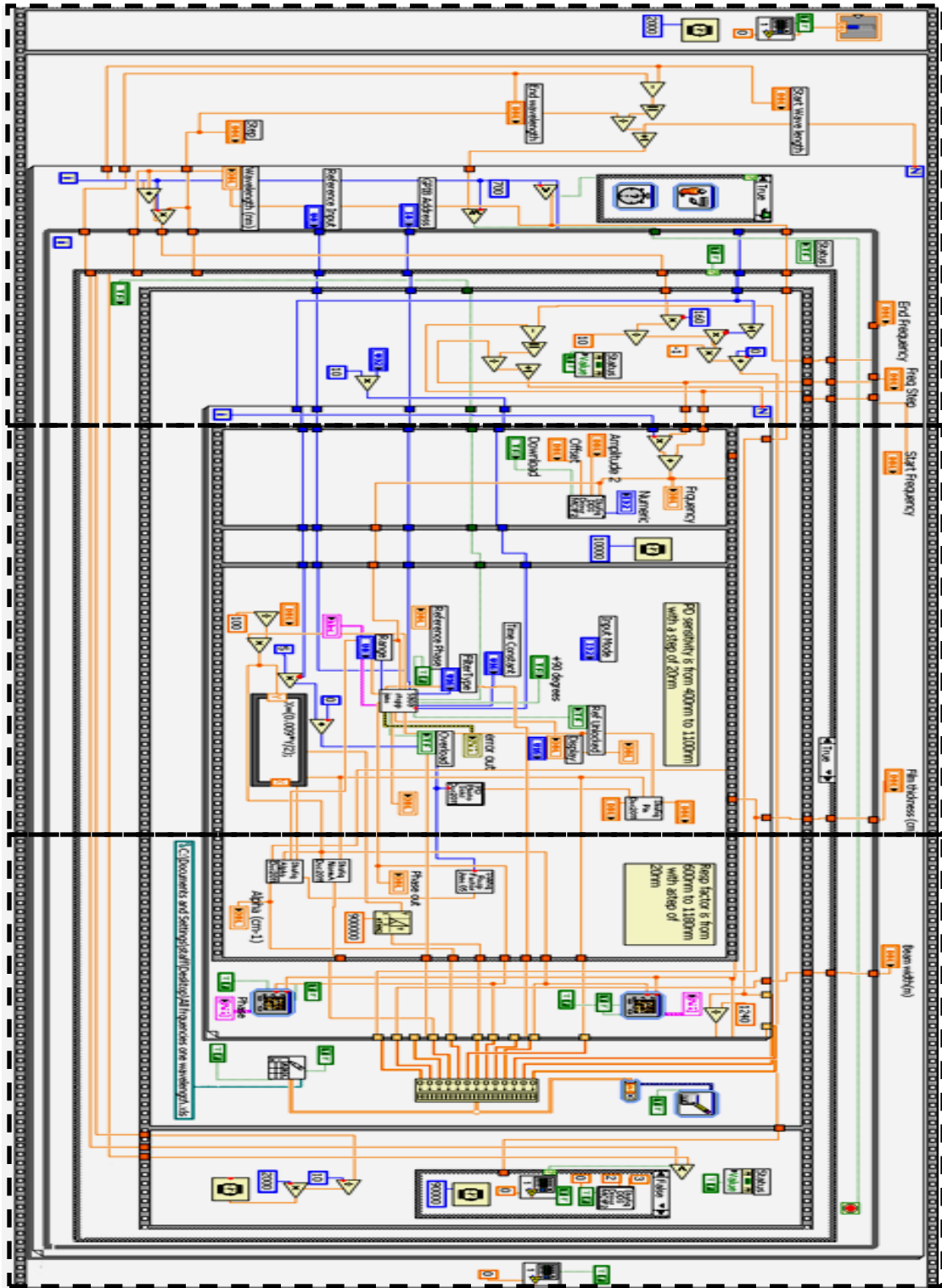


Figure A.3 LabView block diagram of data acquisition and automatic control of the PDS setup (The diagram is magnified and split into three parts - next 3 pages).

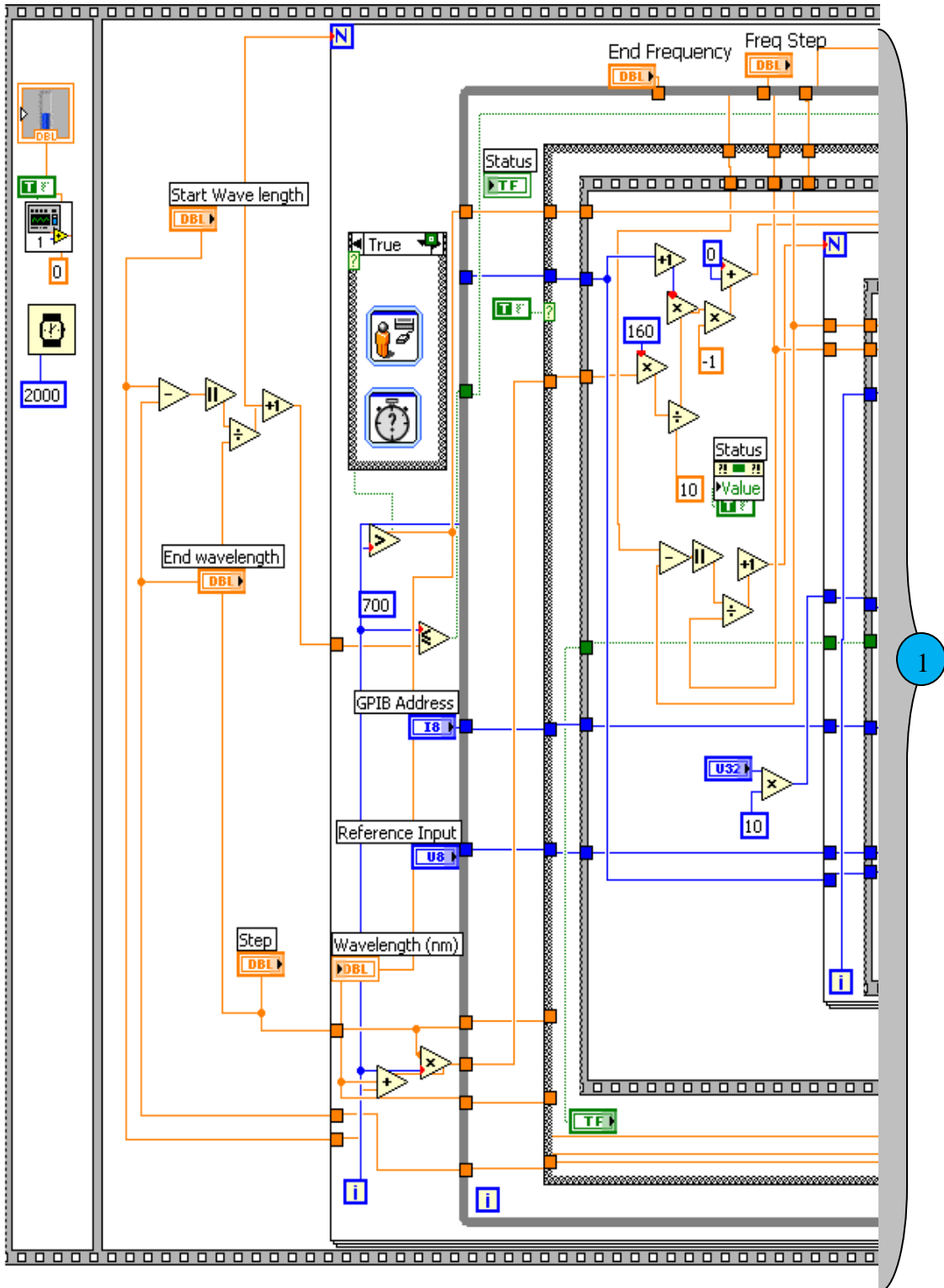


Figure A.3.1 (Left part) LabView block diagram of data acquisition and automatic control of the PDS setup.

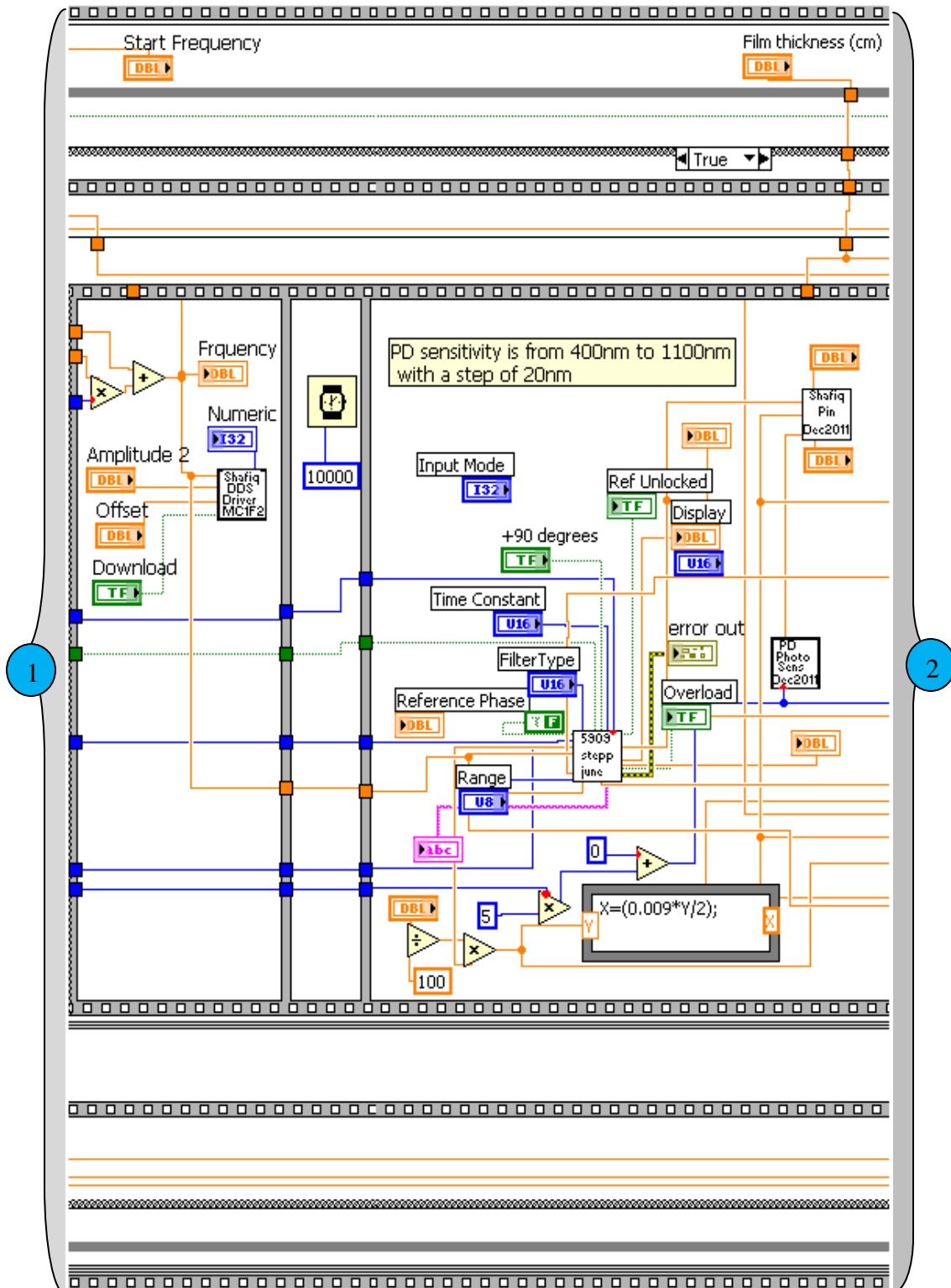


Figure A.3.2 (Central part) LabView block diagram of data acquisition and automatic control of the PDS setup.

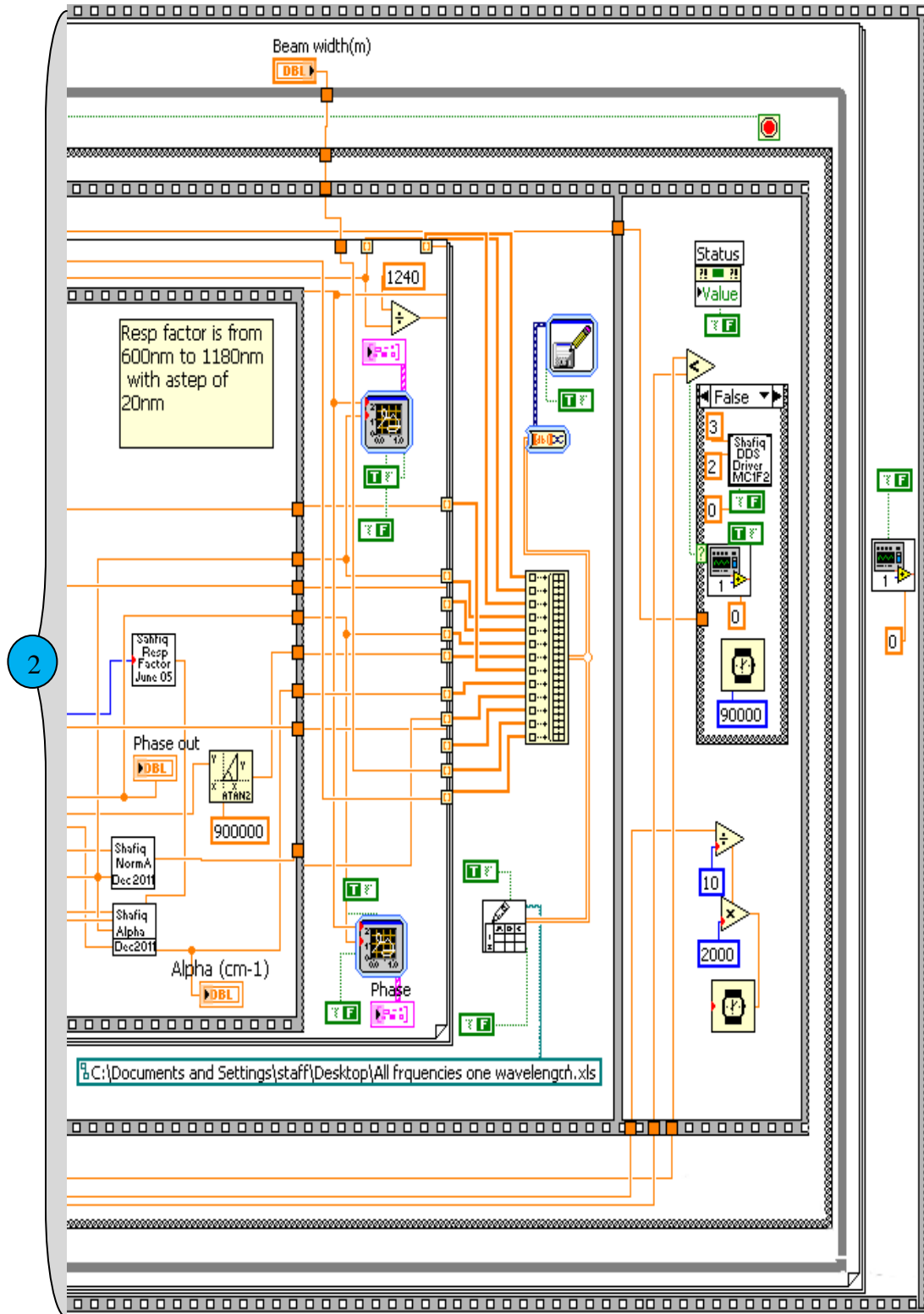


Figure A.3.3 (Right part) LabView block diagram of data acquisition and automatic control of the PDS setup.

A2. 3ω -Method Computer Controlled Data Acquisition.

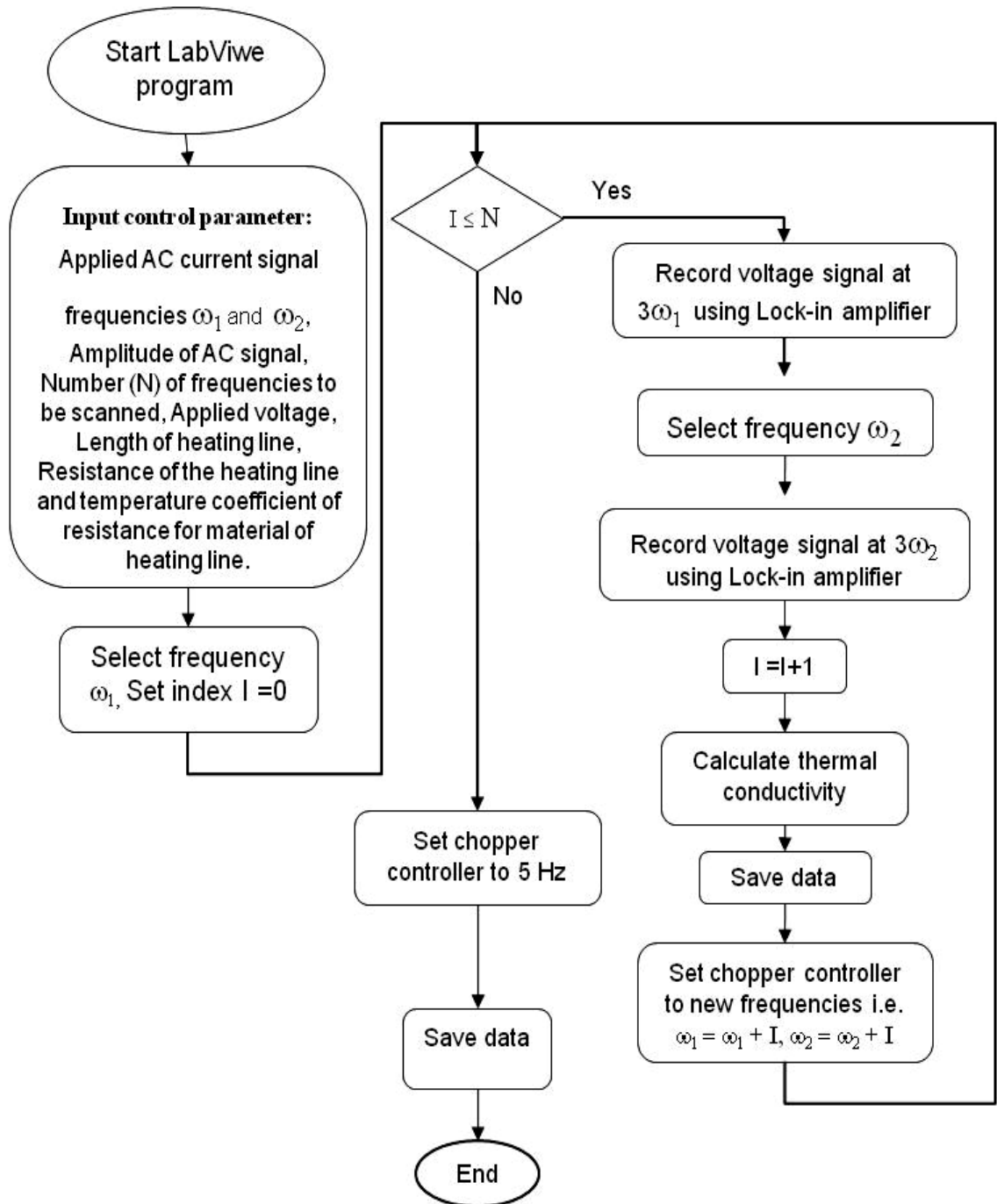


Figure A.4 Flow chart of data acquisition and automatic control of the 3ω setup.

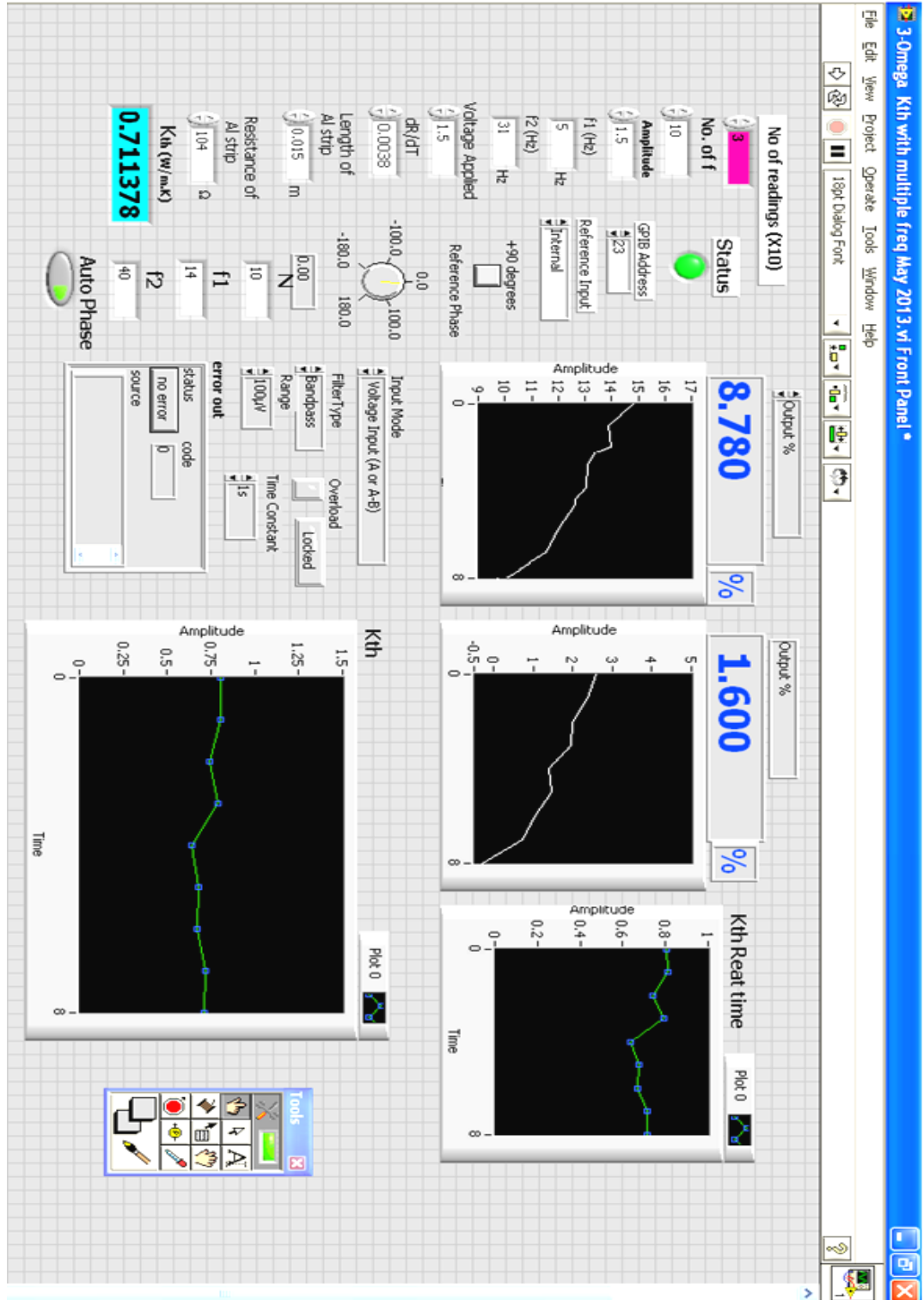


Figure A.5 LabView front panel of data acquisition and automatic control of the 3ω thermal conductivity measurement setup.

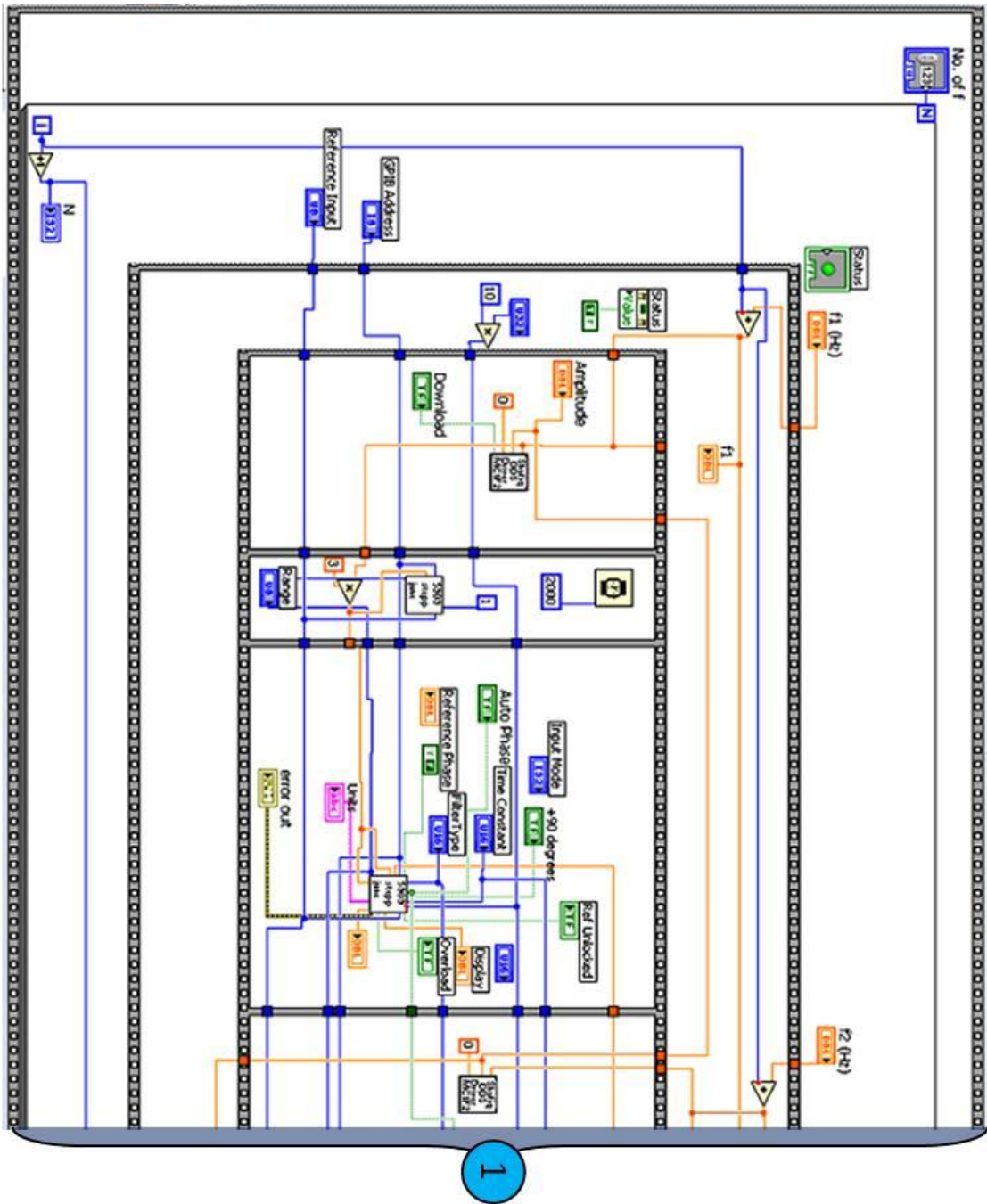


Figure A.6.1 (First half) LabView block diagram of data acquisition and automatic control of the 3ω thermal conductivity measurement setup.

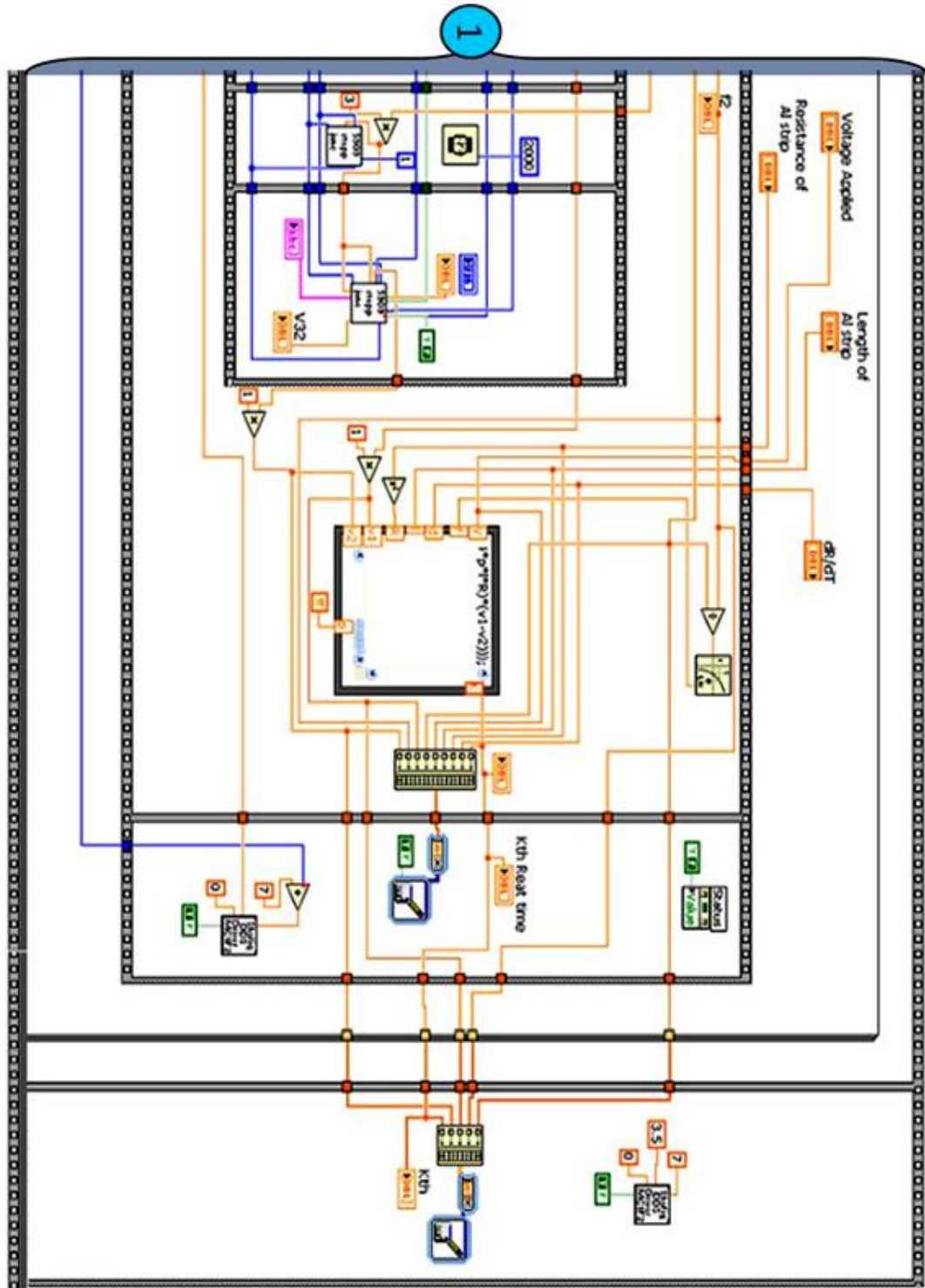


Figure A.6.2 (Second half) LabView block diagram of data acquisition and automatic control of the 3ω thermal conductivity measurement setup.

Appendix B: Convection enhanced photothermal deflection spectroscopy

B1. One-dimensional heat conduction – Thin “pump” beam

Consider a thin film deposited on an optically transparent and thermally non-conducting substrate which is immersed in a photothermal fluid and is exposed to a “pump” beam that is very long in vertical direction and is modulated at a pulse frequency ω . Assume that all of the light that is absorbed in the thin film is converted into heat and that the film is much thinner than the diffusion length [$l_D = (D/2\omega)^{1/2}$] of the thermal wave, while the width of the sample is much bigger than l_D : this assumption is valid for most solar-grade semiconductors irrespectively of their optical absorption coefficient.

Let us also initially assume that the illuminating beam is a thin line source with negligible thickness in the y -direction in which it can be represented by a delta-shaped function, $g(y,t) = P_0 \cdot \delta(y - y_0 = 0) \cdot \exp(j\omega t)$, while it is very long and uniform in the z -direction, as schematically shown in Figure B1(a). In these conditions, the one-dimensional Fourier equation for in-plane diffusion of heat along the y -direction of the film can be used. In such a configuration, heat diffusion equation can be written as:

$$\frac{\partial^2 T_s(y,t)}{\partial y^2} = \frac{1}{D_s} \cdot \frac{\partial T_s(y,t)}{\partial t} \quad (\text{B1})$$

where $T_s(y,t)$ and D_s indicate the temperature and thermal diffusion coefficient of the film, respectively. Far away from the point of illumination, which is set at $y = 0$ as in figure 3.5(a), the sample is at ambient temperature. An inspection of eq. (3.22) suggests that, if $T_s'(y,t)$ is a solution for such equation, also $T_s(y,t) = T_s'(y,t) + \text{constant}$, will satisfy it. Therefore, we will set the ambient temperature as the “zero-temperature” and T_s

will represent temperature in excess to the ambient level. Under this assumption, First type boundary conditions for eq.(3.22) can be written at $y = \pm \infty$:

$$T_s(y = \pm \infty, t) = 0 \quad (\text{B2})$$

At the point of illumination, $y = 0$, the amount of heat generated from the absorption of light must equal to the flux of heat that diffuses away from such point, both to the left ($y > 0$) and to the right ($y < 0$) of it. Symmetry considerations suggest that the heat flux

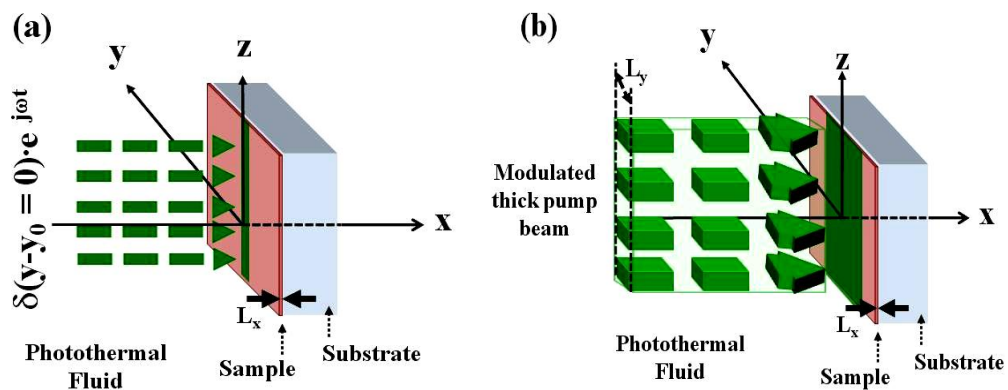


Figure B.1 Thin film sample on a non-absorbing substrate, illuminated by a (a) thin pump beam in the y -direction, and very long and uniform in the z -direction, and (b) thick pump beam in the y -direction (length L_y) and very long in the z -direction. In both cases the probe beam is parallel to the y -axis.

diffusing in each of the two directions is the same and is proportional to the thermal conductivity (K_s) of the thin film sample. Subsequently, boundary conditions of the second type can be written at $y = 0$:

$$\frac{Q_0}{2} \cdot e^{j \cdot \omega \cdot t} = -K_s \frac{\partial T_s(y = 0, t)}{\partial y}, \quad (\text{B3})$$

where Q_0 is the maximum illumination power per unit area of the thin film that is deposited at each pulse of light from pump beam. Q_0 depends on the power P_0 carried at each pulse by the “pump” beam as well as on the optical absorption coefficient (α_s) of the thin film sample.

The heat generated at the point of the sample that is periodically illuminated with frequency ω , is evacuated along the film surface. Let Q_0 be the maximum power deposited per unit surface area of thin film in one pulse and C_s the thermal capacitance of the film. Thus, the energy balance equation at the point of illumination is given by:

$$Q_0 = \frac{P_0}{L_y \cdot L_z} \cdot \int_0^{L_x} e^{-\alpha_s \cdot x} \cdot dx = \frac{P_0}{L_y \cdot L_z} \cdot \left(\frac{1 - e^{-\alpha_s \cdot L_x}}{\alpha_s \cdot L_x} \right) \quad (\text{B4})$$

where the x-axis is oriented as in Figure 3.5 and L_x is the film thickness. It is worth noting that, for optically ultra-thin films, $1 - \exp(-\alpha_s \cdot L_x) \approx \alpha_s \cdot L_x$ so that T_s , as well as the PDS signal, is independent of α_s and no optical properties of the film can be measured by PDS, as predicted in Chapter 2. By replacing eq. (B4) into eq. (B3), and by considering that $K_s = C_s \cdot D_s$, we obtain that

$$\frac{P_0}{L_y \cdot L_z} \cdot \left(\frac{1 - e^{-\alpha_s \cdot L_x}}{\alpha_s \cdot L_x} \right) \cdot e^{-j\omega t} = -C_s \cdot D_s \cdot \frac{\partial T_s(y=0, t)}{\partial t} \quad (\text{B5})$$

A general solution of eq. (B1) can be found by linear superposition of periodic thermal waves of the form,

$$T_s^{\omega'}(y, t) = \Theta_s(y) \cdot e^{j\omega' t} \quad (\text{B6})$$

Since only one specific frequency $\omega' = \omega$ is excited in our case, the solution of eq. (B1) in our specific configuration can be found by replacing eq. (B6) in to (B1) and by

determining the appropriate form of $\Theta_s(y)$ by imposing the boundary condition (B3). We therefore obtain,

$$\frac{\partial^2 \Theta_s(y)}{\partial y^2} = \frac{j \cdot \omega}{D_s} \quad (\text{B7})$$

Let

$$\delta_s^2 = \frac{j\omega}{D_s} \quad (\text{B8})$$

then the solution the solution of eq. (B7) is,

$$\Theta_s(y) = A \cdot e^{-\delta_s \cdot |y|} \quad (\text{B9})$$

where A is constant to be determined using boundary condition (B3).

Substituting $T_s(y)$ from eq. (B9) into eq. (B6) we get,

$$T_s(y,t) = A \cdot e^{-\delta_s \cdot |y|} \cdot e^{j\omega \cdot t} \quad (\text{B10})$$

Using T_s from eq. (B10) in the boundary condition (B3), we get,

$$A = \frac{Q_0}{2 \cdot \sqrt{\omega \cdot D_s} \cdot C_s} \cdot e^{-j\pi/4} \quad (\text{B11})$$

Substituting the value of A from eq. (B11) into eq. (B10), we get,

$$T_s(y,t) = \frac{Q_0}{2 \cdot C_s \cdot \sqrt{D_s \cdot \omega}} \cdot e^{-(1+j)\sqrt{\frac{\omega}{2 \cdot D_s}} \cdot |y|} \cdot e^{j(\omega \cdot t - \pi/4)} \quad (\text{B12})$$

For a square pump beam with height L_z and width L_y , incident on a thin films sample with thickness L_x and absorption coefficient α , we can write the equation for power per unit area Q_0 , as,

$$Q_0 = \frac{1}{L_z \cdot L_x} \frac{dP(y=0)}{dy} \int_0^{L_x} e^{-\alpha \cdot x} \cdot dx = \frac{P_0}{L_y \cdot L_z} \cdot \frac{1 - e^{-\alpha \cdot L_x}}{\alpha \cdot L_x} \quad (\text{B13})$$

where we have assumed that $dP(y)/dy \cong P_0/L_y$.

Using this value of Q_0 into eq. (B12), the temperature profile in the film has the form,

$$T_s(y,t) = \frac{P_0}{2 \cdot L_y \cdot L_z \cdot C_s \cdot \sqrt{D_s} \cdot \omega} \cdot \left(\frac{1 - e^{-\alpha \cdot L_x}}{\alpha \cdot L_x} \right) \cdot e^{-(1+j) \sqrt{\frac{\omega}{2 \cdot D_s}} \cdot |y|} \cdot e^{j(\omega \cdot t - \pi/4)} \quad (\text{B14})$$

B2. One-dimensional heat conduction – Thick “pump” beam

A beam can be defined as thick when its width is comparable to, or larger than, the in-plane diffusion length in the film. Such a thick beam can be considered as sum of a number of thin beams, each one located at $y = y_0$ (where $-L_y/2 < y_0 < L_y/2$) with an intensity $dP_0 = (P_0/L_y) \cdot dy_0$. We can determine the temperature profile in the liquid upon illumination of the sample from a thick beam by superimposing a set of solutions for thin beams using Green’s function method. The Green’s function that determines the resulting temperature at location y from a unit impulse at y_0 , is given as,

$$G(y \rightarrow y_0, t) = \frac{1}{2 \cdot C_s \cdot \sqrt{D_s} \cdot \omega} \cdot e^{-(1+j) \sqrt{\frac{\omega}{2 \cdot D_s}} \cdot |y - y_0|} \cdot e^{j(\omega \cdot t - \pi/4)} \quad (\text{B15})$$

and the resulting temperature can be written as,

$$T_{s0}(y,t) = \int_{-L_y/2}^{L_y/2} Q(y_0) \cdot G(y \rightarrow y_0, t) \cdot dy_0 \quad (\text{B16})$$

which simplifies to,

$$T_{s0}^I(y,t) = \frac{P_0}{2 \cdot L_y^2 \cdot L_z \cdot C_s \cdot \omega} \cdot \left(\frac{1 - e^{-\alpha \cdot L_x}}{\alpha \cdot L_x} \right) \cdot \left[e^{-(1+j) \sqrt{\frac{\omega}{2 \cdot D_s}} \cdot (y - L_y/2)} \right] \cdot e^{j(\omega \cdot t - \pi/2)} \quad \text{for } y \geq 0 \quad (\text{B17a})$$

and

$$T_{s0}^{II}(y,t) = \frac{P_0}{2 \cdot L_y^2 \cdot L_z \cdot C_s \cdot \omega} \cdot \left(\frac{1 - e^{-\alpha \cdot L_x}}{\alpha \cdot L_x} \right) \cdot \left[e^{(1+j) \sqrt{\frac{\omega}{2 \cdot D_s}} \cdot (y + L_y/2)} \right] \cdot e^{j(\omega \cdot t - \pi/2)} \quad \text{for } y \leq 0 \quad (\text{B17b})$$

B3. Temperature Profile with Negligible Convection in the Photothermal Fluid

If convection in a fluid can be ignored, then the Fourier's equation of heat in such fluid can be written as:

$$D_f \left[\frac{\partial^2 T_f(x, y, t)}{\partial x^2} + \frac{\partial^2 T_f(x, y, t)}{\partial y^2} \right] = \frac{\partial T_f(x, y, t)}{\partial t} \quad (\text{B18})$$

where $T_f(x, y, t)$ is the temperature of the photothermal fluid with thermal diffusion coefficient D_f . The fluid is a semi-infinite convective medium in which eq. (B16) can be solved by imposing the Dirichlet condition at the fluid solid interface, from which we must have,

$$T_f(x=0, y, t) = T_{s0}(y, t), \quad (\text{B19})$$

where the right hand side of the eq. (B19) is given by eq. (B14).

The solution of eq. (B18) by using boundary condition (B19) can be found by separating the variables as $T_f(x, y, t) = \phi_f(x) \cdot \psi_f(y) \cdot \exp(j\omega t)$. Which means solving two one-dimensional ordinary differential equations (ODE) in the unknowns x and y of the form:

$$\left\{ \begin{array}{l} \frac{\partial^2 \psi}{\partial y^2} = \gamma^2 \psi \\ \frac{\partial^2 \phi}{\partial x^2} = \left(-\gamma^2 + \frac{j\omega}{D_f} \right) \cdot \phi \end{array} \right\} \quad (\text{B20})$$

Solutions of the first equation are Fourier harmonics of the form

$$\psi_\gamma(y) = A \cdot \exp(-\gamma \cdot |y|) \quad (\text{B21})$$

but only the harmonic eigenfunction with

$$\gamma^2 = j\omega/D_s \quad (\text{B22})$$

projects on the boundary condition.

$$T_f(x=0, y, t) = T_{s0}(y, t) \quad (\text{B23})$$

and all of the other values of γ lead to eigenfunctions orthogonal to $T_{s0}(y, t)$.

Solutions of the second equation are Fourier harmonics of the form,

$$\varphi_\gamma(x) = B \cdot \exp\left[\sqrt{-\gamma^2 + \frac{j\omega}{D_f}} \cdot x\right] \quad \text{for } x \leq 0 \quad (\text{B24})$$

So the γ -value dictated by eq. (B20) is replaced in eqs. (19) and (22) to provide the actual components along x and y for the temperature distribution in the fluid, which becomes,

$$T_f(x, y, t) = \frac{P_0}{2 \cdot L_y \cdot L_z \cdot C_s \cdot \sqrt{D_s} \cdot \omega} \cdot \left(\frac{1 - e^{-\alpha \cdot L_x}}{\alpha \cdot L_x} \right) \cdot e^{-\sqrt{\frac{\omega}{2D_s}} \cdot |y|} \cdot e^{-\sqrt{\frac{\omega}{2D_{\text{eff}}}} \cdot x} \dots$$

$$\dots \exp\left[j \left(\omega \cdot t - \frac{\pi}{4} - \sqrt{\frac{\omega}{2D_s}} \cdot |y| - \sqrt{\frac{\omega}{2D_{\text{eff}}}} \cdot x \right) \right] \quad (\text{B25})$$

where we defined D_{eff} as an effective diffusivity of the film-liquid system that is dominated by the lowest of the twos:

$$\frac{1}{D_{\text{eff}}} = \frac{1}{D_s} + \frac{1}{D_f} \quad (\text{B26})$$

The attenuation of the temperature in the fluid at a distance x from the sample provides an expression for $\phi_f(x)$, that is exponentially decaying with x , while the temperature profile longitudinally to the sample surface is given by $\psi_f(y)$ that has the same dependence of y as that of sample temperature given by $T_{s0}(y, t)$.

B4. Determination of the fluid temperature profile in the presence of convection

In the presence of convective heat transfer, the heat diffusion equation for the fluid can be written as

$$D_f \cdot \frac{\partial^2 T_f(x, y, t)}{\partial x^2} = \frac{\partial T_f(x, y, t)}{\partial t} - H \cdot T_s(y, t), \quad (\text{B27})$$

where H is the heat transfer rate at the fluid/sample interface which is defined as:

$$H = \frac{h_f}{\rho_f \cdot c_f \cdot L_f} \quad (\text{B28})$$

where h_f is the heat transfer coefficient, ρ_f is density of the fluid, L_f is the thickness of thermal boundary layer and c_f is heat capacity of the fluid. It is worth noting that H is measured in Hz. Boundary conditions for eq. (3.38) are given by eq. (3.33) so that

$$T_f(x = -\infty, y = \pm\infty, t) = 0 \quad (\text{B29a})$$

and

$$T_f(x = 0, y, t) = T_s(y, t) \quad (\text{B29b})$$

These boundary conditions mean that the temperature of the fluid far away from the sample is the same as the ambient temperature. Conversely, at the interface between the fluid and sample the fluid temperature must be same as the sample temperature. Heat flows from the sample to the adjoining fluid as a result of temperature difference. The fluid is a semi-infinite convective medium in which eq. (B29) can be solved by imposing the Dirichlet conditions at the fluid solid interface, from which we must have,

$$T_f(x = 0, y, t) = T_{s0}(y, t), \quad \text{for all } y \quad (\text{B30})$$

where the right hand side of the eq. (B28) is given by eq. (B14). The solution of eq. (B27) by using boundary condition (B29) can be obtained by separating the variables as

$T_f(x,y,t) = \phi_f(x) \cdot \psi_f(y) \cdot \exp(j\omega t)$. The attenuation of the temperature in the fluid at a distance x from the sample provides an expression for $\phi_f(x)$, that is exponentially decaying with x , while the temperature profile longitudinally to the sample surface is given by $\psi_f(y)$ that has the same dependence of y as that of sample temperature given by $T_{s0}(y,t)$. A general solution of eq. (B27) can be found by linear superposition of periodic thermal waves of the form,

$$T_f(x, y, t) = \varphi_f(x) \cdot \psi_f(y) \cdot e^{j\omega t} \quad (\text{B31})$$

Substituting $T_f(x,y,t)$ from eq. (B31) into eq. (B27), the temperature profile of the fluid can be obtained by solving the equation,

$$\frac{\partial^2 \varphi_f(x)}{\partial x^2} = \frac{j \cdot \omega}{D_f} \cdot \varphi_f(x) - \frac{H}{D_f} \cdot T_{s0} \quad (\text{B32})$$

Let

$$\delta_f = \sqrt{\frac{j \cdot \omega}{D_f}} \quad (\text{B33})$$

and

$$b = \frac{H}{D_f} \quad (\text{B34})$$

then eq. (B32) becomes,

$$\frac{\partial^2 \varphi_f(x)}{\partial x^2} = \delta_f^2 \cdot \varphi_f(x) - b \cdot T_{s0} \quad (\text{B35})$$

Which is an inhomogeneous differential equation whose solution is sum of a homogeneous and a particular solution i.e.

$$\varphi_f(x) = \varphi_f^H(x) + \varphi_f^P(x) \quad (\text{B36})$$

For homogeneous solution, we substitute $b = 0$ in eq. (B36), which then becomes,

$$\frac{\partial^2 \varphi_f^H(x)}{\partial x^2} = \delta_f^2 \cdot \varphi_f^H(x) \quad (\text{B37})$$

with the boundary condition,

$$\varphi_f^H(x=0) = T_{s0} \quad \text{for all } y \quad (\text{B38})$$

Meaning that temperature profile at fluid/sample interface is continuous.

General solution of eq. (B37) is,

$$\varphi_f^H(x) = C \cdot e^{\delta_f \cdot x} \quad \text{for } x \leq 0. \quad (\text{B39})$$

where C is constant to be determined.

By using the boundary condition (B38), we get, $C = T_{s0}$.

Substituting value of C into eq. (B39), we have,

$$\varphi_f^H(x) = T_{s0} \cdot e^{(1+j)\sqrt{\frac{\omega}{2D_f}} \cdot x} \quad \text{for } x \leq 0 \quad (\text{B40})$$

Now for the particular solution of eq. (B35), we consider the steady state condition i.e.

$$\frac{\partial T_f^P(x, t)}{\partial t} = 0 \quad (\text{B41})$$

which leads to the following equation,

$$\frac{\partial^2 \varphi_f^P(x)}{\partial x^2} = -b \cdot T_{s0} \quad (\text{B42})$$

and its solution, for $x \leq 0$ is,

$$\varphi_f^P(x) = E \cdot e^{\gamma \cdot x} \quad (\text{B43})$$

where

$$\gamma = \sqrt{-b} = j\sqrt{b} \quad (\text{B44})$$

and E is constant to be determined.

To find constant E, we use the boundary condition, $T = T_{s0}$ at $x = 0$, and get $E = T_{s0}$.

Substituting the value of E in eq. (B43) we get,

$$\varphi_f^P(x) = T_{s0} \cdot e^{j\sqrt{\frac{H}{D_f}} \cdot x} \quad \text{for } x \leq 0 \quad (\text{B45})$$

Therefore, the total special solution becomes of eq. (B35) is following,

$$\varphi_f(x) = T_{s0} \cdot \left(e^{(1+j)\sqrt{\frac{\omega}{2 \cdot D_f}} \cdot x} + e^{j\sqrt{\frac{H}{D_f}} \cdot x} \right) \quad (\text{B46})$$

Using eq. (B17) to replace T_{s0} , the fluid temperature becomes,

$$T_f^I(x, y, t) = \frac{P_0}{2 \cdot L_y^2 \cdot L_z \cdot C_s \cdot \omega} \cdot \left(\frac{1 - e^{-\alpha \cdot L_x}}{\alpha \cdot L_x} \right) \cdot \left[e^{-(1+j)\sqrt{\frac{\omega}{2 \cdot D_s}} \cdot (y - L_y/2)} \right] \cdot \left[e^{(1+j)\sqrt{\frac{\omega}{2 \cdot D_{\text{eff}}}} \cdot x} + e^{j\sqrt{\frac{H}{D_{\text{eff}}}} \cdot x} \right] \cdot e^{j(\omega \cdot t - \pi/2)} \quad \text{for } y \geq 0 \quad (\text{B47a})$$

and

$$T_f^{II}(x, y, t) = \frac{P_0}{2 \cdot L_y^2 \cdot L_z \cdot C_s \cdot \omega} \cdot \left(\frac{1 - e^{-\alpha \cdot L_x}}{\alpha \cdot L_x} \right) \cdot \left[e^{(1+j)\sqrt{\frac{\omega}{2 \cdot D_s}} \cdot (y + L_y/2)} \right] \cdot \left[e^{(1+j)\sqrt{\frac{\omega}{2 \cdot D_{\text{eff}}}} \cdot x} + e^{j\sqrt{\frac{H}{D_{\text{eff}}}} \cdot x} \right] \cdot e^{j(\omega \cdot t - \pi/2)} \quad \text{for } y \leq 0 \quad (\text{B47b})$$

B5. Determination of phase and amplitude of angle of photothermal deflection

We can determine the expression for the deflection of probe beam passing through refractive index gradient in the fluid at the fluid sample interface from the temperature profile of fluid the two regions, from $-L_y/2$ to 0 and 0 to $L_y/2$, are shown in Figure B2.

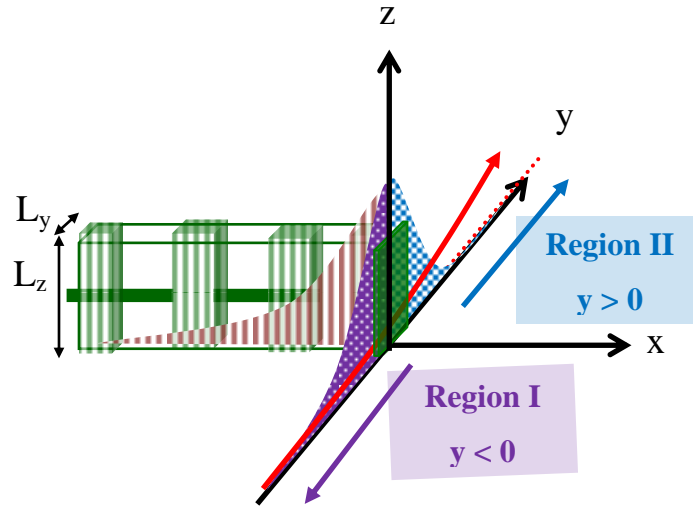


Figure B.2 Schematic of the temperature profile of photothermal fluid under illumination.

The resulting temperature profiles in such two regions are:

$$\begin{aligned}
 T_f^{(I)} &\approx \frac{P_0}{2 \cdot C_s \cdot L_y^2 \cdot L_z} \cdot \frac{1}{\omega} \cdot \left(\frac{1 - e^{-\alpha \cdot L_x}}{\alpha \cdot L_x} \right) \cdot e^{(1+j) \cdot \sqrt{\frac{\omega}{2D_s}} \cdot \left(y + \frac{L_y}{2} \right)} \dots \\
 &\dots \left(e^{(1+j) \cdot \sqrt{\frac{\omega}{2D_{\text{eff}}}} \cdot x} + e^{j \cdot \sqrt{\frac{H}{D_{\text{eff}}}} \cdot x} \right) \cdot e^{j \left(\omega \cdot t - \frac{\pi}{2} \right)} \quad \text{for } x \leq 0 \text{ and } y < y_0 \quad (\text{B48}) \\
 T_f^{(II)} &\approx \frac{P_0}{2 \cdot C_s \cdot L_y^2 \cdot L_z} \cdot \frac{1}{\omega} \cdot \left(\frac{1 - e^{-\alpha \cdot L_x}}{\alpha \cdot L_x} \right) \cdot e^{(1+j) \cdot \sqrt{\frac{\omega}{2D_s}} \cdot \left(\frac{L_y}{2} - y \right)} \dots
 \end{aligned}$$

$$\dots \left(e^{(1+j) \cdot \sqrt{\frac{\omega}{2D_{\text{eff}}}} \cdot x} + e^{j \cdot \sqrt{\frac{H}{D_{\text{eff}}}} \cdot x} \right) \cdot e^{j \left(\omega \cdot t - \frac{\pi}{2} \right)} \text{ for } x \leq 0 \text{ and } y > y_0 \quad (\text{B49})$$

For a thick beam, impinging the sample surface between $-L_y/2 \leq y_0 \leq L_y/2$, the angle of photothermal deflection $A_\phi(t)$ in two regions is given by:

$$A_\phi(t) = \frac{1}{n_f} \left| \frac{dn_f}{dT_f} \right| \cdot \int_{-\infty}^{+L_y/2} \frac{\partial T_f^I}{\partial x} \Big|_{x=0} \cdot dy + \frac{1}{n_f} \left| \frac{dn_f}{dT_f} \right| \cdot \int_{-L_y/2}^{+\infty} \frac{\partial T_f^{II}}{\partial x} \Big|_{x=0} \cdot dy \quad (\text{B50})$$

Schematic of temperature profile of the fluid at the fluid-sample interface is shown in figure B3.

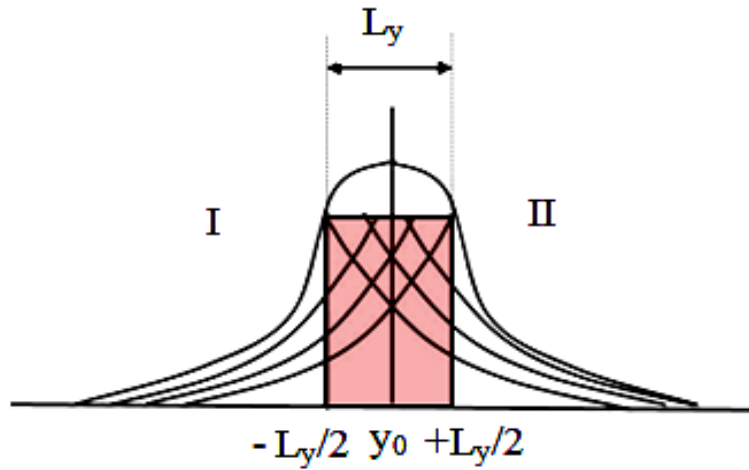


Figure B.3 Schematic of temperature profile of the fluid at the fluid-sample interface, used for the determination of amplitude and phase of angle of photothermal deflection signal.

For region I, i.e. for $y < +L_y/2$, the deflection angle (after few mathematical steps) becomes,

$$A_\phi(t) = \frac{1}{n_f} \left| \frac{dn_f}{dT_f} \right| \cdot \frac{P_0}{C_s \cdot L_y^2 \cdot L_z} \cdot \frac{1}{\omega} \cdot \left(\frac{1 - e^{-\alpha \cdot L_x}}{\alpha \cdot L_x} \right) \cdot \sqrt{\frac{D_s}{D_{\text{eff}}}} \cdot e^{\sqrt{\frac{\omega}{2 \cdot D_s}} \cdot L_y} \cdot e^{j \left(\omega \cdot t - \frac{\pi}{2} + \sqrt{\frac{\omega}{2 \cdot D_s}} \cdot L_y \right)} \cdot \left(1 + \sqrt{\frac{H}{2\omega}} + j \cdot \sqrt{\frac{H}{2\omega}} \right) \quad (\text{B51})$$

Let

$$M = 1 + \sqrt{\frac{H}{2\omega}} \quad (\text{B52})$$

and

$$N = \sqrt{\frac{H}{2\omega}} \quad (\text{B53})$$

then, eq. (B51) can be written as,

$$A_{\phi}(t) = \frac{1}{n_f} \left| \frac{dn_f}{dT_f} \right| \cdot \frac{P_0}{C_s \cdot L_y^2 \cdot L_z} \cdot \frac{1}{\omega} \cdot \left(\frac{1 - e^{-\alpha \cdot L_x}}{\alpha \cdot L_x} \right) \cdot \sqrt{\frac{D_s}{D_{\text{eff}}}} \cdot e^{\sqrt{\frac{\omega}{2 \cdot D_s}} \cdot L_y} \cdot e^{j \left(\omega t - \frac{\pi}{2} + \sqrt{\frac{\omega}{2 \cdot D_s}} \cdot L_y \right)} \cdot (M + j \cdot N) \quad (\text{B54})$$

So the amplitude of PDS signal is,

$$A_{\phi}^{(h)} = \frac{1}{n_f} \left| \frac{dn_f}{dT_f} \right| \cdot \frac{P_0}{C_s \cdot L_y^2 \cdot L_z} \cdot \frac{1}{\omega} \cdot \left(\frac{1 - e^{-\alpha \cdot L_x}}{\alpha \cdot L_x} \right) \cdot \sqrt{\frac{D_s}{D_{\text{eff}}}} \cdot e^{\sqrt{\frac{\omega}{2 \cdot D_s}} \cdot L_y} \cdot \sqrt{M^2 + N^2} \quad (\text{B55})$$

and the phase the is.

$$\Delta_{\phi}^{(h)} = \sqrt{\frac{\omega}{2 \cdot D_s}} \cdot L_y - \frac{\pi}{2} + \tan^{-1} \left(\frac{N}{M} \right) \quad (\text{B56})$$

It is interesting to note that in the case of negligible convection i.e. $h_f = 0$, the expressions for phase and amplitude of the photothermal deflection signal, reduce to the ones with heat transfer by conduction only.

On the other hand, in the case where convection heat transfer dominates i.e. for high h ,

$$\sqrt{\frac{H}{2\omega}} \gg 1 \quad (\text{B57})$$

the equations (B55) and (B56) can be simplified for practical spectroscopic circumstances and reduce to:

$$A_{\phi}^{(h)} = \frac{1}{n_f} \left| \frac{dn_f}{dT_f} \right| \cdot \frac{P_0}{C_s \cdot L_y^2 \cdot L_z} \cdot \frac{1}{\omega^{3/2}} \cdot \left(\frac{1 - e^{-\alpha L_x}}{\alpha \cdot L_x} \right) \cdot \sqrt{\frac{D_s}{D_{\text{eff}}}} \cdot e^{\sqrt{\frac{\omega}{2 \cdot D_s}} \cdot L_y} \cdot H^{1/2} \quad (\text{B58})$$

and

$$\Delta_{\phi}^{(h)} = \sqrt{\frac{\omega}{2 \cdot D_s}} \cdot L_y - \frac{\pi}{2} \quad (\text{B59})$$

The thermal diffusivity by eq. (B59) is the same as calculated without convection, which means that the phase of the thermal wave is unchanged even in the presence of the convection in the case of nanoparticles dispersed in the photothermal fluid. This is indeed the expected result because the phase of the PDS signal depends on the thermal properties of the sample and not on that of the photothermal fluid in which the sample is immersed.

Appendix C: Matlab routine to simulate amplitude of PDS signal

```

% Matlab Routine to simulate the PDS amplitude in the
%presence of convection
clear all
close all
%%%%%%%%%%%%%%%%%%%%%%%%%%%%%%%%%%%%%%%%%%%%%%%%%%%%%%%%%%%%%%%%%%%%%%%%
Lf = 0.3E-3;% 300 micro m
%%%%%%%%%%%%%%%%%%%%%%%%%%%%%%%%%%%%%%%%%%%%%%%%%%%%%%%%%%%%%%%%%%%%%%%%
% Experimental data %%%%%%%%%
% Average amplitude of PDS signal
Ampl_Exp_data =[1.71      2.36      2.92      3.30
2.49      2.66];% [degrees/W] Amplitude normalized with
%absorption of the film and transmittance of fluid in the
%presence of CNTs
Ampl_Exp_data_EB =[0.458      0.435      0.447      0.707
0.617      0.552];% [degrees/W] Amplitude normalized with
absorption of the film and transmittance of fluid with CNTs
fr_exp = [0      0.0012      0.0025      0.0037      0.0050
0.0062];% Volume fraction of CNTs
%%%%%%%%%%%%%%%%%%%%%%%%%%%%%%%%%%%%%%%%%%%%%%%%%%%%%%%%%%%%%%%%%%%%%%%%
% Constants %%%%%%%%%
P0= 0.0298;% Average incident beam power [W] at 2.48eV from
% reference Photodiode signal
T = 300;% Room temperature [K]=23C
Lx = 1.94E-4;% Sample thickness [cm]
Ly = 0.006;% Beam height [m]
Lz = 0.012;% Beam height [m]
w = 20;% Chopping frequency [Hz]
g = 9.8;%m/s2 gravitational acceleration
N_A = 6.02E23;% Avogadro's No
kb = 1.38066E-23;% Boltzmann's constant [J/K]
x = (-0.01:0.001:0);%[m]

```

```

%%%%%%%%%%%%%%%%%%%%%%%%%%%%%%%%%%%%%%%%%%%%%%%%%%%%%%%%%%%%%%%%%%%%%%%%
Lch = (Ly*Lz)/(2*(Ly+Lz));%Critical length for convection
%Area/ perimeter sample
%%%%%%%%%%%%%%%%%%%%%%%%%%%%%%%%%%%%%%%%%%%%%%%%%%%%%%%%%%%%%%%%%%%%%%%% CNTs data %%%%%%%%%
rho_CNT = 1.34E3; % [kg/m3] density of CNTs
m_CNT = 1E-7; % [kg] mass of CNTs i.e 0.1mg
k_CNTs = 2000; % Thermal conductivity of CNTs [W/m/K]
v = m_CNT/rho_CNT; % [m3] volume of CNTs of 0.1 mg of CNTs
%in [mL]
C_CNT = 600; % [J/kgK]
dp=20E-9; % Diameter of CNTs[m]
D_CNT = k_CNTs/(rho_CNT*C_CNT); % Diffusivity of CNTs
fr = [0:max(fr_exp)/1000:max(fr_exp)];
%%%%%%%%%%%%%%%%%%%%%%%%%%%%%%%%%%%%%%%%%%%%%%%%%%%%%%%%%%%%%%%%%%%%%%%% CCl4 data %%%%%%%%%
n_CCl4 = 1.46; %Refractive index of Carbon tetrachloride
dn_dT = 6.1E-4;%temperature coefficient of refractive index
%of CCl4 [K-1]
beta_CCl4 = 1.2E-4; % Temperature coefficient of CCl4[K-1]
k_CCl4 = 0.106; %Thermal conductivity of CCl4[W/mK].
rho_CCl4 = 1.6E3; %Density of CCl4[kg/m3]
C_CCl4 = 850; %Specific heat of CCl4[J/kg/K]
nu_CCl4 = 9.01E-4;%Dynamic Viscosity of CCl4 [kg/m.s]
mu_CCl4 = nu_CCl4/rho_CCl4;%Kinematic viscosity of CCl4
[m2/s]
M_CCl4 = 153.82; % Molecular weight of CCl4
T_fr = 250; % [K]Freezing temperature of CCl4
Df =7.31E-8; % Thermal diffusivity of CCl4 [m2/s]
df = 0.1*((6*M_CCl4)/(N_A*pi*rho_CCl4))^0.333; % Diametor
of fluid molecule, [m]
%%%%%%%%%%%%%%%%%%%%%%%%%%%%%%%%%%%%%%%%%%%%%%%%%%%%%%%%%%%%%%%%%%%%%%%% PEDOT data %%%%%%%%%
k_s = 0.17; %Thermal conductivity of PEDOT film[W/mK]
rho_s = 1.34E3; %Density of PEDOT[kg/m3]

```

```

Ds= 1.14017E-5;% m2/s from Measured Phase of PDS signal
Cs = k_s/Ds; %Thermal capacitance of the thin film sample.
Dsf = (Ds^(-1)+ Df^(-1))^(-1); % Effective Thermal
diffusivity of sample-fluid system [m2/s]
delta_T=(P0*sqrt(w/(2*Ds)*(Ly/2)))/(sqrt(2)*(Ly^2)*Lz*Cs*w)
%%%%%%%%%%%%%%%%%%%%%%%%%%%%%%%%%%%%%%%%%%%%%%%%%%%%%%%%%%%%%%%%%%%%%%%% CCl4 with CNTs %%%%%%%%%%
mu_CCl4_eff = mu_CCl4./(1-(34.87*(dp/df)^(-
0.3))*(fr^(1.03)));
rho_CCl4_eff = ((1-fr).*rho_CCl4)+(fr.*rho_CNT);
C_CCl4_eff = (((1-fr).*C_CCl4*rho_CCl4)+
(fr.*C_CNT*rho_CNT))./(((1-fr).*rho_CCl4)+(fr.*rho_CNT));
beta_CCl4_eff = beta_CCl4;% constant
%%%%%%%%%%%%%%%%%%%%%%%%%%%%%%%%%%%%%%%%%%%%%%%%%%%%%%%%%%%%%%%%%%%%%%%% Dimensionless numbers for CCl4 only%%%%%%%%%
Ra = (g*beta_CCl4*delta_T*Lz^3)/(Df*mu_CCl4)% Rayleigh
number
Pr = mu_CCl4/Df % Prandtl number
Nu = (0.825+0.387*(Ra^(1/6))*(1+(0.492/Pr)^(9/16))^(
8/27))^(2)
%%%%%%%%%%%%%%%%%%%%%%%%%%%%%%%%%%%%%%%%%%%%%%%%%%%%%%%%%%%%%%%%%%%%%%%% Fitting parameters from %%%%%%%%%%
%%%%%%%%%%%%%%%%%%%%%%%%%%%%%%%%%%%%%%%%%%%%%%%%%%%%%%%%%%%%%%%%%%%%%%%% Modeling of CNTs nanofluid %%%%%%%%%%
mmm = 51.84; % (W/(mK))
aaa = 0.441;
bbb = 0.14;
ggg = 0.66;
a_R = 10;% Aspect ratio
%%%%%%%%%%%%%%%%%%%%%%%%%%%%%%%%%%%%%%%%%%%%%%%%%%%%%%%%%%%%%%%%%%%%%%%% Dimensionless numbers for CCl4 with CNTs %%%%%%%%%%
for i=1:length(fr)% Different CNTs concentrations
    k_CCl4_eff(i) = k_CCl4*(1+mmm*((1/dp)^aaa)
    *(a_R^bbb)*(fr(i)^ggg);
    D_eff(i) = k_CCl4_eff(i)/(rho_CCl4_eff(i)
    *C_CCl4_eff(i));

```



```

Dsf_eff(i) = (Ds^(-1)+ D_eff(i)^(-1))^(-1);
Ra_eff(i) = (g*beta_CCl4_eff*delta_T*Lz^3)
/(D_eff(i)*mu_CCl4_eff(i));
Pr_eff(i) = mu_CCl4_eff(i)/D_eff(i);
Nu_eff(i) = (0.825+0.387.*(Ra_eff(i)^(1/6)))*
(1+(0.492/Pr_eff(i))^(9/16))^(8/27))^2;
Lf_eff(i)= Lf*(Ra/Ra_eff(i))^0.25;
h_eff(i)= (Nu_eff(i)*k_CCl4_eff(i))/Lch;
H_eff(i) = h_eff(i)/(rho_CCl4_eff(i)
*C_CCl4_eff(i)*Lf_eff(i));
M(i)= 1+sqrt((H_eff(i)/(2*w)));
N(i) = sqrt((H_eff(i)/(2*w)));

C(i)=((dn_dT*sqrt(Ds/Dsf_eff(i)))/(n_CCl4*Cs*Ly^2*Lz*w
^(1.5))) *exp(sqrt(w/(2*D_s))*Ly)*(sqrt(M(i)^2+N(i)^2)));
for k=1:1:length(x)
    A_eff(i,k)=C(i)*exp(sqrt(w/(2*Dsf_eff(i)))*x(k));
end
end

for i=1:1:length(fr_exp)
    H_exp(i) =
    ((Ampl_Exp_data(i)^2)*(n_CCl4^2)*(Cs^2)*(Ly^4)*(Lz^2)*(w^3)
    )*(Dsf_eff(i)/Ds)*(exp(-2*((w/(2*D_s))^0.5)*Ly))/(dn_dT^2
    H_exp_EB(i)
    =H_exp(i)*(sqrt(2)*(Ampl_Exp_data_EB(i)/Ampl_Exp_data(i)))
    % Assuming that major source of erroer is uncertainty in
    Amplitude
    h_exp(i) = (rho_CCl4_eff(i)*C_CCl4_eff(i)*Lch*H_exp(i));
    h_exp_EB(i) =h_exp(i)*H_exp_EB(i)/H_exp(i); % Assuming
    that major source of error is uncertainty in H_exp
end
end

```

```

figure(1)
errorbar(fr_exp,Ampl_Exp_data, Ampl_Exp_data_EB,
'bs','LineWidth',3)
hold on
plot(fr,A_eff(:,6)*600,'-r','LineWidth',3)
hold off
xlabel ('Volume fraction of CNTs(%)','fontsize',15)
ylabel ('PDS Amplitude(Degrees/W)','fontsize',15)
title('PDS Amplitude')

```

```

figure(2)
errorbar (fr_exp,h_exp,h_exp_EB,'bo','LineWidth',3)
hold on
plot(fr,h_eff,'-r','LineWidth',3)
legend ('Experimental', 'Theoretical')
xlabel ('Volume fraction of CNTs(%)','fontsize',15)
ylabel ('h(W/m2/K1)','fontsize',15)
title('Heat exchange coefficient')

```

```

figure(3)
errorbar( fr_exp,H_exp,H_exp_EB,'bs','LineWidth',3)
hold on
plot( fr,H_eff,'-r','LineWidth',3)
legend ('Experimental', 'Theoretical')
xlabel ('Volume fraction of CNTs(%)','fontsize',15)
ylabel ('H(1/s)','fontsize',15)
title('Heat exchange rate')

```

Appendix D: Copyrights

ELSEVIER LICENSE TERMS AND CONDITIONS

Jul 06, 2013

This is a License Agreement between Muhammad S Ahmed ("You") and Elsevier ("Elsevier") provided by Copyright Clearance Center ("CCC"). The license consists of your order details, the terms and conditions provided by Elsevier, and the payment terms and conditions.

All payments must be made in full to CCC. For payment instructions, please see information listed at the bottom of this form.

Supplier	Elsevier Limited The Boulevard, Langford Lane Kidlington, Oxford, OX5 1GB, UK
Registered Company Number	1982084
Customer name	Muhammad S Ahmed
Customer address	1151 Richmond St. London, ON N6A 3K7
License number	3183371396457
License date	Jul 06, 2013
Licensed content publisher	Elsevier
Licensed content publication	Carbon
Licensed content title	Relationship between electrical and thermal conductivity in graphene-based transparent and conducting thin films
Licensed content author	M. Shafiq Ahmed, Sabastine Ezugwu, Ranjith Divigalpitiya, Giovanni Fanchini
Licensed content date	September 2013
Licensed content volume number	61
Licensed content issue number	
Number of pages	7
Start Page	595

End Page	601
Type of Use	reuse in a thesis/dissertation
Intended publisher of new work	other
Portion	full article
Format	both print and electronic
Are you the author of this Elsevier article?	Yes
Will you be translating?	No
Order reference number	
Title of your thesis/dissertation	PHOTOTHERMAL DEFLECTION SPECTROSCOPY OF AMORPHOUS, NANOSTRUCTURED AND NANOCOMPOSITE THIN FILMS
Expected completion date	Aug 2013
Estimated size (number of pages)	200
Elsevier VAT number	GB 494 6272 12
Permissions price	0.00 USD
VAT/Local Sales Tax	0.00 USD / 0.00 GBP
Total	0.00 USD
Terms and Conditions	

INTRODUCTION

1. The publisher for this copyrighted material is Elsevier. By clicking "accept" in connection with completing this licensing transaction, you agree that the following terms and conditions apply to this transaction (along with the Billing and Payment terms and conditions established by Copyright Clearance Center, Inc. ("CCC"), at the time that you opened your Rightslink account and that are available at any time at <http://myaccount.copyright.com>).

GENERAL TERMS

2. Elsevier hereby grants you permission to reproduce the aforementioned material subject to the terms and conditions indicated.

3. Acknowledgement: If any part of the material to be used (for example, figures) has appeared in our publication with credit or acknowledgement to another source, permission must also be sought from that source. If such permission is not obtained then that material may not be included in your publication/copies. Suitable acknowledgement to the source must be made, either as a footnote or in a reference list at the end of your publication, as follows:

“Reprinted from Publication title, Vol /edition number, Author(s), Title of article / title of chapter, Pages No., Copyright (Year), with permission from Elsevier [OR APPLICABLE SOCIETY COPYRIGHT OWNER].” Also Lancet special credit - “Reprinted from The Lancet, Vol. number, Author(s), Title of article, Pages No., Copyright (Year), with permission from Elsevier.”

4. Reproduction of this material is confined to the purpose and/or media for which permission is hereby given.

5. Altering/Modifying Material: Not Permitted. However figures and illustrations may be altered/adapted minimally to serve your work. Any other abbreviations, additions, deletions and/or any other alterations shall be made only with prior written authorization of Elsevier Ltd. (Please contact Elsevier at permissions@elsevier.com)

6. If the permission fee for the requested use of our material is waived in this instance, please be advised that your future requests for Elsevier materials may attract a fee.

7. Reservation of Rights: Publisher reserves all rights not specifically granted in the combination of (i) the license details provided by you and accepted in the course of this licensing transaction, (ii) these terms and conditions and (iii) CCC's Billing and Payment terms and conditions.

8. License Contingent Upon Payment: While you may exercise the rights licensed immediately upon issuance of the license at the end of the licensing process for the transaction, provided that you have disclosed complete and accurate details of your proposed use, no license is finally effective unless and until full payment is received from you (either by publisher or by CCC) as provided in CCC's Billing and Payment terms and conditions. If full payment is not received on a timely basis, then any license preliminarily granted shall be deemed automatically revoked and shall be void as if never granted. Further, in the event that you breach any of these terms and conditions or any of CCC's Billing and Payment terms and conditions, the license is automatically revoked and shall be void as if never granted. Use of materials as described in a revoked license, as well as any use of the materials beyond the scope of an unrevoked license, may constitute copyright infringement and publisher reserves the right to take any and all action to protect its copyright in the materials.

9. Warranties: Publisher makes no representations or warranties with respect to the licensed material.

10. Indemnity: You hereby indemnify and agree to hold harmless publisher and CCC, and their respective officers, directors, employees and agents, from and against any and all claims arising out of your use of the licensed material other than as specifically authorized pursuant to this license.

11. No Transfer of License: This license is personal to you and may not be sublicensed,

assigned, or transferred by you to any other person without publisher's written permission.

12. **No Amendment Except in Writing:** This license may not be amended except in a writing signed by both parties (or, in the case of publisher, by CCC on publisher's behalf).

13. **Objection to Contrary Terms:** Publisher hereby objects to any terms contained in any purchase order, acknowledgment, check endorsement or other writing prepared by you, which terms are inconsistent with these terms and conditions or CCC's Billing and Payment terms and conditions. These terms and conditions, together with CCC's Billing and Payment terms and conditions (which are incorporated herein), comprise the entire agreement between you and publisher (and CCC) concerning this licensing transaction. In the event of any conflict between your obligations established by these terms and conditions and those established by CCC's Billing and Payment terms and conditions, these terms and conditions shall control.

14. **Revocation:** Elsevier or Copyright Clearance Center may deny the permissions described in this License at their sole discretion, for any reason or no reason, with a full refund payable to you. Notice of such denial will be made using the contact information provided by you. Failure to receive such notice will not alter or invalidate the denial. In no event will Elsevier or Copyright Clearance Center be responsible or liable for any costs, expenses or damage incurred by you as a result of a denial of your permission request, other than a refund of the amount(s) paid by you to Elsevier and/or Copyright Clearance Center for denied permissions.

LIMITED LICENSE

The following terms and conditions apply only to specific license types:

15. **Translation:** This permission is granted for non-exclusive world **English** rights only unless your license was granted for translation rights. If you licensed translation rights you may only translate this content into the languages you requested. A professional translator must perform all translations and reproduce the content word for word preserving the integrity of the article. If this license is to re-use 1 or 2 figures then permission is granted for non-exclusive world rights in all languages.

16. **Website:** The following terms and conditions apply to electronic reserve and author websites:

Electronic reserve: If licensed material is to be posted to website, the web site is to be password-protected and made available only to bona fide students registered on a relevant course if:

This license was made in connection with a course,

This permission is granted for 1 year only. You may obtain a license for future website posting,

All content posted to the web site must maintain the copyright information line on the bottom of each image,

A hyper-text must be included to the Homepage of the journal from which you are

licensing at <http://www.sciencedirect.com/science/journal/xxxxx> or the Elsevier homepage for books at <http://www.elsevier.com> , and

Central Storage: This license does not include permission for a scanned version of the material to be stored in a central repository such as that provided by Heron/XanEdu.

17. **Author website** for journals with the following additional clauses:

All content posted to the web site must maintain the copyright information line on the bottom of each image, and the permission granted is limited to the personal version of your paper. You are not allowed to download and post the published electronic version of your article (whether PDF or HTML, proof or final version), nor may you scan the printed edition to create an electronic version. A hyper-text must be included to the Homepage of the journal from which you are licensing

at <http://www.sciencedirect.com/science/journal/xxxxx> . As part of our normal production process, you will receive an e-mail notice when your article appears on Elsevier's online service ScienceDirect (www.sciencedirect.com). That e-mail will include the article's Digital Object Identifier (DOI). This number provides the electronic link to the published article and should be included in the posting of your personal version. We ask that you wait until you receive this e-mail and have the DOI to do any posting.

Central Storage: This license does not include permission for a scanned version of the material to be stored in a central repository such as that provided by Heron/XanEdu.

18. **Author website** for books with the following additional clauses:

Authors are permitted to place a brief summary of their work online only.

A hyper-text must be included to the Elsevier homepage at <http://www.elsevier.com> . All content posted to the web site must maintain the copyright information line on the bottom of each image. You are not allowed to download and post the published electronic version of your chapter, nor may you scan the printed edition to create an electronic version.

Central Storage: This license does not include permission for a scanned version of the material to be stored in a central repository such as that provided by Heron/XanEdu.

19. **Website** (regular and for author): A hyper-text must be included to the Homepage of the journal from which you are licensing at <http://www.sciencedirect.com/science/journal/xxxxx>. or for books to the Elsevier homepage at <http://www.elsevier.com>

20. **Thesis/Dissertation**: If your license is for use in a thesis/dissertation your thesis may be submitted to your institution in either print or electronic form. Should your thesis be published commercially, please reapply for permission. These requirements include permission for the Library and Archives of Canada to supply single copies, on demand, of the complete thesis and include permission for UMI to supply single copies, on demand, of the complete thesis. Should your thesis be published commercially, please reapply for permission.

21. Other Conditions:

v1.6

If you would like to pay for this license now, please remit this license along with your payment made payable to "COPYRIGHT CLEARANCE CENTER" otherwise you will be invoiced within 48 hours of the license date. Payment should be in the form of a check or money order referencing your account number and this invoice number RLNK501059841.

Once you receive your invoice for this order, you may pay your invoice by credit card. Please follow instructions provided at that time.

**Make Payment To:
Copyright Clearance Center
Dept 001
P.O. Box 843006
Boston, MA 02284-3006**

For suggestions or comments regarding this order, contact RightsLink Customer Support: customercare@copyright.com or +1-877-622-5543 (toll free in the US) or +1-978-646-2777.

Gratis licenses (referencing \$0 in the Total field) are free. Please retain this printable license for your reference. No payment is required.

Curriculum Vitae

Name: Muhammad Shafiq Ahmed

Post-secondary Education and Degrees: University of Azad Jammu and Kashmir
Pakistan.
1987-1990 B.Sc. (Physics, Math)

The University of Punjab
Lahore, Pakistan.
1990-1992 M.Sc. Physics.

The University of Ontario Institute of Technology
Oshawa, Ontario, Canada
2007-2009 M.Sc. Materials Science.

Western University,
London, ON
2009-2013 Ph.D. Condensed Matter Physics (Experimental)

Honours and Awards: Graduate Thesis Research Award 2013.
Best Poster Award, Canadian Association of Physics (CAP) 2012.
Western Graduate Research Scholarship (Physics) 2009-2013.
Western Graduate Scholarship (Science) 2009.
TD Canada Financial Group Graduate Student Scholarship 2009.
Continuing Graduate Student Scholarship
Grad. Studies, University of Ontario Institute of Technology 2008.

Related Work Experience: Teaching Assistant
Western University,
London, Ontario, Canada
2009 – 2013

Teaching Assistant
University of Ontario Institute of Technology,
Oshawa, Ontario, Canada
2007 – 2009

Publications:

1. Relationship between electrical and thermal conductivity in graphene-based transparent and conducting thin films.
M. Shafiq Ahmed, Sabastine Ezugwu, Ranjith Divigalpitiya, and Giovanni Fanchini, *Carbon* **61** (2013) 595.
2. Staebler-Wronski effect, thermal conductivity, and self-repair of hydrogenated amorphous silicon (a-Si:H) during light-induced degradation.
M. Shafiq Ahmed, Franco Gaspari and Giovanni Fanchini.
(Under revision).
3. “Influence of the addition of graphene-based materials on thermophysical properties of Poly(3,4-ethylenedioxythiophene):poly(styrenesulfonate) (PEDOT:PSS) thin film composites”
Sabastine Ezugwu, **M. Shafiq Ahmed**, R. Bauld, R. Divigalpitiya, G. Fanchini, *Thin Solid Films* **534** (2013) 520.
4. Transparent and conducting graphene–RNA based nanocomposites.
F. Sharifi, R. Bauld , **M. Shafiq Ahmed** , and G. Fanchini, *Small* **8** (2012) 699.